



Laporan Akhir Projek Penyelidikan Jangka Pendek

**Development of Carbon Nanotubes
Supported Ionic Liquid Membrane (SILM)
and Their Application in Pervaporation
Process**

by

Assoc. Prof. Dr. Tan Soon Huat

Assoc. Prof. Dr. Sharif Hussein Sharif Zein

2015

Please email a softcopy of this report to rcmo@usm.my

A PROJECT DETAILS	
i	<p>Title of Research:</p> <p>Development of Carbon Nanotubes Suported Ionic Liquid Membranes (SILM) and Their Application in Pervaporation Process</p>
ii	<p>Account Number: 1001/PJKIMIA/814142</p>
iii	<p>Name of Research Leader: Assoc. Prof. Dr. Tan Soon Huat</p>
iv	<p>Name of Co-Researcher:</p> <ol style="list-style-type: none"> 1. Assoc. Prof. Dr. Sharif Hussein Sharif Zein 2. 3.
v	<p>Duration of this research:</p> <ol style="list-style-type: none"> a) Start Date : 15 August 2011 b) Completion Date : 14 August 2014 c) Duration : 36 months d) Revised Date (if any) : 31 August 2015
B ABSTRACT OF RESEARCH	
<p>(An abstract of between 100 and 200 words must be prepared in Bahasa Malaysia and in English. This abstract will be included in the Report of the Research and Innovation Section at a later date as a means of presenting the project findings of the researcher/s to the University and the community at large)</p> <p>Abstrak</p> <p><i>Kajian ini bertujuan untuk membangunkan membran cecair berpenyokong dengan kestabilan yang tinggi dengan menggunakan kertas-bucky sebagai substrat berliang dan diperangkap dengan cecair ionik 1-butil-metilimidazolium tetrafluoroborat [Bmim][BF₄] untuk membentuk membran cecair ionik berpenyokong kertas-bucky. Untuk meningkatkan lagi kestabilan membran, [Bmim][BF₄] telah dicampur dengan polivinil alkohol sebelum diperangkap dalam</i></p>	

kertas-bucky. Prestasi membran cecair ionik berpenyokong kertas-bucky dalam proses penyejattelapan yang melibatkan campuran perduaan yang terdiri daripada etilena glikol dan air menunjukkan keupayaan membran tersebut dalam penyahhidratan larutan akueus etilena glikol. Membran cecair ionik berpenyokong kertas-bucky telah menunjukkan prestasi penyejattelapan yang tinggi dengan fluks penelapan yang bernilai $102 \text{ g}\cdot\text{m}^{-2}\cdot\text{j}^{-1}$, faktor pemisahan setinggi 1014, kebolehtelapan air yang bernilai 13106 GPU dan kememilihan membran untuk air yang bernilai 13 dengan berat air dalam kepekatan larutan suapan sebanyak 10% pada suhu $30 \text{ }^{\circ}\text{C}$ dan 5 mmHg tekanan hilitan. Di samping itu, membran cecair ionik berpenyokong kertas-bucky juga mampu untuk memisahkan campuran pertigaan; etil asetat, etanol dan air yang membentuk azeotrop. Fluks penelapan sebanyak $385 \text{ g}\cdot\text{m}^{-2}\cdot\text{j}^{-1}$, faktor pemisahan yang bernilai 247, kebolehtelapan air 4730 GPU dan kememilihan membran untuk air yang bernilai 39 telah diperolehi pada suhu $30 \text{ }^{\circ}\text{C}$ dan 5 mmHg tekanan hilitan.

Abstract

In the present research work, it is aimed to develop a high stability supported liquid membrane (SLM) by employing buckypaper (BP) as supporting membrane and immobilized with an ionic liquid 1-butyl-3-methylimidazolium tetrafluoroborate [Bmim][BF₄] to form a buckypaper supported ionic liquid membrane (BP-SILM). In order to further enhance the membrane stability, the [Bmim][BF₄] was blended with polyvinyl alcohol (PVA) prior to the immobilization in the BP. The pervaporation performances of the BP-SILM in the binary mixture of ethylene glycol and water showed an excellent capability to dehydrate ethylene glycol aqueous solutions. The BP-SILM exhibited high pervaporation performance with a permeation flux of $102 \text{ g}\cdot\text{m}^{-2}\cdot\text{h}^{-1}$, separation factor as high as 1014, water permeance of 13106 GPU and membrane selectivity of 13 for water with 10 wt.% feed concentration of water at $30 \text{ }^{\circ}\text{C}$ and 5 mmHg downstream pressure. On the other hand, the BP-SILM was also capable to break ternary azeotropic mixtures of ethyl acetate, ethanol and water. A permeation flux of $385 \text{ g}\cdot\text{m}^{-2}\cdot\text{h}^{-1}$, separation factor of 247, water permeance of 4730 GPU and membrane selectivity of 39 for water were obtained at $30 \text{ }^{\circ}\text{C}$ and 5 mmHg downstream pressure.

BUDGET & EXPENDITURE

i

Total Approved Budget : RM238,650.00

Yearly Budget Distributed

Year 1 : RM101,150.00

Year 2 : RM76,250.00

Year 3 : RM62,250.00

Total Expenditure : RM238,617.44

Balance : RM32.56

Percentage of Amount Spent (%) : 99.99%

Please attach final account statement (eStatement) to indicate the project expenditure

.ii Equipment Purchased Under Vot 35000				
No.	Name of Equipment	Amount (RM)	Location	Status
1.	BOC Edward Vacuum Pump, Model:Edward RV3, with gas ballast valve	11,000.00	Bioprocess Lab	Good
2.	Vacuum Pump RV3, Edward	7,000.00	Bioprocess Lab	Good
3.	Cyrogenic Liquid Dewar Tank	9,368.00	Bioprocess Lab	Good
4.	Samsung Galaxy Note Tablet 10.1	2,270.00	Lecturer Office	Good

Please attach the Asset/Inventory Return Form (Borang Penyerahan Aset/Inventori) – Appendix 1

D RESEARCH/ACHIEVEMENTS

i Project Objectives (as stated/approved in the project proposal)

No.	Project Objectives	Achievement
1	To develop SILM by immobilizing an organic liquid phase in the CNT pores before incorporating into the MMM	A novel symmetric supported ionic liquid membrane (SILM) was prepared by infiltrating 1-butyl-3-methylimidazolium tetrafluoroborate [Bmim][BF4] into a buckypaper (BP) to form a so-called buckypaper supported ionic liquid membrane (BP-SILM)
2	To investigate the role of CNTs in the developed SILM	The role of BP as a support can effectively entrap the infiltrated [Bmim][BF4]-PVA in the interstitial pores and supply the necessary mechanical stability for the resulting BP-SILM.
3	To optimize the organic-organic pervaporation separation by using SILM	The BP-SILM exhibited high pervaporation performance for dehydration of ethylene glycol with a permeation flux of 102 g/m ² ·h, a separation factor as high as 1014, and a water permeance of 9046 gpu.

ii Research Output

a) Publications in ISI Web of Science/Scopus

No.	Publication (authors,title,journal,year,volume,pages,etc.)	Status of Publication (published/accepted/ under review)
1.	Ong, Y. T.; Tan, S. H., Pervaporation Separation of a Ternary Azeotrope Containing Ethyl Acetate, Ethanol and Water Using a Buckypaper Supported Ionic Liquid Membrane. <i>Chem. Eng. Res. Des.</i> 2016 , 109, 116-126.	Published
2.	Ong, Y. T.; Tan, S. H., Synthesis of the Novel Symmetric Buckypaper Supported Ionic Liquid Membrane for the Dehydration of Ethylene Glycol by Pervaporation. <i>Sep. Purif. Technol.</i> 2015 , 143, 135-145.	Published
3.	Shuit, S. H.; Ng, E. P.; Tan, S. H., A Facile and Acid-free Approach towards the Preparation of Sulphonated Multi-walled Carbon Nanotubes as a Strong Protonic Acid Catalyst for Biodiesel Production. <i>J. Taiwan Inst. Chem. Eng.</i> 2015 , 52, 100-108.	Published
4.	Shuit, S. H.; Tan, S. H., Biodiesel Production via Esterification of Palm Fatty Acid Distillate Using Sulphonated Multi-walled Carbon Nanotubes as a Solid Acid Catalyst: Process Study, Catalyst Reusability and Kinetic Study. <i>BioEnergy Res.</i> 2015 , 8, (2), 605-617.	Published
5.	Ong, Y. T.; Yee, K. F.; Cheng, Y. K.; Tan, S. H., A Review on the Use and Stability of Supported Liquid Membranes in the Pervaporation Process. <i>Sep. Purif. Rev.</i> 2014 , 43, (1), 62-88.	Published
6.	Cheng, Y. K.; Yeang, Q. W.; Mohamed, A. R.; Tan, S. H., Study on the Reusability of Multiwalled Carbon Nanotubes in Biodegradable Chitosan Nanocomposites. <i>Polym.-Plast. Technol. Eng.</i> 2014 , 53, (12), 1236-1250.	Published
7.	Shuit, S. H.; Tan, S. H., Feasibility Study of Various Sulphonation Methods for Transforming Carbon Nanotubes into Catalysts for the Esterification of Palm Fatty Acid Distillate. <i>Energy Conv. Manag.</i> 2014 , 88, 1283-1289.	Published
8.	Shuit, S. H.; Yee, K. F.; Lee, K. T.; Subhash, B.; Tan, S. H., Evolution Towards the Utilisation of Functionalised Carbon Nanotubes as a New Generation Catalyst Support in Biodiesel Production: An Overview. <i>RSC Advances</i> 2013 , 3, (24), 9070-9094.	Published

b) Publications in Other Journals

No.	Publication (authors,title,journal,year,volume,pages,etc.)	Status of Publication (published/accepted/ under review)

c) Other Publications (book, chapters in book, monograph, magazine, etc.)			
No.	Publication (authors, title, journal, year, volume, pages, etc.)	Status of Publication (published/accepted/ under review)	
d) Conference Proceeding			
No.	Conference (conference name, date, place)	Title of Abstract/Article	Level (International/National)
1.	2nd International Symposium on Green Chemistry, 21 -24 May 2013/La Rochelle, France	Biodiesel Production From Palm Fatty Acid Distillate Using Sulfonated Multi-walled Carbon Nanotubes	International
2.	Chemeca 2012, 23 – 26 September 2012/The Museum of New Zealand Te Papa Tongarewa, Wellington, New Zealand	Structure Modification of Multi-walled Carbon Nanotubes Buckypaper Using Polyvinyl alcohol: Fabrication and Characterization	International
3.	International Conference on Environment 2012 (ICENV 2012), 11 – 13 December 2012/ Parkroyal Hotel, Penang	Separation of Etherification Reaction Mixture Using MWCNTs Buckypaper/Polyvinyl Alcohol Membrane via Pervaporation	International
# Please attach a full copy of the publication/proceeding listed above			
iii Other Research Output/Impact From This Project (patent, products, awards, copyright, external grant, networking, etc.)			
Sanggar Sanjung Award in the category of publication.			

E HUMAN CAPITAL DEVELOPMENT			
a) Graduated Human Capital			
Student	Nationality (No.)		Name
	National	International	
PhD	√		1. Shuit Siew Hoong 2. Ong Yit Thai
MSc	√		1. Cheng Yoke Kooi

Undergraduate	√		1. Ng Gin Shung 2. Nur Syafiq bt. Bajuri 3. Chang Kim Hoe 4. Che Saberi bin Che Hussin 5. Teo Cui Ying 6. Ng Fung Khiang 7. Asrin Haikal
---------------	---	--	--

b) On-going Human Capital

Student	Nationality (No.)		Name
	National	International	
PhD	√		1. Yeang Qian Wen 2.
MSc			1. 2.
Undergraduate			1. 2.

c) Others Human Capital

Student	Nationality (No.)		Name
	National	International	
Post Doctoral Fellow			1. 2.
Research Officer			1. 2.
Research Assistant			1. 2.
Others (.....)			1. 2.

F COMPREHENSIVE TECHNICAL REPORT

Applicants are required to prepare a comprehensive technical report explaining the project. The following format should be used (this report must be attached separately):

- Introduction
- Objectives
- Methods
- Results
- Discussion
- Conclusion and Suggestion
- Acknowledgements
- References

G PROBLEMS/CONSTRAINTS/CHALLENGES IF ANY

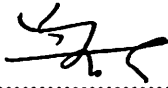
(Please provide issues arising from the project and how they were resolved)

RECOMMENDATION

(Please provide recommendations that can be used to improve the delivery of information, grant management, guidelines and policy, etc.)

RUI grant should award to those who have good research track record.

Project Leader's Signature:



Name :

DR. TAN SOON HUAT

Date :

Associate Professor
School of Chemical Engineering
Engineering Campus
Universiti Sains Malaysia
14300 Nibong Tebal
Pulau Pinang, Malaysia.

11/7/2016

COMMENTS, IF ANY/ENDORSEMENT BY PTJ'S RESEARCH COMMITTEE

Good achievement in terms of knowledge generation,
publication of research articles and training of
undergraduate / postgraduate students.



Signature and Stamp of Chairperson of PTJ's Evaluation Committee

PROFESSOR DR AHMAD ZUHAIRI ABDULLAH
Deputy Dean (Research, Postgraduate & Networking),
School of Chemical Engineering,

Name : Universiti Sains Malaysia, Engineering Campus,
Nibong Tebal, Penang, Malaysia.

Date : 13/07/2016



15/7/16

Signature and Stamp of Dean/ Director of PTJ

Name : PROFESOR AZLINA HARUN @ KAMARUDDIN
Dekan

Date : Pusat Pengajian Kejuruteraan Kimia
Kampus Kejuruteraan
Universiti Sains Malaysia, Seri Ampangan
14300 Nibong Tebal, Seberang Perai Selatan
Pulau Pinang.

UNIVERSITI SAINS MALAYSIA
 UNIT KUMPULAN WANG PENYELIDIKAN/RU
 JABATAN BENDAHARI KAMPUS KEJURUTERAAN
 PENYATA KUMPULAN WANG
 TEMPOH BERAKHIR 9/2015

9/22/2015

Tajuk Projek : DEVELOPMENT OF CARBON NANOTUBES SUPPORT IONIC LIQUID MEMBRANE
 (SILM) AND THEIR APPLICATION IN PERVAPORATION PROCESS
 DR TAN SOO HUAT
 Pusat Pengajian : Pusat Pengajian Kejuruteraan Kimia
 Penyelidik : TAN SOO HUAT

Status Projek : AKTIF

No Projek (Agensi) : KEJURUTERAAN & TEKNOLOGI

Tempoh Projek : 2011 / 8 - 2015 / 9

No Akaun : 1001 / 814142

Vot	Keterangan	Peruntukan	Perbelanjaan	Peruntukan	Tanggung	Belanja	Jumlah Belanja	Baki		%
		Asal	Tahun Lalu	Semasa				(d)	(e)	
		(a)	(b)	(c)						
11000	Gaji	60,365.02	\$0.00	\$0.00	\$0.00	\$20,000.00	\$20,000.00	\$40,365.02		0.00
		\$60,365.02	\$0.00	0.00	\$0.00	\$20,000.00	\$20,000.00	\$40,365.02		0.00
21000	PERJALANAN DAN SARA HIDUP	9,109.00	\$0.00	\$0.00	\$0.00	\$334.10	\$334.10	\$8,774.90		0.00
23000	PERHUBUNGAN DAN UTILITI	(10.20)	\$0.00	\$0.00	\$0.00	\$0.00	\$0.00	(\$10.20)		0.00
24000	SEWAAN	207.83	\$0.00	\$0.00	\$92.82	\$31.62	\$124.44	\$83.39		0.00
27000	BEKALAN DAN ALAT PAKAI HABIS	(30,167.62)	\$0.00	\$0.00	\$0.00	\$1,400.94	\$1,400.94	(\$31,568.56)		0.00
28000	PENYELENGGARAAN DAN PEMBAIKAN KECIL	4,000.00	\$6,560.00	\$0.00	\$0.00	\$400.00	\$400.00	(\$2,960.00)		0.00
29000	PERKHIDMATAN IKTISAS DAN HOSPITALITI	(8,726.99)	\$0.00	\$0.00	\$1,950.00	\$6,305.00	\$8,255.00	(\$16,981.99)		0.00
		(\$25,587.98)	\$6,560.00	0.00	\$2,042.82	\$8,471.66	\$10,514.48	(\$42,662.46)		0.00
35000	HARTA-HARTA MODAL LAIN	11,530.00	\$0.00	\$0.00	\$9,200.00	\$0.00	\$9,200.00	\$2,330.00		0.00
		\$11,530.00	\$0.00	0.00	\$9,200.00	\$0.00	\$9,200.00	\$2,330.00		0.00
		\$46,307.04	\$6,560.00	\$0.00	\$11,242.82	\$28,471.66	\$39,714.48	\$32.56		0.00


BORANG PENYERAHAN ASET / INVENTORI
A. BUTIR PENYELIDIK


1. NAMA PENYELIDIK : Assoc. Prof. Dr. Tan Soon Huat
 2. NO STAF : USM0752/08
 3. PTJ : Pusat Pengajian Kejuruteraan Kimia
 4. KOD PROJEK :
 5. TARIKH TAMAT PENYELIDIKAN : 31 Ogos 2015

B. MAKLUMAT ASET / INVENTORI

BIL	KETERANGAN ASET	NO HARTA	NO. SIRI	HARGA (RM)
1.	BOC Edward Vacuum Pump, Model:Edward RV3, with gas ballast valve	3AK00006697PJKIMIA	119490134	11,000.00
2.	Vacuum Pump RV3, Edward	3AK00007375PJKIMIA	139468977	7,000.00
3.	Cyrogenic Liquid Dewar Tank	3AK00007926PJKIMIA	NPB2015010005J	9,368.00
4.	Samsung Galaxy Note Tablet 10.1	-	RF1CADDG9GE	2,270.00

C. PERAKUAN PENYERAHAN

Saya dengan ini menyerahkan aset/ inventori seperti butiran B di atas kepada pihak Universiti:


 (Dr. Tan Soon Huat)

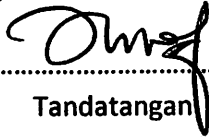
Tarikh: 11/7/2016

D. PERAKUAN PENERIMAAN

Saya telah memeriksa dan menyemak setiap alatan dan didapati :

- Lengkap
 Rosak
 Hilang : Nyatakan.....
 Lain-lain : Nyatakan

Diperakukan Oleh :


 Tandatangan
 Pegawai Aset PTJ

Nama
 Tarikh

MOHD YUSOF BIN ISMAIL
 Panojong Jurutera
 Pusat Pengajian Kejuruteraan Kimia
 Kampus Kejuruteraan
 Universiti Sains Malaysia
 11/7/2016

*Nota : Sesalinan borang yang telah lengkap perlulah dikemukakan kepada Unit Pengurusan Harta, Jabatan Bendahari dan Pejabat RCMO untuk tujuan rekod.



Contents lists available at ScienceDirect

Chemical Engineering Research and Design

journal homepage: www.elsevier.com/locate/cherd

iChemE ADVANCING CHEMICAL ENGINEERING WORLDWIDE



Pervaporation separation of a ternary azeotrope containing ethyl acetate, ethanol and water using a buckypaper supported ionic liquid membrane

Yit Thai Ong, Soon Huat Tan*

School of Chemical Engineering, Engineering Campus, Universiti Sains Malaysia, Seri Ampangan, 14300 Nibong Tebal, S.P.S., Pulau Pinang, Malaysia

ARTICLE INFO

Article history:

Received 15 June 2015

Received in revised form

12 October 2015

Accepted 28 October 2015

Available online 14 January 2016

Keywords:

Buckypaper supported ionic liquid membrane

Ethyl acetate/ethanol/water azeotrope

Pervaporation

ABSTRACT

In this study, the pervaporation separation characteristic of a buckypaper supported ionic liquid membrane (BP-SILM-70) in a ternary azeotropic mixture of ethyl acetate/ethanol/water was investigated. The sorption characteristics of the membrane were assessed through a liquid sorption study, and the preference of the membrane to interact with the components in the feed mixtures was evaluated based on binary interaction parameters. Prior to the pervaporation of the ternary mixture system, pervaporation studies of binary mixture systems composed of ethyl acetate/water, ethanol/water and ethyl acetate/ethanol were performed to evaluate the inter-molecular interaction between these components and their tendency to interact with the BP-SILM-70. The membrane was subsequently applied to the pervaporation separation of the ternary azeotrope system, and the effects of the feed temperature and downstream pressure on the pervaporation performance of the membrane were systemically investigated. The BP-SILM-70 exhibited a good pervaporation performance with a total permeation flux of $385.33 \text{ g}\cdot\text{m}^{-2}\cdot\text{h}^{-1}$ and a separation factor as high as 247 at a temperature of 30°C and a downstream pressure of 0.667 kPa. The pervaporation result suggests that the use of BP-SILM-70 has great potential to attain a good balance in the trade-off between the permeation flux and the separation factor.

© 2016 The Institution of Chemical Engineers. Published by Elsevier B.V. All rights reserved.

1. Introduction

Pervaporation is one of the most studied membrane separation processes in the past several decades. The characteristics of pervaporation make this process particularly useful for the separation of close-boiling-point and azeotropic liquid mixtures. These characteristics are mediated by the chemical activity difference across the membrane and a selective control of the mass transfer based on the affinity of the membrane to interact with a specific component. Pervaporation offers the advantages of lower energy consumption and simplified downstream processing because it avoids the addition of an entrainer, which is commonly used in conventional

distillation to separate azeotropic mixtures. Thus, this process is more economically attractive. Furthermore, pervaporation can be combined with other separation methods, such as distillation, to form a hybrid system that can improve the overall performance of separation processes (Del Pozo Gomez et al., 2008; Koczka et al., 2007). In fact, pervaporation has found its most viable application in the dehydration of organic solvents, the removal of organic compounds from their aqueous solution and the separation of organic–organic mixtures. However, recent interest in the separation of multi-component liquid mixtures represents a challenge to the pervaporation process. The presence of multiple components in liquid mixtures gives rise to a strong competition among the components to interact

* Corresponding author. Tel.: +60 4 5996475; fax: +60 4 5941013.

E-mail address: chshtan@usm.my (S.H. Tan).

<http://dx.doi.org/10.1016/j.cherd.2015.10.051>

0263-8762/© 2016 The Institution of Chemical Engineers. Published by Elsevier B.V. All rights reserved.

with the membrane. In addition, there is also the possibility of the co-permeation of the multi-component mixtures, which would critically affect the separation performance of the membrane in the pervaporation process.

Ethyl acetate is an important solvent for many applications in the chemical industry, such as coatings, adhesives, plasticizers and pharmaceuticals (Hasanoğlu et al., 2007), because it is relatively non-toxic, non-hygroscopic and soluble in most organic liquids. The industrial production of ethyl acetate is primarily based on the classical Fischer esterification process of acetic acid with excess ethanol (McMurry, 2000; Monick, 1968). The resultant ethyl acetate forms an azeotrope with the water and the residual ethanol (Yongquan et al., 2012), which may result in difficulties associated with the purification of ethyl acetate through the conventional distillation process. The conventional process requires the use of an entrainer to effectively separate the azeotropic mixtures. The presence of the entrainer may contaminate the product and complicate the purification process. Therefore, several studies have attempted to break the azeotropic mixture of ethyl acetate, ethanol and water through a pervaporation process (Hu et al., 2012; Xia et al., 2012; Yuan et al., 2011; Zhang et al., 2009), and the outcome seems promising.

Buckypaper supported ionic liquid membrane (BP-SILM-70) is a type of supported ionic liquid membrane. It was prepared by blending an ionic liquid, 1-butyl-3-methylimidazolium tetrafluoroborate ([Bmim][BF₄]), with polyvinyl alcohol (PVA) to form a [Bmim][BF₄]-PVA compound and was subsequently immobilized into the interstitial pores of the buckypaper (BP). The [Bmim][BF₄] served as a liquid membrane phase to selectively regulate the mass transfer while PVA stabilized the ionic liquid through the formation of [Bmim][BF₄]-PVA compound, whereas the BP served as a porous support to hold the [Bmim][BF₄]-PVA in its pores and supply the mechanical stability for the resulted BP-SILM-70. In our previous study, the BP-SILM-70 was successfully applied for the pervaporation-based dehydration of a binary liquid mixture system consisting of ethylene glycol and water (Ong and Tan, 2015). It demonstrated excellent pervaporation performance in the separation of water from the binary mixture system. Thus, in this study, our aim was to investigate the pervaporation performance of the BP-SILM-70 for the separation of a ternary mixture system consisting of ethyl acetate, ethanol and water. As mentioned previously, these three components form an azeotrope; hence, the ability to use the BP-SILM-70 to break the azeotropic mixture via a pervaporation process was studied at different feed temperatures and downstream pressures. Prior to separation of the ternary mixture, pervaporation studies were performed on binary mixture systems composed of two of the three components, i.e., ethyl acetate/water, ethanol/water and ethyl acetate/ethanol. These studies helped elucidate the components' inter-molecular interactions.

2. Experimental

2.1. Materials

Multi-walled carbon nanotubes (MWCNTs) manufactured via the chemical vapour deposition technique were supplied by Chengdu Organic Chemical Co. Ltd, China. These had an outer diameter in the range of 8 to 15 nm, an inner diameter in the range of 3 to 5 nm and a length of approximately 50 μm.

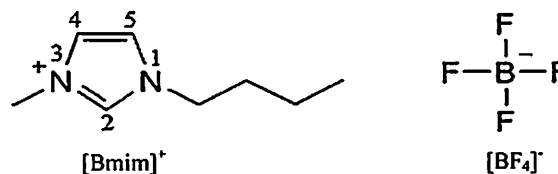


Fig. 1 – Chemical structure of [Bmim]⁺ and [BF₄]⁻ in [Bmim][BF₄].

PVA (95% hydrolysed) with an average molecular weight of 95,000 and [Bmim][BF₄] (98%), which consists of a 1-butyl-3-methylimidazolium cation ([Bmim]⁺) and a tetrafluoroborate anion ([BF₄]⁻), as illustrated in Fig. 1, were purchased from Acros. Sulphuric acid (95–97%), hydrogen peroxide (30%), glutaraldehyde (25% aqueous solution) and ethyl acetate were procured from Merck. Ethanol (96%) and acetone were supplied from HmbG and Fine Chemicals, respectively. Distilled water was used throughout the experiments.

2.2. Membrane preparation

The preparation of BP-SILM-70 has been described elsewhere (Ong and Tan, 2015). In brief, the MWCNTs were chemically oxidized in piranha solution (80 vol.% sulphuric acid and 20 vol.% hydrogen peroxide) and transformed into the BP sheet via a wet processing technique. This step was followed by blending the [Bmim][BF₄] with PVA at a weight ratio of 70/30 and immobilizing the [Bmim][BF₄]-PVA solution into the BP sheet using a vacuum filtration technique. Subsequently, the resultant BP-SILM-70 was dried at room temperature and cross-linked with glutaraldehyde.

2.3. Liquid sorption test

The BP-SILM-70 was weighed using a digital balance and was then immersed into four different sealed vessels containing pure ethyl acetate, ethanol, water, and an azeotropic mixture composed of 82.6 wt.% ethyl acetate, 8.4 wt.% ethanol and 9.0 wt.% water. The membranes were allowed to stand immersed at room temperature for 72 h to enable the membrane sorption to attain equilibrium. The swollen membranes were then rapidly removed from the vessel and weighed immediately after blotting the excess adhered liquid. The total amount of liquid sorbed was determined using the following equation:

$$\text{Degree of swelling} = \frac{M_{\text{BP-SILM}'} - M_{\text{BP-SILM}}}{M_{\text{BP-SILM}}} \quad (1)$$

where $M_{\text{BP-SILM}}$ and $M_{\text{BP-SILM}'}$ represent the weights of the dry and swollen BP-SILM-70, respectively. The binary interaction parameter χ_{im} between component i and the BP-SILM-70 was calculated using the following equation (Guo et al., 2007):

$$\chi_{im} = - \frac{[\ln(1 - v_m) + v_m]}{v_m^2} \quad (2)$$

where v_m denotes the volume fraction of the membrane in the swollen BP-SILM-70, which can be calculated by the swelling of the BP-SILM-70 in pure solutions.

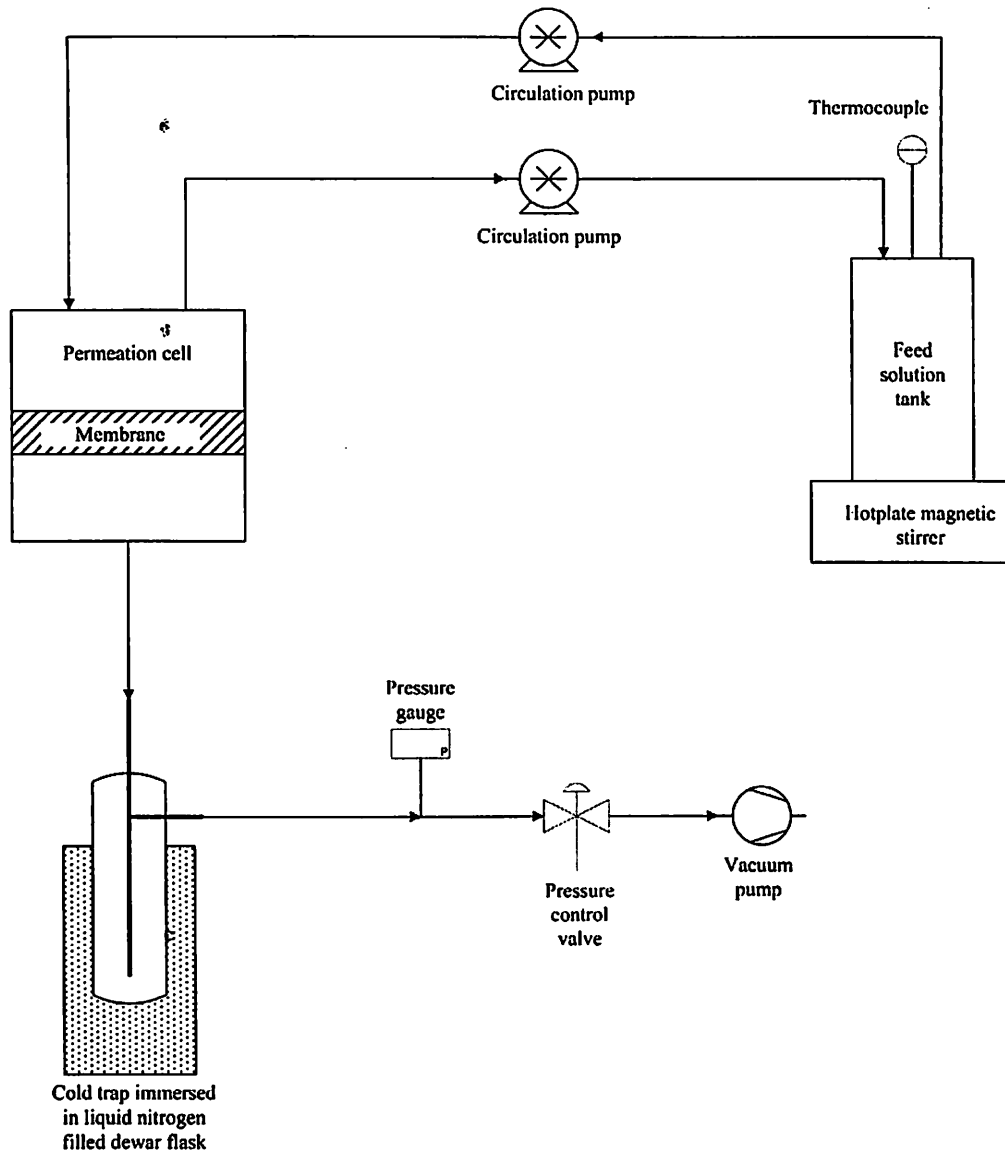


Fig. 2 – Schematic diagram of pervaporation test rig.

2.4. Pervaporation experiments

The pervaporation experiments were conducted using a laboratory-scale pervaporation test rig as shown in Fig. 2. Feed solutions containing different concentrations of binary and ternary mixtures composed of ethyl acetate, ethanol and water were circulated between the feed tank and the permeation cell at a constant flow rate. The operating conditions for the pervaporation of the binary mixtures were fixed at 30 °C and 0.667 kPa. Moreover, for the pervaporation of the ternary mixture, the operating temperature of the feed solutions was varied between 30 °C and 70 °C, and the downstream pressure was varied within a range of 0.667 to 3.333 kPa. The permeate vapour was condensed and collected in a cold trap that was immersed in liquid nitrogen. The collected permeate sample was weighed, and its composition was analysed using a Shimadzu Gas Chromatograph (GC)-2014 equipped with a thermal conductivity detector and using a Supelco Porapak-Q (50/80) packed column 3 m in length and 3.175 mm in diameter with helium as the carrier gas. The temperature of the GC injector was set to 110 °C, and the temperature of the GC oven and detector were set to 180 °C. The pervaporation

performance of the BP-SILM-70 was evaluated in terms of the permeation flux, J , and the separation factor for component i , β , as expressed in the following equations:

$$J = \frac{Q}{A \times t} \quad (3)$$

$$\beta = \left(\frac{Y_i}{1 - Y_i} \right) \left(\frac{1 - X_i}{X_i} \right) \quad (4)$$

where Q refers to the mass (g) of the permeate collected at time t (h), A (m^2) is the effective surface area of the membrane, and X_i and Y_i represent the weight fractions of component i in the feed and permeate, respectively.

The sorption selectivity, β_{sorp} , and the diffusion selectivity, β_{diff} , of the membrane can be defined by the following equations:

$$\beta_{sorp} = \left(\frac{Y_{im}}{1 - Y_{im}} \right) \left(\frac{1 - X_i}{X_i} \right) \quad (5)$$

$$\beta_{diff} = \frac{\beta}{\beta_{sorp}} \quad (6)$$

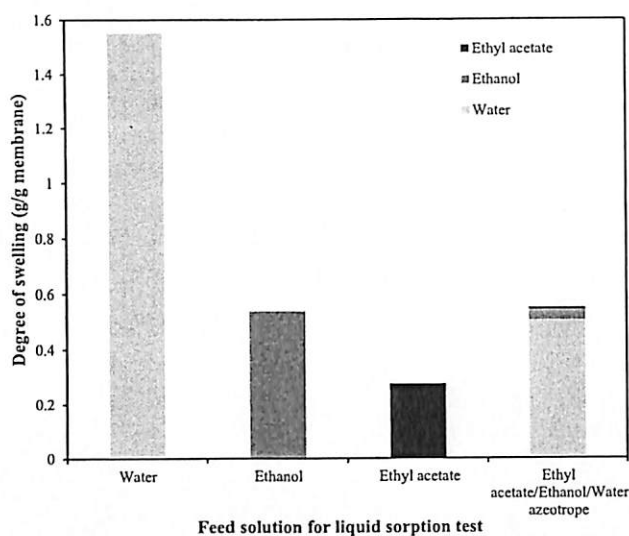


Fig. 3 – Degree of swelling of BP-SILM-70 at various feed solution conditions.

where Y_{im} and X_i denote the weight fraction of component i in the membrane and feed mixtures, respectively, whereas β denotes the separation factor. The sorption selectivity was calculated based on the data collected from liquid sorption test.

Additionally, the intrinsic properties of the membrane were evaluated through an analysis of the permeance, P , and the membrane selectivity, α , which were calculated using the following equations:

$$P_i = \frac{J_i}{MW_i (\gamma_i x_i p_i^{\text{sat}} - y_i p)} \quad (7)$$

$$\alpha = \frac{P_i}{P_j} \quad (8)$$

where MW_i is the molar mass (g/mol) of component i , γ_i , x_i and p_i^{sat} are the activity coefficient, molar fraction and saturated vapour pressure (kPa), respectively, of component i at the feed side, y_i is the mole fraction of component i at the permeate side and p is the total downstream pressure (kPa). The γ_i value for each component was estimated based on the UNIFAC theory (Xia et al., 2012; Randhol and Engeliien, 2000).

3. Results and discussion

3.1. Liquid sorption study

As illustrated in the column chart presented in Fig. 3, the degrees of swelling of the BP-SILM-70 in pure ethyl acetate, ethanol and water were 0.27, 0.54 and 1.55 g/g membrane, respectively. The results indicate that the sorption capacity of the membrane was the highest in water, followed by ethanol and ethyl acetate. The interaction parameters of the membrane with ethyl acetate, ethanol and water, which were calculated using Eq. (2), were 1.32, 0.84, and 0.77 for ethyl acetate, ethanol and water, respectively. This finding indicates that the affinity of the membrane for these three components is in the following descending order: water, ethanol and ethyl acetate. Thus, the differences in membrane sorption capacity are simply due to the preference of the membrane to interact with these components. The sorption behaviour of BP-SILM-70 in water can be explained by the hydrogen bonds formed

between $[\text{BF}_4]^-$ with a hydrogen in water and the hydrogen at C-2 of the imidazolium ring in $[\text{Bmim}]^+$ with an oxygen in water. As the BP-SILM-70 was immersed in pure water, the presence of a greater number of water molecules would facilitate the dissociation of $[\text{Bmim}]^+$ and $[\text{BF}_4]^-$ in $[\text{Bmim}][\text{BF}_4]$. The dissociation of $[\text{Bmim}][\text{BF}_4]$ would cause the structure of the $[\text{Bmim}][\text{BF}_4]$ to become unstable and cause volumetric expansion in the membrane, thereby enabling a higher amount of water to be accommodated and leading to a high sorption of water in the BP-SILM-70. A similar interaction behaviour may also occur in ethanol. The hydrogen of the hydroxyl groups in ethanol could interact with $[\text{BF}_4]^-$ and form strong hydrogen bonds. Additionally, the oxygen of the hydroxyls in ethanol may form hydrogen bonds with the hydrogen at C-2 in $[\text{Bmim}]^+$ (Wu et al., 2009). A relatively low sorption of ethyl acetate was observed in BP-SILM-70 due to its lower affinity with the membrane. This finding can be credited to the poor miscibility of ethyl acetate in $[\text{Bmim}][\text{BF}_4]$. It is hypothesized that a weak polar- π interaction may form between the $[\text{Bmim}]^+$ and ethyl acetate (Cao et al., 2014).

When the BP-SILM-70 was immersed in the azeotropic mixture of ethyl acetate/ethanol/water, the membrane became swollen with a swelling degree of 0.55 g/g membrane. As clearly shown in Fig. 3, the composition of the sorbed liquid predominantly consisted of water, which constituted 91.8 wt.% of the total composition of the sorption, whereas ethanol and ethyl acetate appear as minor components of the composition, with contents of 6.9 and 1.3 wt.%, respectively. This result can be attributed to the higher affinity of BP-SILM-70 for water as a result of the presence of $[\text{Bmim}][\text{BF}_4]$, which improves the hydrophilicity of the membrane (Ong and Tan, 2015). Moreover, the strong interaction between ethyl acetate and ethanol would also weaken their capability to interact with the membrane (Zhang et al., 2008), hence favouring the sorption of water. It can be noted that the swelling degree of BP-SILM-70 in the ternary azeotropic mixture is considerably lower than that in water. The main reason for this phenomenon may be due to a significant reduction in the sorption of water. In the ternary azeotropic mixture, the low water content (approximately 9.0 wt.%) limits the sorption of water in BP-SILM-70 because the interaction of water molecules with $[\text{Bmim}]^+$ and $[\text{BF}_4]^-$ may not be sufficient to cause the dissociation of $[\text{Bmim}][\text{BF}_4]$, thereby reducing the sorption capacity of water. In addition to this result, the sorption of ethanol was found to be approximately five-fold higher than that of ethyl acetate. This finding can be explained by the fact that ionic liquids tend to exhibit a greater attractive interaction with molecules of greater polarity (Mutelet et al., 2006). In this case, the polarities of ethyl acetate and ethanol are 0.520 and 0.656, respectively (Li et al., 2006). Hence, ethanol is prone to exhibit a greater interaction with $[\text{Bmim}][\text{BF}_4]$ in BP-SILM-70 than ethyl acetate.

3.2. Pervaporation of a binary mixture of ethyl acetate and water

The pervaporation of a binary mixture composed of ethyl acetate and water using BP-SILM-70 was studied using various concentrations of water in the feed ranging from 10 to 50 wt.%.

The pervaporation performances of BP-SILM-70 as a function of the feed concentration of water are illustrated in Fig. 4. The permeation fluxes of both water and ethyl acetate shown in Fig. 4(a) were increased with an increase in the feed

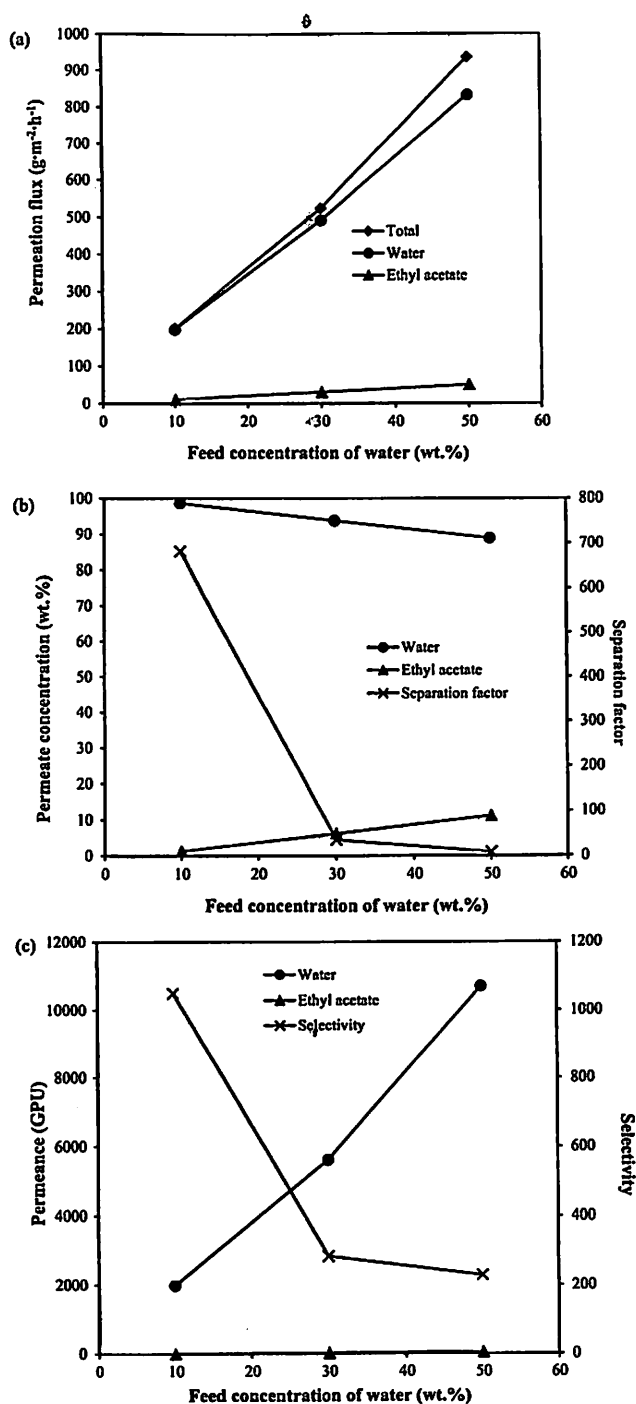


Fig. 4 – Effect of the feed concentration of water on the (a) permeation flux, (b) permeate concentration and separation factor and (c) permeance and selectivity in the separation of ethyl acetate/water by pervaporation.

concentration of water, which eventually increased the total permeation flux. From the aspect of the intrinsic properties of the membrane, as shown in Fig. 4(c), an approximately five-fold increase from 1991.22 to 10,693.58 gas permeation unit (GPU) was observed in the permeance of water when the feed concentration of water was increased from 10 to 50 wt.%, whereas an approximately twenty-five-fold increase from 1.90 to 46.60 GPU was observed in the permeance of ethyl acetate. However, as shown in Fig. 4(b), increasing the feed concentration of water was found to decrease the concentration of water in the permeate but to increase the permeate

concentration of ethyl acetate, thereby decreasing the separation factor of the membrane for water. The more notable increment obtained for the permeance of ethyl acetate eventually decreased the selectivity of the membrane for water. The marked increase in both the permeation flux and the permeance of water with an increase in the feed concentration of water may be attributed to the stronger affinity of BP-SILM-70 for water. Additionally, as mentioned previously in the discussion of the liquid sorption study, ethyl acetate is not favoured to form any interaction with [Bmim][BF₄] in BP-SILM-70; therefore, the competition between the water and ethyl acetate molecules to interact with the membrane becomes negligible, causing a rapid permeation of water molecules. However, the high tendency of [Bmim][BF₄] in BP-SILM-70 to interact with water molecules is expected to increase the amount of water sorbed with an increase in the feed concentration of water. This effect would reduce the electrostatic attractions between the [Bmin]⁺ and [BF₄]⁻ in [Bmim][BF₄] and cause an expansion of the free volume of the membrane to accommodate a higher amount of water molecules (Seddon et al., 2000). The increased sorption of water molecules in the membrane would certainly increase the amount of dissolved ethyl acetate in water, even though ethyl acetate has a limited solubility in water of approximately 8.3 g in 100 g of water (Altshuller and Everson, 1953). Furthermore, the increased sorption of water would reduce the cohesive energy in [Bmim][BF₄] and increase the membrane's free volume (Seddon et al., 2000). This has an effect in reducing the mass transport resistance offered by [Bmim][BF₄] and easing the permeation of molecules across the membrane. Because of the combined effects of an increase in the concentration of dissolved ethyl acetate and an increase in membrane's free volume, the permeance and permeation flux of ethyl acetate increased with an increase in the feed concentration of water, but the separation factor and selectivity of BP-SILM-70 for water decreased.

3.3. Pervaporation of a binary mixture of ethanol and water

Similarly, the pervaporation of a mixture of ethanol/water using BP-SILM-70 was also conducted with various feed concentrations of water ranging from 10 to 50 wt.%, and the pervaporation performances demonstrated by BP-SILM-70 are plotted in Fig. 5.

As shown in Fig. 5(a), the total permeation flux increased with an increase in the feed concentration of water. Interestingly, a further analysis of the permeation flux of the individual components revealed that increasing the feed concentration of water from 10 to 50 wt.% led to an increment of approximately 300% in the permeation flux of water but a decrement of approximately 25% in the permeation flux of ethanol. The permeate concentration of water, as depicted in Fig. 5(b), was found to increase with an increase in the feed concentration of water, whereas the opposite trend was observed for the permeate concentration of ethanol. Despite the increased permeate concentration of water, the separation factor of BP-SILM-70 for water decreased with an increase in the feed concentration of water. The permeance plot presented in Fig. 5(c) shows a significant increase in the permeance of water, whereas only a slight increase was observed in the permeance of ethanol. Overall, the permeance of water was higher than that of ethanol over the tested range of feed concentrations. This result indicates that the intrinsic properties of the membrane favoured the permeation of water rather

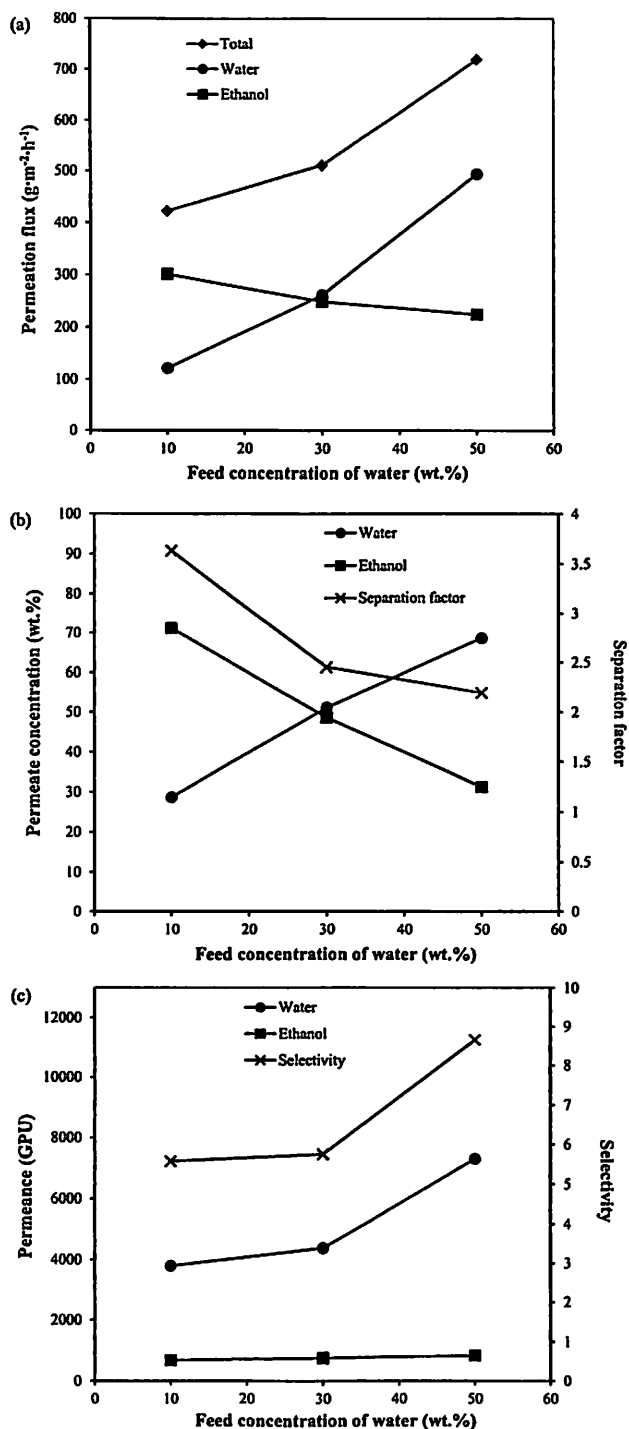


Fig. 5 – Effect of the feed concentration of water on the (a) permeation flux, (b) permeate concentration and separation factor and (c) permeance and selectivity in the separation of ethanol/water by pervaporation.

than ethanol. For this reason, the selectivity of the membrane for water increased with an increase in the feed concentration of water.

The available data on the performance of BP-SILM-70 for the pervaporation of an ethanol/water binary mixture suggest the existence of competition between the water and ethanol molecules for interaction with the [Bmim][BF₄] in BP-SILM-70. As observed in Fig. 5(a) and (b), ethanol molecules demonstrate a favoured position over water molecules by attaining a higher permeation flux and appearing as a major

component in the permeate at a feed concentration of water of 10 wt.%. However, the competitive position of the ethanol molecules becomes feeble when the feed concentration of water is further increased to 50 wt.%. This effect enables water to demonstrate a higher permeation flux and become a major component in the permeate. Because the intrinsic properties of BP-SILM-70 favours the permeation of water, it can be inferred that the high permeation flux of ethanol at a low feed water concentration, as observed in Fig. 5(a), is mostly due to the driving force created across the membrane. Based on Henry's law, the high saturated vapour pressure and high concentration of ethanol in the feed mixture would create a higher partial pressure on the feed side, thereby inducing a greater driving force for the permeation of ethanol. However, with an increase in the feed concentration of water, the partial pressure of ethanol created on the feed side would be relatively lower. This result would eventually weaken the driving force for the permeation of ethanol and benefit the water molecules in their competition for permeation across the membrane, which will lead to an increased permeation flux of water and a decreased permeation flux of ethanol.

3.4. Pervaporation of a binary mixture of ethyl acetate and ethanol

Unlike the previous ethyl acetate/water and ethanol/water systems, which characterized the ability of BP-SILM-70 to dehydrate an aqueous solution, the pervaporation separation of an ethyl acetate/ethanol mixture explores the separation characteristics of BP-SILM-70 in an organophilic pervaporation system. In this case, pervaporation was performed by varying the feed concentrations of ethanol from 10 to 50 wt.%. The main concern regarding setting the feed concentration of ethanol to a value in the range of 10 to 50 wt.% was to approximate the conditions of the ternary azeotropic mixtures such that ethyl acetate appears as a major component.

As depicted in Fig. 6(a), the permeation fluxes of ethanol and ethyl acetate were both increased when the feed concentration of ethanol was increased from 10 to 50 wt.%, thereby increasing the total permeation flux. However, as shown in Fig. 6(b), an increase in the feed concentration of ethanol was found to decrease the permeate concentration of ethanol but to increase the permeate concentration of ethyl acetate. These effects eventually decreased the separation factor of the membrane for ethanol. The permeance values of both ethanol and ethyl acetate, as observed in Fig. 6(c), were increased with an increase in the feed concentration of ethanol. It is interesting to note that the permeance of ethanol is significantly higher than that of ethyl acetate over the tested range of feed concentrations of ethanol. This finding implies the preferential nature of the membrane for the permeation of ethanol compared with ethyl acetate. However, the membrane selectivity for ethanol was found to decrease with an increase in the feed concentration of ethanol.

Based on the permeance plot presented in Fig. 6(c), BP-SILM-70 demonstrated a stronger affinity to interact with ethanol molecules. This result is indeed consistent with the earlier finding detailed in the discussion of the results of the liquid sorption study, which showed that the stronger polarities of ethanol molecules permit their greater interaction with the [Bmim][BF₄] in BP-SILM-70. However, the inter-molecular interaction between ethanol and ethyl acetate is rather strong because ethanol molecules preferentially interact with the carbonyl oxygen of the ethyl acetate (Grunwald and Coburn,

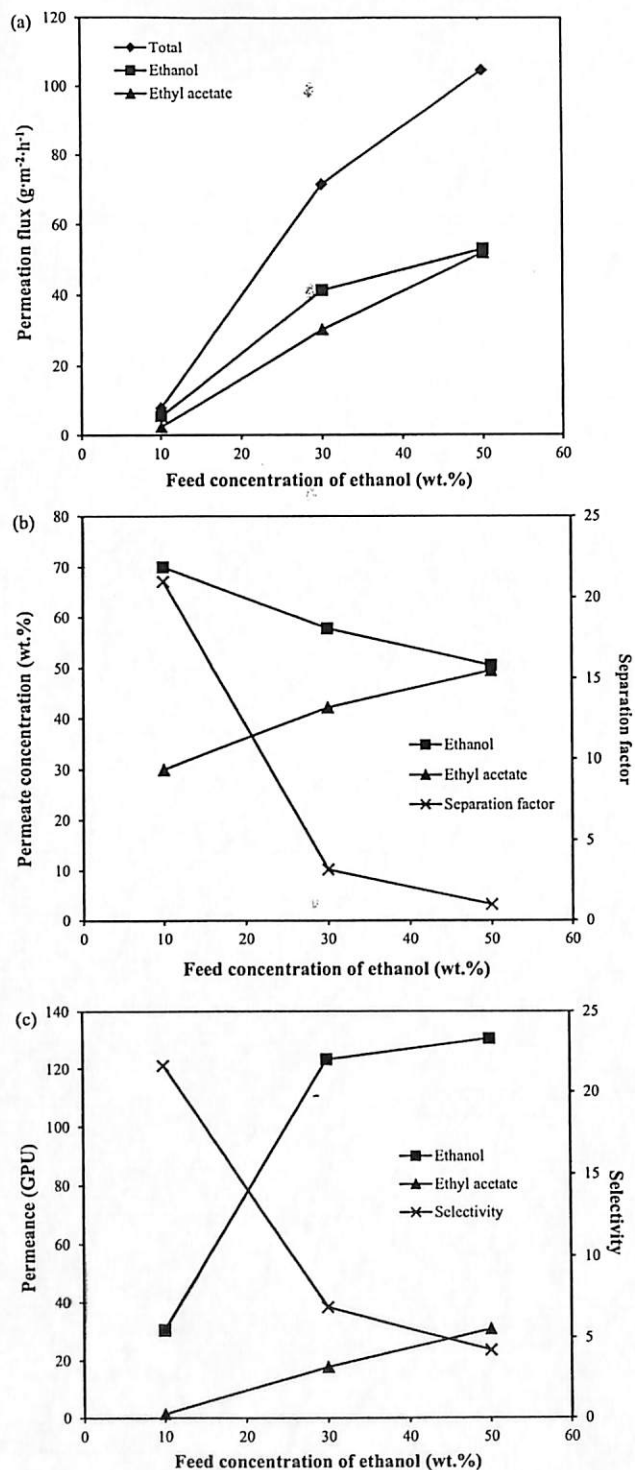


Fig. 6 – Effect of the feed concentration of ethanol on the (a) permeation flux, (b) permeate concentration and separation factor and (c) permeance and selectivity in the separation of ethyl acetate/ethanol by pervaporation.

1958). Thus, at lower feed concentrations of ethanol (high feed concentrations of ethyl acetate), the presence of an excessive number of ethyl acetate molecules would weaken the interaction between ethanol molecules and [Bmim][BF₄] in BP-SILM-70 because the ethanol molecules become the primary interactors with ethyl acetate. Moreover, the ethyl acetate molecules are not likely to form any interaction with the membrane due to their limited solubility in [Bmim][BF₄]. Hence, the above-mentioned effects explain the low permeation flux

Table 1 – Performance of BP-SILM-70 for the pervaporation of the ternary azeotropic mixture of ethyl acetate/ethanol/water at 30 °C and 0.667 kPa.

Ethyl acetate/ethanol/water	
Feed concentration (wt.%)	82.6/8.4/9
Permeation flux (g·m ⁻² ·h ⁻¹)	
Total	385.33
Ethyl acetate	5.09
Ethanol	10.09
Water	370.16
Permeate concentration (wt.%)	
Ethyl acetate	1.32
Ethanol	2.62
Water	96.06
Permeance (GPU)	
Ethyl acetate	3.94
Ethanol	118.56
Water	4729.93
Separation factor, β	246.65
β_{sorp}	113.20
β_{diff}	2.18
Selectivity for water	38.61

and permeance of both components at a feed concentration of ethanol of 10 wt.%. Moreover, the increased number of ethanol molecules obtained with an increase in the feed concentration of ethanol to 50 wt.% would intensify the interaction between ethanol and [Bmim][BF₄], hence increasing the membrane permeance and permeation flux of ethanol. However, the increased permeation of ethanol in BP-SILM-70 may also increase the mutual solubility of [Bmim][BF₄] and ethyl acetate, thereby causing an increase in the permeation flux and permeance of ethyl acetate, but eventually trade-off the separation factor and the selectivity of the membrane for ethanol.

3.5. Pervaporation of a ternary azeotropic mixture of ethyl acetate, ethanol and water

The pervaporation data summarized in Table 1 clearly demonstrate the capability of BP-SILM-70 to dehydrate the ternary azeotropic mixture of ethyl acetate, ethanol and water via a pervaporation process. The permeation flux and concentration of water showed that water appeared to be a major component in the permeate, followed by ethanol and ethyl acetate. Moreover, the separation factor as well as the intrinsic properties of the membrane expressed in terms of permeance and selectivity also indicate the high preference of the membrane for the permeation of water compared with the permeation of ethanol and ethyl acetate. According to the solution-diffusion mechanism, the separation ability of the membrane is dependent on both its sorption selectivity and diffusion selectivity (Ma et al., 2010). However, the data shown in Table 1 clearly suggest that the permeation in BP-SILM-70 is governed by the sorption process because the sorption selectivity of BP-SILM-70 for water is apparently higher than the diffusion selectivity. The separation behaviour demonstrated in BP-SILM-70 in the pervaporation process is consistent with the outcome obtained in the liquid sorption study. Indeed, the separation behaviour exhibited by BP-SILM-70 in the pervaporation of the ternary azeotropic mixture of ethyl acetate/ethanol/water can be traced from the binary pervaporation performed previously. The weight percentage ratio of ethyl acetate to water in the ternary azeotropic mixture is

almost equivalent to the binary mixture of 90/10 wt.% ethyl acetate/water. As shown in Fig. 4, the permeation flux and permeance of water are significantly higher than those of ethyl acetate in a 90/10 wt.% ethyl acetate/water mixture. This finding can be attributed to the limited interaction between ethyl acetate with water and [Bmim][BF₄] in BP-SILM-70, which promotes the permeation of water in BP-SILM-70. On the other hand, the weight percentage ratio of ethanol to water in the ternary azeotropic mixture is approximately equivalent to 50/50 wt.% ethanol/water. As observed in Fig. 5, the permeation flux and permeance of water are considerably higher than those of ethanol in 50/50 wt.% ethanol/water due to the lower driving force for the permeation of ethanol created on the feed side and the intrinsic properties of BP-SILM-70, which favours the permeation of water. Moreover, the weight percentage ratio of ethyl acetate to ethanol in the ternary azeotropic mixture is almost equivalent to 90/10 wt.% ethyl acetate/ethanol. As depicted in Fig. 6, the results revealed an extremely low permeation flux and an extremely low permeance for both ethanol and ethyl acetate at a ratio of 90/10 wt.% ethyl acetate/ethanol, which is caused by the tendency of ethanol to form interactions with ethyl acetate. This finding would diminish the interaction of ethanol with [Bmim][BF₄] in BP-SILM-70. Thus, in the ternary azeotropic pervaporation system, this phenomenon would reduce the ability of ethanol to compete with water for interaction with the membrane. Therefore, the above-mentioned inter-molecular interactions among the feed components and the membrane actually enhance the permeation of water molecules in BP-SILM-70 and enable the membrane to effectively dehydrate the ternary azeotropic mixtures of ethyl acetate/ethanol/water.

3.5.1. Effect of the feed temperature on the pervaporation of the ternary azeotropic mixture

The effect of the feed temperature was examined by varying the temperature of the feed solution from 30 to 70 °C with a constant downstream pressure of 0.667 kPa. The pervaporation performances of BP-SILM-70 in terms of permeation flux, separation factor, permeance and selectivity are plotted as a function of the feed temperature in Fig. 7. As shown in Fig. 7(a), the permeation fluxes of ethyl acetate, ethanol and water gradually increased as the feed temperature was increased from 30 to 70 °C, thereby increasing the overall permeation flux. On the other hand, as observed in Fig. 7(b), the permeate concentration of water was steadily decreased and the concentrations of ethyl acetate and ethanol were slightly increased with elevations in the feed temperature. This eventually caused a decline in the separation factor of BP-SILM-70 for water with an increase in the feed temperature.

In general, an increase in the feed temperature would increase the partial pressure of ethyl acetate, ethanol and water on the feed side as a result of increases in their vapour pressures at higher temperature. This increase would therefore induce a greater driving force for the permeation of these three components across the membrane. Moreover, an increase in the feed temperature may also supply the necessary energy to break the cohesive forces within the molecules in the feed mixtures and accelerate their mobility in the membrane. In addition, thermal expansion in the membrane would generate free volume in the membrane, which would allow easier permeation of the molecules. Thus, the combination of all of these effects explains the increase in permeation flux obtained with an increase in the feed temperature at the cost of reducing the separation factor of the membrane for water.

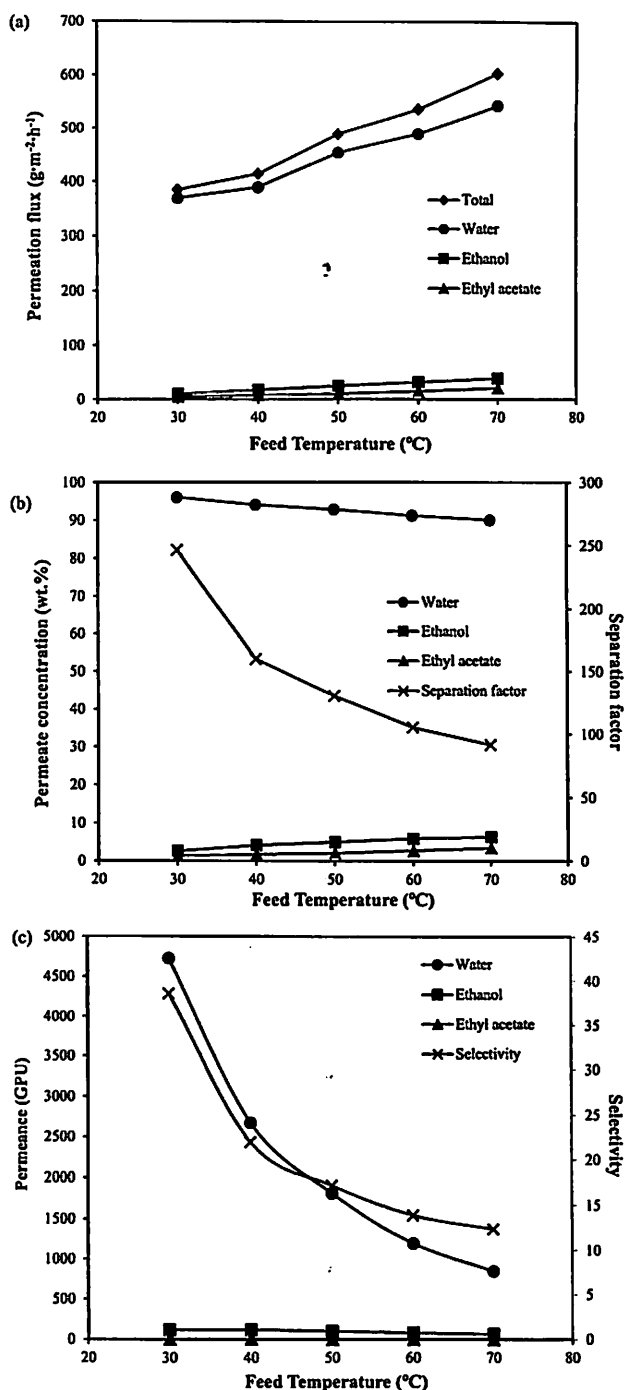


Fig. 7 – Effect of the feed temperature on the (a) permeation flux, (b) permeate concentration and separation factor and (c) permeance and selectivity in the separation of the ternary azeotropic mixture of ethyl acetate/ethanol/water through pervaporation.

Based on the plot of the permeance as a function of the feed temperature presented in Fig. 7(c), the permeance of water is apparently higher than the permeance of ethanol and ethyl acetate, which implies the preference of the membrane for the permeation of water compared with ethanol and ethyl acetate. However, with an increase in the feed temperature, the permeance of water steeply decreased, whereas slight decreases in the permeance values of both ethanol and ethyl acetate were obtained. The steep decrease in the permeance of water

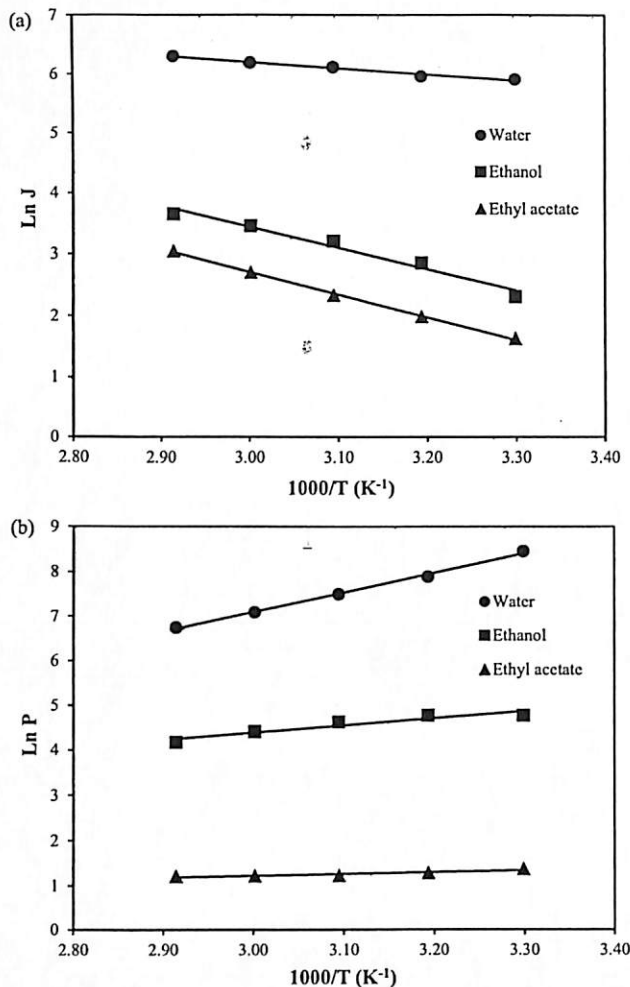


Fig. 8 – Semi-logarithmic Arrhenius plot of the (a) permeation flux and (b) permeance obtained for separation of the ternary azeotropic mixture of ethyl acetate/ethanol/water through pervaporation as a function of the reciprocal of the absolute temperature.

obtained with an increase in the feed temperature eventually decreased the selectivity of the membrane for water.

The temperature dependence of the permeation flux and permeance were then expressed through Arrhenius relations as follows:

$$J_i = J_{i0} \exp\left(-\frac{E_{ji}}{RT}\right) \quad (9)$$

$$P_i = P_{i0} \exp\left(-\frac{E_{pi}}{RT}\right) \quad (10)$$

where E_{ji} represents the activation energy for the permeation of component i , which takes into account the impact of driving force, E_{pi} represents the permeation activation energy, which characterises the dependence of the membrane permeance on the temperature, J_{i0} and P_{i0} represent the pre-exponential factor of the permeation flux and permeance, respectively, R denotes the gas constant, and T denotes the absolute temperature. The activation energies, E_{ji} and E_{pi} , were determined from the slope of the Arrhenius plot presented in Fig. 8 and are summarized in Table 2.

Based on the data shown in Table 2, the highest E_{ji} value obtained in ethyl acetate imply that the permeation flux of ethyl acetate is more sensitive to variation in feed

Table 2 – Activation energy, E_{ji} and E_{pi} , for ethyl acetate, ethanol and water.

Activation energy (kJ/mol)		
	E_{ji}	E_{pi}
Ethyl acetate	30.87	-3.24
Ethanol	28.78	-13.27
Water	8.64	-36.69

temperature. On the other hand, the lowest E_{pi} value obtained in water indicates a strong temperature dependence on the permeance of water. Note that the lower activation energy values for E_{ji} and E_{pi} obtained for water may also reflect its higher affinity for the membrane. This phenomenon may arise from the fact that the activation energy can be considered the minimum energy required for permeation, and a lower activation energy enables the water to more easily permeate through the membrane. As mentioned by Feng and Huang (1997), E_{pi} involves the combination of the activation energy of diffusion and the enthalpy of dissolution of the component in the membrane. Thus, the negative E_{pi} value obtained denotes the dominance of the dissolution process in permeance, revealing an eventual decrease in the permeance with an increase in the feed temperature because the dissolution process decreases with an increase in temperature.

3.5.2. Effect of the downstream pressure on the pervaporation of the ternary mixture

The effect of the downstream pressure on the pervaporation performance of BP-SILM-70 in the dehydration of the ternary azeotropic mixture of ethyl acetate/ethanol/water was investigated by varying the downstream pressure from 0.667 to 3.333 kPa. As clearly demonstrated by the data shown in Fig. 9(a), the permeation flux of water was markedly decreased and the permeation fluxes of ethanol and ethyl acetate were slightly increased with increases in the downstream pressure. The permeate concentration of water, as observed in Fig. 9(b), was found decrease from 96.1 to 78.7 wt.%, whereas the permeate concentrations of ethyl acetate and ethanol increased from 1.7 to 5.4 wt.% and from 2.2 to 15.9 wt.%, respectively. Accordingly, the separation factor of the membrane for water decreased with an increase in the downstream pressure.

Decreases in the downstream pressure are essential for the creation of a chemical potential gradient and for inducing a driving force for mass transfer across the membrane. An increase in downstream pressure will increase the pressure in the permeate side and lower the driving force created between the feed and permeate sides of the membrane. The lower driving force would exert a weaker dragging force, which may slow the diffusion and desorption rates of a component across the membrane and may cause a reduction in the permeation flux, as observed for the permeation flux of water. However, the increases in the permeation fluxes of ethyl acetate and ethanol obtained with increases in the downstream pressure, as observed in Fig. 9(a), can be explained by the intrinsic properties of the membrane.

The plot of the permeance as a function of the downstream pressure, which is shown in Fig. 9(c), demonstrates that the permeance of water, ethanol and ethyl acetate gradually increased with increases in the downstream pressure. Permeance characterizes the solubility and diffusion of a component in the membrane. The reduced driving force obtained as a result of increases in the downstream pressure would

Table 3 – Comparison of the pervaporation performances of PVA-based membranes for the dehydration of a ternary azeotropic mixture of ethyl acetate/ethanol/water.

Membrane	Feed concentration of water (wt.%)	Temperature (°C)	Permeation flux (g·m ⁻² ·h ⁻¹)	Separation factor	Ref.
PVA-ceramic	9	35	1100	173.73	Xia et al. (2012)
	9	60	2100	188.14	
PVA-poly(acrylonitrile)	8	30	133.6	664.97	Yuan et al. (2011)
	8	60	182.2	180.17	
BP-SILM-70	9	30	385.33	246.65	Present work
	9	60	537.24	105.66	

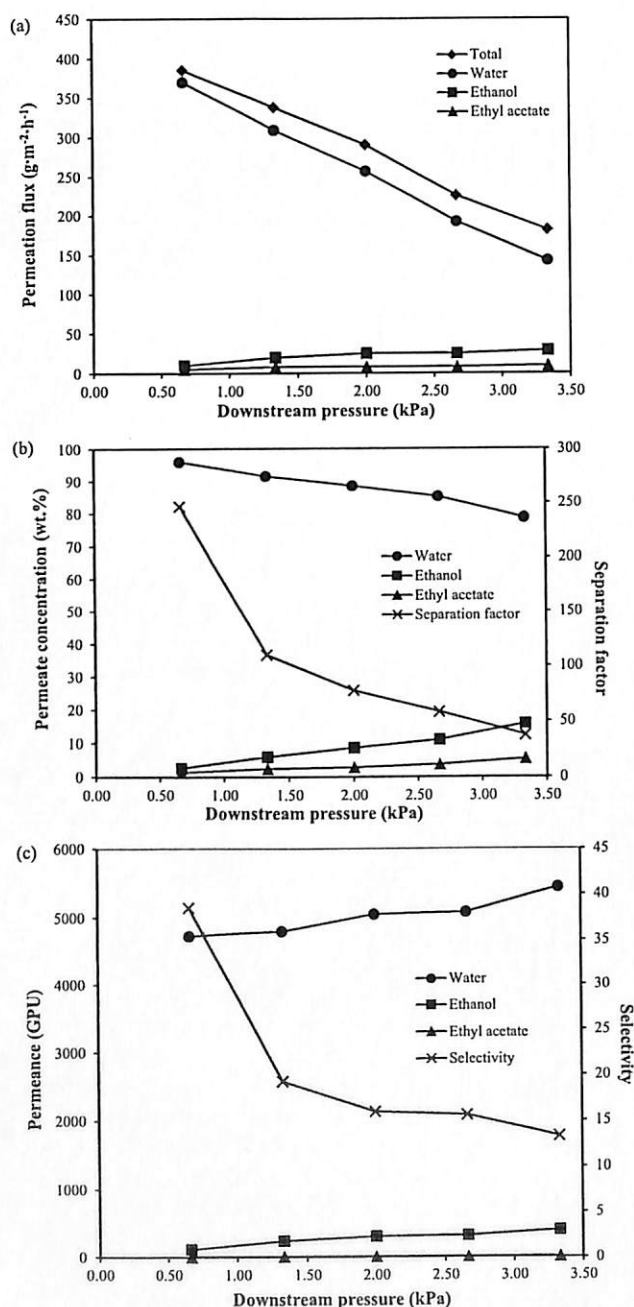


Fig. 9 – Effect of the downstream pressure on the (a) permeation flux, (b) permeate concentration and separation factor and (c) permeance and selectivity in the separation of the ternary azeotropic mixture of ethyl acetate/ethanol/water through pervaporation.

definitely hinder the diffusivity of a component and its desorption from the membrane, which would cause the sorbed components to be trapped inside the membrane. As discussed in Section 3.1, the sorbed components (mainly water molecules due to their higher affinity) may cause the membrane to suffer from swelling, thereby increasing the solubility and permeation of both ethyl acetate and ethanol in the membrane. As a consequence, the permeation fluxes of ethyl acetate and ethanol increased but compromised the separation factor and selectivity of the membrane for water.

3.6. Comparison with data reported in the literature

The pervaporation performance of the BP-SILM-70 membranes in the dehydration of ethyl acetate/ethanol/water azeotropic mixture was compared with those of other PVA based membranes discussed in the literature, as listed in Table 3. The permeation flux and separation factor values obtained for BP-SILM-70 were comparable with those literature-reported PVA-based membranes. Trade-off between permeation flux and separation factor is a usual phenomenon in pervaporation process. It is interesting to note that the PVA-ceramic (Xia et al., 2012) gave a high permeation flux but low separation factor. Conversely, the PVA-poly(acrylonitrile) (Yuan et al., 2011) gave a high separation factor but low permeation flux. However, BP-SILM-70, which can also be considered as a PVA-based membrane, exhibited a good balance in the trade-off between the permeation flux and the separation factor, particularly at low feed temperature (30 °C). This result can be attributed to the presence of [Bmim][BF₄], which enhances the selectivity of BP-SILM-70, and the use of BP as the support, which provides an additional transport pathway and thereby enhances the permeation of a component across the membrane.

4. Conclusions

A pervaporation-based separation of a ternary azeotropic mixture of ethyl acetate/ethanol/water was successfully performed using BP-SILM-70. This membrane exhibited high affinity for the sorption of water, followed by ethanol and ethyl acetate. In the pervaporation of the ternary mixture, BP-SILM-70 demonstrated good separation capability for the dehydration of the ethyl acetate/ethanol/water azeotrope under various operating conditions. The separation capability of BP-SILM-70 is basically governed by sorption selectivity rather than diffusion selectivity. The ability of BP-SILM-70 to dehydrate an ethyl acetate/ethanol/water azeotropic mixture can be simply attributed to the inter-molecular interactions in

the ternary mixture. The high tendency of ethanol to interact with ethyl acetate weakens the competition of ethanol with water molecules for interaction with [Bmim][BF₄], and the weak interactions of ethyl acetate with [Bmim][BF₄], as well as the strong inter-molecular interactions between ethanol and ethyl acetate enable the rapid permeation of water molecules across BP-SILM-70. Compared with other literature-reported PVA-based membranes, the BP-SILM-70 membrane not only demonstrated comparable pervaporation performance but also presents a strong potential to attain a good balance in the trade-off between the permeation flux and the separation factor.

Acknowledgments

The authors acknowledge MyPhD fellowships provided by the Ministry of Higher Education of Malaysia. This research work was financially supported by a Universiti Sains Malaysia Research University (RU) grant (A/C: 814142) and the Postgraduate Research Grant Scheme (PRGS) (A/C: 8045034).

References

- Altshuller, A.P., Everson, H.E., 1953. The solubility of ethyl acetate in water. *J. Am. Chem. Soc.* 75, 1727.
- Cao, Y., Xing, H., Yang, Q., Li, Z., Chen, T., Bao, Z., Ren, Q., 2014. Biphasic systems that consist of hydrophilic ionic liquid, water, and ethyl acetate: the effects of interactions on the phase behavior. *Ind. Eng. Chem. Res.* 53, 10784–10790.
- Del Pozo Gomez, M.T., Klein, A., Repke, J.U., Wozny, G., 2008. A new energy-integrated pervaporation distillation approach. *Desalination* 224, 28–33.
- Feng, X., Huang, R.Y.M., 1997. Liquid separation by membrane pervaporation: a review. *Ind. Eng. Chem. Res.* 36, 1048–1066.
- Grunwald, E., Coburn Jr., W.C., 1958. Calculation of association constants for complex formation from spectral data. Infrared measurements of hydrogen bonding between ethanol and ethyl acetate, and ethanol and acetic anhydride. *J. Am. Chem. Soc.* 80, 1322–1325.
- Guo, R., Hu, C., Li, B., Jiang, Z., 2007. Pervaporation separation of ethylene glycol/water mixtures through surface crosslinked PVA membranes: coupling effect and separation performance analysis. *J. Membr. Sci.* 289, 191–198.
- Hasanoğlu, A., Salt, Y., Keleşer, S., Özkan, S., Dinçer, S., 2007. Pervaporation separation of organics from multicomponent aqueous mixtures. *Chem. Eng. Process.: Process Intensif.* 46, 300–306.
- Hu, W.W., Zhang, X.H., Zhang, Q.G., Liu, Q.L., Zhu, A.M., 2012. Pervaporation dehydration of water/ethanol/ethyl acetate mixtures using poly(vinyl alcohol)-silica hybrid membranes. *J. Appl. Polym. Sci.* 126, 778–787.
- Koczka, K., Manczinger, J., Mizsey, P., Fonyo, Z., 2007. Novel hybrid separation processes based on pervaporation for THF recovery. *Chem. Eng. Process.: Process Intensif.* 46, 239–246.
- Li, W., Zhang, Z., Zhang, J., Han, B., Wang, B., Hou, M., Xie, Y., 2006. Micropolarity and aggregation behavior in ionic liquid + organic solvent solutions. *Fluid Phase Equilib.* 248, 211–216.
- Ma, J., Zhang, M., Jiang, Z., Nie, M., Liu, G., 2010. Facile fabrication of structurally stable hyaluronic acid-based composite membranes inspired by bioadhesion. *J. Membr. Sci.* 364, 290–297.
- McMurry, J., 2000. *Organic Chemistry*, fifth ed. Brooks/Cole, Pacific Grove, CA.
- Monick, J.A., 1968. *Alcohols*. Reinhold Book Corporation, New York, NY.
- Mutelet, F., Jaubert, J.N., Rogalski, M., Boukherissa, M., Dicko, A., 2006. Thermodynamic properties of mixtures containing ionic liquids: Activity coefficients at infinite dilution of organic compounds in 1-propyl boronic acid-3-alkylimidazolium bromide and 1-propenyl-3-alkylimidazolium bromide using inverse gas chromatography. *J. Chem. Eng. Data* 51, 1274–1279.
- Ong, Y.T., Tan, S.H., 2015. Synthesis of the novel symmetric buckypaper supported ionic liquid membrane for the dehydration of ethylene glycol by pervaporation. *Sep. Purif. Technol.* 143, 135–145.
- Randhol, P., Engelen, J.K., 2000. xLUNIFAC Version 1.0, A Computer Program for Calculation of Liquid Activity Coefficients Using the UNIFAC Model. Free Software Foundation Inc, Available via (<http://www.pvv.org/~randhol/xlunifac/>) (last accessed on January 2016).
- Seddon, K.R., Stark, A., Torres, M.J., 2000. Influence of chloride, water, and organic solvents on the physical properties of ionic liquids. *Pure Appl. Chem.* 72, 2275–2287.
- Wu, B., Zhang, Y., Wang, H., 2009. Insight into the intermolecular interactions in ionic liquid-ethanol-water mixtures by near-infrared spectroscopy. *Z. Phys. Chem.* 223, 849–856.
- Xia, S., Wei, W., Liu, G., Dong, X., Jin, W., 2012. Pervaporation properties of polyvinyl alcohol/ceramic composite membrane for separation of ethyl acetate/ethanol/water ternary mixtures. *Korean J. Chem. Eng.* 29, 228–234.
- Yongquan, D., Ming, W., Lin, C., Mingjun, L., 2012. Preparation, characterization of P(VDF-HFP)/[bmim] BF₄ ionic liquids hybrid membranes and their pervaporation performance for ethyl acetate recovery from water. *Desalination* 295, 53–60.
- Yuan, H.-K., Ren, J., Ma, X.-H., Xu, Z.-L., 2011. Dehydration of ethyl acetate aqueous solution by pervaporation using PVA/PAN hollow fiber composite membrane. *Desalination* 280, 252–258.
- Zhang, D.L., Deng, Y.F., Li, C.B., Chen, J., 2008. Separation of ethyl acetate-ethanol azeotropic mixture using hydrophilic ionic liquids. *Ind. Eng. Chem. Res.* 47, 1995–2001.
- Zhang, X.H., Liu, Q.L., Xiong, Y., Zhu, A.M., Chen, Y., Zhang, Q.G., 2009. Pervaporation dehydration of ethyl acetate/ethanol/water azeotrope using chitosan/poly(vinyl pyrrolidone) blend membranes. *J. Membr. Sci.* 327, 274–280.



ELSEVIER

Contents lists available at ScienceDirect

Separation and Purification Technology

journal homepage: www.elsevier.com/locate/seppur

Synthesis of the novel symmetric buckypaper supported ionic liquid membrane for the dehydration of ethylene glycol by pervaporation



Yit Thai Ong, Soon Huat Tan*

School of Chemical Engineering, Engineering Campus, Universiti Sains Malaysia, Seri Ampangan, 14300 Nibong Tebal, SPS, Pulau Pinang, Malaysia

ARTICLE INFO

Article history:

Received 24 November 2014

Received in revised form 14 January 2015

Accepted 16 January 2015

Available online 28 January 2015

Keywords:

Buckypapers

Carbon nanotubes

Supported ionic liquid membrane

Pervaporation

ABSTRACT

In this study, a novel symmetric supported ionic liquid membrane (SILM) was prepared by infiltrating 1-butyl-3-methylimidazolium tetrafluoroborate [Bmim][BF₄] into a buckypaper (BP) to form a so-called buckypaper supported ionic liquid membrane (BP-SILM). The [Bmim][BF₄] was blended with polyvinyl alcohol (PVA) prior to the infiltration. The role of BP as a support can effectively entrap the infiltrated [Bmim][BF₄]-PVA in the interstitial pores and supply the necessary mechanical stability for the resulting BP-SILM. The BP-SILM structure, in which the membrane and support phases were merged into a single layer, was found to be different from that of conventional asymmetric membranes. The BP-SILM structure allows the formation of a thinner symmetric membrane without compromising its mechanical properties. During the application of the BP-SILM in the pervaporation process to dehydrate ethylene glycol aqueous solution, the presence of BP and [Bmim][BF₄] was observed to significantly enhance the separation performance and enhance the intrinsic membrane permeability. The BP-SILM exhibited high pervaporation performance with a permeation flux of 102 g m⁻² h⁻¹, a separation factor as high as 1014, and a water permeance of 9046 gpu. The BP-SILM also demonstrated a robust pervaporation performance over an operation of 120 h.

© 2015 Elsevier B.V. All rights reserved.

1. Introduction

Ethylene glycol is the most important dihydroxyl alcohol and is well-known due to its usage as a non-volatile antifreeze and as a raw material for the production of polyester. Ethylene glycol is commercially produced through the hydrolysis of ethylene oxide, during which a large excess of water is required to increase the yield. Due to its complete miscibility with water and the lack of formation of any azeotrope over an entire composition range, the purification of ethylene glycol can be simply performed by multi-stage distillation. However, the distillation process consumes a large amount of energy because ethylene glycol has a high boiling point of 198 °C. Hence, increasing attention is being paid to the use of pervaporation as an alternative pathway.

In the past several decades, pervaporation has been recognised as an energy-efficient process, and its excellent capability to separate liquid–liquid mixtures has enabled it to become one of the most-studied membrane separation processes. Its distinguished separation characteristics, i.e., its phase change from liquid to vapour mediated by a driving force induced by a chemical activity

difference, provide high efficiency to the separation of close-boiling-point and azeotrope mixtures. To date, most studies on the dehydration of ethylene glycol via the pervaporation process have focused on the use of solid membranes fabricated from a pure polymer, such as poly(vinyl alcohol) (PVA) [1,2] and chitosan [3,4], or a mix-matrix membrane [5,6] that incorporates an inorganic filler into the polymer.

Instead of using solid membranes, many studies have started to use a supported liquid membrane (SLM) in the pervaporation process. The emergence of using SLMs is attractive due to the lower mass transfer resistances demonstrated in the liquid membrane [7]. Briefly, SLM consists of a liquid membrane that is immobilised into a porous support. The porous support is used to supply the necessary mechanical stability to the SLM, whereas the liquid membrane, which usually involves the use of an organic solvent, acts as a semi-permeable barrier and governs the mass transport. Other than organic solvents, recent developments involve the use of an ionic liquid to form the so-called supported ionic liquid membrane (SILM). Ionic liquid is an organic liquid salt that possesses a relatively low melting point, which enables it to remain in the liquid state at room temperature. Compared with an organic solvent, ionic liquid has a better thermal stability and a low-to-negligible vapour pressure, which make it difficult to vaporise. Numerous studies on the applications of SILM in pervaporation

* Corresponding author. Tel.: +60 4 5996475; fax: +60 4 5941013.

E-mail address: chshtan@usm.my (S.H. Tan).

Nomenclature

A	membrane effective surface area (m^2)	Q	mass of the permeate (g)
E_{ji}	activation energy for the permeation of component i (kJ/mol)	t	time interval (h)
E_{Pi}	permeation activation energy on permeability for component i (kJ/mol)	v_m	volume fraction of membrane
J	permeation flux ($\text{g m}^{-2} \text{h}^{-1}$)	X_i	mass fraction of component i in the feed
M_{BP}	weight of BP (g)	x_i	molar fraction of component i
$M_{BP-SILM}$	weight of dry BP-SILM (g)	Y_i	mass fraction of component i in the permeate
$M_{BP-SILM}^*$	weight of swollen BP-SILM (g)	y_i	molar fraction of component i
MW_i	molar mass of component i (g/mol)	α	membrane selectivity
P	permeance (GPU)	β	separation factor
p	total downstream pressure (kPa)	γ_i	activity coefficient of component i
p_i^{sat}	saturated vapour pressure of component i (kPa)	χ_{im}	Flory–Huggins binary interaction parameter

for the separation of organic compounds from dilute aqueous solutions have been reported [8–14]. Although the use of SILM is always associated with an instability problem caused by the leaching of the liquid membrane from the porous support, particularly under high pressure or vacuum conditions, several methods have been proposed to overcome this limitation, and these include re-immobilisation of the liquid membrane [15], surface coating [16], and mixing with a base polymer to form a thin, stable film [17]. In addition, the use of a porous support with a smaller pore diameter would also help enhance the SILM stability [18,19].

Other than providing physical stability, the porous support also plays a significant role as a medium to entrap and firmly hold the liquid membrane. Most of the porous supports that have been developed to date are prepared from a polymeric substance, such as polypropylene [15], polyvinylidene fluoride [20] and polysulfone [21]. To improve the performance of SILMs, this study presents the novel production of a high-stability SILM using buckypaper (BP) as a porous support. BP is one of the carbon-nanotubes (CNTs)-based membranes that are solely composed of entangled assemblies of CNTs held together by van der Waals interactions at tube-tube junctions and arranged as a planar film [22]. The entanglement of the randomly orientated CNT bundles could form a highly porous network structure with a free volume up to 70% of its total volume [23]. BP has exhibited vast potential applications in hydrogen storage [24], actuators [25], sensors [26] and artificial muscles [27]. Recent studies conducted by Yee et al. [28] also reported the application of BP in the membrane separation process. The introduction of BP as a pre-selective layer in an asymmetric membrane was found to control the permeability and enhance the pervaporation performance of the resulting asymmetric membrane. Therefore, in this study, a BP was fabricated from multi-walled carbon nanotubes (MWCNTs) through the wet-processing technique and was immobilised using a hydrophilic ionic liquid membrane, namely 1-butyl-3-methylimidazolium tetrafluoroborate [Bmim][BF₄], via a vacuum-based immobilisation technique to form a so-called buckypaper-supported ionic liquid membrane (BP-SILM). To enhance the liquid membrane stability, [Bmim][BF₄] was blended with PVA prior to immobilisation to enable the formation of a thin stable compound that can be firmly held inside the porous support. Note that the resulting symmetric BP-SILM, in which the immobilised membrane and the support layer are merged into a single layer, as illustrated in Fig. 1, is different from that of a conventional asymmetric structure membrane. This difference may help promote the formation of a thinner membrane and reduce the mass transport resistance. Unlike the reported SILMs that favour the use of a membrane filter as a porous support, the BP support has a tendency to secure the immobilised liquid

membrane through its randomly entangled CNT structure. The BP-SILM was then applied to the pervaporation process for the dehydration of ethylene glycol. The effects of the [Bmim][BF₄] content and the operating parameters on the pervaporation performance of the BP-SILM were investigated. Also, the stability of the BP-SILM was evaluated by operating at a prolong operation period.

2. Experimental

2.1. Materials

MWCNTs manufactured via the chemical vapour deposition technique were supplied by Chengdu Organic Chemical Co., Ltd. These had an outer diameter in the range of 8–15 nm, an inner diameter in the range of 3 to 5 nm and a length of approximately 50 μm . PVA (95% hydrolysed) with an average molecular weight of 95,000 and [Bmim][BF₄] (98%) were purchased from Acros. Sulphuric acid (95–97%), hydrogen peroxide (30%), glutaraldehyde (25% aqueous solution) and ethylene glycol were procured from Merck. Absolute ethanol (96%) and acetone were supplied from HmbG and Fine Chemicals, respectively. Distilled water was used throughout the experiments.

2.2. MWCNT treatment

The MWCNTs were chemically oxidised through their addition into a piranha solution (80 vol.% sulphuric acid and 20 vol.% hydrogen peroxide) at a ratio of 1 mL to 1 mg of MWCNTs and then refluxed at 70 °C for 6 h. Subsequently, the oxidised MWCNTs were separated using vacuum filtration through a 0.22- μm PVDF membrane filter and then repeatedly washed with distilled water until the pH of the solution became neutral. The oxidised MWCNTs were then dried at 120 °C for 24 h.

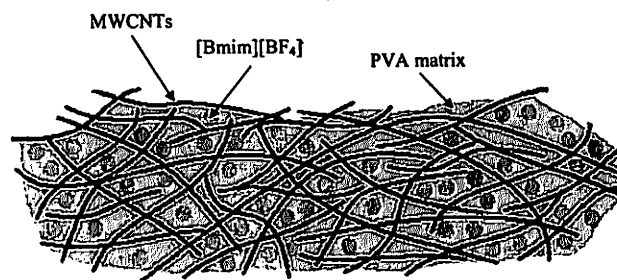


Fig. 1. Schematic diagram of the BP-SILM formed using the vacuum-based immobilisation technique.

2.3. Preparation of PVA and [Bmim][BF₄]

The PVA solution was prepared by dissolving 5 wt.% PVA powder in distilled water under vigorous stirring at 80 °C for 6 h. After the PVA powder was fully dissolved in water, the stirring process was maintained at room temperature overnight. In addition, the [Bmim][BF₄] solution was prepared by dissolving 5 wt.% [Bmim][BF₄] in distilled water and stirring at room temperature. Both the [Bmim][BF₄] and PVA solutions were carefully mixed to form a [Bmim][BF₄]-PVA solution at weight ratios of 30/70, 50/50, and 70/30. The mixture solutions were stirred for 24 h to ensure their homogeneity.

2.4. Preparation of BP and BP-SILM

The oxidised MWCNTs were transformed into BP sheets with diameters of 90 mm through a wet processing technique. A pre-weighed amount of oxidised MWCNTs was dispersed in ethanol and sonicated for 15 min, and the MWCNT suspension subjected then to vacuum filtration through a 0.45- μ m nylon membrane filter. The resulting BP was then washed with distilled water. Five different weights of BPs, ranging from 3.44 to 5.88 mg/cm² of MWCNTs, were prepared. The vacuum filtration process was continued to immobilise the [Bmim][BF₄]-PVA solution in the BP, and the process was stopped once a thin visible layer of excess [Bmim][BF₄]-PVA solution was observed on the surface of the BPs. The excess [Bmim][BF₄]-PVA was removed using a transfer pipette, and the as-formed BP-SILM was then peeled off from the membrane filter and dried at room temperature. After drying, the BP-SILM was immersed in a cross-linking bath containing 2.5 mL of glutaraldehyde, 2.5 mL of hydrochloric acid and water-acetone mixtures (30/70 vol.%). The efficiency of the BP to entrap [Bmim][BF₄]-PVA was calculated based on the following equation:

$$\text{Immobilised content} = \frac{M_{\text{BP-SILM}} - M_{\text{BP}}}{M_{\text{BP}}} \quad (1)$$

where $M_{\text{BP-SILM}}$ and M_{BP} refer to the weights of the BP-SILM and BP, respectively.

2.5. Liquid sorption study

The dry weights of the BP-SILMs were measured using a digital balance. The BP-SILMs were then immersed into two different solutions, namely pure ethylene glycol and distilled water, and placed in a sealed vessel, and the sorption process was then continued at room temperature for 72 h until the equilibrium state was achieved. The swollen BP-SILMs were rapidly removed from the vessel and weighed immediately after blotting the excess adhered liquid. The total amount of liquid sorbed was determined using the following equation:

$$\text{Degree of swelling} = \frac{M_{\text{BP-SILM}'} - M_{\text{BP-SILM}}}{M_{\text{BP-SILM}}} \quad (2)$$

where $M_{\text{BP-SILM}}$ and $M_{\text{BP-SILM}'}$ represent the weights of the dry and swollen BP-SILMs, respectively. According to the Flory-Huggins theory, the binary interaction parameter χ_{im} between component i and the BP-SILM was calculated using the following equation [29]:

$$\chi_{im} = -\frac{\ln(1 - v_m) + v_m}{v_m^2} \quad (3)$$

where v_m is the volume fraction of the membrane in the swollen BP-SILM.

2.6. Pervaporation experiments

The pervaporation experiments were performed using a laboratory-scale pervaporation test rig. The BP-SILM was mounted onto a stainless-steel permeation cell supported with a porous stainless-steel plate and supplied an effective surface area of 8.6 cm². Feed solutions containing ethylene glycol and water mixtures at five different concentrations ranging from 50 to 90 wt.% ethylene glycol were circulated between the feed tank and the permeation cell at a constant flow rate. The operating temperatures of the feed solutions were maintained between 30 °C and 70 °C using a hotplate magnetic stirrer, and the downstream pressure was generated using a vacuum pump and maintained at 0.667 kPa. Upon stabilisation, the pervaporation process was operated for 4 h, and the permeate vapour was condensed and collected in cold traps immersed in liquid nitrogen. The collected permeate sample was weighed, and its composition was analysed using a Karl Fisher moisture titrator. The pervaporation performance of the BP-SILM was assessed in terms of the permeation flux, J , and the separation factor for component i , β , as expressed in the following equations:

$$J = \frac{Q}{A \times t} \quad (4)$$

$$\beta = \left(\frac{Y_i}{1 - Y_i} \right) \left(\frac{1 - X_i}{X_i} \right) \quad (5)$$

where Q refers to the mass (g) of the permeate collected at time interval t (h), A (m²) is the membrane effective surface area, and X_i and Y_i represent the mass fractions of component i in the feed and permeate, respectively.

In addition, the membrane intrinsic properties can be evaluated in terms of the permeance, P , and the membrane selectivity, α , which were calculated using the following equations:

$$P_i = \frac{J_i}{MW_i(\gamma_i x_i p_i^{\text{sat}} - y_i p)} \quad (6)$$

$$\alpha = \frac{P_i}{P_j} \quad (7)$$

where MW_i is the molar mass (g/mol) of component i , γ_i , x_i and p_i^{sat} are the activity coefficient, molar fraction and saturated vapour pressure (kPa), respectively, of component i at the feed side, y_i is the mole fraction of component i at the permeate side and p is the total downstream pressure (kPa).

2.7. Characterisation

Thermogravimetric analysis (TGA) of the MWCNT powder and the BP-SILMs was performed using a TA Instruments Thermogravimetry SDT Q600 V20.9 apparatus. The specimens were placed in an alumina crucible and heated from room temperature to 900 °C with a heating rate of 10 °C/min under air conditions. The dispersion of the MWCNT suspensions were characterised in quartz cuvettes using a Cary 60 UV-Vis spectrophotometer. The absorption spectra of the suspensions were recorded over the spectral range of 300–1000 nm at room temperature. All of the suspensions were diluted with distilled water to fit within the optimal absorbance limit of the instrument. The surface morphology and cross section of each of the BP-SILMs and the elemental compositions of the samples were visualised using a Quanta 450 FEG scanning electron microscope (SEM) equipped with an energy dispersive X-ray (EDX) apparatus. The membranes were fractured in liquid nitrogen to avoid any polymer deformation prior to the test.

2.8. Contact angle measurement

The contact angles of water on the membranes were measured via the sessile drop technique using a Rame-Hart standard goniometer Model 250 equipped with a video camera at room temperature. A controlled volume of 6 μL of deionised water was carefully dropped onto the sample. The image of each drop shape was captured using a video camera, and the corresponding contact angle was determined using the supplied software.

2.9. Determination of the mechanical properties

The mechanical properties of the membrane were examined using an Instron table-mounted universal testing machine. Each of the specimens was cut into a dumbbell shape with a gauge length of 22 mm. The load cell was set to maximum with a constant crosshead speed of 1 mm/min. The tensile strength and elongation at break were determined.

3. Results and discussion

3.1. Characterisation

The thermal behaviours of the raw and oxidised MWCNTs are presented in the weight loss-versus-heating temperature plots shown in Fig. 2. Both types of the MWCNTs underwent thermal decomposition upon heating up to 900 °C under air conditions. The onset temperatures for the raw and oxidised MWCNTs were observed to be 400 °C and 450 °C, respectively, implying the enhanced thermal stability of the oxidised MWCNTs. The thermal delay effect observed with the oxidised MWCNTs can be attributed to the reduced content of amorphous carbon after the chemical oxidation treatment with piranha solution. The presence of amorphous carbon has a tendency to lower the decomposition temperature because of the lower activation energy in amorphous carbon, which allows them to be oxidised at a lower temperature [28]. The reaction heat of oxidation in amorphous carbon likely increases the local temperature and leads to oxidation of the intact layer of MWCNTs. Despite this increased local temperature, the chemical oxidation of the MWCNTs could lead to the attachment of a carboxyl group on the surface of the MWCNTs, and the carboxyl group can form a hydrogen bond within the MWCNTs, which increases the activation energy of oxidation and therefore delays the onset temperature for the decomposition of MWCNTs.

The thermal stability of the [Bmim][BF₄]-PVA blended membranes and the pure [Bmim][BF₄] and PVA membranes were also

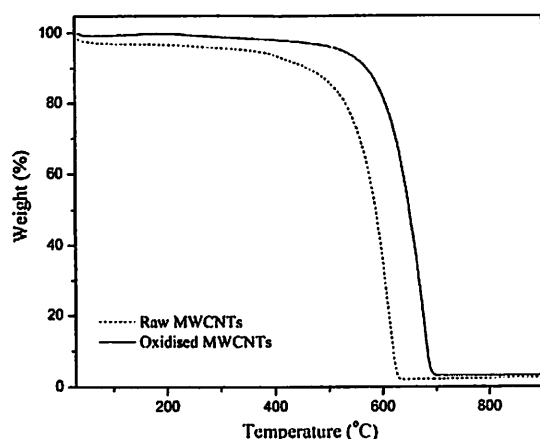


Fig. 2. Thermogravimetric thermogram of raw MWCNTs and oxidised MWCNTs.

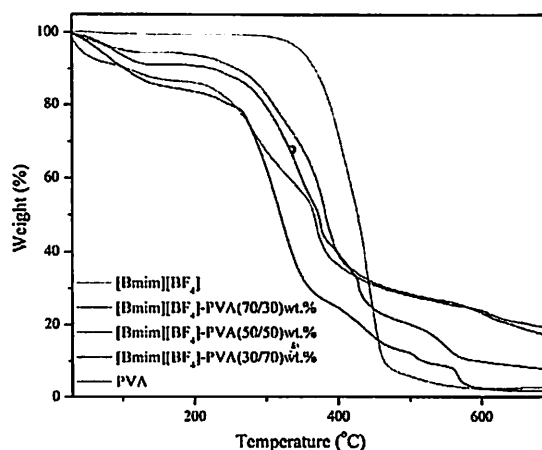


Fig. 3. Thermogravimetric thermogram of pure [Bmim][BF₄], [Bmim][BF₄]-PVA in 30/70, 50/50 and 70/30 wt.%, and pure PVA.

determined using TGA. As shown in the TGA thermogram presented in Fig. 3, pure [Bmim][BF₄] exhibited a single-stage degradation, which started at 300 °C and was completed at 550 °C. Pure PVA membrane exhibited degradation at three different temperature ranges: the first degradation below 100 °C involves removal of the residual moisture, the subsequent stage at a temperature between 180 and 400 °C appears to involve the elimination of side groups, and the last stage at 400–600 °C appears to be due to breakdown of the polymer backbone [30]. A decrease in thermal stability was observed in the blended membranes compared with the pure [Bmim][BF₄]. However, note that the decomposition temperature of the blend membrane was increased in the ascending order of 30/70, 50/50 and 70/30 wt.% [Bmim][BF₄]-PVA. This observation reveals that the thermal stability of the blended membrane increased with respect to the content of [Bmim][BF₄] in the blend.

Sonication is widely used to exfoliate MWCNT aggregates and enhance their dispersion. Previous studies have demonstrated that the dispersion of MWCNTs improves with increased sonication time and reaches an equilibrium state with further sonication [31]. However, excess sonication may result in the formation of defects and shortening of the MWCNTs. Thus, the effect of the sonication time was studied as a parameter to evaluate the dispersion of the MWCNTs in ethanol using a UV-Vis spectrophotometer and to determine the minimum sonication time that is sufficient to disperse the MWCNTs. Fig. 4(a) shows the effect of the sonication time on the dispersion of MWCNTs in ethanol. The overall absorbance was clearly observed to increase with increasing sonication time, and this effect can be attributed to the presence of a greater amount of exfoliated MWCNTs because aggregated MWCNTs do not exhibit distinct features in the wavelength range of 300–1000 nm. Thus, this result implies that the dispersion of MWCNTs improves with increasing sonication time. To determine the minimum sonication time, the effect of the sonication period on the extent of exfoliated MWCNTs was further assessed by plotting the absorbance of the sample at 908 nm as a function of the sonication time, as shown in Fig. 4(b). This particular wavelength is related to the absorption band arising from the van Hove singularities [32]. Note that the absorbance increased rapidly as the sonication time increased to 15 min. The dispersion of MWCNTs started to achieve equilibrium as their absorbance started to form a plateau after 15 min of sonication. Therefore, a sonication time of 15 min was selected as being sufficient for the dispersion of MWCNTs without prolonged exposure to ultrasonic energy.

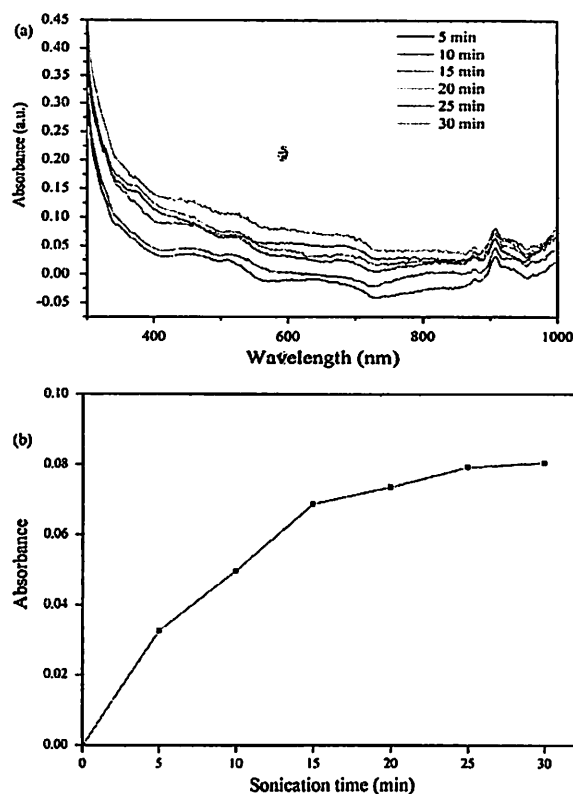


Fig. 4. (a) UV-Vis absorption spectrum of MWCNT dispersion in ethanol with different sonication times. (b) Absorbance at 908 nm as a function of the sonication time.

The SEM surface morphologies of the BP and BP-SILM are shown in Fig. 5. The MWCNT threads were clearly visible, and the MWCNTs were randomly entangled with each other and predominately horizontal to the surface of the BP without any significant agglomeration. The entanglement of MWCNTs in the BP formed a rather small interstitial pore, whereas the surface of the BP-SILM was denser, and the MWCNTs were found to be covered by [Bmim][BF₄]-PVA. From the cross-sectional view, the texture of the BP-SILM was found to be more closely and neatly packed than the BP. This observation can be attributed to the capability of [Bmim][BF₄]-PVA to penetrate and be immobilised in the deeper interstitial pores in the BP. The presence of [Bmim][BF₄]-PVA in the BP-SILM was further verified through EDX: 1.06% fluorine atoms were detected in the cross-section of BP-SILM, which may be associated with the presence of [Bmim][BF₄]. Thus, the result confirmed that [Bmim][BF₄]-PVA can be effectively immobilised in the interstitial pores of the BP via the vacuum-based technique.

The effect of the MWCNT content in BP on the immobilisation of [Bmim][BF₄]-PVA was determined using immobilised [Bmim][BF₄]-PVA with five different contents of MWCNTs ranging from 3.44 mg/cm² to 5.88 mg/cm²; the results are summarised in Table 1. Because polymeric membrane filters are commonly used in the fabrication of SILMs, a 0.22- μ m PVDF membrane filter was used for comparison purposes. The results revealed that the content of immobilised [Bmim][BF₄]-PVA in BP was significantly higher than that found in the PVDF membrane filters. This difference can be attributed to the tortuosity of the porous structure and the interstitial pore size of BP. Based on the SEM image shown in Fig. 5, the porous structure of BP was considerably more tortuous because the interstitial pores are smaller and not uniformly organised; thus, the pores enable the BP to efficiently entrap [Bmim][BF₄]-PVA during the immobilisation process. As the

loading of MWCNTs increased, the content of the immobilised [Bmim][BF₄]-PVA also increased until an optimum MWCNT loading in BP of 5.31 mg/cm², at which the immobilisation achieved an optimum content of 0.71 g/g MWCNTs. A further increase in the MWCNT loading in the BP resulted in a decrease in the immobilised [Bmim][BF₄]-PVA content, which may be caused by the fact that aggregated MWCNTs eventually decreased the interstitial pore distribution in the resulting BP, thereby reducing their efficiency to entrap [Bmim][BF₄]-PVA. In addition to the immobilised [Bmim][BF₄]-PVA content, the thickness of the resulting BP-SILM exhibited an increase in the MWCNT content of the BP, and the use of BP as a porous support enabled the formation of a thinner-layer membrane compared with the SILM formed using a PVDF membrane filter as a support.

The stress-strain curves shown in Fig. 6 demonstrate that all of the BP-SILMs behave as ductile materials because they demonstrated a linear elastic behaviour followed by plastic deformation before breaking. Based on the mechanical properties presented in Table 2, the tensile stress and the elongation of the BP-SILMs were significantly increased with an increase in the MWCNT loading of the BP, and the optimum tensile stress was achieved with a MWCNT content in the BP-SILM of 5.31 mg/cm². The increase in the mechanical properties with an increase in the MWCNT loading of the BP may be due to the increase in the number of entangled MWCNTs, which strengthens the MWCNT network. Furthermore, the immobilised [Bmim][BF₄]-PVA may serve as a binder to tighten the connection between the MWCNTs in the BP and extend the elongation and flexibility of the resulting BP-SILM. However, a decrease in the mechanical properties of the BP-SILM was observed at loadings greater than the optimum MWCNT loading of 5.31 mg/cm². As mentioned earlier, increasing the MWCNT content up to 5.88 mg/cm² caused the formation of aggregated MWCNTs, which impairs the mechanical stability of the BP structure. Moreover, the MWCNT network in the BP with 5.88 mg/cm² MWCNT may be loosely bound because the immobilised content of [Bmim][BF₄]-PVA, which served as a binding agent in the 5.88 mg/cm² BP, was reduced. Therefore, after the optimum immobilisation capacity and the mechanical properties were determined, the subsequent experiments were performed using the BP-SILM with 5.31 mg/cm² MWCNT BP.

The contact angle measurements presented in Table 3 indicate that the contact angle of PVA after infiltration in BP was slightly higher compared with that obtained with a pure PVA membrane: an increase in the contact angle from 55.4° to 73.5° was observed. This increase can be ascribed to the intrinsic hydrophobicity of the MWCNTs. However, the contact angle of the BP-SILM decreased from 68.6° to 46.9° when the content of [Bmim][BF₄] in BP-SILM was increased from 30 to 70 wt.%. This behaviour indicated an increase in the hydrophilicity of the membrane because the presence of [BF₄]⁻ anions in [Bmim][BF₄] tends to form hydrogen bonds with water [33], thereby reducing the surface tension of the water droplet and increasing the wettability of the BP-SILM surface. The increased hydrophilicity and the affinity of BP-SILM as a function of the [Bmim][BF₄] content were further verified through a liquid sorption test. Based on the degree of swelling presented in Table 4, the sorption capability of BP-SILM in water and ethylene glycol was found to be increased with an increase in the content of [Bmim][BF₄] in the BP-SILM. The increase in the sorption of water with increasing [Bmim][BF₄] is simply due to the tendency of the [BF₄]⁻ anions to interact with water and form hydrogen bonds. In addition, the increase in the sorption in ethylene glycol with increasing content of [Bmim][BF₄] in BP-SILM can be attributed to the hydrophobic interaction and the hydrogen bond formed between the [Bmim]⁺ cation with the -O- of the terminal-OH in ethylene glycol [34,35]. Although the presence of [Bmim][BF₄] increased the sorption of both water and ethylene glycol, the affin-

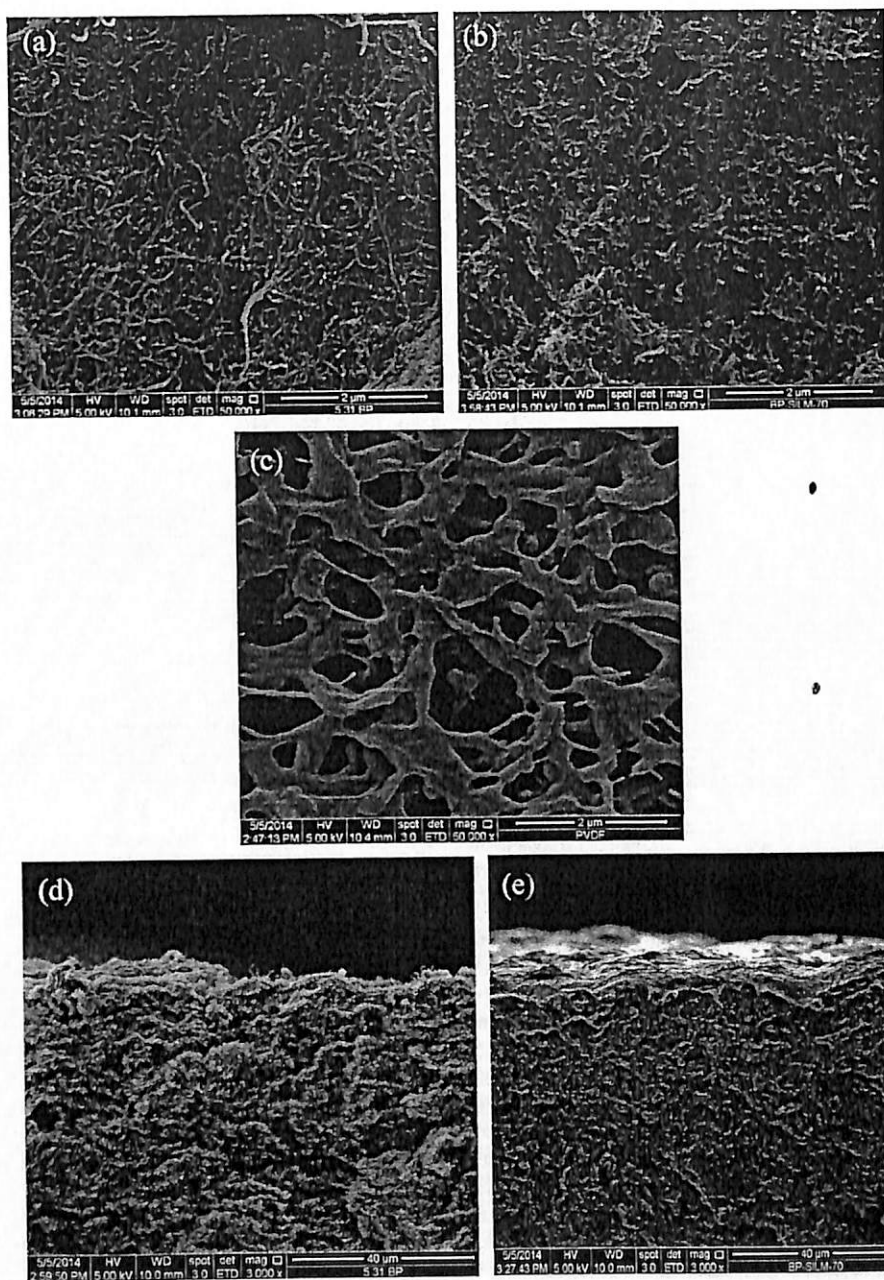


Fig. 5. SEM image of the surface morphologies of (a) BP, (b) BP-SILM, and (c) PVDF membrane filter and the cross-sectional views of (d) BP and (e) BP-SILM.

Table 1
Effect of the CNT content in the BP on the immobilisation of PVA-[Bmim][BF₄].

CNT content in the BP (mg/cm ²)	Immobilised content (g/g MWCNTs)	Thickness (μm)
3.44	0.60	76
4.01	0.63	84
4.59	0.68	90
5.31	0.71	117
5.88	0.65	123
0.22-μm PVDF membrane filter	0.08	125

ity of the membrane can still be traced to the binary interaction parameter, χ_{im} : a stronger affinity between the component and membrane is usually indicated by a lower χ_{im} value. As shown in Table 4, the values of χ_{im} for both water and ethylene glycol with

BP-SILM decreased with an increase in the [Bmim][BF₄] content, suggesting a stronger interaction between the water and ethylene glycol with the increased [Bmim][BF₄] content in the BP-SILM. However, note that the χ_{im} value of water is lower than that of ethylene glycol. This behaviour implies that the interaction of BP-SILM with water is greater than that with ethylene glycol; therefore, the effect of the [Bmim][BF₄] content in the BP-SILM toward the sorption capacity is more pronounced in water.

3.2. Pervaporation performances

3.2.1. Effect of the [Bmim][BF₄] content in the BP-SILM

The pervaporation experiments were performed under the operating conditions of 10 wt.% water in the feed solution at 30 °C and a downstream pressure of 0.667 kPa. The impact of the

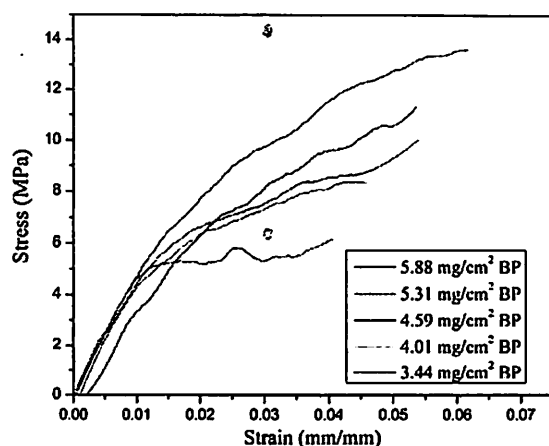


Fig. 6. Stress vs. strain curves for BP-SILMs with different contents of MWCNTs in the BP.

Table 2
Effect of the CNT content in the BP on the mechanical properties of the BP-SILM.

CNT content in the BP (mg/cm ²)	Tensile stress (MPa)	Elongation at break (%)
3.44	6.83	3.77
4.01	9.15	4.56
4.59	11.34	5.24
5.31	14.18	6.46
5.88	10.62	5.33

Table 3
Contact angle measurements as a function of the weight fraction of [Bmim][BF₄] in the BP-SILM.

Type of membrane	Contact angle (°)
PVA membrane	55.4
BP-PVA ^a	73.5
BP-SILM-30 ^b	68.6
BP-SILM-50 ^c	53.5
BP-SILM-70 ^d	46.9

^a BP infiltrated with pure PVA.

^b BP infiltrated with [Bmim][BF₄]-PVA (30/70) wt.%.

^c BP infiltrated with [Bmim][BF₄]-PVA (50/50) wt.%.

^d BP infiltrated with [Bmim][BF₄]-PVA (70/30) wt.%.

Table 4
Sorption data of the BP-SILMs as a function of the weight fraction of [Bmim][BF₄].

Type of BP-SILMs	Degree of swelling (g/g membrane)		Interaction parameter, χ_{im}	
	Water	Ethylene glycol	Water	Ethylene glycol
BP-SILM-30	1.2185	0.6890	0.6990	0.8508
BP-SILM-50	1.3352	0.7867	0.6837	0.8152
BP-SILM-70	1.5520	0.8170	0.6607	0.8057

presence of BP was also studied by comparing the pervaporation performance between the pure PVA and the BP-PVA membranes. As depicted in Fig. 7, the permeation flux of BP-PVA was approximately threefold higher than that of the pure PVA membranes, but its separation factor was a slightly lower. This finding demonstrates that the presence of BP increases the permeability of the membrane due to the additional frictionless transport pathway for the permeation of molecules provided by the inner hollow core of the MWCNTs in the BP. The pervaporation performance can be

further enhanced with the addition of [Bmim][BF₄]. As observed in Fig. 7, the permeation flux and separation factor were markedly increased when the content of [Bmim][BF₄] was increased up to 70 wt.%. The impact of the [Bmim][BF₄] content in the BP-SILM is consistent with the finding obtained in the liquid sorption study. The increase in the [Bmim][BF₄] content improved the hydrophilicity of the membrane, which could facilitate the contact of water with the membrane surface. Additionally, the presence of [Bmim][BF₄] could contribute to a decrease in the mass transfer resistance, thus enabling the rapid permeation of the components through the membrane. Overall, the BP-SILM-70 exhibits the highest separation factor among these three BP-SILMs; therefore, the subsequent pervaporation studies were conducted using the BP-SILM-70.

3.2.2. Effect of the feed concentration

The effect of the feed concentration on the pervaporation performance of the BP-SILM-70 was studied using a feed water concentration in the range of 10–50 wt.% at 30 °C and a downstream pressure maintained at 0.667 kPa. As shown in Fig. 8(a), the permeation flux was clearly increased with an increase in the feed water concentration, whereas the separation factor exhibited the opposite trend. At the lower feed water concentration, ethylene glycol, which possesses a higher dipole moment than water, may occupy the membrane surface, and the high viscosity and slow motion of ethylene glycol provide a steric effect that hinders the transportation of water molecules through the channel. Furthermore, the high polarity of ethylene glycol with two hydroxyl groups in each molecule may easily form hydrogen bonds with water molecules, causing a delay in the water transport. In addition, a lower feed water concentration results in a lower water activity in the feed side and creates a smaller chemical potential gradient across the membrane, thus leading to a lower permeation flux at lower feed water concentrations. An increase in the feed water concentration caused the BP-SILM-70 to promptly swell because of its hydrophilicity. The swelling phenomenon eventually increased the free volume in the membrane and caused the membrane to become susceptible to the permeation of both water and ethylene glycol molecules, thereby leading to an increase in the permeation flux but compromising the separation factor. To evaluate the effect of the feed concentration on the intrinsic properties of the membrane, the pervaporation performance of the BP-SILM-70 was expressed in terms of the permeance by normalising the driving force. Fig. 8(b) clearly shows that the permeances of BP-SILM-70 are dependent on the concentration after eliminating the driving force contribution. Increasing the water concentration in the feed solution markedly increased the permeability for ethylene glycol and caused the membrane to be less water selective. Nevertheless, the permeation flux of ethylene glycol, as shown in Fig. 8(a), was much lower than that of water, particularly at a feed water concentration of 50 wt.%, even though the permeance of ethylene glycol as shown in Fig. 8(b) is higher. This behaviour may be due to the extremely low vapour pressure of ethylene glycol, which forms a rather weak driving force for the permeation.

3.2.3. Effect of the feed temperature

The effect of the feed temperature was investigated by performing the pervaporation experiments at a feed temperature in the range of 30–70 °C with a feed water concentration of 10 wt.% and a downstream pressure of 0.667 kPa. The BP-SILM-70 demonstrated good thermal stability over the temperature range tested. Based on the results shown in Fig. 9(a), the permeation flux progressively increased with increasing feed temperature, but the separation factor declined with increasing feed temperature. This behaviour could be the result of the ascending saturated vapour pressure of both water and ethylene glycol with elevated temper-

Fig. 7. Effect of the [Bmim][BF₄] content on the pervaporation performances of BP-SILM-70 in terms of (a) the permeation flux and the separation factor.

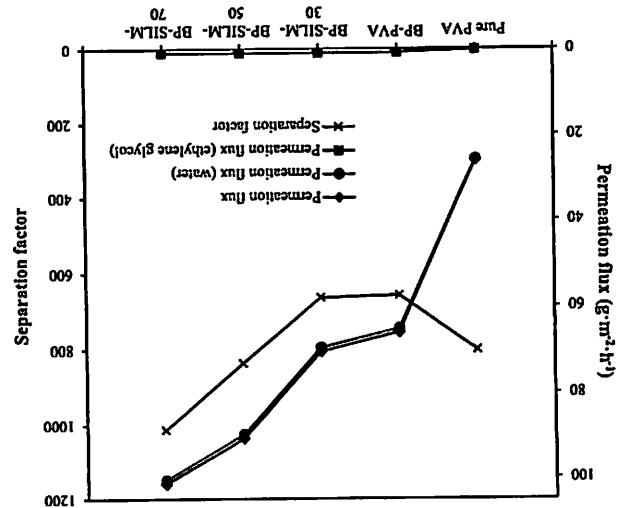


Fig. 8. Effect of the feed concentration on the pervaporation performances of BP-SILM-70 in terms of (a) the permeation flux and the separation factor and (b) the permeance and the selectivity.

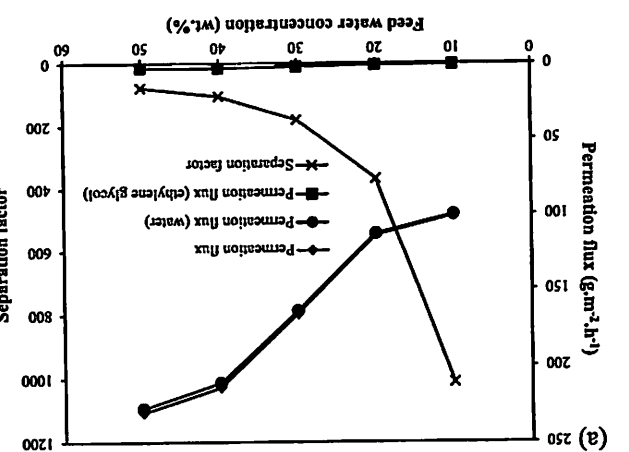
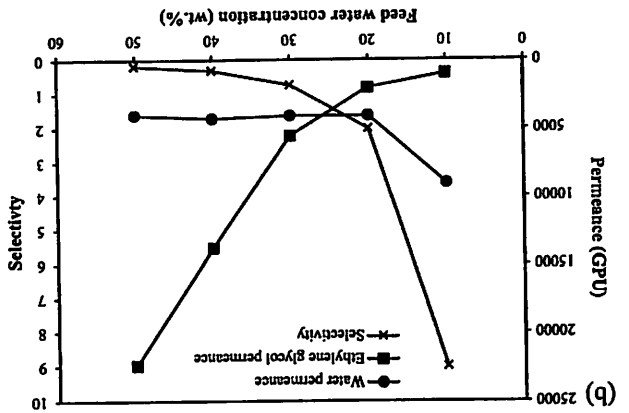
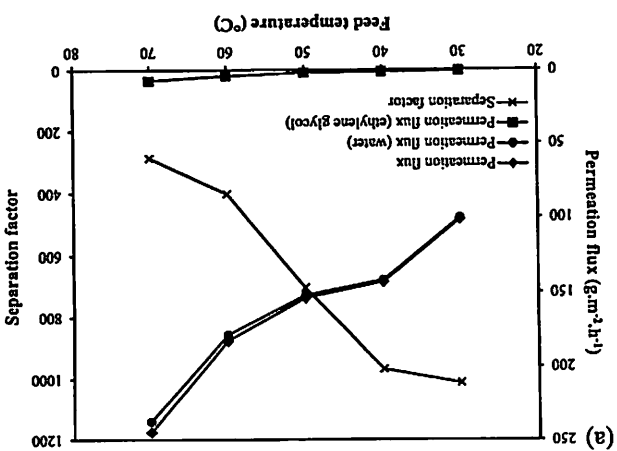
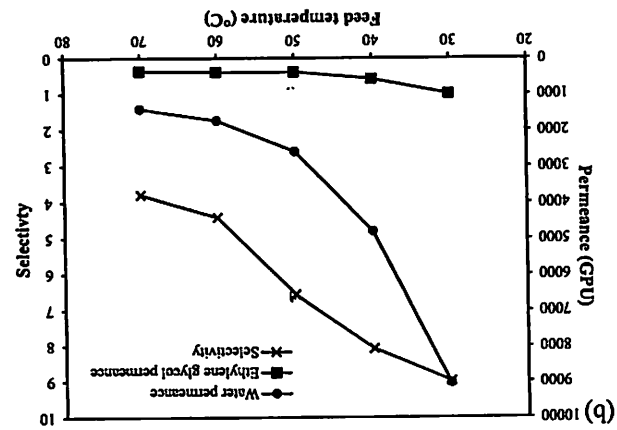


Fig. 9. Effect of the feed temperature on the pervaporation performances of BP-SILM-70 in terms of (a) the permeation flux and the separation factor and (b) the permeance and the selectivity.



$$J_i = J_{i0} \exp\left(-\frac{E_{Fi}}{RT}\right) \quad (8)$$

where E_{Fi} represents the activation energy for the permeation of component i , which takes into account the impact of the driving force. The related Arrhenius parameters were estimated from the Arrhenius plot in Fig. 10 and summarised in Table 5. As shown in Table 5, the E_{Fi} values, which were obtained from the slope of a semi-logarithmic plot of the permeation flux as a function of the reciprocal of the absolute temperature ($1/T$) as showed in Fig. 10(a), were 17 kJ/mol and 46 kJ/mol for the permeation of water and ethylene glycol, respectively. The obtained E_{Fi} values implied that the effect of temperature on the permeation of water is greater than that on the permeation of ethylene glycol. Thus, the E_{Fi} values explained the higher permeation flux observed in water over the experimental temperature range.

However, note that both the membrane permeance and the selectivity were found to decrease at elevated feed temperatures.

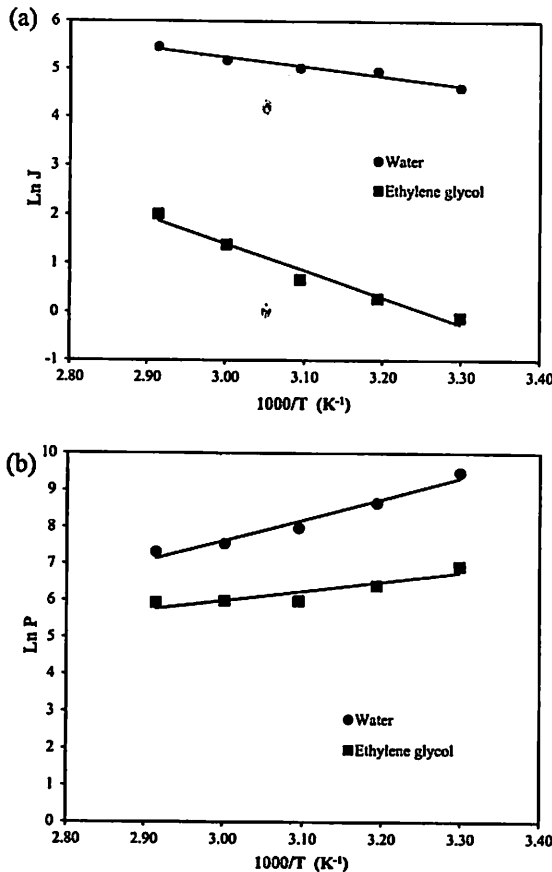


Fig. 10. Arrhenius plot of (a) the permeation flux and (b) the permeance.

Table 5
Arrhenius parameters of permeation flux and permeance for water and ethylene glycol.

Arrhenius parameters	Water	Ethylene glycol
Permeation flux, J		
Pre-exponential factor, J_0	8.39×10^4	6.28×10^7
Activation energy, E_{Ji} (kJ/mol)	16.86	45.89
Permeance, P		
Pre-exponential factor, P_0	8.11×10^{-5}	1.84×10^{-1}
Activation energy, E_{Pi} (kJ/mol)	-47.25	-21.31

The effect of temperature on the permeance was also expressed by an Arrhenius relationship:

$$P_i = P_{i0} \exp\left(-\frac{E_{Pi}}{RT}\right) \quad (9)$$

where E_{Pi} is the permeation activation energy that characterised the dependence of the membrane permeability on temperature. As seen in Table 5, the E_{Pi} values for water and ethylene glycol were -47 kJ/mol and -21 kJ/mol, respectively. According to the solution-diffusion mechanism, the permeance was based on the diffusion and sorption of the permeating component; for this reason, the permeation activation energy is the total of the heat of sorption and the activation energy for diffusion [36]. In most cases, the sorption is usually an exothermic process, whereas the diffusion is generally endothermic; therefore, the negative permeation activation energy appears to suggest that the membrane permeance is governed by the exothermic sorption process. Thus, the decreasing permeance observed with elevated temperature may be due to the reduction

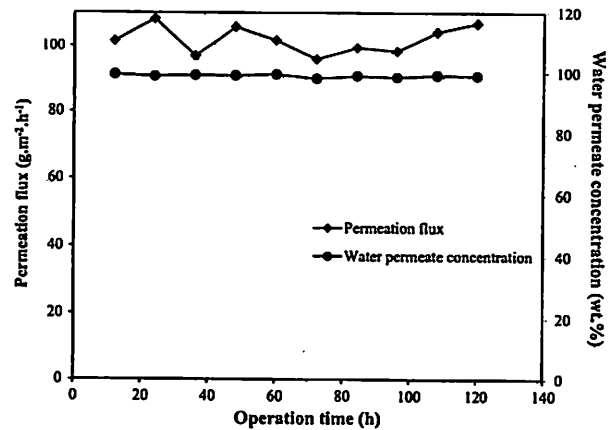


Fig. 11. Pervaporation performances of BP-SILM-70 at 120 h operation time.

in sorption. This finding can be explained by the fact that the molecules are energetic at higher temperatures, which results in the molecules being more disordered and highly dispersed, thereby reducing the possibilities for each molecule to interact with the membrane. Despite this decreased permeance, the increases in the permeation flux of both water and ethylene glycol, as observed in Fig. 9(a), indicated the dominant impact of the driving force induced from the elevated feed temperature on the intrinsic transport properties of the membrane.

3.3. Membrane stability

Membrane stability is one of the important criteria in SLM. The instability of the SLM through the loss of liquid membrane from the membrane support could critically impact the membrane separation ability. The stability of the BP-SILM-70 was assessed by continuous operation for 120 h with 10 wt.% feed concentration of water at 30 °C and the downstream pressure was maintained at 0.667 kPa. A fresh feed mixture was prepared at every 12 h of operation.

As shown in Fig. 11, the BP-SILM-70 demonstrated a robust pervaporation performance over an operating period of 120 h. The permeation fluxes were within 5% deviation with value in the range of 101–108 $\text{g m}^{-2} \text{h}^{-1}$. However, the separation factor may not be appropriate to evaluate the efficiency of the membrane to separate water from the ethylene glycol aqueous mixtures over a prolong operation period since the separation factor of the membrane is very sensitive toward a small changes in the permeate concentration of water. Therefore, the permeate concentration of water was used instead of separation factor for the stability study purpose. It is clearly showed that the water permeate concentration were observed in between 98 and 99 wt.%. In addition, it is interesting to note that there was no significant change in the weight of the BP-SILM-70 throughout the operating periods. The result implied a considerably good long-term physical stability exhibited in BP-SILM-70 without any significant loss of the liquid membrane. This can be credited to the formation of stable compound as a result of the blending of the [Bmim][BF₄] with PVA which enable the [Bmim][BF₄] to be strongly held inside the interstitial pores of BP and withstand its displacement from the BP under higher transmembrane pressure condition. Apart from that, the good stability in the BP-SILM-70 can also attributed to the use of BP as a membrane support. The highly tortuous porous structure and smaller interstitial pore size in BP could aid in securing the immobilized liquid membrane.

Table 6
Comparison of the pervaporation performance for the dehydration of ethylene glycol.

Membrane	Feed water concentration (wt.%)	Temperature (°C)	Permeation flux ($\text{g m}^{-2} \text{h}^{-1}$)	Separation factor	Water ^a permeance (gpu)	Selectivity ^a	Refs.
Chitosan–PVA	10	70	460	663	2603	8.48	[1]
PVA–silica	20	70	67	311	228	3.93	[6]
Crosslinked PVA	20	70	211	933	719	11.80	[29]
Polyvinylamine–PVA–CNTs on polysulfone	1	70	146	1156	7135	16.58	[37]
PVA–zeolite 4A on polypropylene	20	70	143	972	513	12.88	[38]
PVA	10	30	26	802	2328	6.84	This study
BP-SILM-70	10	30	102	1014	9046	9.00	This study

^a The water permeance and selectivity of the literature-reported membrane were calculated using Eqs. (6) and (7), respectively.

3.4. Comparison of the present pervaporation performance with the reported data

The pervaporation performance of the BP-SILM-70 membranes on the dehydration of ethylene glycol was compared with that of other available literature-reported PVA membranes [1,6,29,37,38], as listed in Table 6. The BP-SILM-70 was capable of exhibiting a comparative permeation flux and a relatively high separation factor. As the comparison was made based on the intrinsic permeability of the membrane, the insights indicated that the BP-SILM-70 was highly susceptible for water permeance, whereas the selectivity remained competitive with the membranes listed in Table 6. In fact, compared with the pure PVA membrane, the BP-SILM-70 exhibited improved permeation flux, separation factor, water permeance and selectivity. Note that the optimum performance of the membranes reported in the literature requires operation at a relatively higher temperature in the range of 70–80 °C, whereas the BP-SILM exhibited competitive performance with a feed temperature as low as 30 °C. This finding can be attributed to the presence of [Bmim][BF₄], which can eventually reduce the mass transfer resistance and enhance the diffusivity. Therefore, the use of BP-SILM can potentially reduce the overall energy consumption of the pervaporation process.

4. Conclusions

A novel symmetric SILM was successfully prepared by infiltrating BP with a [Bmim][BF₄]-PVA blend to form a BP-SILM. The novel BP-SILM was applied for the dehydration of ethylene glycol via the pervaporation process. A sonication time of 15 min was found to be sufficient to disperse the MWCNTs used for the synthesis of the BP via a wet processing technique, whereas the immobilisation via a vacuum-based technique allowed the entrapment of the [Bmim][BF₄]-PVA inside the deeper interstitial pores of the BP. The structure of the BP-SILM, in which the support and selective membrane layer of BP-SILM are merged into a single layer to form a symmetric membrane, was found to be different from structure of conventional asymmetric membranes. This novel structure reduced the overall membrane thickness and mass transport resistance. In addition, the use of BP as a support enhanced the thermal and mechanical stability of the BP-SILM and improved the immobilised capacity of the [Bmim][BF₄]-PVA, which can be attributed to the presence of a tortuous pore structure and the small interstitial pore size of the BP. Furthermore, the BP also provided an additional transport pathway to enhance the permeation of the BP-SILM. The interaction of BP-SILM with water was found to increase with an increase in the content of [Bmim][BF₄] because the presence of a higher content of [Bmim][BF₄] significantly improved the hydrophilicity of the BP-SILM. The pervaporation studies on BP-SILM revealed its capability to dehydrate ethylene glycol, and

a higher content of [Bmim][BF₄] in BP-SILM improved the pervaporation performance. The optimum pervaporation performance was obtained using the BP-SILM-70. The BP-SILM-70 also demonstrated considerably good membrane stability and a robust pervaporation performance over an operating period of 120 h. Compared with other membranes reported in the literature, the pervaporation performance of BP-SILM-70 remained competitive, particularly in terms of the intrinsic transport properties, where the BP-SILM-70 exhibited a higher permeability toward water at lower feed temperatures, which can be attributed to the presence of [Bmim][BF₄], which eventually reduced the mass transfer resistance and increased the diffusivity.

Acknowledgements

The authors acknowledge MyPhD fellowship supports from the Ministry of Higher Education of Malaysia. This research work was financially supported by a Universiti Sains Malaysia Research University (RU) Grant (A/C:814142) and the Postgraduate Research Grant Scheme (PRGS) (A/C:8045034).

References

- [1] M.N. Hyder, P. Chen, Pervaporation dehydration of ethylene glycol with chitosan-poly(vinyl alcohol) blend membranes: effect of CS-PVA blending ratios, *J. Membr. Sci.* 340 (2009) 171–180.
- [2] M. Shahverdi, T. Mohammadi, A. Pak, Separation of ethylene glycol–water mixtures with composite poly(vinyl alcohol)–polypropylene membranes, *J. Appl. Polym. Sci.* 119 (2011) 1704–1710.
- [3] P.S. Rao, S. Sridhar, Y.W. Ming, A. Krishnaiah, Pervaporative separation of ethylene glycol/water mixtures by using cross-linked chitosan membranes, *Ind. Eng. Chem. Res.* 46 (2007) 2155–2163.
- [4] A.S. Reddy, N.S. Kumar, M.V. Subbaiah, M. Suguna, A. Krishnaiah, Maleic anhydride crosslinked alginate–chitosan blend membranes for pervaporation of ethylene glycol–water mixtures, *J. Macromol. Sci. Part A Pure Appl. Chem.* 46 (2009) 1069–1077.
- [5] H. Dogan, N.D. Hilmioglu, Chitosan coated zeolite filled regenerated cellulose membrane for dehydration of ethylene glycol/water mixtures by pervaporation, *Desalination* 258 (2010) 120–127.
- [6] R. Guo, X. Ma, C. Hu, Z. Jiang, Novel PVA–silica nanocomposite membrane for pervaporative dehydration of ethylene glycol aqueous solution, *Polymer* 48 (2007) 2939–2945.
- [7] Y.T. Ong, K.F. Yee, Y.K. Cheng, S.H. Tan, A review on the use and stability of supported liquid membranes in the pervaporation process, *Sep. Purif. Rev.* 43 (2014) 62–88.
- [8] J. Yu, H. Li, H. Liu, Recovery of acetic acid over water by pervaporation with a combination of hydrophobic ionic liquids, *Chem. Eng. Commun.* 193 (2006) 1422–1430.
- [9] D. Yongquan, W. Ming, C. Lin, L. Mingjun, Preparation, characterization of P(VDF-HFP)/[bmim]BF₄ ionic liquids hybrid membranes and their pervaporation performance for ethyl acetate recovery from water, *Desalination* 295 (2012) 53–60.
- [10] H. Cascon, S. Choudhary, Separation performance and stability of PVDF-co-HFP/alkylphosphonium dicyanamide ionic liquid gel-based membrane in pervaporative separation of 1-butanol, *Sep. Sci. Technol. (Philadelphia)* 48 (2013) 1616–1626.

- [11] S. Heitmann, J. Krings, P. Kreis, A. Lennert, W.R. Pitner, A. Görak, M.M. Schulte, Recovery of n-butanol using ionic liquid-based pervaporation membranes, *Sep. Purif. Technol.* (2012)
- [12] A. Plaza, G. Merlet, A. Hasanoglu, M. Isaacs, J. Sanchez, J. Romero, Separation of butanol from ABE mixtures by sweep gas pervaporation using a supported gelled ionic liquid membrane: analysis of transport phenomena and selectivity, *J. Membr. Sci.* 444 (2013) 201–212.
- [13] A.B. Beltran, G.M. Nisola, E.L. Vivas, W. Cho, W.J. Chung, Poly(octylmethylsiloxane)/oleyl alcohol supported liquid membrane for the pervaporative recovery of 1-butanol from aqueous and ABE model solutions, *J. Ind. Eng. Chem.* 19 (2013) 182–189.
- [14] P. Izák, W. Ruth, Z. Fei, P.J. Dyson, U. Kragl, Selective removal of acetone and butan-1-ol from water with supported ionic liquid-polydimethylsiloxane membrane by pervaporation, *Chem. Eng. J.* 139 (2008) 318–321.
- [15] Y. Qin, J.P. Sheth, K.K. Sirkar, Pervaporation membranes that are highly selective for acetic acid over water, *Ind. Eng. Chem. Res.* 42 (2003) 582–595.
- [16] Y. Qin, J.P. Sheth, K.K. Sirkar, Supported liquid membrane-based pervaporation for VOC removal from water, *Ind. Eng. Chem. Res.* 41 (2002) 3413–3428.
- [17] M. Matsumoto, Y. Murakami, K. Kondo, Separation of 1-butanol by pervaporation using polymer inclusion membranes containing ionic liquids, *Solvent Extr. Res. Dev. – Jpn.* 18 (2011) 75–83.
- [18] Q. Gan, D. Rooney, M. Xue, G. Thompson, Y. Zou, An experimental study of gas transport and separation properties of ionic liquids supported on nanofiltration membranes, *J. Membr. Sci.* 280 (2006) 948–956.
- [19] P. Izák, M. Köckerling, U. Kragl, Stability and selectivity of a multiphase membrane, consisting of dimethylpolysiloxane on an ionic liquid, used in the separation of solutes from aqueous mixtures by pervaporation, *Green Chem.* 8 (2006) 947–948.
- [20] L.C. Branco, J.G. Crespo, C.A.M. Afonso, Studies on the selective transport of organic compounds by using ionic liquids as novel supported liquid membranes, *Chem. – Eur. J.* 8 (2002) 3865–3871.
- [21] T. He, Towards stabilization of supported liquid membranes: preparation and characterization of polysulfone support and sulfonated poly(ether ether ketone) coated composite hollow fiber membranes, *Desalination* 225 (2008) 82–94.
- [22] A.I. López-Lorente, B.M. Simonet, M. Valcárcel, The potential of carbon nanotube membranes for analytical separations, *Anal. Chem.* 82 (2010) 5399–5407.
- [23] C.J. Frizzell, M. In Het Panhuis, D.H. Coutinho, K.J. Balkus, A.I. Minett, W.J. Blau, J.N. Coleman, Reinforcement of macroscopic carbon nanotube structures by polymer intercalation: the role of polymer molecular weight and chain conformation, *Phys. Rev. B – Condens. Matter Mater. Phys.* 72 (2005) 1–8.
- [24] C. Liu, Y.Y. Fan, M. Liu, H.T. Cong, H.M. Cheng, M.S. Dresselhaus, Hydrogen storage in single-walled carbon nanotubes at room temperature, *Science* 286 (1999) 1127–1129.
- [25] R.H. Baughman, C. Cui, A.A. Zakhidov, Z. Iqbal, J.N. Barisci, G.M. Spinks, G.G. Wallace, A. Mazzoldi, D. De Rossi, A.G. Rinzler, O. Jaschinski, S. Roth, M. Kertesz, Carbon nanotube actuators, *Science* 284 (1999) 1340–1344.
- [26] P. Dharap, Z. Li, S. Nagarajaiah, E.V. Barrera, Nanotube film based on single-wall carbon nanotubes for strain sensing, *Nanotechnology* 15 (2004) 379–382.
- [27] U. Vohrer, I. Kolaric, M.H. Haque, S. Roth, U. Detlaff-Weglikowska, Carbon nanotube sheets for the use as artificial muscles, *Carbon* 42 (2004) 1159–1164.
- [28] K.F. Yee, Y.T. Ong, A.R. Mohamed, S.H. Tan, Novel MWCNT-buckypaper/polyvinyl alcohol asymmetric membrane for dehydration of etherification reaction mixture: fabrication, characterisation and application, *J. Membr. Sci.* 453 (2014) 546–555.
- [29] R. Guo, C. Hu, B. Li, Z. Jiang, Pervaporation separation of ethylene glycol/water mixtures through surface crosslinked PVA membranes: coupling effect and separation performance analysis, *J. Membr. Sci.* 289 (2007) 191–198.
- [30] A. Ballistreri, S. Foti, G. Montaudo, E. Scamporrino, Evolution of aromatic compounds in the thermal decomposition of vinyl polymers, *J. Polym. Sci. Part A – 1, Polym. Chem.* 18 (1980) 1147–1153.
- [31] K. Yang, Z.L. Yi, Q.F. Jing, R.L. Yue, W. Jiang, D.H. Lin, Sonication-assisted dispersion of carbon nanotubes in aqueous solutions of the anionic surfactant SDBS: the role of sonication energy, *Chin. Sci. Bull.* 58 (2013) 2082–2090.
- [32] M. Tahhan, Carbon nanotubes and conducting polymer composites, in: *Intelligent Polymers Research Institute – Faculty of Science, University of Wollongong*, 2004.
- [33] C. Chiappe, D. Pieraccini, Ionic liquids: solvent properties and organic reactivity, *J. Phys. Org. Chem.* 18 (2005) 275–297.
- [34] T. Singh, A. Kumar, Fluorescence behavior and specific interactions of an ionic liquid in ethylene glycol derivatives, *J. Phys. Chem. B* 112 (2008) 4079–4086.
- [35] S. Trivedi, S. Pandey, Interactions within a [ionic liquid + poly(ethylene glycol)] mixture revealed by temperature-dependent synergistic dynamic viscosity and probe-reported microviscosity, *J. Phys. Chem. B* 115 (2011) 7405–7416.
- [36] X. Feng, R.Y.M. Huang, Liquid separation by membrane pervaporation: a review, *Ind. Eng. Chem. Res.* 36 (1997) 1048–1066.
- [37] S.Y. Hu, Y. Zhang, D. Lawless, X. Feng, Composite membranes comprising of polyvinylamine-poly(vinyl alcohol) incorporated with carbon nanotubes for dehydration of ethylene glycol by pervaporation, *J. Membr. Sci.* 417–418 (2012) 34–44.
- [38] M. Shahverdi, B. Baheri, M. Rezakazemi, E. Motae, T. Mohammadi, Pervaporation study of ethylene glycol dehydration through synthesized (PVA-4A)/polypropylene mixed matrix composite membranes, *Polym. Eng. Sci.* 53 (2013) 1487–1493.

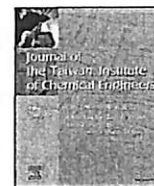
D

F



Contents lists available at ScienceDirect

Journal of the Taiwan Institute of Chemical Engineers

journal homepage: www.elsevier.com/locate/jtice

A facile and acid-free approach towards the preparation of sulphonated multi-walled carbon nanotubes as a strong protonic acid catalyst for biodiesel production

Siew Hoong Shuit^{a,b}, Eng Poh Ng^c, Soon Huat Tan^{a,*}^a School of Chemical Engineering, Universiti Sains Malaysia, Engineering Campus, Seri Ampangan, 14300 Nibong Tebal, Pulau Pinang, Malaysia^b Department of Chemical Engineering, Faculty of Engineering and Science, Universiti Tunku Abdul Rahman, Jalan Genting Kelang, Setapak, 53300 Kuala Lumpur, Malaysia^c School of Chemical Sciences, Universiti Sains Malaysia, 11800 Pulau Pinang, Malaysia

ARTICLE INFO

Article history:

Received 16 October 2014

Revised 2 February 2015

Accepted 8 February 2015

Available online 28 February 2015

Keywords:

Multi-walled carbon nanotubes

Sulphonation

Thermal decomposition

Biodiesel

Esterification

ABSTRACT

The process of grafting multi-walled carbon nanotubes (MWCNTs) with SO_3H groups is known as sulphonation. The most common method to sulphonate MWCNTs is via thermal treatment with concentrated sulphuric acid. However, the major drawbacks of this sulphonation process are that it is time consuming, energy intensive and requires the use of concentrated acid. In contrast, in this study, sulphonated MWCNTs (s-MWCNTs) were prepared using a facile and acid-free approach via the thermal decomposition of ammonium sulphate $(\text{NH}_4)_2\text{SO}_4$ with the aid of ultrasonication. The effects of the concentration of the $(\text{NH}_4)_2\text{SO}_4$ solution and the ultrasonication period of MWCNTs in the $(\text{NH}_4)_2\text{SO}_4$ solution were studied and optimised to enhance the catalytic activity of s-MWCNTs. These results showed that s-MWCNTs with the best performance could be obtained by ultrasonating the purified MWCNTs in a 10 wt.% $(\text{NH}_4)_2\text{SO}_4$ solution for 10 min followed by heating at 235 °C for 30 min. The resulting s-MWCNTs can produce a biodiesel yield of 84.9%. The high solubility of palm fatty acid distillate (PFAD) and the good dispersion behaviour of s-MWCNTs in methanol caused a reduction in reaction phases and thus minimised the mass transfer limitation encountered by conventional heterogeneous catalysts used for biodiesel production.

© 2015 Taiwan Institute of Chemical Engineers. Published by Elsevier B.V. All rights reserved.

1. Introduction

Biodiesel, which is also known as fatty acid methyl ester (FAME), is believed to have the potential to replace conventional petroleum-derived fuel because of its biodegradability, renewability, non-toxicity and low emission profile [1,2]. Transesterification or esterification is the most widely used method to produce biodiesel [1]. The common lipid feedstocks currently used for biodiesel production are non-edible oils, such as jojoba oil [3], waste cooking oil [4], crude *Jatropha curcas* oil [5,6], PFAD [7] and even microalgae oil [8] which contain high level of free fatty acids (FFAs) to avoid competing with food resources. The use of these oils has resulted in the use of only acid catalysts in transesterification or esterification [9]. However, the use of homogeneous acid catalysts, such as sulphuric acid (H_2SO_4) or hydrochloric acid (HCl), is not encouraged because of the corrosive nature of the catalysts and the difficulty in handling the generated wastewater [4,10,11]. Thus, heterogeneous acid catalysts are preferred over homogeneous acid catalysts because the products

are easy to separate and the catalysts are reusable; thus, the process is more environmentally friendly [12].

The common solid acid catalysts used for biodiesel production include ion-exchange resins [13,14], sulphated oxides [15], Mobil composite material number 41 (MCM-41) [16] and Nafion [17]. The major drawback of these solid acid catalysts is that the acid sites of the catalysts are easily reduced by the hydration of acidic hydroxyl groups (OH), which act as Brønsted acid sites in the presence of water [18]. Thus, carbon-based acid catalysts are an alternative for biodiesel production because the hydration of OH groups can be prevented by the hydrophobic properties of the carbon sheet [19]. The recently reported carbon-based solid acid catalysts used in biodiesel production include sugar catalysts prepared via the sulphonation of incompletely carbonised D-glucose/starch [20–24], ordered mesoporous carbon [4,25], vegetable oil asphalt-based carbon catalyst [26], sulphonated multi-walled carbon nanotubes (s-MWCNTs) prepared via thermal treatment with concentrated sulphuric acid [27], sulphonated biochar and sulphonated activated carbon [28,29]. Among the reported carbon materials, MWCNTs are believed to be a more promising candidate to serve as catalyst support for the sulphonic group (SO_3H) because of their intrinsic properties, such as high surface area; high

* Corresponding author. Tel.: +60 4 5996475; fax: +60 4 5941013.

E-mail address: chshtan@usm.my (S.H. Tan).

purity compared to activated carbon, which can avoid self-poisoning; and well-developed surface morphology and porosity [15,30]. The most common method for synthesising sulphonated carbon catalysts is thermal treatment with concentrated sulphuric acid in an inert environment. The major disadvantages of this method include the use of a hazardous and corrosive acid as the sulphoning agent, the process is time consuming and wastewater is generated from the washing process after sulphonation. Thus, the main objective of this study is to present a facile and acid-free sulphonation method to prepare s-MWCNTs, which consists of thermal decomposition of $(\text{NH}_4)_2\text{SO}_4$ with the incorporation of ultrasonication treatment. Ultrasonication treatment is usually used to break the agglomerates and to disperse MWCNTs in the sulphoning agent prior to the sulphonation process. However, the roles and the effects of ultrasonication treatment in sulphonation process have not been thoroughly studied. Thus, this study also focuses on the effects of different ultrasonication periods to the MWCNTs/ $(\text{NH}_4)_2\text{SO}_4$ solution mixture to obtain s-MWCNTs with the best catalytic performance. The effects of the concentration of the $(\text{NH}_4)_2\text{SO}_4$ solution (ranging from 1 to 20 wt.%) and the ultrasonication period of MWCNTs in $(\text{NH}_4)_2\text{SO}_4$ solution (ranging from 1 to 20 min) were studied and optimised. The catalytic activity of the s-MWCNTs was investigated through the esterification of PFAD with methanol to produce FAME.

2. Experimental

2.1. Materials

MWCNTs with diameters (40–60 nm) and lengths (1–2 μm) were purchased from Shenzhen Nanotechnologies Port Co. PFAD was obtained from a local edible oil manufacturing company. Nitric acid (HNO_3), which was purchased from JT Baker with a purity of 69–70%, was used to purify the raw MWCNTs. $(\text{NH}_4)_2\text{SO}_4$, methanol and *n*-hexane were purchased from Fisher Scientific. Methyl heptadecanoate was purchased from Sigma Aldrich.

2.2. Purification of MWCNTs

The process for purifying the MWCNTs is based on previously reported literatures [31,32]. One gram of pristine MWCNTs was mixed with 100 mL of HNO_3 , and the mixture was ultrasonicated for 1 h before heating at 80 °C for 8 h. The purified MWCNTs were filtered, washed with distilled water until the pH of the filtrate was similar to the pH of distilled water before drying at 120 °C for 12 h. The purified MWCNTs were denoted as MWCNTs-COOH.

2.3. Sulphonation of MWCNTs

The sulphonation procedures were modified according to previously reported literatures [33,34]. The major modification was the incorporation of the ultrasonication treatment to the mixture of MWCNTs-COOH and $(\text{NH}_4)_2\text{SO}_4$ solution to improve the colloidal dispersion to enhance the sulphonation of MWCNTs. In this process, 0.4 g of MWCNTs-COOH was mixed with 30 mL of different concentrations of a $(\text{NH}_4)_2\text{SO}_4$ solution (1, 5, 10, 15 and 20 wt.%) and the mixture was ultrasonicated for certain durations (1, 5, 10, 15 and 20 min). The mixture was then heated at 235 °C for 30 min. The mixture was washed with distilled water to remove excess $(\text{NH}_4)_2\text{SO}_4$ and prior to dried at 120 °C for 12 h. The final product was defined as s-MWCNTs.

2.4. Esterification reaction

The esterification of PFAD with methanol was performed in a pressurised batch reactor equipped with a thermocouple and a magnetic stirrer. The reactor was pressurised to 10 bars to avoid the evaporation of reactants, particularly methanol. The reaction was performed

under the following conditions: reaction temperature of 170 °C, reaction period of 3 h, methanol-to-PFAD ratio of 20 and s-MWCNTs loading of 2 wt.%. Prior to the reaction, the s-MWCNTs were stirred in methanol for 10 min. This is to avoid the adsorption of PFAD to the active sites that has tendency to deactivate the catalysts [35]. Upon completion of the reaction period, the reaction mixture was cooled and filtered.

2.5. FAME analysis

The composition and yield of FAME or biodiesel were analysed using a PerkinElmer Clarus 500 gas chromatograph equipped with a flame ionisation detector (FID) and a Nukol™ capillary column. *n*-Hexane and helium were used as the solvent and carrier gas, respectively. The oven temperature was set at 110 °C and then increased to 220 °C at a rate of 10 °C/min. The temperatures of the detector and injector were set at 220 and 250 °C, respectively. Methyl heptadecanoate was used as an internal standard [36,37]. The yield of FAME in the samples was calculated using the following equation:

$$\text{Yield (\%)} = \frac{(\sum \text{Concentration of each methyl esters}) \times (\text{Volume of oil layer})}{10 \text{ g of PFAD}} \times 100\%$$

2.6. Catalyst characterisation

2.6.1. FTIR analysis

Pyridine FTIR spectra were recorded using a Nicolet 6700 FT-IR spectrometer. The s-MWCNTs samples were first ground with KBr salt (mass ratio 5:1) and pressed into a wafer of 13 mm diameter prior to activated under vacuum (10^{-6} mbar) at 220 °C for 1 h. The background spectrum was recorded first after cooling the sample to room temperature. Pyridine vapour was then introduced to the sample for 2 min. The sample was evacuated at 100 °C to desorb pyridine and the spectrum was recorded after the evacuation step. All the spectra were recorded with a 16 cm^{-1} resolution and 300 scans accumulation. The presence of SO_3H groups was confirmed by FTIR analysis using a SHIMADZU IRPrestige-21 spectrometer over the frequency range of $4000\text{--}400 \text{ cm}^{-1}$. A mixture of MWCNTs and potassium bromide was pelleted into a thin pellet, and the IR spectrum was collected after 32 scans.

2.6.2. Pulse chemisorption

The density of the acid sites of the catalyst was determined by pulse chemisorption using a Micromeritics: Auto Chem II 2920 instrument. The gas used to quantify the total acid sites of the catalyst was 15% NH_3 in helium. In addition, 50 mg of sample was placed in a U-shape quartz tube in a temperature-controlled oven and connected to a thermal conductivity detector (TCD). The sample was first degassed at 120 °C with a heating rate of 10 °C in helium ($30 \text{ cm}^3/\text{min}$) for 1 h. The temperature was then cooled to 40 °C under the same helium flow. Next, 15% NH_3 in helium was introduced using a pulse method.

2.6.3. Raman spectroscopy analysis

Raman spectroscopy is a non-destructive method used to analyse the morphology of MWCNTs. The intensity ratio of the D- to G-band (I_D/I_G) in the Raman spectrum is a measure of the average defectiveness of MWCNTs. In this study, a Renishaw Via (Wotton-under-edge, UK) Raman microscope with a laser excitation of 633 nm was used to investigate the degree of defects in the MWCNTs caused by different ultrasonication periods.

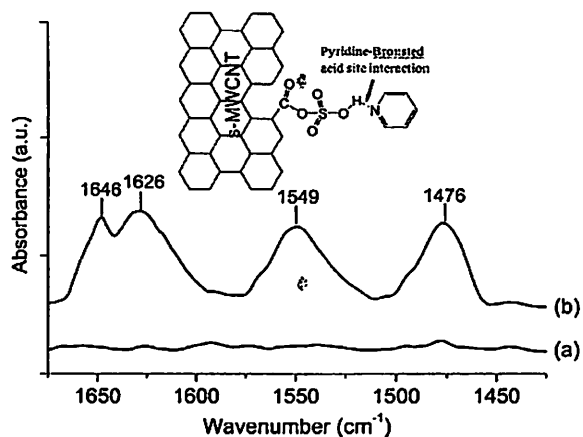


Fig. 1. Pyridine-FTIR spectra of (a) *s*-MWCNTs before pyridine adsorption (b) *s*-MWCNTs after pyridine adsorption at room temperature (10^{-6} mbar at equilibrium for 2 min).

2.6.4. Dispersion of *s*-MWCNTs in methanol

The dispersion of *s*-MWCNTs in methanol was examined using an Agilent Technologies Cary 60 UV–Vis at a wavelength of 500 nm. Prior to transfer into the cuvette, methanol solution containing *s*-MWCNTs (5 mg/L) was sonicated using a tip sonicator (Hielscher UP200S).

2.6.5. TGA analysis

The thermal degradation and stability of pristine MWCNTs, MWCNTs-COOH and *s*-MWCNTs were investigated using a TA Instruments SDT Q600. Typically, the samples in powder form were placed in the alumina crucibles and the samples were heated under air atmosphere at a heating rate of 10 °C/min from room temperature to 900 °C.

2.6.6. Nitrogen sorption analysis

The specific surface area, average pore width and pore volume were measured by nitrogen sorption analysis using a Micromeritics ASAP2020 surface analyser. The specific surface area was calculated using a Brunauer–Emmer–Teller (BET) plot in a relative pressure range (P/P_0) of 0.05–0.3. The total pore volume was determined from the amount of N_2 adsorbed at a P/P_0 of 0.99. In addition, the average pore diameter was determined using Barrett–Joyner–Halenda (BJH) model based on the desorption branch of the isotherm.

3. Results and discussion

3.1. Mechanism of FAME formation using *s*-MWCNTs as a catalyst

The type of acid sites in the *s*-MWCNTs needs to be determined before predicting the mechanism of FAME formation using *s*-MWCNTs as a catalyst. Lewis or Brønsted acidity of the catalyst sample can be identified through pyridine-FTIR spectroscopy. Fig. 1 shows the pyridine-FTIR spectra of *s*-MWCNTs before and after pyridine adsorption. The peaks at 1646, 1626, 1549 and 1476 cm^{-1} appear only in the spectra of the *s*-MWCNTs after pyridine adsorption (Fig. 1b). The peaks at 1646, 1626, 1549 cm^{-1} were assigned to the vibration of pyridinium (PyH^+) species [38–40], indicating the presence of Brønsted acid site in the *s*-MWCNTs. The peak at 1476 cm^{-1} could also be due to the coordination of pyridine to Brønsted acid site since no IR bands corresponding to Lewis acid site was observed at 1455 cm^{-1} [41].

The mechanism of FAME formation using *s*-MWCNTs as a catalyst is shown in Fig. 2. The three electronegative oxygen atoms in the SO_3H group are strong electron withdrawing atoms favouring the dissociation of hydrogen atom into hydrogen ion. As a result, the hydrogen ion tends to be attached by the carbonyl oxygen atom of the fatty acid forming a carbocation (step 1). This is followed by the interaction between the methanol molecule with the carbocation via a nucleophilic attack to form a tetrahedral intermediate (step 2). The proton is then transferred from one oxygen atom to another (step 3). The proton is then transferred from one oxygen atom to another (step 4). The proton is then transferred from one oxygen atom to another (step 5).

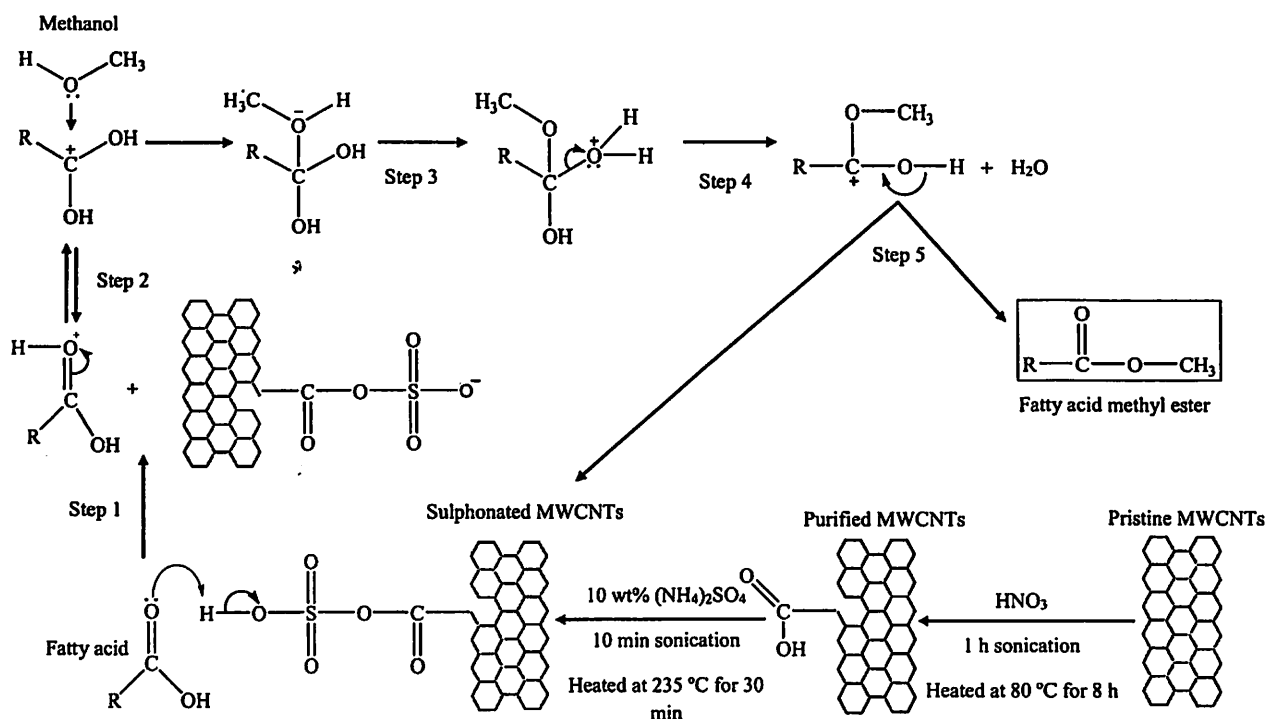


Fig. 2. Mechanism of FAME formation using *s*-MWCNTs as a catalyst.

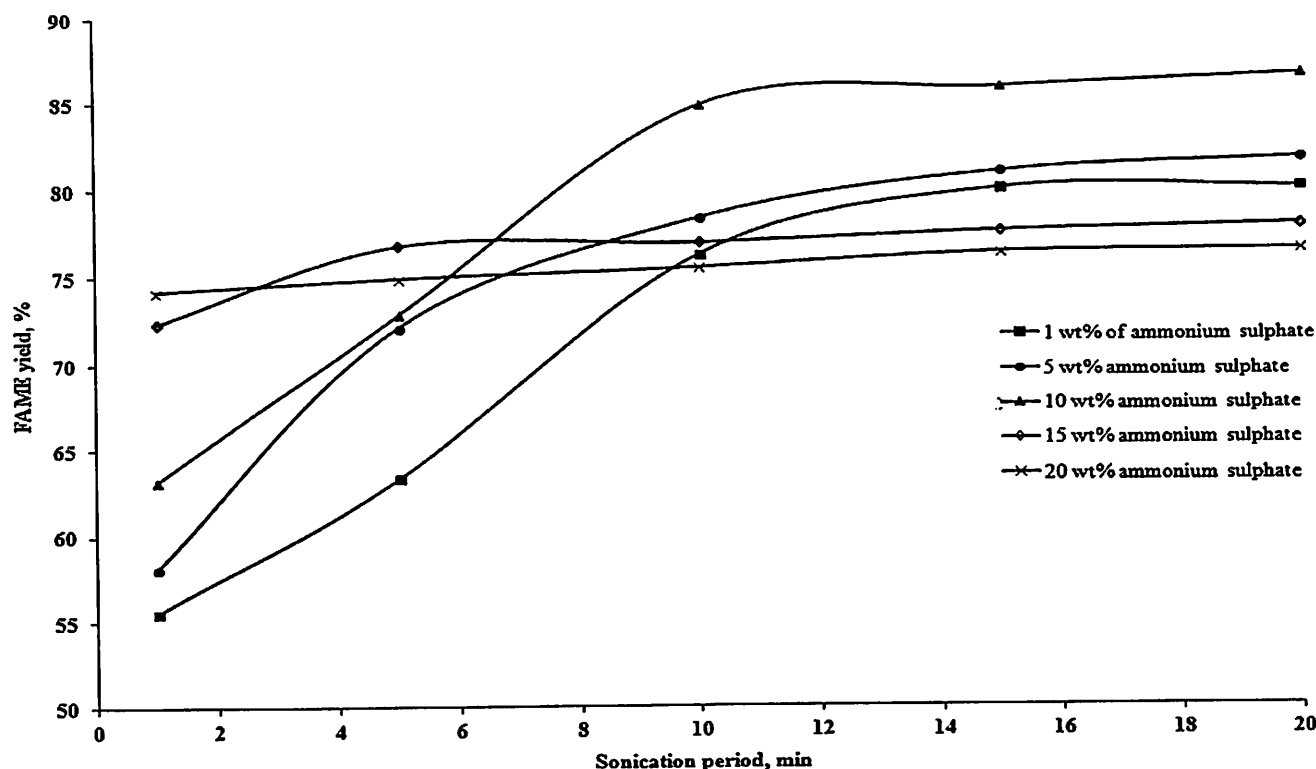


Fig. 3. FAME yield achieved by s-MWCNTs prepared using different ultrasonication periods and concentrations of $(\text{NH}_4)_2\text{SO}_4$ solution.

and a water molecule is eliminated by the tetrahedral intermediate (step 4). Finally, the loss of the acidic proton and elimination of water molecule regenerates the SO_3H group on the surface of MWCNTs and an atom of fatty acid methyl ester is produced (step 5).

3.2. Effect of the ultrasonication treatment period

The FAME yield achieved by s-MWCNTs synthesised using different ultrasonication periods and concentrations of $(\text{NH}_4)_2\text{SO}_4$ solution is shown in Fig. 3. The MWCNTs-COOH sulphonated with 1, 5 and 10 wt.% $(\text{NH}_4)_2\text{SO}_4$ exhibited similar result trends in which the FAME yield significantly increased when the ultrasonication period of the mixture increased from 1 to 10 min. Next, the FAME yield increased gradually and eventually became constant with further increasing the ultrasonication period to 15 min and 20 min, respectively. Due to weak van der Waals interactions, MWCNTs often aggregate into bundles or ropes, in which each bundle can consist of up to several hundred MWCNTs arranged in a hexagonal lattice [42,43]. In this work, ultrasonication treatment served to disperse and mix homogeneously the MWCNTs-COOH with the $(\text{NH}_4)_2\text{SO}_4$ solution, enabling easy interactions of the MWCNTs-COOH with $(\text{NH}_4)_2\text{SO}_4$ solution. As a result, the FAME yield increased with a longer ultrasonication period because the mixing intensity of the MWCNTs in the $(\text{NH}_4)_2\text{SO}_4$ solution was higher, thus improving the contact between MWCNTs-COOH and the $(\text{NH}_4)_2\text{SO}_4$ solution.

The surface of MWCNTs will be attacked by the generated localised sonochemistry causing defects in it [44]. These defects can be verified using Raman spectroscopy analysis. The D-band in a Raman spectrum indicates the presence of structural defects, and the G-band is referred to as graphite in nanotubes. Changes in the D- and G-bands in Raman spectra are a useful information for monitoring the structural modifications of the nanotube sidewalls caused by defects or the attachment of different chemical species [45]. The I_D/I_G ratio for the pristine MWCNTs was 0.90 (less than 1), indicating that the pristine MWCNTs

Table 1

Effects of different sonication periods on the I_D/I_G ratio and acid density of MWCNTs sulphonated with a 10 wt.% $(\text{NH}_4)_2\text{SO}_4$ solution.

Sonication period (min)	I_D/I_G ratio ^a	Acid density (mmol/g) ^b
1	1.02	0.015
5	1.08	0.021
10	1.17	0.030
15	1.22	0.033
20	1.35	0.034

^a Results of the I_D/I_G ratio were obtained from Raman spectroscopy analysis.

^b Results of acid density were obtained using pulse chemisorption.

contained more graphite than defect sites. When the pristine MWCNTs were subjected to acid purification coupled with 1 h of ultrasonication treatment to produce MWCNTs-COOH, the I_D/I_G ratio increased to 1.01, indicating that acid purification and ultrasonication treatment caused defects on the surface of the MWCNTs. This claim was strengthened by the results of the Raman spectra shown in Table 1, in which the I_D/I_G ratio of the s-MWCNTs increased when the ultrasonication period of the sulphonation mixture increased. The carbon atoms located at the opened tube caps are sp^2 hybridised, in which a double bond exists between two carbon atoms. These sp^2 -hybridised carbons are relatively more reactive than the sp^3 -hybridised carbons located in the regular graphene framework. The generated SO_3H groups will attack the partial carbon-carbon double bonds to transform the sp^2 -hybridised carbon atoms into more chemically stable sp^3 -hybridised carbon atoms [46]. Thus, the role of ultrasonication treatment in this sulphonation process is not only to mix and disperse the MWCNTs-COOH in $(\text{NH}_4)_2\text{SO}_4$ solution but also to open the tube caps and create defects along the sidewall for sulphonation. This finding was supported by the relationship between the I_D/I_G ratio of the Raman spectrum and the acid density of the s-MWCNTs (Table 1), where the acid density of the s-MWCNTs

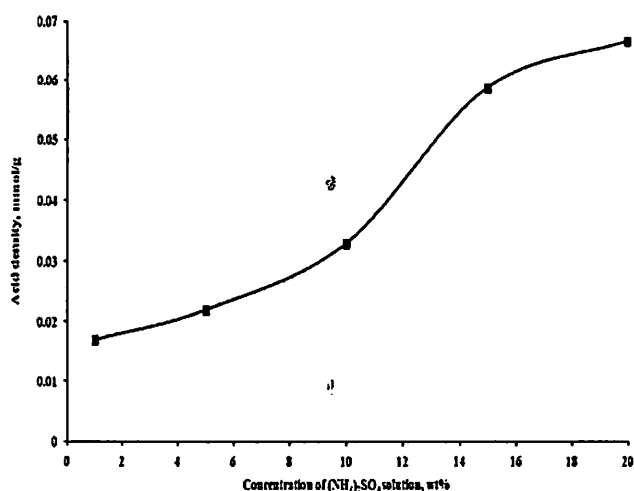


Fig. 4. Effect of the concentration of (NH₄)₂SO₄ solution on acid density of s-MWCNTs subjected to 20 min of ultrasonication period.

increased with longer ultrasonication treatment resulting from more defects (higher I_D/I_G ratio) on the surface of the MWCNTs.

Interestingly, as shown in Fig. 3 the increase in sonication period was found to have insignificant effect to the FAME yield when the s-MWCNTs were prepared at high (NH₄)₂SO₄ concentration (15 and 20 wt.%). The FAME yield of MWCNTs-COOH sulphonated with 15 wt.% (NH₄)₂SO₄ only showed an increase of 5% when the sonication period was extended from 1 to 5 min. Next, the FAME yield was constant although the sonication period was increased. In addition, the increase in sonication period did not cause any significant effect to the FAME yield produced by the MWCNTs-COOH sulphonated with 20 wt.% (NH₄)₂SO₄. The FAME yield was almost constant (increment not more than 4%) throughout the period of ultrasonication of the mixture from 1 to 20 min. This observation was believed to be caused by the interaction effect between sonication period and the concentration of (NH₄)₂SO₄ solution which will be discussed in the following section. The above results indicated that the optimum duration of the ultrasonication treatment to produce the s-MWCNTs in this study was 10 min.

3.3. Effect of (NH₄)₂SO₄ solution concentration

As shown in Fig. 3, two different result trends were obtained in the sulphonation of MWCNTs-COOH using different (NH₄)₂SO₄ solution concentrations. The first result trend was exhibited by s-MWCNTs prepared using low concentrations of (NH₄)₂SO₄ solution (1, 5 and 10 wt.%), in which the yield of FAME increased gradually when the concentration of the (NH₄)₂SO₄ solution increased. In addition, the other result trend was exhibited by MWCNTs-COOH sulphonated using high concentrations of (NH₄)₂SO₄ solution (15 and 20 wt.%), in which the catalysts underperformed compared to the catalysts prepared using low concentrations of the (NH₄)₂SO₄ solution.

Both result trends can be explained through Fig. 4, which shows the acid site density of s-MWCNTs prepared using different concentrations of the (NH₄)₂SO₄ solution. These results indicated that the acid site density of the catalysts increased when the concentration of the (NH₄)₂SO₄ solution increased. In sulphonation using the thermal decomposition of (NH₄)₂SO₄, the generated SO₃H groups will react with the surface hydrogen atoms that naturally contain MWCNTs-COOH and with the carboxyl groups created during acid purification to form the SO₃H groups [15,33]. Thus, when the concentration of the (NH₄)₂SO₄ solution increased, more SO₃ groups were produced to form a higher density of SO₃H groups, which served as the active sites for the esterification of PFAD with methanol.

However, extremely high concentrations of (NH₄)₂SO₄ solution may cause an adverse effect on the catalysts. Although there was a significant increase in acid site density (more than two-fold) when the concentration of the (NH₄)₂SO₄ solution was increased from 10 to 20 wt.% as shown in Fig. 4, but the FAME yield achieved by the s-MWCNTs prepared using high concentrations of (NH₄)₂SO₄ solution and a long ultrasonication treatment period was the lowest among all s-MWCNTs. This was due to the interaction effect between long sonication period and high concentration of (NH₄)₂SO₄ solution. The viscosity of the solution mixture (MWCNTs in (NH₄)₂SO₄ solution) may increase in high concentration of (NH₄)₂SO₄ which could affect the dispersibility of MWCNTs-COOH in the resultant solution. As a result, the MWCNTs remain agglomerate. Therefore, only the MWCNTs that located at the outer perimeter of the bundle will be exposed to the (NH₄)₂SO₄ solution. The degree of defect created on the surface of MWCNTs was believed to decrease. Moreover, under high concentration of (NH₄)₂SO₄, the defect-surface will be oversaturated by SO₃H groups [34]. In addition, when the surface of s-MWCNTs was saturated with SO₃H groups, the surface became highly negatively charged and thus causing difficulty for the lone-pair electron of the carbonyl group of the fatty acids to reach the OH groups of the SO₃H. From these results, the optimum concentration of (NH₄)₂SO₄ solution for this sulphonation process is 10 wt.%. The reusability of the s-MWCNTs was investigated through five consecutive runs. The s-MWCNTs prepared via thermal decomposition of (NH₄)₂SO₄ could maintain the FAME yield at 76.4% after five reaction runs, indicating high reusability of the s-MWCNTs.

3.4. Characterisation results of s-MWCNTs

3.4.1. IR spectral analysis of s-MWCNTs

The presence of sulphur groups in s-MWCNTs was confirmed using FTIR, as shown in Fig. 5. Significant differences can be observed in the spectra of the s-MWCNTs compared to the spectra of the pristine MWCNTs and MWCNTs-COOH, in which new peaks appeared after the sulphonation of MWCNTs. The broad absorption band at 3686 cm⁻¹ was attributed to the -OH stretching mode in hydroxyl groups, which indicated the presence of -COOH groups and -SO₃H groups [47]. The peak at 1392 cm⁻¹ was associated with the stretching mode of sulphate groups [48]. The absorption band at 1245 cm⁻¹ was assigned to the presence of sulphonate groups [49]. Furthermore, the presence of asymmetric and symmetric O=S=O stretching vibrations and the S-O groups in s-MWCNTs were confirmed by the absorption bands at 1061 and 668 cm⁻¹, respectively [50–52]. These results indicated that the SO₃H groups were successfully grafted onto the surface of the MWCNTs via the thermal decomposition of (NH₄)₂SO₄.

3.4.2. Dispersibility of s-MWCNTs in methanol

The UV-Vis spectra of the pristine MWCNTs, MWCNTs-COOH and s-MWCNTs were shown in Fig. 6. As indicated by the unstable absorbance spectrum which decreased since the beginning of the analysis, the pristine MWCNTs were proven to have poor dispersibility in methanol. This was due to the hydrophobic property of the carbon framework and the intrinsic van der Waals interactions that caused the agglomeration of pristine MWCNTs into bundle [47]. On the other hand, the UV-Vis spectra showed that the MWCNT-COOH and s-MWCNTs remained colloidal stable and well dispersed in methanol after 720 min (12 h). The absorbance of the s-MWCNTs and methanol mixture decreased gradually at the beginning of the analysis, which was most likely due to the aggregation of the MWCNTs to a micron-sized cluster that then settled to the bottom of the cuvette. The s-MWCNTs were stable and remained dispersed after 100 min until 720 min. The dispersibility of the s-MWCNTs in methanol was caused by the surface modification of the introduced SO₃H and COOH groups onto the surface of MWCNTs via the acid purification and sulphonation process. The SO₃H and COOH groups on the surface of

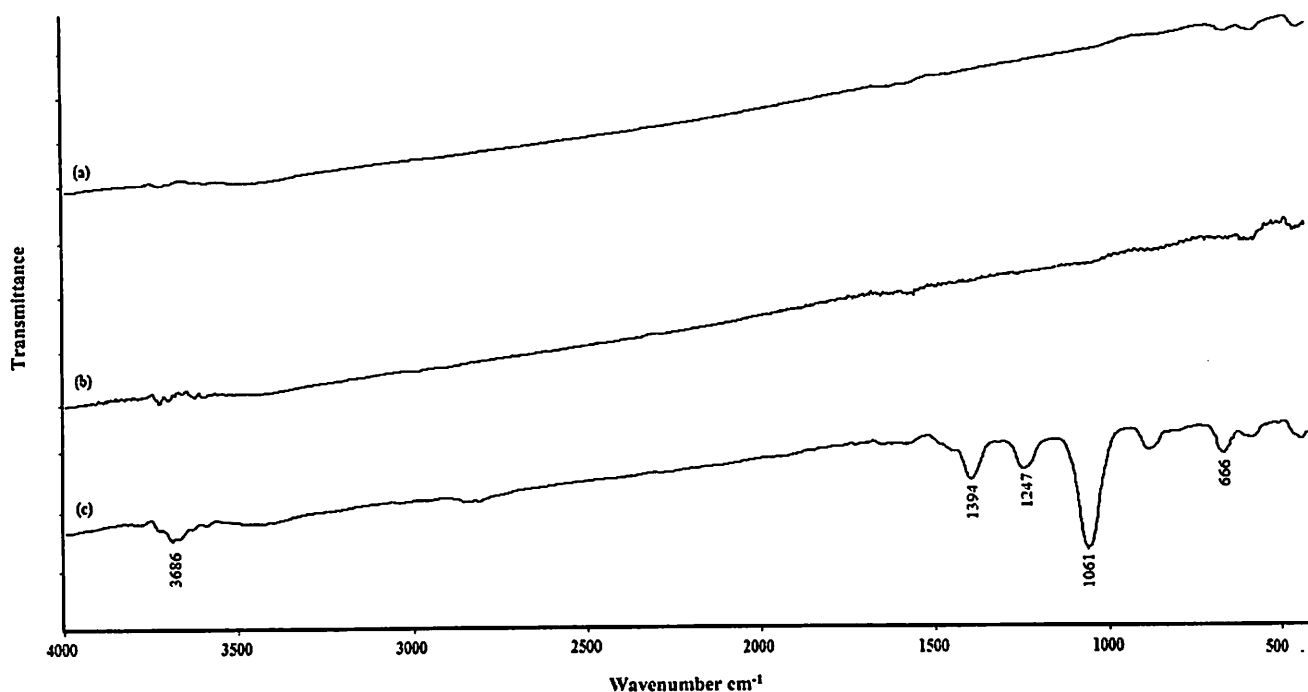


Fig. 5. FTIR spectra of (a) pristine MWCNTs, (b) MWCNTs-COOH and (c) s-MWCNTs sulphonated via the thermal decomposition of $(\text{NH}_4)_2\text{SO}_4$.

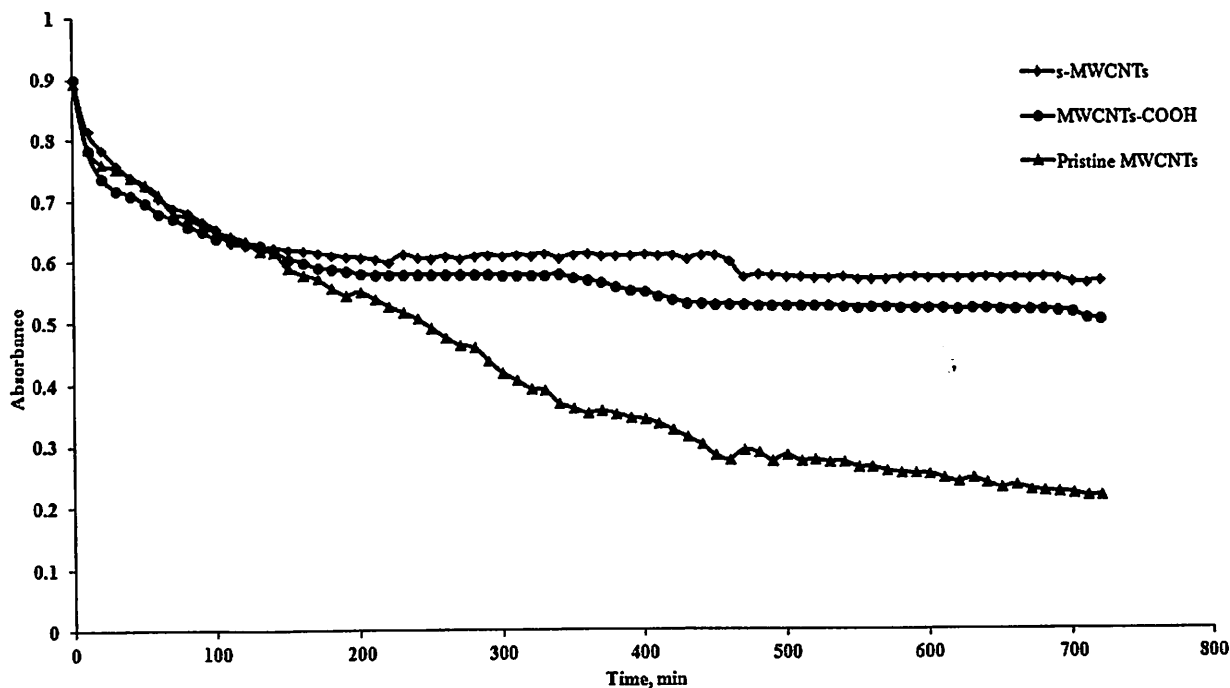


Fig. 6. Sedimentation curve of s-MWCNTs, MWCNTs-COOH and pristine MWCNTs in methanol at a concentration of 0.005 mg/mL.

the MWCNTs were believed to form hydrogen bonds with methanol and thus enabling the s-MWCNTs to remain dispersed in methanol. However, the interactions between the SO_3H and COOH groups of the s-MWCNTs and alcohol were considered a weak interaction [47], resulting in a slight decrease in absorbance after 460 min. The absorbance spectrum of MWCNTs-COOH in methanol mixture was similar to that of s-MWCNTs, indicating that surface modification (acid purification and sulphonation) could improve the dispersibility of the hydrophobic MWCNTs in hydrophilic solvent.

The above dispersibility results implied that s-MWCNTs were able to form a homogeneous solution with methanol during the esterification of PFAD. The dispersibility behaviour of s-MWCNTs is required for the application of s-MWCNTs as a heterogeneous catalyst. The major drawback in heterogeneous-catalysed transesterification/esterification is the presence of the three-phase-system (triglycerides/fatty acids, alcohol and solid catalyst) in the reaction mixture, which prohibits the diffusion of fatty acids and reduces the availability of active sites for the reaction, thus decreasing the reaction rate

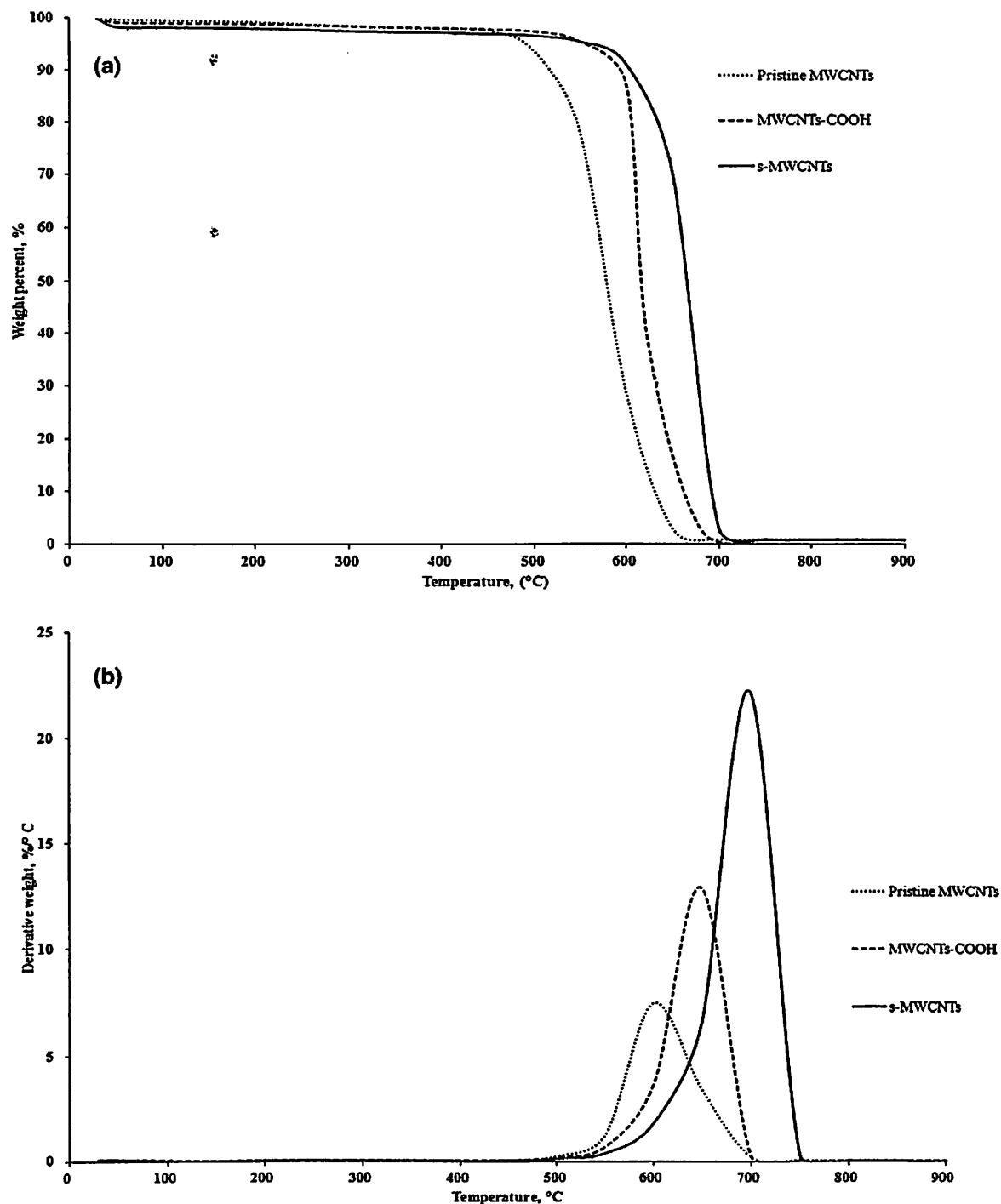


Fig. 7. TGA analysis of (a) weight (wt.%) (b) derivative weight (wt.%/°C) of pristine MWCNTs, MWCNTs-COOH and s-MWCNTs.

[53,54]. Thus, the dispersibility of the s-MWCNTs and the high miscibility of PFAD in methanol can minimise the mass transfer resistance due to the reduction of reaction phases.

3.4.3. Thermal degradation and stability of pristine MWCNTs, MWCNTs-COOH and s-MWCNTs

The weight loss and derivative weight loss curves for pristine MWCNTs, MWCNTs-COOH and s-MWCNTs are shown in Figs. 7(a) and (b). The results in Fig. 7(b) indicated that all of the samples were stable up to 500 °C, with a negligible weight loss. Thus, the s-MWCNTs should possess good thermal stability at the reaction temperature of

170 °C. Among the three MWCNT samples, the pristine MWCNTs underwent thermal decomposition at the lowest temperature, in which a sharp weight loss was observed at 500 °C, and then completely decomposed at 650 °C. In addition, the starting and complete decomposition temperatures of MWCNTs-COOH were extended to 550 °C and 680 °C, respectively. This observation indicated that the thermal stability of MWCNTs was increased after acid purification by HNO₃ because of the removal of metal catalysts and amorphous carbon. The thermal stability of MWCNTs was further increased by the sulphonation process, in which the s-MWCNTs started to decompose at 600 °C and completely decomposed at 700 °C. The s-MWCNTs decomposed

Table 2
BET surface area, average pore width and pore volume of pristine MWCNTs and s-MWCNTs.

Carbon-based acid catalysts	Pore diameter (nm)	BET surface area (m ² /g)	Pore volume (cm ³ /g)
Pristine MWCNTs	7.85	27.26	0.05
s-MWCNTs ^a	12.3	92.37	0.25

^a The s-MWCNTs were prepared by 10 wt.% of (NH₄)₂SO₄ solution, 10 min of ultrasonication treatment and heating at 235 °C for 30 min.

at a higher temperature because more energy was required to decompose the grafted SO₃H groups to release oxygen into the environment [55] prior to the decomposition of carbon.

3.4.4. BET surface area analysis

The BET surface area, average pore diameter and pore volume of the s-MWCNTs (synthesised from a 10 wt.% (NH₄)₂SO₄ solution coupled with 10 min of ultrasonication treatment) and the pristine MWCNTs are presented in Table 2. The results indicated that the BET surface area, average pore width and pore volume of the s-MWCNTs produced in this study increased significantly compared to those of pristine MWCNTs. The increase in the BET surface area of s-MWCNTs was due to the repulsion force induced by COOH and SO₃H groups on the surface of MWCNTs, which resulted in debundling of the MWCNTs. In addition, the s-MWCNTs possessed a larger average pore width than the pristine MWCNTs because the acid purification and ultrasonication treatment enhanced the defects on the surface of the MWCNTs. Moreover, the BET surface area and pore diameter of s-MWCNTs obtained in this study were larger than those of the majority of reported carbon-based catalysts used for biodiesel production [20,22–24,26].

The mass transfer limitation faced by heterogeneous-catalysed transesterification/esterification can be greatly reduced using a catalyst support with a high BET surface area. However, this limitation will still exist if the catalyst support contains only micropores, particularly if large molecules (fatty acids) are involved, because the active sites located in the micropores prohibit accessibility to reactants [15]. These results showed that although the BET surface area and acid density of s-MWCNTs (obtained in this study) were lower than those of other carbon-based catalysts, such as sulphonated biochar [28], sulphonated ordered mesoporous carbon [25], H₂SO₄ sulphonated peanut hull char and H₂SO₄ sulphonated MeadWestvaco activated carbon [29], the FAME yield produced by the s-MWCNTs was actually higher than those obtained using carbon-based catalysts. This was due to the larger pore width of s-MWCNTs, which enabled easy access of methanol and bulky fatty acids to the active sites for reaction. The spatial widths of stearic acid, oleic acid and linoleic acid are 0.25, 0.72 and 1.13 nm, respectively [56]. Thus, the pore width of 12.3 nm exhibited by the s-MWCNTs in this study was sufficiently large to enable fatty acid molecules to easily diffuse and reach the active sites.

Comparing to other sulphonation methods that used concentrated H₂SO₄ to graft the surface of carbon catalysts with SO₃H groups, the sulphonating agent, (NH₄)₂SO₄ solution, used in this study was more environmentally benign. Although the sulphonation temperature of MWCNTs via the thermal decomposition of (NH₄)₂SO₄ was high, it required only 30 min of sulphonation time compared to other sulphonated carbon-based catalysts prepared via thermal treatment with concentrated H₂SO₄, which required a minimum sulphonation period of 10 h [20,22–24,26,28,29]. In addition, sulphonation via the thermal decomposition of (NH₄)₂SO₄ did not require an inert environment, thus helping to reduce the number of operating steps and cost in preparing the catalyst for biodiesel production. Moreover, the sulphonation method used in this study required less sonication time compared to the sulphonation process via thermal treatment with concentrated H₂SO₄ [47]. Thus, these findings indicated that s-MWCNTs not only can be synthesised using a simpler and faster

method but also possess a high BET surface area and a well-developed pore size.

3.4.5. Comparison of reaction parameters between s-MWCNTs and other carbon-based catalysts used in biodiesel production

The oil source used for the production of FAME using sulphonated carbon-based catalysts has only been limited to a pure and single component, such as oleic acid and triacetin [20,22–25,27]. Thus far, there have only been two studies reported on the application of sulphonated carbon-based catalysts in the production of biodiesel using cottonseed and soybean oil as feedstock [26,29]. Thus, unlike previous studies, the current study showed the ability of s-MWCNTs to produce a high FAME yield using the low-value industrial by-product (PFAD) as an oil source.

The esterification/transesterification was performed at low temperature (60–80 °C) when pure components (oleic acid and triacetin) were used as a feedstock and methanol was used as an alcohol source [22–25]. However, when PFAD and cottonseed oil were used, a higher reaction temperature was required (between 170 and 260 °C) [26], which might be due to the higher viscosity of triglycerides and mixture of fatty acids in PFAD. The methanol-to-oil ratio required for s-MWCNTs was almost similar to that in studies using cottonseed or soybean as an oil source. Interestingly, the s-MWCNTs obtain in this study required a lower catalyst concentration than most of the reported carbon-based catalysts to achieve a similar FAME yield [20,22,25,29]. In addition, a high FAME yield can be achieved within 3 h using the s-MWCNTs as catalysts compared to some reported sulphonated carbon-based catalysts, which required 5–10 h [22,23,25,29] to obtain a similar FAME yield. The reduction in catalyst concentration and reaction time can further reduce the overall production costs of biodiesel.

4. Conclusions

In conclusion, this study demonstrated the feasibility of producing s-MWCNTs via the thermal decomposition of (NH₄)₂SO₄ with the aid of ultrasonication. The optimum conditions to synthesise s-MWCNTs with strong and stable SO₃H groups were a 10 wt.% (NH₄)₂SO₄ solution coupled with 10 min of ultrasonication treatment and heating at 235 °C for 30 min. The s-MWCNTs were able to achieve a biodiesel yield of 84.9% PFAD as the feedstock. This sulphonation method is more commercially viable compared to the thermal treatment with concentrated H₂SO₄ due to the simple sulphonation steps, short sulphonation time and elimination of the use of any hazardous and corrosive acids. These results demonstrated that the s-MWCNTs prepared in this study possessed good thermal stability, which enabled the catalyst to be stable at high reaction temperatures. Furthermore, the good dispersibility of s-MWCNTs in methanol can minimise the mass transfer limitation. In addition, the s-MWCNTs obtained in this study exhibited a high BET surface area coupled with a large pore width, which could further reduce the mass transfer limitation and thus increase the rates of diffusion and reaction. Taken together, the application of s-MWCNTs prepared via the thermal decomposition of a (NH₄)₂SO₄ solution to produce biodiesel from a low-value industrial by-product may be a potential breakthrough technology for biodiesel production.

Acknowledgements

Siew Hoong Shuit acknowledges the support of the Ministry of Higher Education of Malaysia through the MyPhD Fellowship. This study was also financially supported by the Universiti Sains Malaysia Research University (RU) grant (A/C: 814142), USM Membrane Cluster Grant, Fundamental of Research Grant Scheme (FRGS) (A/C: 6071212) and Postgraduate Research Grant Scheme (PRGS) (A/C: 8044028).

References

- Shuit SH, Ong YT, Lee KT, Subhash B, Tan SH. Membrane technology as a promising alternative in biodiesel production: a review. *Biotechnol Adv* 2012;30:1364–80.
- Ju Y-H, Zullaikah S. Effect of acid-catalyzed methanolysis on the bioactive components of rice bran oil. *J Taiwan Inst Chem Eng* 2013;44:924–8.
- Shah M, Ali S, Tariq M, Khalid N, Ahmad F, Khan MA. Catalytic conversion of jojoba oil into biodiesel by organotin catalysts, spectroscopic and chromatographic characterization. *Fuel* 2014;118:392–7.
- Wang L, Dong X, Jiang H, Li G, Zhang M. Ordered mesoporous carbon supported ferric sulfate: a novel catalyst for the esterification of free fatty acids in waste cooking oil. *Fuel Process Technol* 2014;128:10–16.
- Chen L-Y, Chen Y-H, Hung Y-S, Chiang T-H, Tsai C-H. Fuel properties and combustion characteristics of jatropha oil biodiesel–diesel blends. *J Taiwan Inst Chem Eng* 2013;44:214–20.
- Zarei A, Amin NAS, Talebian-Kiakalaieh A, Zain NAM. Immobilized lipase-catalyzed transesterification of jatropha curcas oil: optimization and modeling. *J Taiwan Inst Chem Eng* 2014;45:444–51.
- Cho HJ, Kim J-K, Hong SW, Yeo Y-K. Development of a novel process for biodiesel production from palm fatty acid distillate (PFAD). *Fuel Process Technol* 2012;104:271–80.
- Daghri R, Igonnet L, Brar S-K, Drogui P. Novel electrochemical method for the recovery of lipids from microalgae for biodiesel production. *J Taiwan Inst Chem Eng* 2014;45:153–62.
- Corro G, Bañuelos F, Vidal E, Cebada S. Measurements of surface acidity of solid catalysts for free fatty acids esterification in jatropha curcas crude oil for biodiesel production. *Fuel* 2014;115(0):625–8.
- Wu Q, Wan H, Li H, Song H, Chu T. Bifunctional temperature-sensitive amphiphilic acidic ionic liquids for preparation of biodiesel. *Catal Today* 2013;200(0):74–9.
- Paterson G, Issariyakul T, Baroi C, Bassi A, Dalai A. Ion-exchange resins as catalysts in transesterification of triolein. *Catal Today* 2013;212(0):157–63.
- Mahdavi V, Monajemi A. Optimization of operational conditions for biodiesel production from cottonseed oil on CaO–MgO/Al₂O₃ solid base catalysts. *J Taiwan Inst Chem Eng* 2014;45(5):2286–92.
- Boffito DC, Pirola C, Galli F, Di Michele A, Bianchi CL. Free fatty acids esterification of waste cooking oil and its mixtures with rapeseed oil and diesel. *Fuel* 2013;108(0):612–19.
- Chouhan APS, Sarma AK. Modern heterogeneous catalysts for biodiesel production: a comprehensive review. *Renewable Sustainable Energy Rev* 2011;15(9):4378–99.
- Shuit SH, Yee KF, Lee KT, Subhash B, Tan SH. Evolution towards the utilisation of functionalised carbon nanotubes as a new generation catalyst support in biodiesel production: an overview. *RSC Adv* 2013;3(24):9070–94.
- Pérez-Pariente J, Díaz I, Mohino F, Sastre E. Selective synthesis of fatty monoglycerides by using functionalised mesoporous catalysts. *Appl Catal, A* 2003;254(2):173–88.
- Ngaosuwan K, Lotero E, Suwannakarn K, Goodwin JG, Praserttham P. Hydrolysis of triglycerides using solid acid catalysts. *Ind Eng Chem Res* 2009;48(10):4757–67.
- Shu Q, Gao J, Nawaz Z, Liao Y, Wang D, Wang J. Synthesis of biodiesel from waste vegetable oil with large amounts of free fatty acids using a carbon-based solid acid catalyst. *Appl Energy* 2010;87(8):2589–96.
- Sharma YC, Singh B, Korstad J. Advancements in solid acid catalysts for ecofriendly and economically viable synthesis of biodiesel. *Biofuels, Bioprod Biorefin* 2011;5(1):69–92.
- Takagaki A, Toda M, Okamura M, Kondo JN, Hayashi S, Domen K, et al. Esterification of higher fatty acids by a novel strong solid acid. *Catal Today* 2006;116(2):157–61.
- Mo X, Lotero E, Lu C, Liu Y, Goodwin J. A novel sulfonated carbon composite solid acid catalyst for biodiesel synthesis. *Catal Lett* 2008;123(1):1–6.
- Zong M-H, Duan Z-Q, Lou W-Y, Smith TJ, Wu H. Preparation of a sugar catalyst and its use for highly efficient production of biodiesel. *Green Chem* 2007;9(5):434–7.
- Mar WW, Somsook E. Sulfonic-functionalized carbon catalyst for esterification of high free fatty acid. *Procedia Eng* 2012;32(0):212–18.
- Mo X, López DE, Suwannakarn K, Liu Y, Lotero E, Goodwin Jr JG, et al. Activation and deactivation characteristics of sulfonated carbon catalysts. *J Catal* 2008;254(2):332–8.
- Liu R, Wang X, Zhao X, Feng P. Sulfonated ordered mesoporous carbon for catalytic preparation of biodiesel. *Carbon* 2008;46(13):1664–9.
- Shu Q, Zhang Q, Xu G, Nawaz Z, Wang D, Wang J. Synthesis of biodiesel from cottonseed oil and methanol using a carbon-based solid acid catalyst. *Fuel Process Technol* 2009;90(7–8):1002–8.
- Shu Q, Zhang Q, Xu G, Wang J. Preparation of biodiesel using s-MWCNT catalysts and the coupling of reaction and separation. *Food Bioprod Process* 2009;87(3):164–70.
- Dehkhoda AM, Ellis N. Biochar-based catalyst for simultaneous reactions of esterification and transesterification. *Catal Today* 2013;207(0):86–92.
- Kastner JR, Miller J, Geller DP, Locklin J, Keith LH, Johnson T. Catalytic esterification of fatty acids using solid acid catalysts generated from biochar and activated carbon. *Catal Today* 2012;190(1):122–32.
- Farahzadi M, Towfighi J, Mohamadizadeh A. Catalytic oxidation of isopropyl mercaptan over nano catalyst of tungsten oxide supported multiwall carbon nanotubes. *Fuel Process Technol* 2012;97(0):15–23.
- Shuit SH, Tan SH. Feasibility study of various sulphonation methods for transforming carbon nanotubes into catalysts for the esterification of palm fatty acid distillate. *Energy Convers Manage* 2014;88(0):1283–9.
- Shuit S, Tan S. Biodiesel production via esterification of palm fatty acid distillate using sulphonated multi-walled carbon nanotubes as a solid acid catalyst: process study, catalyst reusability and kinetic study. *BioEnergy Res* 2014. doi:10.1007/s12155-014-9545-2.
- Du CY, Zhao TS, Liang ZX. Sulfonation of carbon-nanotube supported platinum catalysts for polymer electrolyte fuel cells. *J Power Sources* 2008;176(1):9–15.
- Xu Z, Qi Z, Kaufman A. Superior catalysts for proton exchange membrane fuel cells. *Electrochem Solid-State Lett* 2005;8(6):A313–A15.
- Villa A, Tessonnier J-P, Majoulet O, Su DS, Schlögl R. Transesterification of triglycerides using nitrogen-functionalized carbon nanotubes. *ChemSusChem* 2010;3(2):241–5.
- Shuit SH, Lee KT, Kamaruddin AH, Yusup S. Reactive extraction and in situ esterification of jatropha curcas L. seeds for the production of biodiesel. *Fuel* 2010;89(2):527–30.
- Shuit SH, Lee KT, Kamaruddin AH, Yusup S. Reactive extraction of jatropha curcas L. seed for production of biodiesel: process optimization study. *Environ Sci Technol* 2010;44(11):4361–7.
- Ng EP, Hadi N, Mohd Nazlan MM, Halimatun H. Sulphated AIMCM-41: mesoporous solid Brønsted acid catalyst for dibenzoylation of biphenyl. *Catal Today* 2006;114(2–3):257–62.
- Ng E-P, Mohd Subari SN, Marie O, Mukti RR, Juan J-C. Sulfonic acid functionalized MCM-41 as solid acid catalyst for tert-butylolation of hydroquinone enhanced by microwave heating. *Appl Catal, A* 2013;450(0):34–41.
- Upare PP, Yoon J-W, Kim MY, Kang H-Y, Hwang DW, Hwang YK, et al. Chemical conversion of biomass-derived hexose sugars to levulinic acid over sulfonic acid-functionalized graphene oxide catalysts. *Green Chem* 2013;15(10):2935–43.
- Venezia AM, Di Carlo G, Liotta LF, Pantalco G, Kantcheva M. Effect of Ti(IV) loading on CH₄ oxidation activity and SO₂ tolerance of Pd catalysts supported on silica SBA-15 and HMS. *Appl Catal, B* 2011;106(3–4):529–39.
- Kis A, Csanyi G, Salvatir JP, Lee T-N, Couteau E, Kulik AJ, et al. Reinforcement of single-walled carbon nanotube bundles by intertube bridging. *Nat Mater* 2004;3(3):153–7.
- Donaldson K, Aitken R, Tran L, Stone V, Duffin R, Forrest G, et al. Carbon nanotubes: a review of their properties in relation to pulmonary toxicology and workplace safety. *Toxicol Sci* 2006;92(1):5–22.
- Wang J, Sui L, Wan Q, Luo F, Tian L, Pan L, et al. Effects of ultrasonic radiation intensity on the oxidation of singlewalled carbon nanotubes in a mixture of sulfuric and nitric acids. *Nano* 2013;08(04):1350040.
- Dresselhaus MS, Dresselhaus G, Saito R, Jorio A. Raman spectroscopy of carbon nanotubes. *Phys Rep* 2005;409(2):47–99.
- Balasubramanian K, Burghard M. Chemically functionalized carbon nanotubes. *Small* 2005;1(2):180–92.
- Zhou W, Xiao J, Chen Y, Zeng R, Xiao S, Nie H, et al. Sulfonated carbon nanotubes/sulfonated poly(ether sulfone ether ketone ketone) composites for polymer electrolyte membranes. *Polym Adv Technol* 2010;22(12):1747–52.
- Peng F, Zhang L, Wang H, Lv P, Yu H. Sulfonated carbon nanotubes as a strong protonic acid catalyst. *Carbon* 2005;43(11):2405–8.
- Tripathi BP, Schieda M, Shahi VK, Nunes SP. Nanostructured membranes and electrodes with sulfonic acid functionalized carbon nanotubes. *J Power Sources* 2011;196(3):911–19.
- Lin Y-W, Wu T-M. Synthesis and characterization of externally doped sulfonated polyaniline/multi-walled carbon nanotube composites. *Compos Sci Technol* 2009;69(15–16):2559–65.
- Sun Z-P, Zhang X-G, Liu R-L, Liang Y-Y, Li H-L. A simple approach towards sulfonated multi-walled carbon nanotubes supported by Pd catalysts for methanol electro-oxidation. *J Power Sources* 2008;185(2):801–6.
- Yu H, Jin Y, Li Z, Peng F, Wang H. Synthesis and characterization of sulfonated single-walled carbon nanotubes and their performance as solid acid catalyst. *J Solid State Chem* 2008;181(3):432–8.
- Mbaraka I, Shanks B. Conversion of oils and fats using advanced mesoporous heterogeneous catalysts. *J Am Oil Chem Soc* 2006;83(2):79–91.
- Shuit SH, Tan KT, Lee KT, Kamaruddin AH. Oil palm biomass as a sustainable energy source: a Malaysian case study. *Energy* 2009;34(9):1225–35.
- Adams L, Oki A, Grady T, McWhinney H, Luo Z. Preparation and characterization of sulfonic acid-functionalized single-walled carbon nanotubes. *Physica E* 2009;41(4):723–8.
- Cook HW, McMaster CR. Chapter 7 fatty acid desaturation and chain elongation in eukaryotes. In: Vance JE, Vance DE, editors. *Biochemistry of lipids, lipoproteins and Membranes*, 4th edition Elsevier; 2002. p. 181–204.

Biodiesel Production via Esterification of Palm Fatty Acid Distillate Using Sulphonated Multi-walled Carbon Nanotubes as a Solid Acid Catalyst: Process Study, Catalyst Reusability and Kinetic Study

Siew Hoong Shuit · Soon Huat Tan

Published online: 21 October 2014
© Springer Science+Business Media New York 2014

Abstract This study reports on biodiesel production via the esterification of palm fatty acid distillate (PFAD) using sulphonated multi-walled carbon nanotubes (s-MWCNTs) as a catalyst. The process parameters studied included the methanol-to-PFAD ratio (8–30), catalyst loading (1–3 wt%), reaction temperature (80–200 °C) and reaction time (1–5 h). A fatty acid methyl ester (FAME) yield of 93.5 % was obtained at a methanol-to-PFAD ratio of 20, catalyst loading of 3 wt%, reaction temperature of 170 °C and reaction time of 2 h. The s-MWCNTs exhibited good catalytic activity, with a FAME yield higher than 75 % even after five repeated runs. Moreover, the regeneration of the spent s-MWCNTs (after five runs) with sulphuric acid was able to restore the catalytic activity to its original level. The catalyst stability and activity were enhanced by acid regeneration to achieve a FAME yield of 86.2 %, even at the fifth cycle of reaction after acid regeneration. A pseudo-homogeneous kinetic model for the esterification of PFAD with methanol using s-MWCNTs as a catalyst was then developed based on the experimental results. The pre-exponential factor, molar heat and activation energy for the esterification were found to be $1.9 \times 10^2 \text{ L mol}^{-1} \text{ min}^{-1}$, 84.1 kJ mol^{-1} and 45.8 kJ mol^{-1} , respectively.

Keywords Heterogeneous esterification · Palm fatty acid distillate (PFAD) · Sulphonated multi-walled carbon nanotubes · Kinetic model · Acid regeneration

Introduction

The major challenges in biodiesel production have always been related to the selection of raw materials and conversion technologies. Currently, the most common approach to produce biodiesel is via sodium hydroxide- or sodium methoxide-based transesterification using refined vegetable oil as the feedstock. However, approximately 70 % of the total biodiesel production cost comes from refined oil [1, 2]. Therefore, non-edible feedstocks, such as municipal sewage sludge [1], *Jatropha* [3, 4], castor [4], sea mango [5], waste cooking oil [2, 6, 7] and palm fatty acid distillate (PFAD) [8], appear to be a promising alternative feedstock for biodiesel production. Among the non-edible feedstocks, PFAD has the most potential because it is a low-value by-product generated during the fatty acid stripping and deodorisation stages in the refining of palm oil. Currently, Indonesia and Malaysia are the world's largest producers of palm oil, with crude palm oil productions in 2009 of 20.9 and 17.5 million metric tons, respectively. Most of the crude palm oil in Malaysia is refined locally for food applications, generating nearly 700,000 metric tons (MT) of PFAD annually. The selling price for PFAD in early 2010 was approximately 700 USD/MT, which was 14.3 % lower than the price of crude palm oil [9].

Heterogeneous catalysis is preferred over other conversion technologies such as homogeneous catalysis and supercritical technology because of several advantages, such as the catalysts being recyclable, minimal wastewater generation and lower energy consumption compared to supercritical technology [10–12]. Recently, research on the catalysts used in biodiesel production has been focused on carbon-based acid catalysts, such as sugar catalysts (incompletely carbonized D-glucose or incompletely carbonized biomass-based vermicelli) [13–16], sulphonated ordered mesoporous carbon [17], vegetable oil asphalt-based carbon [18], sulphonated multi-

S. H. Shuit · S. H. Tan (✉)
School of Chemical Engineering, Universiti Sains Malaysia,
Engineering Campus, Seri Ampangan, 14300 Nibong Tebal, Pulau
Pinang, Malaysia
e-mail: chshstan@usm.my

walled carbon nanotubes (s-MWCNTs) [19], sulphonated biochar and sulphonated activated carbon [20], because the hydrophobic carbon sheet can prevent the hydration of hydroxyl groups [21]. In addition, s-MWCNTs have been demonstrated to possess good thermal stability and a high BET surface area, coupled with a large pore width and good dispersibility in methanol.

The high solubility of PFAD in methanol [22] and the good dispersibility of s-MWCNTs in methanol [23] make a perfect combination of feedstock and catalyst for biodiesel production because of the phase reduction in the reaction system, which could reduce the mass transfer resistance encountered by the common heterogeneous catalysts. However, the esterification of PFAD with methanol using s-MWCNTs as a catalyst has been minimally studied because, before this study, s-MWCNTs had only been applied in pure or single components, such as glyceryl tributyrate and oleic acid [10]. Therefore, in this work, the process parameters, such as reaction temperature, methanol-to-PFAD ratio, catalyst loading and reaction period, for the esterification of PFAD using s-MWCNTs were studied. This was followed by the determination of the kinetic parameters, such as the reaction rate constants, pre-exponential factor, molar heat and activation energy, for the esterification of PFAD using a derived kinetic model. Moreover, the reusability and regeneration of the s-MWCNTs were also investigated.

Experimental

Materials and Methods

MWCNTs with diameters and lengths ranging from 40 to 60 nm and 1 to 2 μm , respectively, were purchased from Shenzhen Nanotechnologies Port Co. PFAD was obtained from a local edible oil manufacturing company. The PFAD contains 98.5 wt% of major free fatty acid (FFA) for the synthesis of fatty acid methyl ester (FAME): 48.0 wt% palmitic acid, 36.3 wt% oleic acid, 8.7 wt% linoleic acid, 4.3 wt% stearic acid, 1.2 wt% myristic acid and 1.5 wt% others (arachidic acid, α -linolenic acid, palmitoleic acid, eicosenoic acid, lauric acid, margaric acid, heptadecenoic acid, heneicosanoic acid and tricosylic acid). Sulphuric acid (H_2SO_4), ammonium sulphate ($(\text{NH}_4)_2\text{SO}_4$), methanol and *n*-hexane were purchased from Fisher Scientific. Methyl heptadecanoate was purchased from Sigma Aldrich. Nitric acid (HNO_3) with a purity of 69–70 % was purchased from JT Baker.

Catalyst Preparation

The purification and sulphonation of MWCNTs was performed as described in the literature [24]. Briefly, the pristine

MWCNTs were purified using HNO_3 coupled with 1 h of ultrasonication treatment prior to refluxing at 80 °C for 8 h. After washing, the purified MWCNTs were dried in an oven at 120 °C for 12 h. s-MWCNTs were prepared by mixing with 10 wt% $(\text{NH}_4)_2\text{SO}_4$, and then the mixture was sonicated for 10 min using a tip sonicator. Subsequently, the mixture was heated to 235 °C for 30 min.

Esterification

The esterification to convert PFAD to biodiesel was performed in a pressurised batch reactor equipped with a thermocouple and a magnetic stirrer. The reactor was made of stainless steel. Owing to the acidic nature of PFAD, the esterification reaction was carried out in a Teflon cup placed inside the stainless steel reactor. Prior to the addition of 10 g of PFAD, a pre-determined amount of s-MWCNTs was stirred in methanol for 10 min to avoid the adsorption of PFAD to the active sites that would cause deactivation of the catalysts [25]. In this study, the molar ratios of methanol to PFAD were 8, 10, 15, 20 and 30. The reaction temperatures were set at 80, 100, 150, 170 and 200 °C. Furthermore, the catalyst loadings used in this study were 1.0, 1.5, 2.0, 2.5 and 3.0 wt% (based on the weight of PFAD). The reactor was then pressurised to 10 bars to prevent the evaporation of methanol. The reactants were stirred at 230 rpm to maintain a uniform temperature and suspension. The reaction mixture was then heated to the desired temperature for the necessary duration (1–5 h). Upon completion, the reaction mixture was cooled to room temperature and filtered. The filtered s-MWCNTs were rinsed repeatedly with methanol. The excess methanol in the reaction mixture was recovered using a rotary evaporator. After methanol evaporation, two layers of liquids were formed. The upper layer was yellow in colour containing crude biodiesel while the bottom layer was water. The volume of the biodiesel layer was measured and recorded.

Catalyst Reusability and Regeneration

The reusability of the s-MWCNTs was evaluated through five consecutive runs performed under the determined reaction conditions. The filtered s-MWCNTs were sonicated in methanol for 20 min. Then, the s-MWCNTs were filtered and washed repeatedly with methanol. The washed s-MWCNTs were then dried at 120 °C for 12 h.

The regeneration of the s-MWCNTs was performed by mixing the catalyst with concentrated H_2SO_4 followed by refluxing at 100 °C for 5 h. The regenerated s-MWCNTs were then cooled, filtered and washed with distilled water until the pH of the filtrate was similar to the pH of distilled water. Subsequently, the regenerated s-MWCNTs were dried at 120 °C for 12 h. The regenerated s-MWCNTs were then subjected to another five runs of esterification.

Analytical Methods

The composition and the yield of FAME or biodiesel were analysed using a PerkinElmer Clarus 500 gas chromatograph equipped with a flame ionisation detector (FID) and a Nukol™ capillary column. *n*-Hexane and helium were used as the solvent

and carrier gas, respectively. The oven temperature was set to 110 °C and then increased to 220 °C at a rate of 10 °C/min. The temperatures of the detector and injector were set at 220 and 250 °C, respectively. Methyl heptadecanoate was used as an internal standard. The yield of FAME in the samples was calculated using the following equation:

$$\text{Yield(\%)} = \frac{\left(\sum \text{Concentration of each methylesters, } \frac{\text{g}}{\text{cm}^3}\right) \times (\text{Volume of oil layer, cm}^3)}{10 \text{ g of PFAD}} \times 100\%$$

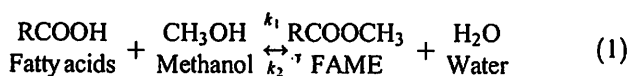
The Fourier transform infrared spectroscopy (FT-IR) spectra of the s-MWCNTs after each reaction run were recorded using a Shimadzu IRPrestige-21 spectrometer over the frequency range of 4000–400 cm⁻¹. s-MWCNTs were mixed with potassium bromide and then pelletised into a thin pellet. The IR spectra were collected after 32 scans. The as-synthesised s-MWCNTs and the regenerated s-MWCNTs were also characterised using a transmission electron microscope (TEM; Philips, model CM12). In addition, the density and strength of the acid sites of s-MWCNTs were determined by ammonia temperature-programmed desorption (NH₃-TPD) and pulse chemisorption, respectively, with 15 % NH₃ in helium using a Micromeritics: Auto Chem II 2920 instrument.

Kinetic Model

In general, the kinetic model for heterogeneously catalysed esterification can be well represented by a pseudo-homogeneous model. Therefore, in this study, a pseudo-homogeneous model was developed to illustrate the kinetics of the esterification of PFAD with methanol using s-MWCNTs as catalyst based on the following assumptions [26–29]:

- (1) The rate of the esterification reaction under the operating conditions is kinetically controlled.
- (2) The entire reaction system is considered to be an ideal solution in which internal and external mass transfer resistance does not exist.
- (3) The rate of non-catalysed and self-catalysed esterification is negligible relative to the reaction rate catalysed by the s-MWCNTs.

The esterification of PFAD with methanol to produce FAME as the main product and water as a by-product in the presence of s-MWCNTs is illustrated as:



Using an elementary second-order reversible reaction, the rate of esterification above can be expressed as:

$$\frac{d[\text{RCOOH}]}{dt} = k_1[\text{RCOOH}][\text{CH}_3\text{OH}] - k_2[\text{RCOOCH}_3][\text{H}_2\text{O}] \quad (2)$$

where [RCOOH] is the molar concentration of PFAD, [CH₃OH] is the molar concentration of methanol, [RCOOCH₃] is the molar concentration of FAME, [H₂O] is the molar concentration of water, and *k*₁ and *k*₂ are the forward and backward reaction rate constants, respectively.

The concentrations of the reactants and products that correspond to the PFAD conversion are expressed as follows:

$$[\text{RCOOH}] = [\text{RCOOH}]_0 - x[\text{RCOOH}]_0 = [\text{RCOOH}]_0(1-x) \quad (3)$$

$$[\text{CH}_3\text{OH}] = [\text{CH}_3\text{OH}]_0 - x[\text{RCOOH}]_0 \quad (4)$$

$$[\text{RCOOCH}_3] = x[\text{RCOOH}]_0 \quad (5)$$

$$[\text{H}_2\text{O}] = x[\text{RCOOH}]_0 \quad (6)$$

where [RCOOH]₀ is the initial concentration of PFAD and *x* is the conversion of PFAD.

Substituting Eqs. 3, 4, 5 and 6 into Eq. 2 and let [CH₃OH]₀ = *θ* and *k_e* = *k*₁/*k*₂

$$\Rightarrow \frac{dx}{dt} = k_1[\text{RCOOH}]_0 \left[\left(1 - \frac{1}{k_e}\right)x^2 - (1-\theta)x + \theta \right] \quad (7)$$

where *θ* is the molar ratio of methanol to PFAD and *k_e* is the equilibrium rate constant.

At the equilibrium state, $\frac{dx}{dt} = 0$ and *x* = *x_e* (*x_e* is the PFAD conversion at equilibrium), Eq. 7 can be rearranged into Eq. 8. Thus, *k_e* can be determined experimentally on the basis of the conversion of PFAD at equilibrium.

$$\Rightarrow k_e = \frac{x_e^2}{(\theta - x_e)(1 - x_e)} \quad (8)$$

Once k_c is determined, Eq. 7 is integrated to obtain a linear equation to determine k_1 numerically.

$$\int_0^x \frac{1}{\left(1 - \frac{1}{k_c}\right)x^2 - (1 + \theta)x + \theta} dx = \int_0^t k_1 [\text{RCOOH}]_0 dt \quad (9)$$

From the integral formula table, Eq. 9 can be transformed into:

$$\Rightarrow \ln \left[\frac{(-1 - \theta + \beta)x + 2\theta}{(-1 - \theta - \beta)x + 2\theta} \right] = \beta k_1 [\text{RCOOH}]_0 t \quad (10)$$

$$\text{where } \left(1 - \frac{1}{k_c}\right) = \alpha \text{ and } \sqrt{(1 + \theta)^2 - 4\alpha\theta} = \beta,$$

Rearrangement of Eq. 10 can provide an explicit expression for x (Eq. 11) to determine the variation in the conversion of PFAD with time.

$$x = \frac{2\theta [e^{\beta k_1 [\text{RCOOH}]_0 t} - 1]}{(-1 - \theta + \beta) + (1 + \theta + \beta)e^{\beta k_1 [\text{RCOOH}]_0 t}} \quad (11)$$

The influence of temperature on the reaction rate was examined using the Arrhenius equation,

$$k_1 = A_1 e^{-E_1/RT} \quad (12)$$

$$k_c = A_c e^{-E_c/RT} \quad (13)$$

where A_1 and A_c are the pre-exponential or frequency factors for the forward reaction rate constant and the equilibrium constant, respectively. Furthermore, E_1 and E_c represent the activation energy of the forward and equilibrium reactions, respectively. R is the gas constant, and T is the reaction temperature in units of Kelvin.

Results and Discussion

Effect of the Methanol-to-PFAD Ratio

Figure 1 shows the effect of different methanol-to-PFAD ratios on the FAME yield at a reaction temperature of 170 °C and a catalyst loading of 2 wt%. The FAME yield increased gradually as the methanol-to-PFAD ratio increased from 8 to 20. However, the highest methanol-to-PFAD ratio of 30 caused an adverse effect on the FAME yield, in which the FAME yield not only decreased significantly but also underperformed compared to the lowest methanol-to-PFAD ratio of 8. According to Le Chatelier's principle, an excess amount of methanol is required to drive the reversible reaction forward toward the formation of FAME [30]. In addition, it is believed that the reaction mechanism of esterification using sulphonated catalysts begins with the attachment of fatty acids

to the active sites of the catalysts through chemisorption. This step is followed by the protonation of the chemisorbed molecules at the carbonyl group to form carbocations. FAME is produced when the carbocations are attacked by methanol molecules. Therefore, in the condition of excess methanol, the collisions between the carbocations and methanol molecules are increased, thus enhancing the conversion. However, if the methanol-to-PFAD ratio is too extreme, fatty acids are prohibited from forming carbocations because the catalyst active sites are flooded with methanol instead of fatty acids [19, 18, 10], thereby causing deactivation of the catalyst. Moreover, the FAME yield decreases in an environment of excess methanol due to the slower reaction caused by dilution of the reaction system [31]. Therefore, the most suitable methanol-to-PFAD ratio in this study was 20 because high FAME yield was obtained in this ratio.

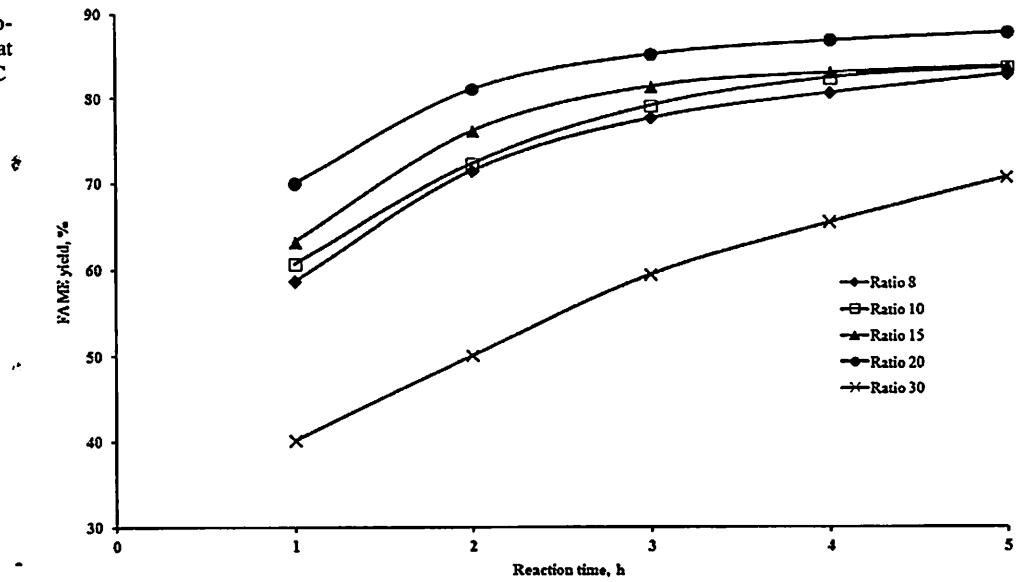
Effect of Catalyst Loading

The effect of s-MWCNTs loading on the FAME yield is illustrated in Fig. 2. The reaction was carried out at a reaction temperature of 170 °C and a methanol-to-oil ratio of 20. The FAME yield was found to be positively affected by the catalyst loading, in which the yield increased when the amount of catalysts used for the reaction increased. This relationship was related to the increase in the total number of active sites available for esterification with an increase in the catalyst concentration [2, 10]. If the catalyst loading was below 2 wt%, the equilibrium of the reaction was achieved after 3 h of reaction time. However, as the catalyst loading increased to 3 wt%, only 2 h of reaction time was required to bring the reaction to the equilibrium state. Furthermore, an increase of only 0.5 wt% (2.5 to 3 wt%) in the catalyst loading caused a substantial increase in the FAME yield, increasing from 83.0 to 93.5 % in only 2 h of reaction time. Therefore, this result further strengthens the fact that the rate of esterification reaction was enhanced by the use of the catalyst. Note that the FAME yield produced using 3 wt% s-MWCNTs in 2 h of reaction time was very close to the ester content (96.5 %) stated in the European Standard (EN 14214) for biodiesel. Therefore, the selected catalyst loading for the subsequent study was 3 wt%.

Effect of Reaction Temperature

Figure 3 illustrates the effect of the reaction temperature on the FAME yield at a catalyst loading of 3 wt% and a methanol-to-oil ratio of 20. At low reaction temperatures (80 and 100 °C), the maximum FAME yield was merely 25.0 %, even at 5 h of reaction time. However, when the reaction temperature increased from 100 to 150 °C, a threefold increase in the FAME yield was observed. Subsequently, an average increment of 8 % was observed when the reaction temperature was

Fig. 1 Effect of the methanol-to-PFAD ratio on the FAME yield at a reaction temperature of 170 °C and a catalyst loading of 2 wt%



further increased to 170 °C. With the further increase of the reaction temperature to 200 °C, the FAME yield was barely changed (less than 4 % on average). Similar to transesterification, esterification is also an endothermic process, in which the enthalpy of the process is positive. Therefore, by increasing the temperature, the equilibrium of the reaction was shifted to the forward direction, which favoured the conversion of PFAD into FAME. In addition, as the reaction temperature increased, the methanol and PFAD molecules gained more kinetic energy, causing the collision frequency between the reactant molecules to increase, thereby eventually enhancing the mass transfer rate of the reaction system. Reaction temperature of 170 °C was selected in the subsequent study because no significant increase in FAME

yield was observed when the reaction temperature was increased to 200 °C.

Effect of Reaction Time

As shown in Figs. 1, 2 and 3, the FAME yield was found to increase with longer reaction times until equilibrium was achieved. Note that the reaction time always reflects the rate of a reaction. However, it is believed that the time required for a reaction to achieve complete conversion or equilibrium state was correlated to other reaction parameters, such as alcohol ratio, catalyst loading and reaction temperature. In this study, the reaction time was influenced by the catalyst loading and reaction temperature. The reaction time to reach the

Fig. 2 Effect of the catalyst loading on the FAME yield at a reaction temperature of 170 °C and a methanol-to-oil ratio of 20

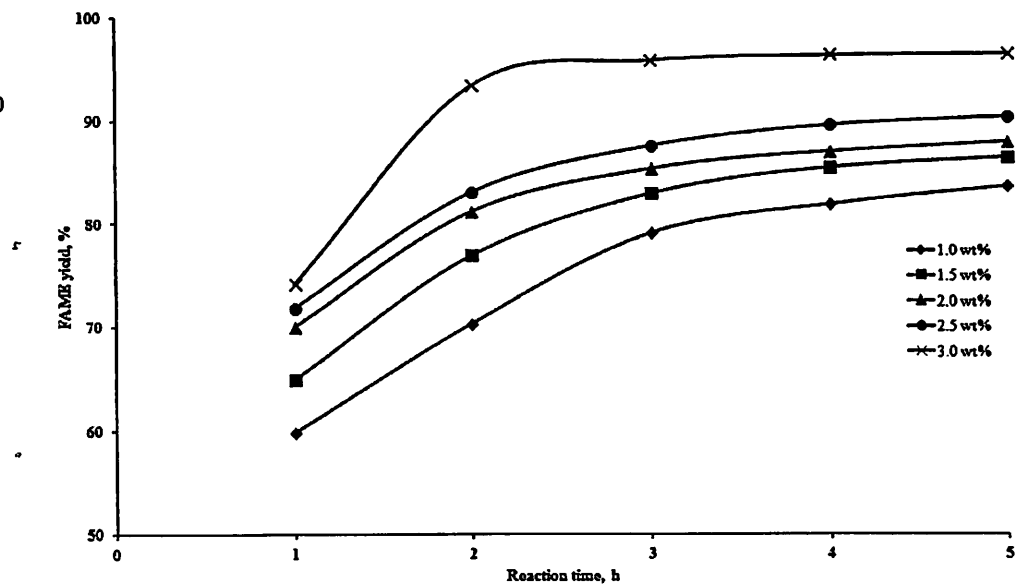
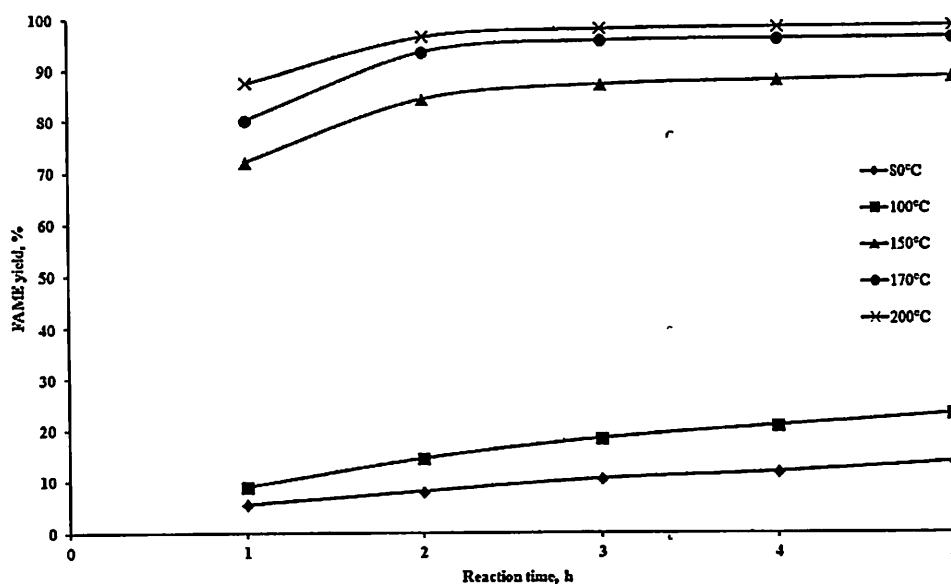


Fig. 3 Effect of the reaction temperature on the FAME yield at a catalyst loading of 3 wt% and a methanol-to-oil ratio of 20



equilibrium state was reduced to 2 h at higher catalyst loadings, as shown in Fig. 2. In addition, the reaction time was also reduced at a higher reaction temperature. From Fig. 3, at low reaction temperatures (80 and 100 °C), equilibrium was hardly observed, even with a high concentration of catalyst used to catalyse the reaction. However, at temperatures of 150 °C and above, the equilibrium of the reaction was reached at 2 h of reaction time. Through process study, a high FAME yield of 93.5 % can be obtained under the following conditions: reaction temperature of 170 °C, catalyst loading of 3 wt%, methanol-to-PFAD ratio of 20 and reaction time of 2 h.

Kinetic Parameters Estimation

Reaction Rate Constants

The equilibrium rate constant k_c can be determined from the final PFAD conversion using Eq. 8. Then, by using the

calculated k_c , the values of α and β can be obtained. As defined in Eq. 10, the reaction rate constant k_1 must be determined by the experimental conversion of PFAD obtained for different reaction times. Figures 4, 5 and 6 show the correlation between $\ln \left[\frac{(-1-\theta+\beta)x+2\theta}{(-1-\theta-\beta)x+2\theta} \right]$ and $\beta[\text{RCOOH}]_0 t$, under all the experimental conditions presented in Figs. 1, 2 and 3. The straight lines with high R^2 (more than 0.93) observed in Figs. 4, 5 and 6 demonstrated the validity of the proposed kinetic model. Hence, the values of k_1 were obtained as the slope of each straight line in the figures.

The calculated values of k_1 for different methanol-to-PFAD ratios, catalyst loadings and reaction temperatures are summarised in Table 1. The values of k_1 were observed to increase as the catalyst loading and reaction temperature increased. The k_1 of the methanol-to-PFAD ratio increased when the ratio increased from 8 to 20 which indicated that the rate of the esterification can also be increased by using a higher content of methanol. However, the k_1 for a methanol-to-

Fig. 4 Correlation between $\ln \left[\frac{(-1-\theta+\beta)x+2\theta}{(-1-\theta-\beta)x+2\theta} \right]$ and $\beta[\text{RCOOH}]_0 t$ at different levels of the methanol-to-PFAD ratio

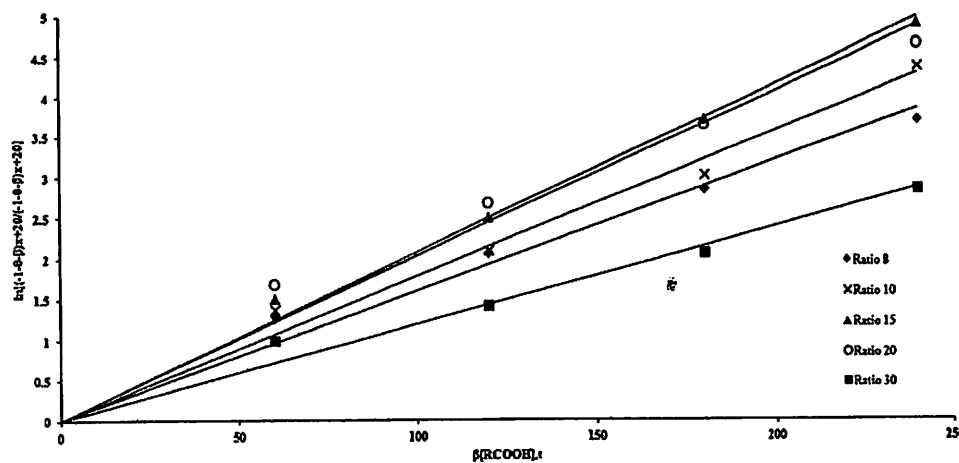
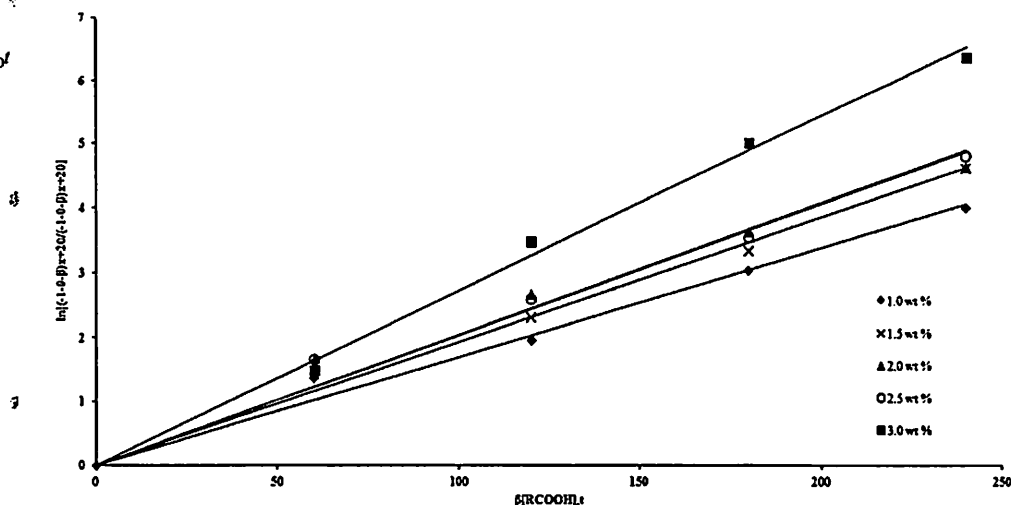


Fig. 5 Correlation between $\ln \left[\frac{(-1-\theta+\beta)x+2\theta}{(-1-\theta-\beta)x+2\theta} \right]$ and $\beta[\text{RCOOH}]_0 t$ at different levels of the catalyst loading



PFAD ratio of 30 were much lower than those of the other ratios because deactivation of the catalyst occurred at extremely high methanol content.

The current study further verified the fact that esterification is an endothermic reaction because, compared to other parameters, such as methanol-to-PFAD ratio and catalyst loading, the k_1 increased significantly with an increase in the reaction temperature. This result was in agreement with those reported in the literature [32–34, 28, 29].

Activation Energy, Pre-exponential Factor and Enthalpy of Reaction

As shown above, k_1 was significantly affected by the reaction temperature. Therefore, the dependence of k_c and k_1 on the reaction temperature can be illustrated by the Arrhenius equations. Equations 12 and 13 were linearised, and the Arrhenius-van't Hoff plot was used by plotting $\ln k$ as a function of the

reciprocal temperature (in units of Kelvin) to determine the pre-exponential factor, activation energy and enthalpy of the esterification. The Arrhenius-van't Hoff plot is shown in Fig. 7; the pre-exponential factor was obtained from the intercept of the straight line, while the activation energy (for forward and backward) and the enthalpy of esterification were obtained from the slope of the straight line. The pre-exponential factors of the forward and equilibrium reactions were 1.9×10^2 and $2.7 \times 10^9 \text{ L mol}^{-1} \text{ min}^{-1}$, respectively. The activation energy for forward reaction was 45.8 kJ mol^{-1} . The high value of the activation energy implied that the esterification reaction was a temperature-dependent reaction. This high value of activation energy also indicated that the esterification was kinetically controlled instead of diffusion controlled [28, 29], which further verified the assumption of the absence of external and internal mass transfer resistance in the pseudo-homogeneous kinetic model. The endothermic nature of the esterification

Fig. 6 Correlation between $\ln \left[\frac{(-1-\theta+\beta)x+2\theta}{(-1-\theta-\beta)x+2\theta} \right]$ and $\beta[\text{RCOOH}]_0 t$ at different levels of the reaction temperature

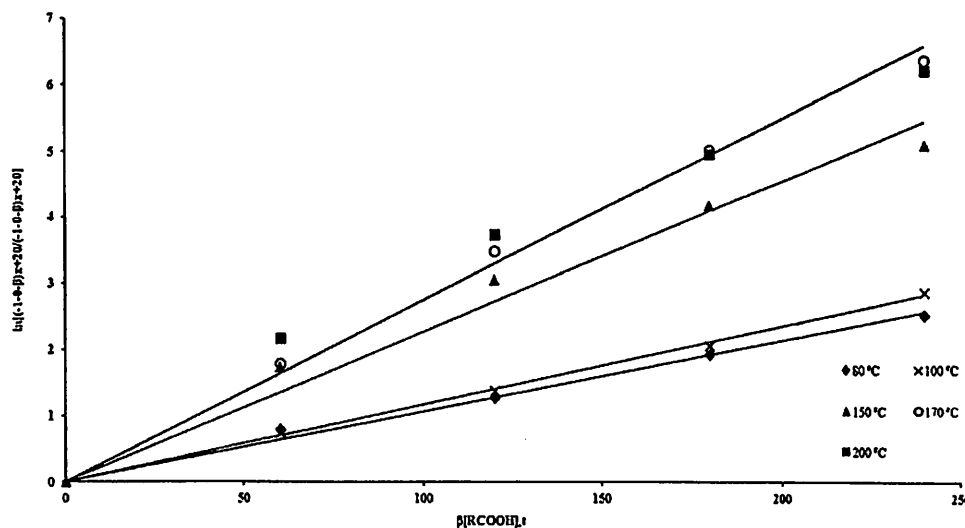


Table 1 The kinetic parameters for the esterification of PFAD with methanol using s-MWCNTs as a catalyst for different levels of methanol-to-PFAD ratio, catalyst loading and reaction temperature

Reaction parameters	Forward reaction rate, k_1 ($L \cdot mol^{-1} \cdot min^{-1}$)	R^2
Methanol/PFAD ratio		
8	4.97×10^{-4}	0.9502
10	5.08×10^{-4}	0.9722
15	5.77×10^{-4}	0.9882
20	6.17×10^{-4}	0.9329
30	2.45×10^{-4}	0.9565
Catalyst loading (wt%)		
1.0	4.72×10^{-4}	0.9675
1.5	5.66×10^{-4}	0.9765
2.0	6.17×10^{-4}	0.9329
2.5	6.51×10^{-4}	0.9574
3.0	9.81×10^{-4}	0.9920
Reaction temperature ($^{\circ}C$)		
80	3.05×10^{-5}	0.9851
100	6.00×10^{-5}	0.9965
150	7.00×10^{-4}	0.9363
170	9.80×10^{-4}	0.9905
200	1.03×10^{-3}	0.9317

of PFAD with methanol was confirmed due to the positive value of the reaction enthalpy (84.1 kJ mol^{-1}).

However, the activation energy for the backward reaction was found to have a negative value ($-38.3 \text{ kJ mol}^{-1}$) that was much smaller than the activation energy of the forward reaction. The negative or low activation energy indicated that the reaction rate decreased when the reaction temperature increased, which also meant that the reaction was mass transfer controlled [35, 28, 36]. Therefore, for the reversible endothermic reaction, such as esterification, the increase in the reaction

temperature not only increased the reaction rate of the forward reaction but also suppressed the backward reaction.

Table 2 presents the comparison of the activation energy exhibited by s-MWCNTs and various biodiesel production catalysts [37, 26, 38, 39, 27, 28, 40–43, 29, 44]. Note that the activation energy obtained in this study was actually lower than the activation energy exhibited by most of the catalysts, especially the popular KOH. A lower activation energy indicated that a heterogeneous process is not necessarily more energy intensive than the homogeneous process in biodiesel production. As defined in Eq. 12, the esterification reaction rate is inversely proportional to the activation energy, in which the lower the activation energy is, the higher is the reaction rate. The reaction can be effectively enhanced by the reduction of the activation energy. Therefore, the s-MWCNTs appear to be an attractive and promising alternative for the catalyst in biodiesel production because of the lower activation energy required for the reaction.

Goodness-of-Fit of the Experimental Data to the Developed Kinetic Model

After all the kinetic parameters were determined, the model was used to simulate the predicted PFAD conversion at the reaction conditions used in the actual experiments. Equation 11 was used to compute the simulated PFAD conversion. Figure 8 shows the correlation between the simulated and experimental PFAD conversions. A line of unit slope with almost perfect fit with many points corresponding to zero error between the experimental and predicted values was observed. The simulated values matched the experimental values very well, with R^2 value very close to unity of 0.9853. This agreement indicated that the developed kinetic model was reliable in representing this particular esterification reaction system and can thus be used to predict the PFAD

Fig. 7 Arrhenius-van't Hoff plot for the forward, backward and equilibrium reactions in the temperature range of 353–473 K

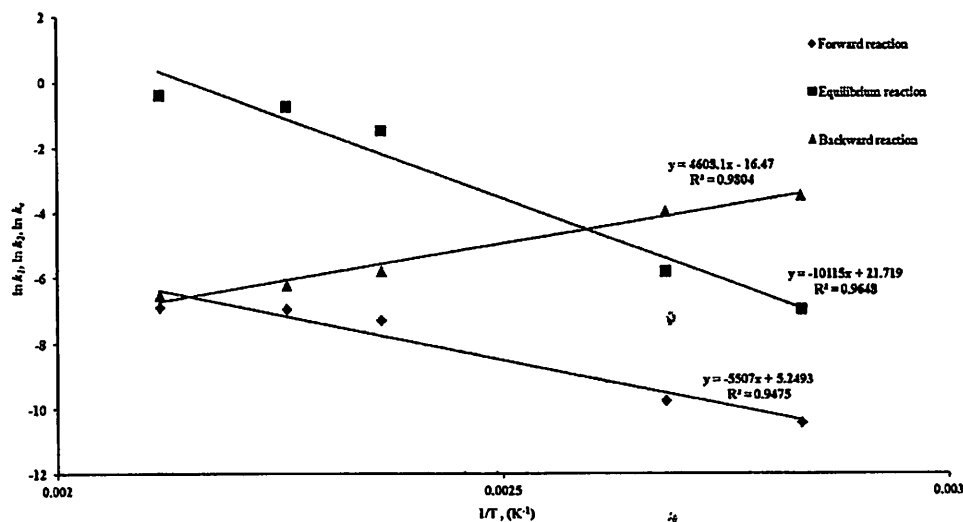


Table 2 Comparison of the activation energy of biodiesel production using different catalysts

Oil source	Reaction temperature (°C)	Catalysts	Catalyst loading (wt% of oil)	Alcohol source	Alcohol-to-oil molar ratio	Activation energy (kJ mol ⁻¹)	Reference
PFAD	170	s-MWCNTs	3.0	Methanol	20.0	45.80	This study
Palm oil	50–65	KOH	1.0–1.2	Methanol	6.0	147.70	[37]
Oleic acid	50–100	Acid sulphonic resin, Relite CFS	3.5–8.8	Methanol	8.3–10.7	58.58	[26]
Free fatty acids in vegetable oils	90–120	Purolite CT275	2.0	Methanol	6.6 (methanol/free fatty acid)	70.34	[38]
<i>Brassica carinata</i> oil	25–65	KOH	1.5	Methanol	6.0	209.21	[39]
Sunflower oil	60	H ₂ SO ₄	5.0 (based on oleic acid)	Methanol	60.0 (methanol/oleic acid ratio)	50.75	[27]
Fatty acid by enzymatic hydrolysis of soybean oil	60–80	Cation-exchange resin, Dowex Monosphere 88	26.8	Methanol	1.0–20.0	59.44	[28]
Palm oil	130–160	Methanesulphonic acid	0.05	Methanol	10.0	15.84	[40]
	130–160	H ₂ SO ₄	0.05	Methanol	10.0	27.31	
<i>Jatropha</i> oil	50–70	KNO ₃ /Al ₂ O ₃	6.0	Methanol	12.0	112.79	[41]
Soybean oil	65	SrO	2.0	Methanol	12.0	40.17	[42]
	65	Ca(OCH ₂ CH ₃) ₂	2.0	Methanol	12.0	54.39	
	65	CaO	2.0	Methanol	12.0	81.17	
	65	Ca(OCH ₃) ₂	2.0	Methanol	12.0	73.64	
Waste cooking oil	65	Amberlyst-15	4.0	Methanol	15:1	77.17	[43]
Fatty acid by enzymatic hydrolysis of soybean oil	30–70	HCl	0.1–1.0 M	Methanol	1.0–20.0	44.86	[29]
<i>Ceiba Pentandra</i> oil	65	KOH	1.0	Methanol	6.0	105.42	[44]

conversion of the reaction under other operating parameters as well.

Reusability and Leaching Analysis

The most significant advantage for using heterogeneous catalysts over homogeneous catalysts is the ability of the heterogeneous catalysts to be recovered, reused and regenerated. Therefore, the

s-MWCNTs were subjected to five consecutive runs to evaluate the reusability of the catalysts under the reaction conditions: reaction temperature of 170 °C, methanol-to-PFAD ratio of 20, catalyst loading of 3 wt% and reaction time of 2 h. After each run, the reaction mixtures were carefully separated, and then the s-MWCNTs were recovered and washed with methanol before being subjected to a new reaction run with fresh reactants. The FAME yield achieved by the s-MWCNTs in five consecutive

Fig. 8 Correlation between the simulated and the experimental FAME yield

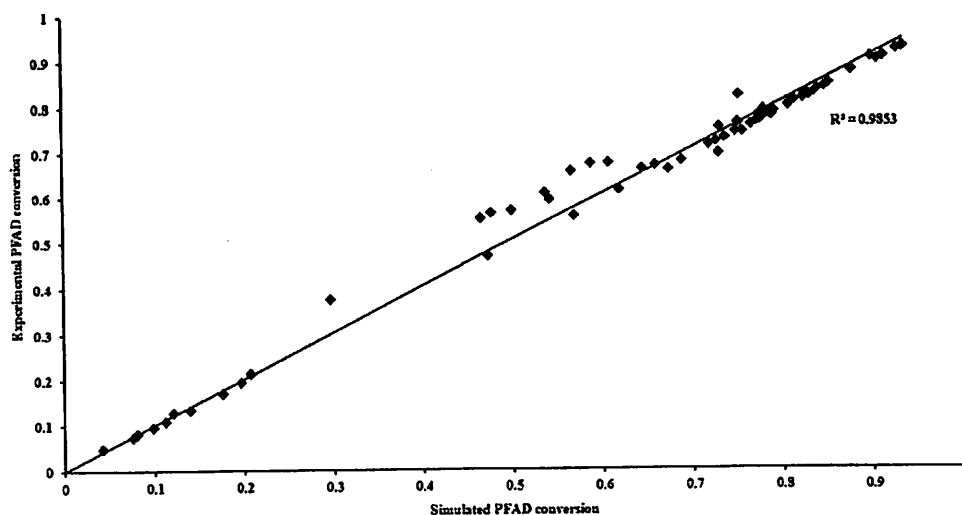
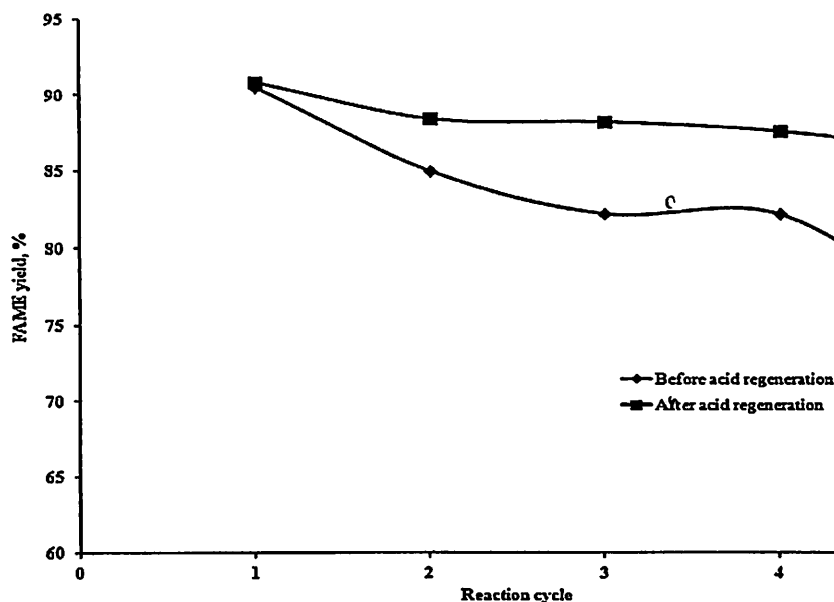


Fig. 9 Reusability of the s-MWCNTs and the regenerated s-MWCNTs in the esterification of PFAD under reaction conditions: methanol-to-PFAD ratio of 20, catalyst loading of 3 wt%, reaction temperature of 170 °C and reaction time of 2 h



runs is shown in Fig. 9. Although the catalytic activity of s-MWCNTs declined with repeated use, they were still able to maintain the FAME yield at 75 % after five catalytic runs. As reported in the literature, for alkaline earth metal oxide catalysts, such as CaO, BrO and SrO, the FAME yields dropped significantly to the level below 30 % at the third use; even under an ultrasonic-assisted reaction, the FAME yields achieved at the third use were still below 70 % [45]. In addition, for sulphated zirconia, tungstated zirconia or even some popular commercial biodiesel catalysts, such as Amberlyst-15, Nafion NR50 and ETS 10, the triacetin conversion was reported to be lower than 30 % at the fifth use of the catalysts [46]. Therefore, the s-MWCNTs exhibited better catalytic performance and higher reusability than the conventional biodiesel catalysts. The decrease in the catalytic activity of the s-MWCNTs may be due to two reasons: the blockage of acid sites by the deposition of organic matter on the catalyst surface and the leaching

of the sulphonic groups into the reaction medium [47, 48, 22].

The hypothesis of the deactivation of s-MWCNTs due to acid site blockage by hydrocarbon species was rejected based on the FT-IR analysis. Figure 10 shows the IR spectra in the range of 400–4000 cm^{-1} for the reused s-MWCNTs from the first to the fifth run. The absence of strong signals at 1600–1800 cm^{-1} indicated that carbonaceous materials, such as fatty acids and FAME, were not present on the surface of the s-MWCNTs. This lack of blockage by hydrocarbon species further indicated that the simple methanol washing used in this study can effectively remove the fatty acids or FAME that adsorbed onto the catalyst surface.

The leaching of sulphonic groups into the reaction medium was determined according to the ASTM D5453 testing method. Prior to testing, the reaction product mixture was not subjected to any washing or purification treatment. The test

Fig. 10 FT-IR spectra of spent s-MWCNTs for different repeated reaction runs: *a* first use, *b* second use, *c* third use, *d* fourth use, and *e* fifth use

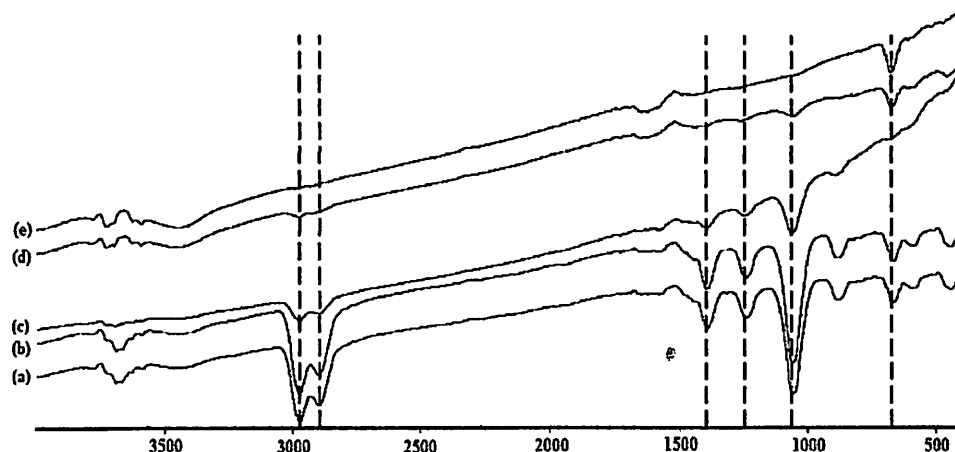
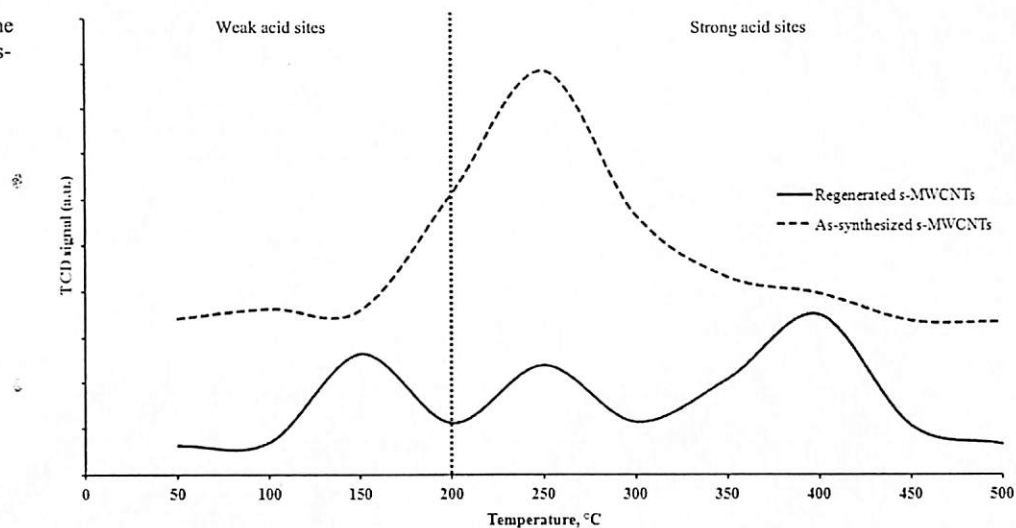


Fig. 11 NH_3 -TPD profiles for the as-synthesised and regenerated s-MWCNTs



result indicated that the sulphur content in FAME was 0.01 %. Therefore, the declining catalytic activity of the s-MWCNTs was due to the leaching of sulphonic groups into the reaction medium. Although the TPD analysis shown in Fig. 11 demonstrated that the acid strength of the as-synthesised s-MWCNTs occurred at 250 °C, leaching of the active sites into the reaction medium at a reaction temperature of 170 °C was still possible. However, the leaching of the sulphonic groups suffered by the s-MWCNTs was not at a severe level because the sulphur content in the reaction product complied with the ASTM D6751 standard, in which the maximum limit of sulphur content is 0.05 %.

Regeneration of s-MWCNTs

Regeneration of the spent catalyst was required because the catalytic activity of the s-MWCNTs declined after repeated use. Reflux in concentrated acid (H_2SO_4) was used to regenerate the spent s-MWCNTs. After acid regeneration, the regenerated s-MWCNTs were subjected to another five consecutive esterification runs under the same reaction conditions, and the FAME yields achieved are shown in Fig. 9. The results indicated that the activity of the regenerated s-MWCNTs was restored to its original level. Moreover, the regenerated s-MWCNTs exhibited better and higher catalytic performance than the un-regenerated s-MWCNTs because the high FAME yields of 86.2 % can be obtained after five repeated uses. The improved catalytic performance of the regenerated s-MWCNTs was due to the increase in the acid site density after acid regeneration. In comparison to the as-synthesised s-MWCNTs with an acid site density of 0.03 mmol g^{-1} (determined by pulse chemisorption), the acid density of the regenerated s-MWCNTs increased significantly to 0.28 mmol g^{-1} . In addition, the strength and thermal stability of the acid sites of the regenerated s-MWCNTs were improved after acid

regeneration. As shown in Fig. 11, the ammonia desorption peak of the regenerated s-MWCNTs was extended to 400 °C, which was a much higher temperature compared to the as-

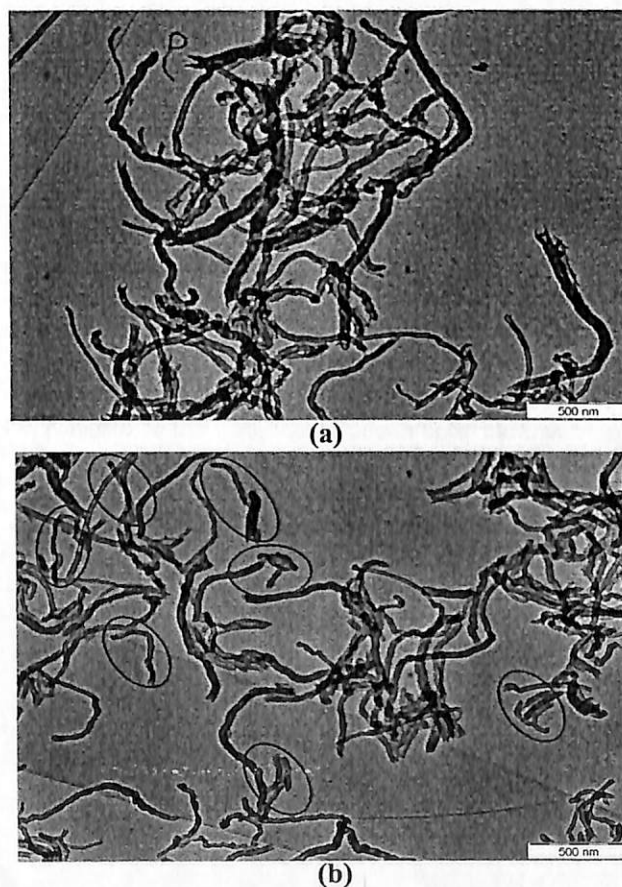


Fig. 12 TEM images of the as-synthesised and regenerated s-MWCNTs: **a** as-synthesised s-MWCNTs (scale bar of 500 nm) and **b** regenerated s-MWCNTs (scale bar of 500 nm)

synthesised s-MWCNTs, in which the ammonia desorption peak was observed at 250 °C.

Figure 12 shows the TEM images of the as-synthesised s-MWCNTs and the regenerated s-MWCNTs. The TEM observations revealed that the as-synthesised s-MWCNTs possessed a longer open-ended tube length (Fig. 12a) compared to that of the regenerated s-MWCNTs (Fig. 12b). After acid regeneration, the s-MWCNTs were cut into shorter tubes, as highlighted in Fig. 12b. Therefore, the surface area available for the esterification reaction was enhanced.

Conclusion

The present study demonstrated the high potential and promise of the use of s-MWCNTs as a catalyst for biodiesel production from a typical low-grade industrial by-product PFAD. A high FAME yield of 93.5 % was obtained under the following conditions: reaction temperature of 170 °C, methanol-to-PFAD ratio of 20, catalyst loading of 3 wt% and reaction time of 2 h. The kinetics of the esterification of PFAD with methanol was well represented by a pseudo-homogeneous model because of the good agreement between the simulated and experimental FAME yields. The lower activation energy observed in this study indicated that the esterification catalysed by s-MWCNTs can proceed at a faster reaction rate than that of the common heterogeneous catalysts used in biodiesel production. In addition, the s-MWCNTs used in this study exhibited high reusability: the catalyst can maintain a FAME yield of more than 75 % after five repeated reaction runs. The reduction in catalytic activity of the s-MWCNTs was due to the leaching of sulphonic groups into the reaction medium. However, the leaching effect was not severe because the sulphur content of the FAME obtained still complied with the international standard. Acid regeneration was found to increase the catalytic activity and the strength of acid sites because the acid site density was increased and the thermal stability of acid sites was extended up to 400 °C. A FAME yield of 86.2 % was produced by the regenerated s-MWCNTs at the fifth repeated run.

Acknowledgments Siew Hoong Shuit acknowledges the support of the Ministry of Higher Education of Malaysia through the MyPhD Fellowship. This research was also financially supported by the Universiti Sains Malaysia Research University (RU) grant (A/C:814142), the USM Membrane Cluster Grant and the Postgraduate Research Grant Scheme (PRGS) (A/C: 8044028).

References

- Kargbo DM (2010) Biodiesel production from municipal sewage sludges. *Energy Fuels* 24(5):2791–2794. doi:10.1021/ef1001106
- Shah K, Parikh J, Maheria K (2014) Optimization studies and chemical kinetics of silica sulfuric acid-catalyzed biodiesel synthesis from waste cooking oil. *Bioenerg Res* 7(1):206–216. doi:10.1007/s12155-013-9363-y
- Shuit SH, Lee KT, Kamaruddin AH, Yusup S (2010) Reactive extraction of *Jatropha curcas* L. seed for production of biodiesel: process optimization study. *Environ Sci Technol* 44(11):4361–4367. doi:10.1021/es902608v
- Koberg M, Gedanken A (2012) Direct transesterification of castor and *Jatropha* seeds for FAME production by microwave and ultrasound radiation using a SrO catalyst. *Bioenerg Res* 5(4):958–968. doi:10.1007/s12155-012-9210-6
- Kansedo J, Lee KT, Bhatia S (2009) *Cerbera odollam* (sea mango) oil as a promising non-edible feedstock for biodiesel production. *Fuel* 88(6):1148–1150. doi:10.1016/j.fuel.2008.12.004
- Alberici R, Souza V, Sá G, Morelli S, Eberlin M, Daroda R (2012) Used frying oil: a proper feedstock for biodiesel production? *Bioenerg Res* 5(4):1002–1008. doi:10.1007/s12155-012-9216-0
- Shibasaki-Kitakawa N, Tsuji T, Kubo M, Yonemoto T (2011) Biodiesel production from waste cooking oil using anion-exchange resin as both catalyst and adsorbent. *Bioenerg Res* 4(4):287–293. doi:10.1007/s12155-011-9148-0
- Cho HJ, Kim J-K, Cho H-J, Yeo Y-K (2012) Techno-economic study of a biodiesel production from palm fatty acid distillate. *Ind Eng Chem Res* 52(1):462–468. doi:10.1021/ie301651b
- Cheah KY, Toh TS, Koh PM (2010) Palm fatty acid distillate biodiesel. *INFORM*:264–266
- Shuit SH, Yee KF, Lee KT, Subhash B, Tan SH (2013) Evolution towards the utilisation of functionalised carbon nanotubes as a new generation catalyst support in biodiesel production: an overview. *RSC Advances* 3(24):9070–9094. doi:10.1039/c3ra22945a
- Borges ME, Diaz L (2013) Catalytic packed-bed reactor configuration for biodiesel production using waste oil as feedstock. *Bioenerg Res* 6(1):222–228. doi:10.1007/s12155-012-9246-7
- Lin L, Li X, Cui F, Zhou H, Shen X, Dong M (2012) Transesterification of rapeseed oil to biodiesel on CaO/ α -Fe hollow fiber catalyst: optimization by response surface methodology. *Bioenerg Res* 5(4):949–957. doi:10.1007/s12155-012-9209-z
- Takagaki A, Toda M, Okamura M, Kondo JN, Hayashi S, Domen K, Hara M (2006) Esterification of higher fatty acids by a novel strong solid acid. *Catal Today* 116(2):157–161. doi:10.1016/j.cattod.2006.01.037
- Mo X, Lotero E, Lu C, Liu Y, Goodwin J (2008) A novel sulfonated carbon composite solid acid catalyst for biodiesel synthesis. *Catal Lett* 123(1):1–6. doi:10.1007/s10562-008-9456-y
- Zong M-H, Duan Z-Q, Lou W-Y, Smith TJ, Wu H (2007) Preparation of a sugar catalyst and its use for highly efficient production of biodiesel. *Green Chem* 9(5):434–437
- Mar WW, Somsook E (2012) Sulfonic-functionalized carbon catalyst for esterification of high free fatty acid. *Procedia Eng* 32(0):212–218. doi:10.1016/j.proeng.2012.01.1259
- Liu R, Wang X, Zhao X, Feng P (2008) Sulfonated ordered mesoporous carbon for catalytic preparation of biodiesel. *Carbon* 46(13):1664–1669
- Shu Q, Zhang Q, Xu G, Nawaz Z, Wang D, Wang J (2009) Synthesis of biodiesel from cottonseed oil and methanol using a carbon-based solid acid catalyst. *Fuel Process Technol* 90(7–8):1002–1008. doi:10.1016/j.fuproc.2009.03.007
- Shu Q, Zhang Q, Xu G, Wang J (2009) Preparation of biodiesel using s-MWCNT catalysts and the coupling of reaction and separation. *Food Bioprod Process* 87(3):164–170. doi:10.1016/j.fbp.2009.01.004
- Kastner JR, Miller J, Geller DP, Locklin J, Keith LH, Johnson T (2012) Catalytic esterification of fatty acids using solid acid catalysts generated from biochar and activated carbon. *Catal Today* 190(1):122–132. doi:10.1016/j.cattod.2012.02.006

21. Sharma YC, Singh B, Korstad J (2011) Advancements in solid acid catalysts for ecofriendly and economically viable synthesis of biodiesel. *Biofuels Bioprod Bioref* 5(1):69–92. doi:10.1002/bbb.253
22. Lee JS, Saka S (2010) Biodiesel production by heterogeneous catalysts and supercritical technologies. *Bioresour Technol* 101(19):7191–7200. doi:10.1016/j.biortech.2010.04.071
23. Zhou W, Xiao J, Chen Y, Zeng R, Xiao S, Nie H, Li F, Song C (2010) Sulfonated carbon nanotubes/sulfonated poly(ether sulfone ether ketone) composites for polymer electrolyte membranes. *Polym Adv Technol* 22(12):1747–1752. doi:10.1002/pat.1666
24. Shuit SH, Tan SH (2014) Feasibility study of various sulphonation methods for transforming carbon nanotubes into catalysts for the esterification of palm fatty acid distillate. *Energ Convers Manage*. doi:10.1016/j.enconman.2014.01.035
25. Villa A, Tessonnier J-P, Majoulet O, Su DS, Schlögl R (2010) Transesterification of triglycerides using nitrogen-functionalized carbon nanotubes. *ChemSusChem* 3(2):241–245. doi:10.1002/cssc.200900181
26. Tesser R, Di Serio M, Guida M, Nastasi M, Santacesaria E (2005) Kinetics of oleic acid esterification with methanol in the presence of triglycerides. *Ind Eng Chem Res* 44(21):7978–7982. doi:10.1021/ie050588o
27. Berrios M, Siles J, Martín MA, Martín A (2007) A kinetic study of the esterification of free fatty acids (FFA) in sunflower oil. *Fuel* 86(15):2383–2388. doi:10.1016/j.fuel.2007.02.002
28. Su C-H, Fu C-C, Gomes J, Chu IM, Wu W-T (2008) A heterogeneous acid-catalyzed process for biodiesel production from enzyme hydrolyzed fatty acids. *AIChE J* 54(1):327–336. doi:10.1002/aic.11377
29. Su C-H (2013) Kinetic study of free fatty acid esterification reaction catalyzed by recoverable and reusable hydrochloric acid. *Bioresour Technol* 130(0):522–528. doi:10.1016/j.biortech.2012.12.090
30. Shuit SH, Ong YT, Lee KT, Subhash B, Tan SH (2012) Membrane technology as a promising alternative in biodiesel production: a review. *Biotechnol Adv* 30(6):1364–1380. doi:10.1016/j.biotechadv.2012.02.009
31. Lam MK, Lee KT, Mohamed AR (2009) Sulfated tin oxide as solid superacid catalyst for transesterification of waste cooking oil: an optimization study. *Appl Catal, B* 93(1–2):134–139. doi:10.1016/j.apcatb.2009.09.022
32. Goto S, Tagawa T, Yusoff A (1991) Kinetics of the esterification of palmitic acid with isobutyl alcohol. *Int J Chem Kinet* 23(1):17–26. doi:10.1002/kin.550230103
33. Bart HJ, Reidetschlagel J, Schatka K, Lehmann A (1994) Kinetics of esterification of levulinic acid with n-butanol by homogeneous catalysis. *Ind Eng Chem Res* 33(1):21–25. doi:10.1021/ie00025a004
34. Aafaqi R, Mohamed AR, Bhatia S (2004) Kinetics of esterification of palmitic acid with isopropanol using p-toluene sulfonic acid and zinc ethanoate supported over silica gel as catalysts. *J Chem Technol Biotechnol* 79(10):1127–1134. doi:10.1002/jctb.1102
35. Nijhuis TA, van Koten G, Kapteijn F, Moulijn JA (2003) Separation of kinetics and mass-transport effects for a fast reaction: the selective hydrogenation of functionalized alkynes. *Catal Today* 79–80(0):315–321. doi:10.1016/S0920-5861(03)00055-5
36. Melero JA, Iglesias J, Morales G (2009) Heterogeneous acid catalysts for biodiesel production: current status and future challenges. *Green Chem* 11(9):1285–1308
37. Darnoko D, Cheryan M (2000) Kinetics of palm oil transesterification in a batch reactor. *J Am Oil Chem Soc* 77(12):1263–1267. doi:10.1007/s11746-000-0198-y
38. Pasiás S, Barakos N, Alexopoulos C, Papayannakos N (2006) Heterogeneously catalyzed esterification of FFAs in vegetable oils. *Chem Eng Technol* 29(11):1365–1371. doi:10.1002/ccat.200600109
39. Vicente G, Martínez M, Aracil J (2006) Kinetics of Brassica carinata oil methanolysis. *Energy Fuels* 20(4):1722–1726. doi:10.1021/cf060047r
40. Aranda DG, Santos RP, Tapanes NO, Ramos A, Antunes O (2008) Acid-catalyzed homogeneous esterification reaction for biodiesel production from palm fatty acids. *Catal Lett* 122(1–2):20–25. doi:10.1007/s10562-007-9318-z
41. Vyas AP, Subrahmanyam N, Patel PA (2009) Production of biodiesel through transesterification of Jatropha oil using KNO₃/Al₂O₃ solid catalyst. *Fuel* 88(4):625–628. doi:10.1016/j.fuel.2008.10.033
42. Liu X, Piao X, Wang Y, Zhu S (2010) Model study on transesterification of soybean oil to biodiesel with methanol using solid base catalyst. *J Phys Chem A* 114(11):3750–3755. doi:10.1021/jp9039379
43. Gan S, Ng HK, Chan PH, Leong FL (2012) Heterogeneous free fatty acids esterification in waste cooking oil using ion-exchange resins. *Fuel Process Technol* 102(0):67–72. doi:10.1016/j.fuproc.2012.04.038
44. Sivakumar P, Sindhanaiselvan S, Gandhi NN, Devi SS, Renganathan S (2013) Optimization and kinetic studies on biodiesel production from underutilized Ceiba Pentandra oil. *Fuel* 103(0):693–698. doi:10.1016/j.fuel.2012.06.029
45. Mootabadi H, Salamatnia B, Bhatia S, Abdullah AZ (2010) Ultrasonic-assisted biodiesel production process from palm oil using alkaline earth metal oxides as the heterogeneous catalysts. *Fuel* 89(8):1818–1825. doi:10.1016/j.fuel.2009.12.023
46. López DE, Goodwin JG Jr, Bruce DA, Lotero E (2005) Transesterification of triacetin with methanol on solid acid and base catalysts. *Appl Catal A Gen* 295(2):97–105. doi:10.1016/j.apcata.2005.07.055
47. Alonso DM, Mariscal R, Moreno-Tost R, Poves MDZ, Granados ML (2007) Potassium leaching during triglyceride transesterification using K/γ-Al₂O₃ catalysts. *Catal Commun* 8(12):2074–2080. doi:10.1016/j.catcom.2007.04.003
48. Lee DW, Park YM, Lee KY (2009) Heterogeneous base catalysts for transesterification in biodiesel synthesis. *Catal Surv Asia* 13:63–77

A Review on the Use and Stability of Supported Liquid Membranes in the Pervaporation Process

YIT THAI ONG, KIAN FEI YEE, YOKE KOOI CHENG,
and SOON HUAT TAN

*School of Chemical Engineering, Engineering Campus, Universiti Sains Malaysia,
Pulau Pinang, Malaysia*

In recent decades, pervaporation has been one of the most studied membrane separation processes and has undergone substantial progress and exciting breakthroughs due to its effectiveness in separating azeotropic mixtures and its low energy consumption. Often, pervaporation processes are operated using a solid membrane. However, the inherent limitations of solid membranes prompted the use of supported liquid membranes (SLMs), which are formed by immobilizing the liquid membrane with a porous supporting membrane. The idea of using a SLM in pervaporation is attractive because the rate of molecular diffusion in liquid is much higher than that in a solid membrane. This short article reviews the role of SLMs as a pervaporation membrane. The effects of operating parameters on the pervaporation performance of SLMs as well as concerns on the stability of SLMs and methods to improve its stability are discussed. At the end of this article, we propose the use of carbon nanotubes (CNTs) in SLMs and perform an evaluation of the commercial value of SLMs.

KEYWORDS *Pervaporation, supported liquid membrane, carbon nanotubes*

Received 24 February 2012, Accepted 23 July 2012

Address correspondence to Soon Huat Tan, School of Chemical Engineering, Engineering Campus, Universiti Sains Malaysia, Seri Ampangan, 14300, Nibong Tebal, SPS, Pulau Pinang, Malaysia. E-mail: chshtan@eng.usm.my

INTRODUCTION

Coined from two terms (permeation and evaporation), pervaporation is a membrane separation process that has undergone substantial progress and exciting breakthroughs during the past few decades. The phenomenon of pervaporation was first observed by Kober (1), who defined the term when reporting the selective permeation of water from aqueous solutions of albumin and toluene through a cellulose nitrate film. In general, pervaporation involves a membrane that serves as a selective barrier between two compartments that regulates the transport of specific substances that possess a high affinity for the membrane. Unlike other membrane processes, the permeation of substances in pervaporation involves a phase change from liquid to vapor. Often, a vacuum pump or sweeping gas is employed at the downstream side to create a driving force for continuous mass transport. Pervaporation is considered to be a clean technology or a pollution prevention alternative that is suitable for the treatment, recycling and reuse of contaminated water (2). Compared to other conventional separation processes, the low energy consumption and high efficiency of pervaporation in separating azeotropic mixtures are advantages that have increased its viable application in the dehydration of solvents (3, 4) and the separation of organic liquid mixtures (5, 6).

The pervaporation membrane plays a significant role as a separation barrier, with a primary function in selectively controlling mass transfer. Hence, the selection of the proper membrane material is a critical task. Generally, the selection of membrane material depends on the permeation flux, selectivity and stability of the membrane (7). As shown in Eq. (1) and (2) (8), the permeation flux (J) quantifies the permeated component (Q) through a specific surface area (A) over a given unit of time (t); the selectivity, α , describes the affinity of the membrane toward the specific component in the binary mixture.

$$J = \frac{Q}{At} \quad (1)$$

$$\alpha = \frac{(Y_i/Y_j)}{(X_i/X_j)} \quad (2)$$

where X and Y refer to the weight fractions of components i and j in the feed and permeate streams, respectively. Membrane stability is defined as the capability of a membrane to maintain both its permeability and selectivity under specific system conditions for an extended period of time.

Over the past decade, most pervaporation processes have involved the use of solid membranes. Polymeric membranes, including poly(vinyl alcohol) (9–13), poly(vinylidene difluoride) (14–19), polysulfone (20–23), poly(dimethyl siloxane) (24–29) and chitosan (30–33), are commonly used

due to their low cost and ease of handling. However, these membranes are associated with swelling and weak mechanical properties, which often reduce the performance of polymeric membrane separations. Though the emergence of inorganic materials as membranes was able to overcome these limitations (34–38), the high membrane fabrication cost remains a significant constraint on their application in pervaporation processes. Thus, the deficiencies of these materials have led to increased research on membrane composed of both polymeric and inorganic materials (39–42). Despite their excellent mechanical and thermal resistance, the use of these membranes is not yet practical.

Recently, there has been a new trend of adopting a liquid membrane in pervaporation processes rather than a solid membrane. Liquid membranes make use of a liquid phase to serve as a semipermeable barrier. As illustrated in Figure 1, liquid membranes can exist in various forms and can be classified as either a bulk liquid membrane (BLM), an emulsion liquid membrane (ELM) or a supported liquid membrane (SLM) (43). BLMs contain a layer of bulk liquid membrane that separates the feed and receiving phases, whereas in ELMs, the liquid membrane forms an emulsion with the receiving phase. In SLMs, liquid membrane is supported by a porous membrane. Of these three configurations, the presence of a porous supporting membrane in SLM demonstrates better stability, making it the most promising candidate as a pervaporation membrane (44, 45).

This short review focuses on the use of SLMs in pervaporation processes. First, we introduce SLMs and methods for their preparation. We then follow with an overview of the use of SLMs in pervaporation and the requirement of liquid and supporting membranes. In addition, the effects of operating parameters on the pervaporation performance of SLMs are discussed. Subsequently, concerns about SLM stability and methods to improve stability are presented. Specifically, a proposal on the use of carbon nanotubes (CNTs) in enhancing SLM stability is presented. Finally, the commercial value of SLMs is evaluated.

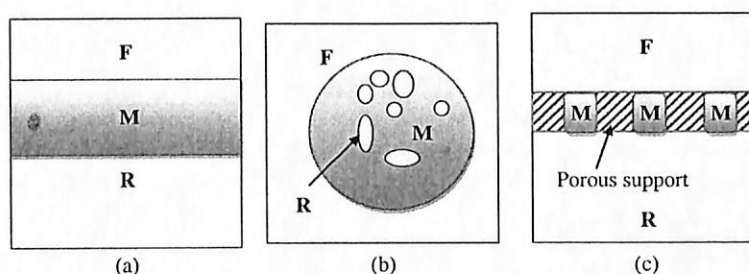


FIGURE 1 Configuration of liquid membrane: (a) bulk liquid membrane (BLM), (b) emulsion liquid membrane (ELM) and (c) supported liquid membrane (SLM). F is the feed phase, M is the membrane phase, and R is the receiving phase.

SUPPORTED LIQUID MEMBRANES AND THEIR PREPARATION METHODS

SLMs were first reported by Scholander (46), who used a thin cellulose acetate filter immobilized with an aqueous hemoglobin solution for oxygen transport in 1960. Studies involving SLMs only started receiving attention in the 1980s, when researchers found that SLMs were capable of separating metal and organic compounds and were easy to implement into a continuous flow system (47). Briefly, SLM systems consist of a liquid membrane that is immobilized in a porous supporting membrane through capillary force. The SLM system usually appears in two different geometries, a flat sheet or hollow fiber. A flat sheet SLM is useful in laboratory-scale experiments, and this system involves simply placing the flat sheet SLM in between the feed and permeate streams. In contrast, a hollow fiber SLM is preferable for industrial use, as it provides a higher surface area to volume ratio. This system is mainly composed of a bundle of individual fibers in a cylindrical shell, with feed solution circulated through the lumen side while permeate flows on the shell side.

Preparation of the SLM involves the immobilization of the liquid membrane in the supporting membrane. This immobilization is often implemented using either direct immersion (48) or a pressure- (49, 50) or vacuum-based technique (51, 52). In direct immersion, immobilization is achieved by immersing the supporting membrane into the liquid membrane for a period of time. With a pressure-based technique, the supporting membrane is filled with the liquid membrane and subjected to nitrogen pressure to force the liquid membrane into the pores of the support. The pressure is released once a thin layer of liquid membrane is formed on the supporting membrane (53). Using a vacuum-based technique, a vacuum suction is applied after the supporting membrane is submerged in the liquid membrane so the air from the pores can be released and enable the liquid membrane to fill in the porous structure of the supporting membrane (53).

OVERVIEW OF THE SUPPORTED LIQUID MEMBRANE IN PERVAPORATION

Pervaporation using SLMs has long been suggested (54–56). The idea of using SLMs is attractive because molecular diffusion is much higher in liquid than in solid materials like polymeric or inorganic membranes. The diffusion coefficient in liquid phase is reported to be at least 3 to 4 times higher than in solid phase (57, 58), which could promote higher flux and selectivity. Moreover, it is well known that a membrane with higher selectivity consumes less energy, while a membrane with higher flux requires a smaller surface area (59). Therefore, a high efficiency separation SLM can be prepared with

a small amount of liquid membrane, resulting in a lower capital cost and decreased usage of the expensive liquid (60–63).

Similar to solid pervaporation membranes, the transportation of the targeted component across the liquid membrane can be explained by the solution-diffusion model, which is a combination of the following three fundamental steps (64):

- i) sorption of the targeted component from the feed liquid to the membrane,
- ii) diffusion of the targeted component in the membrane and
- iii) desorption of the targeted component to the vapor phase on the downstream side of the membrane.

Based on the solution-diffusion model, the transport mechanism of the targeted component in the liquid membrane consists of either simple permeation or facilitated transport. Both mechanisms obey Fick's law, where the solute is transported from high to low chemical potential. In simple permeation, the targeted component passes through the membrane based on its solubility in the liquid membrane. The targeted component remains in the same form without any reaction during the transfer (47). Facilitated transport involves the use of a carrier to mediate the transport of the targeted component. This method is useful for targeted components that have lower solubility in the liquid membrane. The purpose of adding a carrier is to form a complex that is soluble in the liquid membrane by reversibly reacting with the targeted component at the feed-membrane interface, releasing it on the permeate side (47). However, it is important to ensure that the complex formed is not soluble in the feed solution. The mechanisms of simple and facilitated transport in SLM systems are shown in Figure 2.

The use of a SLM as a pervaporation membrane creates a tendency toward higher selectivity and permeation flux. Prior to its application in

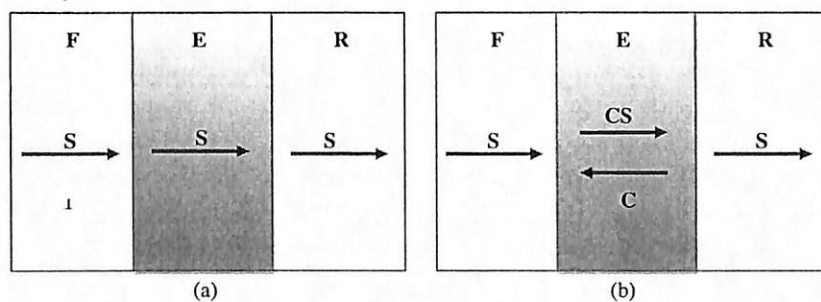


FIGURE 2 Schematic mechanism of (a) simple transport, and (b) facilitated transport in supported liquid membranes (SLM). S is the solute to be separated, C is the carrier, F is the feed phase, E is the liquid membrane and R is the receiving phase.

pervaporation processes, it is necessary to ensure that the partial pressure of the targeted component is high enough to provide a driving force for separation. Furthermore, the requirement for the liquid and supporting membranes should be considered so that the SLM can be successfully applied in the pervaporation process.

Requirements for the Liquid Membrane

The liquid membrane greatly influences the transport properties and stability of the SLM. The most important aspect to be considered is the solubility of the targeted component in the liquid membrane, as the transport of the targeted component across the SLM depends on this property, and a liquid membrane with high solubility toward the targeted component should be chosen. The viscosity of the liquid membrane is critical in controlling the quality of the immobilized liquid membrane and the SLM stability. A liquid membrane with low viscosity makes the immobilization process easier and creates a thin liquid membrane layer. However, under high vacuum, the low viscosity causes the displacement of the immobilized liquid from the supporting membrane, eventually compromising the stability of the SLM (65, 66).

The volatility of the liquid membrane indicates the susceptibility of the liquid membrane vaporization and therefore should be as low as possible. This should minimize the possibility of liquid membrane loss through evaporation (67, 68). Surface tension is responsible for holding the immobilized liquid membrane in the pores of the supporting membrane (69, 70). Generally, it is desirable for the liquid membrane to have low surface tension so that it can wet the supporting membrane by forming a zero or near-zero contact angle.

Since the early development of SLMs as pervaporation membranes, organic solvents have been a popular choice for the liquid membrane due to their high solubility toward liquid solutes. The most commonly used organic solvents are hydrophobic ethers and esters, hydrocarbons and long chain alcohols. Other than organic solvents, recent studies have suggested using ionic liquids as liquid membranes (67, 71–73).

Ionic liquids are organic salts composed of a combination of mostly cations and anions or short-lived ion pairs, with a melting point below 100°C (74). They have been recognized as a possible environmentally benign alternative to the classical organic solvents due to their ability to dissolve a large range of organic molecules and transition metal complexes (75–77). In addition, ionic liquids possess negligible vapor pressure, high thermal stability and non-flammability (71, 78, 79). Ionic liquids are often called “tailor-made or tunable materials” because their properties can be tuned according to the desired task using variations of different possible cations and anions, resulting in a large number of ionic liquids with different properties (80–83).

Requirements for the Supporting Membrane

In addition to providing physical stability and chemical resistance, the supporting membrane serves as a medium to hold the liquid membrane and plays a key role in determining the separation efficiency of the SLM. In general, the supporting membrane for the SLM is selected based on its surface characteristics, porosity, pore size, porous structure, thickness, and tortuosity and the mechanical and chemical properties of the support material (84–86).

The surface of the supporting membrane can be either hydrophilic or hydrophobic, according to its affinity for water molecules, and thus reflects the wettability of the supporting membrane, which affects the interaction between the liquid and supporting membranes. Proper selection of surface characteristics allows more efficient immobilization. Support porosity indicates the percentage of the void space present in a predetermined volume. This property determines the total amount of liquid membrane that can be immobilized because the SLM is formed by filling the pores of the supporting membrane with the liquid membrane. Thus, a supporting membrane with high porosity is preferable.

Meanwhile, a supporting membrane with a smaller pore size is favorable due to the increased surface area on which the liquid membrane can be immobilized and the increased contact between the liquid membrane and the feed solutions (87). Moreover, smaller pore size is also one of the key ways of enhancing SLM stability (88, 89). The porous structure of the supporting membrane may appear symmetric, where the pore diameters are uniform over the cross-section of the membrane, or asymmetric, where the pore diameters vary over the cross-section of the membrane by a factor of 10–1000. Often, an asymmetric porous structure is chosen over a symmetric structure, especially in pressure-driven membrane processes, due to its unique properties of a high mass transfer rate and sufficient mechanical stability (90).

Thickness plays an important role in the mass transport rate. The supporting membrane should be as thin as possible to reduce both mass transport resistance and the path length for diffusion. However, a thin support layer is often associated with low mechanical stability, so the thickness of the supporting membrane should be balanced with maintaining adequate mechanical strength to withstand transmembrane pressure (85). In addition to thickness, tortuosity, τ , is another parameter that influences the mass transport rate because it correlates with the diffusion path length. Tortuosity describes the deviation of the porous structure from a straight line (85, 91) and can be expressed as the ratio of the actual distance traveled, Δl , by the species per unit length, Δx , of the medium as follows (91):

$$\tau = \frac{\Delta l}{\Delta x} \quad (3)$$

Therefore, it is beneficial to minimize the tortuosity of the porous structure in the supporting membrane to avoid slowing transport across the membrane (26, 92, 93).

In addition, consideration of the chemical properties of the supporting membrane is essential, particularly the reactivity of the supporting membrane upon contact with the feed phase. In a pervaporation process, contact between the supporting membrane and the feed solution is inevitable. The occurrence of a chemical reaction between the supporting membrane and the feed solution, especially when dealing with acidic or basic feed solutions, would result in corrosion of the supporting membrane. Additionally, an interaction with the feed solution could induce sorption in the supporting membrane, causing it to swell. The amount of immobilized liquid membrane would be reduced proportionally to the swelling behavior because the pore size and pore volume of the support material would decrease significantly (94). To avoid any deviation in support morphology, a chemically inert supporting membrane is preferable.

To date, the most widely accepted supporting membranes are made from polymeric substances due to their economic feasibility and simple preparation. Various polymers, including poly(vinylidene fluoride) (50, 95–97), polypropylene (54, 59, 98, 99), polytetrafluoroethylene (100), polycarbonate (95), cellulose acetate (101) and polyamide (49), are frequently used as supporting membranes. Alternatively, inorganic materials such as ceramic and zeolite have also been used due to their high physical, thermal and chemical stability.

APPLICATION OF SUPPORTED LIQUID MEMBRANES IN THE PERVAPORATION PROCESS

The application of SLMs in pervaporation processes has been widely studied. The pervaporation processes primarily addressed in these studies involved the separation of a volatile fermentation product and volatile organic compounds (VOCs) from dilute aqueous solutions. Matsumara et al. (54) reported a pervaporation of a dilute aqueous butanol solution using a SLM prepared by immobilizing oleyl alcohol in a microporous polypropylene support. A separation factor of 180 was obtained, and the outcome was superior to separation using a solid silicone rubber membrane. Subsequently, a similar SLM was integrated with diacetyl fermentation by Ishii et al. (56), and they reported a permeation flux of $9 \text{ g}\cdot\text{m}^{-2}\cdot\text{h}^{-1}$ and a diacetyl selectivity of 36, with no membrane fouling during operation. In an analogous study, Christen et al. (55) developed a SLM that consisted of isotridecanol and a porous Teflon support to extract ethanol produced from a semi-continuous fermentation of *Saccharomyces bayanus*. The capability of this SLM to extract ethanol through pervaporation was evident when the ethanol concentration

obtained in the collected permeate was 4 times greater than that of the fermentation broth. This SLM demonstrated a separation factor of 7.2 and a permeation flux of $39 \text{ g}\cdot\text{m}^{-2}\cdot\text{h}^{-1}$.

Qin *et al.* (59) utilized SLMs in pervaporation processes for the separation of two different VOCs from their dilute aqueous solutions. Initially, an SLM assembled from hexadecane and a porous propylene support was used to separate trichloroethylene from its aqueous solution. Because of the large partition coefficient between hexadecane and trichloroethylene, this SLM exhibited a selectivity as high as 30,000. In another pervaporation process, Qin *et al.* (98) immobilized the porous propylene support with trioctylamine and used it to separate acetic acid from its aqueous solution. Their results showed that the selectivity of the SLM toward acetic acid can reach as high as 33; however, the permeation flux is relatively low due to the low porosity and high tortuosity of the supporting membrane. The trioctylamine and porous propylene SLM was later employed by Thongsukmak *et al.* (99) in a pervaporation process to remove acetone, ethanol and butanol from aqueous mixtures. The selectivities of the SLM for butanol, acetone and ethanol were 275, 220 and 80, respectively, while the permeation fluxes were 11.0, 5.0 and $1.2 \text{ g}\cdot\text{m}^{-2}\cdot\text{h}^{-1}$, respectively. The permeation fluxes increased as much as 5 times when using an ultrathin liquid membrane produced by mixing the trioctylamine with hexane prior to its immobilization (99, 102).

Yu *et al.* (103) introduced a hydrophobic ionic liquid, 1-butyl-3-methylimidazolium hexafluorophosphate (bmim) (PF_6), as a third phase located between an aqueous phase and a plain polydimethylsiloxane (PDMS) membrane in a pervaporation process to remove acetic acid from its aqueous solution. They reported an improvement in selectivity compared to using a plain PDMS membrane and attributed this to the rejection of water molecules in the ionic liquid phase. The results indicated that using the ionic liquid as an extractant prior to pervaporation improved the permeation flux and selectivity of acetic acid.

Izak *et al.* (89) immobilized an ionic liquid of tetrapropylammonium tetracyanoborate ($(\text{C}_3\text{H}_7)_4\text{N})(\text{B}(\text{CN})_4$) in a ceramic nanofiltration module and applied it to the separation of 1,3-propanediol from aqueous solution. The hydrophobicity of the ionic liquid renders the permeation of 1,3-propanediol with a selectivity value as high as 177. In another study, Izak *et al.* (104) prepared mixtures of PDMS with two different ionic liquids (1-ethenyl-3-imidazolium hexafluorophosphate [PDMS-IL1] and tetrapropylammonium tetracyanoborate [PDMS-IL2]) and immobilized the resulting mixtures into a ceramic ultrafiltration membrane. The SLMs were then used to separate butanol from water. Higher permeation flux was observed in the presence of ionic liquid because of the higher diffusion coefficient of butanol in an ionic liquid. In the pervaporation separation of a ternary mixture of butanol, acetone and water, the selectivity of acetone and butanol was increased from 2.3 to 3.2 and from 2.2 to 3.1, respectively, using a PDMS-IL1-based

SLM in comparison with the PDMS membrane. When using the PDMS-IL2-based SLM, the selectivity of acetone increased from 2.3 to 7.9, and the selectivity of butanol increased from 2.2 to 10.9 (105). Due to the higher selectivity exhibited by the PDMS-IL2-based SLM, it was later applied to remove acetone-butanol-ethanol (ABE) from a *Clostridium acetobutylicum* fermentation (106). They reported that the concentration of butanol in the permeate had increased more than 5 times compared to that in the culture vessel, while the other products of the fermentation (ethanol and acetone) were also enriched several times in the permeate. The effective removal of ABE using the SLM pervaporation membrane helped the cells survive lethal butanol concentrations.

The overall pervaporation performances of the SLM are summarized in Table 1 and the data are compared with the literature on the solid pervaporation membranes. SLM exhibited comparative permeation flux and selectivity in separating the organic compound from its dilute aqueous solutions. Moreover, it is noticed that the selectivity of the membrane could be greatly enhanced with the use of SLM.

EFFECT OF OPERATING PARAMETERS

Variations in operating parameters, including feed concentration, downstream pressure and feed temperature, could influence the separation performance of SLMs in pervaporation processes. Hence, an analysis of the influence of different operating parameters is important to understand the separation characteristics of SLMs.

Effect of Feed Concentration

Variation in feed concentration could significantly affect the separation efficiency of SLMs in pervaporation. According to Fick's laws of diffusion, solubility and diffusivity are concentration dependent, where molecules tend to move from regions of high concentration to regions of low concentration. The presence of a concentration gradient across a barrier or SLM induces a driving force for the molecule to move across the membrane. Increasing the concentration of the targeted component in the feed solution would result in a steeper concentration gradient between the feed side and the downstream side, intensifying the mass transfer rate of the targeted component to penetrate through the SLM during pervaporation. Qin et al. (98) observed that both the permeation flux and the concentration of acetic acid in the permeate increased when the feed concentration of acetic acid was increased because the high feed concentration creates a high driving force across the SLM. Similar findings were also reported by Izak et al. (106), who observed that the permeation of butanol increased with its concentration in the culture vessel.

TABLE 1 Summary of the studies on the application of SLMs in pervaporation process and comparison of the pervaporation performance of SLMs with other solid membranes

Supported Liquid Membranes	Solid Membrane	Feed Phase	Permeation flux ($\text{g}\cdot\text{m}^{-2}\cdot\text{h}^{-1}$)	Selectivity	Ref.
Oleyl alcohol supported by microporous polypropylene	–	Butanol/water	–	180	(54)
	Poly(1-trimethylsilyl-1-propyne)	Butanol/water	–	78	(107)
	Polydimethylsiloxane/ceramic	Butanol/water	–	26	(108)
Isotridecanol supported by porous teflon sheet	–	Ethanol/water	39	7.2	(55)
	Polydimethylsiloxane/ polyetherimide	Ethanol/water	–	11.3	(109)
	Polydimethylsiloxane/polysulfone	Ethanol/water	265	6.4	(110)
	Silicalite filled polydimethylsiloxane	Ethanol/water	170	4.8	(111)
Oleyl alcohol supported by microporous polypropylene	–	Diacetyl/water	9	36	(56)
	Polydimethylsiloxane/ Polycarbonate	Diacetyl/water	53	38	(112)
Hexadecane supported by polypropylene	–	Trichloroethylene/water	–	30,000	(59)
	Polyetherimide–polyethersulfone	Trichloroethylene/water	–	5759	(113)
	Cross-linked poly(acrylate-co-acrylic acid)/ polysulfone	Trichloroethylene/water	–	6000	(114)
1-butyl-3-methylimidazolium hexafluorophosphate supported by polydimethylsiloxane	–	Acetic acid/water	–	–	(103)

Trioctylamine supported by polypropylene	–	Acetic acid/water	–	33	(98)
	Silica-filled polydimethylsiloxane Sn-substituted ZSM-5 zeolite	Acetic acid/water	42.09	2.74	(115)
Tetrapropylammonium tetracyanoborate supported by ceramic nanofiltration module	–	Acetic acid/water	490	7.7	(116)
	–	1,3-propanediol/water ^a	3.86	177	(89)
1-ethenyl-3-ethylimidazolium/polydimethylsiloxane supported by ceramic nanofiltration module	–	Butanol/acetone/water	–	3.1 (butanol)	(105)
	–	–	–	3.2 (acetone)	
Tetrapropylammonium tetracyanoborate/polydimethylsiloxane supported by ceramic nanofiltration module	–	Butanol/acetone/water	–	10.9 (butanol)	(105)
	–	–	–	7.9 (acetone)	
Trioctylamine supported by polypropylene	Silicone rubber-coated silicalite	Butanol/acetone/water	16 (butanol)	60 (butanol)	(117)
	–	–	1 (acetone)	10 (acetone)	
Trioctylamine supported by polypropylene	Hydroxyterminated polybutadiene-based polyurethaneurea	Butanol/acetone/water	–	17.6 (butanol)	(118)
	–	–	–	18.9 (acetone)	
Trioctylamine supported by polypropylene	–	Acetone/butanol/ethanol/water	11 (butanol)	275 (butanol)	(99)
	–	–	5 (acetone)	220 (acetone)	
	–	–	1.2 (ethanol)	80 (ethanol)	
Trioctylamine supported by polypropylene	Poly(ether block amide)	Acetone/butanol/ethanol/water	6.60 (butanol)	13.2 (butanol)	(119)
	–	–	1.05 (acetone)	6.5 (acetone)	
Trioctylamine supported by polypropylene	Polydimethylsiloxane/ceramic	Acetone/butanol/ethanol/water	0.73 (ethanol)	4.4 (ethanol)	
			–	16.56 (butanol)	(120)
				27.78 (acetone)	
				7.15 (ethanol)	

^aThe pervaporation separation of 1,3-propanediol/water mixture was unable to compare because it has been scarcely reported in literature.

Effect of Downstream Pressure

Downstream pressure appears to be a critical factor in maintaining the stability of the SLM. The downstream pressure is applied to create the driving force for the transport of a molecule in pervaporation. Lower downstream pressure is used to obtain high selectivity and permeation flux, which is in agreement with Qin et al. (98). They claimed that a lower downstream pressure always leads to a higher permselectivity toward acetic acid. An increase in downstream pressure would decrease the acetic acid permeation flux as well as selectivity.

However, a lower downstream pressure could eventually increase the pressure difference across the SLM, resulting in the loss of immobilized liquid membrane from the supporting membrane (121). Thus, it is important to ensure that the pressure difference across the SLM does not exceed a certain critical value so that the liquid membrane is not pushed out from the pores of the supporting membrane. This critical value, also known as the minimum transmembrane pressure, P_c , can be defined as the minimum pressure required to push the immobilized liquid membrane out of the largest pores. Often, the minimum transmembrane pressure is calculated based on the Laplace equation as shown below (122):

$$P_c = \frac{2\gamma \cos \theta}{r} \quad (4)$$

where γ is the interfacial tension between the feed solution and the SLM, θ is the contact angle between the membrane pores and the immobilized liquid membrane and r is the pore radius.

Effect of Feed Temperature

Feed temperature plays a crucial role in determining the solubility and diffusion properties of a SLM. Qin et al. (98) and Thongsukmak et al. (99, 102) reported that higher permeation flux and selectivity were obtained with elevated temperatures. When subjected to a higher feed temperature, the vapor pressure of the feed solution would increase and induce a higher driving force for pervaporation due to the increased difference between the equilibrium partial pressure on the feed side and the partial pressure on the permeate side.

Higher feed temperatures also help reduce the viscosity of the liquid membrane and the resistance to mass transport in the SLM, promoting greater diffusivity of the targeted component to pass through the SLM (98). Although higher feed temperatures enhance the separation properties of a SLM, the thermal stability of the porous support and the liquid membrane need to be considered when raising the temperature to avoid any degradation or loss of the liquid membrane, especially when using an organic solvent.

STABILITY OF SUPPORTED LIQUID MEMBRANES

Although SLMs have many advantages, insufficient stability has always been an obstacle to its adoption for large-scale applications. This problem is mainly due to the displacement of liquid membrane, which influences both the permeation flux and selectivity. Studies on the stability of SLMs have revealed that the major mechanisms attributed to the displacement of liquid membrane can be accounted for by progressive wetting of the pores in the membrane support by the aqueous phase (122–124), the pressure difference across the membrane (72, 76), dissolution of the liquid membrane in aqueous phase (68, 125), the formation of an emulsion in the liquid membrane (69, 126) and the blockage of membrane pores by precipitation of the carrier complex (127).

A number of attempts have been made to improve SLM stability. Qin et al. (98) developed an on-line re-immobilizing technique by periodically injecting fresh liquid membrane from the shell side. Unlike the conventional two-exit hollow fiber module, they fabricated a three shell exit module in their study. The third exit, which was placed in the middle of the shell, was occasionally used to re-immobilize the liquid membrane in the porous support material, but was mostly used as an exit for permeate. This technique was shown to stabilize the operational performance of the SLM. However, a decrease in permeation flux and selectivity was observed after 500 hours of operation as a result of the gradual change in the properties of the supporting membrane. This degradation may also be due to the loss of liquid membrane through evaporation and solubilization to the feed solution during operation.

Instead of compensating for the loss of liquid membrane through periodic re-immobilization, proactive steps have been taken to prevent the loss of liquid membrane via surface coating. An ultrathin, plasma-polymerized coating of nonporous silicone on the outside diameter of the hollow fiber was suggested by Qin et al. (59). The nonporous silicone coating was hypothesized to extend the SLM lifetime by dramatically reducing vaporization loss on the permeate side of the SLM without offering any high, additional resistance to mass transport. This coating made the SLM behave like a polymer membrane and protected it from sudden trans-membrane variation. The stability test on the performance of this SLM indicated a 30% decrease in both permeation flux and selectivity when operated for 4 months. Alternatively, Thongsukmak et al. (99) coated the porous hollow fiber substrate with nanoporous fluorosilicone. The nanoporous coating on the SLM demonstrated excellent stability performance over 300 hours without the need to re-immobilize the liquid membrane and prevented the loss of liquid membrane to the feed aqueous solution.

Use of a polymer inclusion membrane is another way to stabilize the SLM (77, 128). This membrane is usually formed as a thin, stable film

by casting a viscous mixture solution composed of a liquid membrane, a plasticizer and a base polymer such as cellulose triacetate and poly(vinyl chloride) (129). This integrated supporting membrane is considerably more stable compared to the conventional SLM system where the liquid membrane is held in the porous support. The polymer inclusion membrane has been shown to prolong the lifetime of SLMs under continuous operation without any displacement of the liquid membrane (130, 131). The separation efficiency of the polymer inclusion membrane increased with the content of the liquid membrane (77, 132).

The stability of the SLM can also be improved via gelation of the liquid membrane (121, 133, 134). Through the formation of a gel liquid membrane, the high viscosity of this solid-like membrane prevents the liquid membrane from being displaced from the porous support. Gelled SLMs can be prepared by immobilizing the gelled liquid membrane in the pores of the supporting membrane or by coating a thin, dense layer on the surface of the supporting membrane. In addition to good mechanical stability, the gelled liquid membrane does not create the mass transfer resistance found with solid membranes and has transport properties similar to that of the liquid phase (134).

CARBON NANOTUBES IN SUPPORTED LIQUID MEMBRANES

As reported by Iijima (135) and Bethune *et al.* (136), CNTs are seamless macromolecules with a radius from a few nanometers up to several micrometers in length. The walls of CNTs are constructed by a hexagonal lattice of carbon atoms, with ends that are usually capped by a fullerene structure. CNTs possess high flexibility, low mass density and a large aspect ratio (137, 138). The excellent mechanical, chemical and thermal properties supplied by their unique structure make them attractive for use in SLMs.

Since the early development of CNTs, they have been widely used as a reinforcing agent in polymer matrices to form a new class of membranes, namely, nanocomposite membranes. Upon the incorporation of CNTs, nanocomposite membranes are found to enhance the properties of a polymer matrix, including its mechanical, chemical and thermal stability (139), and extend the lifetime of the membrane. These enhanced properties enable nanocomposite membranes to replace conventional polymeric or inorganic membranes and serve as the supporting membrane for SLMs. Using a nanocomposite supporting membrane would increase the robustness of the resulting SLM and allow it to operate in a harsh environment. Often, the nanocomposite supporting membrane can be prepared through a phase inversion process (140–143), which involves the preparation of suspended CNTs in a polymer solution (CNTs/polymer) followed by casting of the solution on a glass plate.

Subsequently, the casting solution is immersed into a nonsolvent to allow for precipitation through the exchange of the solvent and nonsolvent, and a thin film porous membrane is formed. The stability of the nanocomposite SLM could be affected by the CNT content because this controls the porosity and pore size of the nanocomposite supporting membrane. Morphological studies on the nanocomposite membrane reported that an increase in CNT content may reduce the pore size of the nanocomposite supporting membrane (142–144) due to the increased viscosity of the CNTs/polymer solution resulting from an increase in CNT content. The increased viscosity can suppress the overall diffusion between components in the phase inversion system by delaying the exchange of solvent and non-solvent (145), slowing down the precipitation rate and restraining the formation of larger pores.

The use of CNTs also permits endohedral functionalization, where the inner cavity of CNTs offers space for storage of the liquid membrane (146,147). Chen et al. (148) demonstrated the immobilization of an ionic liquid, (bmim)(PF₆), in the inner cavity of CNTs. Continuously impregnated tubes observed in HRTEM images indicates the encapsulation of (bmim) (PF₆) in the hollow interior of CNTs. The small inner core diameter provided by the CNTs could minimize the possibility for displacement of the liquid membrane, which increases the surface area of the immobilized liquid membrane.

The use of CNTs has the potential to become a new trend in the design of SLMs. In addition to enhancing the properties of the supporting membrane, the use of CNT can improve the stability of the SLM. Unfortunately, to our knowledge, there have been few, if any, studies involving the use of CNTs in SLMs.

COMMERCIAL VALUE AND ECONOMIC ASPECTS OF SLMs

To date, SLMs are not a commercially viable technology. However, their potential in industrial applications is apparent. As previously mentioned, the high molecular diffusion in the liquid phase enables the separation of the targeted component in an SLM with a small volume of liquid membrane. This advantage makes it appealing for industrial applications in which a high efficiency separation method is necessary. The ability of SLMs to be designed and operated in a hollow fiber module fulfills the requirement for industrial use by providing a high surface area to volume ratio and promoting mass transfer. In addition, hollow fiber SLMs can be easily scaled up to a larger capacity. The materials needed for the fabrication of SLMs for industrial purposes are readily available. For instance, the hollow fiber membrane contactor is commercially available with an area up to 220 m² (61). Furthermore, the improved stability shown in SLMs through modification strategies, including surface coating or gelation, certainly increases its commercial value.

From an economic perspective, the major concern when using SLMs is the capital cost. Although the use of an ionic liquid as the liquid membrane in SLMs might not be cost effective due to the high cost of ionic liquids, the small volume required for highly efficient separation could eventually offset its capital cost. There is also the potential to integrate SLMs in a hybrid process, which is often considered an effective way to reduce energy consumption and capital cost. Previous studies reported (99, 106) the ability of SLMs to separate solvents such as acetone, butanol and ethanol present in fermentation broth and showed the potential of integrating the SLM into the fermentation broth. This hybrid process allows the production and separation of solvents to occur simultaneously, thereby enabling mass production of solvent and increasing the gross revenue from production.

CONCLUSION

SLMs are one of the configurations of liquid membranes that offer better stability compared to bulk and emulsion liquid membranes. Its advantage in providing greater molecular diffusion makes it attractive as a pervaporation membrane. However, SLMs can operate in a pervaporation process only if the liquid membrane possesses a lower vapor pressure and the partial pressure of the targeted component is high enough to create a separation driving force. Previous studies on the application of SLMs in pervaporation processes have shown the ability of SLMs to separate the volatile fermentation product and VOCs from their dilute aqueous solution. Similar to conventional pervaporation, variation in operating parameters, including feed concentration, downstream pressure and feed temperature, can eventually change the separation characteristics of the SLM.

Although the use of SLMs in pervaporation processes offers many advantages, its insufficient stability is often a major obstacle that prevents their use in large-scale applications. A number of stability studies on SLMs have proposed several approaches to overcome this limitation, such as continuous re-immobilization of the liquid membrane, surface coating, and gelation. In addition, the use of CNTs is believed to enhance SLM stability through its unique structure and smaller inner core diameter. Based on the advantages offered by SLMs, there is no doubt that they possess great commercial value even though they have not yet been applied in industrial activities.

ACKNOWLEDGMENTS

The authors acknowledge fellowship support from the MyPhD program of the Ministry of Higher Education, Malaysia, and the USM. This research was also financially supported by a Universiti Sains Malaysia Research University

(RU) grant, a USM Membrane Cluster Grant and a Fundamental of Research Grant Scheme (FRGS).

REFERENCES

1. Kober, P.A. (1917) Pervaporation, perstillation and percrystallization *J. Am. Chem. Soc.*, 39: 944–948.
2. Quiñones-Bolaños, E., Zhou, H., and Parkin, G. (2005) Membrane pervaporation for wastewater reuse in microirrigation. *J. Environ. Eng.*, 131: 1633–1643.
3. Kurkuri, M.D. and Aminabhavi, T.M. (2003) Pervaporation separation of water and dioxane mixtures with sodium alginate-g-polyacrylamide copolymeric membranes. *J. Appl. Polym. Sci.*, 89: 300–305.
4. Sridhar, S., Smitha, B., Madhavi Latha, U.S., and Ramakrishna, M. (2004) Pervaporation of 1,4-Dioxane/water mixtures using poly(vinyl alcohol) membranes crosslinked with Toluylene-2,4-diisocyanate. *J. Polym. Mater.*, 21: 181–188.
5. Smitha, B., Suhanya, D., Sridhar, S., and Ramakrishna, M. (2004) Separation of organic-organic mixtures by pervaporation – A review. *J. Membr. Sci.*, 241: 1–21.
6. Garcia Villaluenga, J. P. and Tabe-Mohammadi, A. (2000) A review on the separation of benzene/cyclohexane mixtures by pervaporation processes. *J. Membr. Sci.*, 169: 159–174.
7. Feng, X. and Huang, R. Y. M. (1997) Liquid separation by membrane pervaporation: A review. *Ind. Eng. Chem. Res.*, 36: 1048–1066.
8. Shao, P. and Huang, R.Y.M. (2007) Polymeric membrane pervaporation. *J. Membr. Sci.*, 287: 162–179.
9. Xiao, S., Huang, R.Y.M., and Feng, X. (2006) Preparation and properties of trimesoyl chloride crosslinked poly(vinyl alcohol) membranes for pervaporation dehydration of isopropanol. *J. Membr. Sci.*, 286: 245–254.
10. Teli, S.B., Gokavi, G.S., Sairam, M., and Aminabhavi, T.M. (2007) Mixed matrix membranes of poly(vinyl alcohol) loaded with phosphomolybdic heteropoly-acid for the pervaporation separation of water-isopropanol mixtures. *Coll. Surf. A: Physicochem. Eng. Asp.*, 301: 55–62.
11. Singha, N.R., Parya, T.K., and Ray, S.K. (2009) Dehydration of 1,4-dioxane by pervaporation using filled and crosslinked polyvinyl alcohol membrane. *J. Membr. Sci.*, 340: 35–44.
12. Mali, M.G., Magalad, V.T., Gokavi, G.S., Aminabhavi, T.M., and Raju, K.V.S.N. (2011) Pervaporation separation of isopropanol-water mixtures using mixed matrix blend membranes of poly(vinyl alcohol)/poly(vinyl pyrrolidone) loaded with phosphomolybdic acid. *J. Appl. Polym. Sci.*, 121: 711–719.
13. Yuan, H.K., Ren, J., Ma, X.H., and Xu, Z. L. (2011) Dehydration of ethyl acetate aqueous solution by pervaporation using PVA/PAN hollow fiber composite membrane. *Desalination*, 280: 252–258.

14. Srinivasan, K., Palanivelu, K., and Navaneetha Gopalakrishnan, A. (2007) Recovery of 1-butanol from a model pharmaceutical aqueous waste by pervaporation. *Chem. Eng. Sci.*, 62: 2905–2914.
15. Jian, K. and Pintauro, P.N. (1997) Asymmetric PVDF hollow-fiber membranes for organic/water pervaporation separations. *J. Membr. Sci.*, 135: 41–53.
16. She, M. and Hwang, S.T. (2004) Concentration of dilute flavor compounds by pervaporation: Permeate pressure effect and boundary layer resistance modeling. *J. Membr. Sci.*, 236: 193–202.
17. Zhan, X., Li, J., Huang, J., and Chen, C. (2010) Enhanced pervaporation performance of multi-layer PDMS/PVDF composite membrane for ethanol recovery from aqueous solution. *Appl. Biochem. Biotechnol.*, 160: 632–642.
18. Ong, Y.K., Widjojo, N., and Chung, T.S. (2011) Fundamentals of semi-crystalline poly(vinylidene fluoride) membrane formation and its prospects for bio-fuel (ethanol and acetone) separation via pervaporation. *J. Membr. Sci.*, 378: 149–162.
19. Jian, K. and Pintauro, P.N. (1993) Integral asymmetric poly (vinylidene fluoride) (PVDF) pervaporation membranes. *J. Membr. Sci.*, 85: 301–309.
20. Chen, S.H., Liou, R.M., Lin, Y.Y., Lai, C.L., and Lai, J.Y. (2009) Preparation and characterizations of asymmetric sulfonated polysulfone membranes by wet phase inversion method. *Eur. Polym. J.*, 45: 1293–1301.
21. Chen, S.H., Liou, R.M., Shih, C.Y., Lai, C.L., and Lai, J.Y. (2007) Pervaporation separation of water/ethanol mixture using asymmetric ion-exchange membranes containing aluminum ions. *J. Appl. Polym. Sci.*, 106: 1412–1420.
22. Lai, C.L., Liou, R.M., Chen, S.H., Shih, C.Y., Chang, J.S., Huang, C.H., Hung, M.Y. and Lee, K.R. (2011) Dehydration of ethanol/water mixture by asymmetric ion-exchange membranes. *Desalination*, 266: 17–24.
23. Mao, Z., Jie, X., Cao, Y., Wang, L., Li, M., and Yuan, Q. (2011) Preparation of dual-layer cellulose/polysulfone hollow fiber membrane and its performance for isopropanol dehydration and CO₂ separation. *Sep. Purif. Technol.*, 77: 179–184.
24. Aliabadi, M., Aroujalian, A., and Raisi, A. (2011) Pervaporative removal of acrylonitrile from aqueous streams through polydimethylsiloxane membrane. *Water Sci. Technol.*, 63: 2820–2826.
25. Garg, P., Singh, R.P., Pandey, L.K., and Choudhary, V. (2010) Pervaporative studies using polyimide-filled PDMS membrane. *J. Appl. Polym. Sci.*, 115: 1967–1974.
26. Rutkiewicz, I., Kujawski, W., and Namiesnik, J. (2010) Pervaporation of volatile organohalogen compounds through polydimethylsiloxane membrane. *Desalination*, 264: 160–164.
27. Salehi Shahrabi, S., Mortaheb, H.R., Barzin, J., and Ehsani, M.R. (2012) Pervaporative performance of a PDMS/blended PES composite membrane for removal of toluene from water. *Desalination*, 287: 281–289.
28. Tanaka, S., Chao, Y., Araki, S., and Miyake, Y. (2010) Pervaporation characteristics of pore-filling PDMS/PMHS membranes for recovery of ethylacetate from aqueous solution. *J. Membr. Sci.*, 348: 383–388.
29. Zhang, Q.G., Fan, B.C., Liu, Q.L., Zhu, A.M., and Shi, F.F. (2011) A novel poly(dimethyl siloxane)/poly(oligosilsesquioxanes) composite membrane for pervaporation desulfurization. *J. Membr. Sci.*, 366: 335–341.

30. Anjali Devi, D., Smitha, B., Sridhar, S., and Aminabhavi, T.M. (2006) Novel crosslinked chitosan/poly(vinylpyrrolidone) blend membranes for dehydrating tetrahydrofuran by the pervaporation technique. *J. Membr. Sci.*, 280: 45–53.
31. Ageev, E.P., Matushkina, N.N., and Vikhoreva, G.A. (2007) Pervaporation properties of thermally modified chitosan films. *Coll. J.*, 69: 272–277.
32. Veerapur, R.S., Gudasi, K.B., and Aminabhavi, T.M. (2007) Pervaporation dehydration of isopropanol using blend membranes of chitosan and hydroxypropyl cellulose. *J. Membr. Sci.*, 304: 102–111.
33. Teli, S.B., Gokavi, G.S., Tak, T.M., and Aminabhavi, T.M. (2009) Chitosan/Gelatin blend membranes for pervaporation dehydration of 1,4-dioxane. *Separ. Sci. Technol.*, 44: 3202–3223.
34. Sommer, S. and Melin, T. (2005) Influence of operation parameters on the separation of mixtures by pervaporation and vapor permeation with inorganic membranes. Part 1: Dehydration of solvents. *Chem. Eng. Sci.*, 60: 4509–4523.
35. Asaeda, M., Ishida, M., and Waki, T. (2005) Pervaporation of aqueous organic acid solutions by porous ceramic membranes. *J. Chem. Eng. Jpn.*, 38: 336–343.
36. Asaeda, M., Sakou, Y., Yang, J., and Shimasaki, K. (2002) Stability and performance of porous silica-zirconia composite membranes for pervaporation of aqueous organic solutions. *J. Membr. Sci.*, 209: 163–175.
37. Wee, S.L., Tye, C.T., and Bhatia, S. (2010) Process optimization studies for the dehydration of alcohol-water system by inorganic membrane based pervaporation separation using design of experiments (DOE). *Sep. Purif. Technol.*, 71: 192–199.
38. Wee, S.-L., Tye, C.-T., and Bhatia, S. (2008) Membrane separation process—Pervaporation through zeolite membrane. *Sep. Purif. Technol.*, 63: 500–516.
39. Ismail, A.F., Goh, P.S., Sanip, S.M., and Aziz, M. (2009) Transport and separation properties of carbon nanotube-mixed matrix membrane. *Sep. Purif. Technol.*, 70: 12–26.
40. Shirazi, Y., Tofighy, M.A., and Mohammadi, T. (2011) Synthesis and characterization of carbon nanotubes/poly vinyl alcohol nanocomposite membranes for dehydration of isopropanol. *J. Membr. Sci.*, 378: 551–561.
41. Xia, S., Wei, W., Liu, G., Dong, X., and Jin, W. (2012) Pervaporation properties of polyvinyl alcohol/ceramic composite membrane for separation of ethyl acetate/ethanol/water ternary mixtures. *Kor. J. Chem. Eng.*, 29: 228–234.
42. Ong, Y.T., Ahmad, A.L., Zein, S.H.S., Sudesh, K., and Tan, S.H. (2011) Poly(3-hydroxybutyrate)-functionalised multi-walled carbon nanotubes/chitosan green nanocomposite membranes and their application in pervaporation. *Sep. Purif. Technol.*, 76: 419–427.
43. Vladimir, K. (2010) *Liquid Membranes: Principles and Applications in Chemical Separations and Wastewater Treatment*; Elsevier: Amsterdam.
44. Román, S.M.F., Bringas, E., Ibañez, R., and Ortiz, I. (2010) Liquid membrane technology: Fundamentals and review of its applications. *J. Chem. Technol. Biotechnol.*, 85: 2–10.
45. Kentish, S.E. and Stevens, G.W. (2001) Innovations in separations technology for the recycling and re-use of liquid waste streams. *Chem. Eng. J.*, 84: 149–159.
46. Scholander, P.F. (1960) Oxygen transport through hemoglobin solutions. *Science*, 131: 585–590.

47. Dzygiel, P. and Wieczorek, P.P. (2010) Supported liquid membranes and their modifications: definition, classification, theory, stability, application and perspectives. In *Liquid Membranes*; Vladimir, S.K., ed.; Elsevier: Amsterdam.
48. Scovazzo, P., Kieft, J., Finan, D. A., Koval, C., DuBois, D., and Noble, R. (2004) Gas separations using non-hexafluorophosphate (PF₆)⁻ anion supported ionic liquid membranes. *J. Membr. Sci.*, 238: 57–63.
49. de los Ríos, A.P., Hernández-Fernández, F.J., Rubio, M., Tomás-Alonso, F., Gómez, D., and Villora, G. (2008) Prediction of the selectivity in the recovery of transesterification reaction products using supported liquid membranes based on ionic liquids. *J. Membr. Sci.*, 307: 225–232.
50. Wang, B., Lin, J., Wu, F., and Peng, Y. (2008) Stability and selectivity of supported liquid membranes with ionic liquids for the separation of organic liquids by vapor permeation. *Ind. Eng. Chem. Res.*, 47: 8355–8360.
51. Fortunato, R., González-Muñoz, M.J., Kubasiewicz, M., Luque, S., Alvarez, J.R., Afonso, C.A.M., Coelho, I.M., and Crespo, J. G. (2005) Liquid membranes using ionic liquids: The influence of water on solute transport. *J. Membr. Sci.*, 249: 153–162.
52. Zhang, B., Gozzelino, G., and Baldi, G. (2001) Membrane liquid loss of supported liquid membrane based on n-decanol. *Coll. Surf. A-Physicochem. Eng. Asp.*, 193: 61–70.
53. Hernandez-Fernandez, F.J., de los Ríos, A.P., Tomás-Alonso, F., Palacios, J.M., and Villora, G. (2009) Preparation of supported ionic liquid membranes: Influence of the ionic liquid immobilization method on their operational stability. *J. Membr. Sci.*, 341: 172–177.
54. Matsumura, M., Kataoka, H., Sueki, M., and Araki, K. (1988) Energy saving effect of pervaporation using oleyl alcohol liquid membrane in butanol purification. *Bioprocess. Eng.*, 3: 93–100.
55. Christen, P., Minier, M., and Renon, H. (1990) Ethanol extraction by supported liquid membrane during fermentation. *Biotechnol. Bioeng.*, 36: 116–123.
56. Ishii, N., Matsumura, M., Kataoka, H., Tanaka, H., and Araki, K. (1995) Diacetyl fermentation coupled with pervaporation using oleyl alcohol supported liquid membrane. *Bioprocess. Eng.*, 13: 119–123.
57. Liley, P.E., Reid, R.C., and Buck, E. (1984) *Physical and Chemical Data*; McGraw-Hill Book Co.: Singapore.
58. Lyman, W.J., Reehl, W.F., and Rosenblatt, D.H. (1982) *Handbook of Chemical Property Estimation Methods*; McGraw-Hill: New York.
59. Qin, Y., Sheth, J.P., and Sirkar, K.K. (2002) Supported liquid membrane-based pervaporation for VOC removal from water. *Ind. Eng. Chem. Res.*, 41: 3413–3428.
60. Izák, P., Köckerling, M., and Kragl, U. (2006) Solute transport from aqueous mixture through supported ionic liquid membrane by pervaporation. *Desalination*, 199: 96–98.
61. Kocherginsky, N.M., Yang, Q., and Seelam, L. (2007) Recent advances in supported liquid membrane technology. *Sep. Purif. Technol.*, 53: 171–177.
62. De Gyves, J. and De San Miguel, E.R. (1999) Metal ion separations by supported liquid membranes. *Ind. Eng. Chem. Res.*, 38: 2182–2202.

63. Yang, X.J., Fane, A.G., and Soldenhoff, K. (2003) Comparison of liquid membrane processes for metal separations: Permeability, stability, and selectivity. *Ind. Eng. Chem. Res.*, 42: 392–403.
64. Binning, R.C., Lee, R.J., Jennings, J.F., and Martin, E.C. (1958) Separation of liquid mixtures by permeation. *Preprints*, 3: 131–141.
65. Sastre, A.M., Kumar, A., Shukla, J.P., and Singh, R.K. (1998) Improved techniques in liquid membrane separations: An overview. *Sep. Purif. Meth.*, 27: 213–298.
66. Hernández-Fernández, F.J., de los Ríos, A.P., Tomás-Alonso, F., Palacios, J.M., and Vllora, G. (2011) Understanding the influence of the ionic liquid composition and the surrounding phase nature on the stability of supported ionic liquid membranes. *AIChE J.*, 58: 583–590.
67. Fortunato, R., Afonso, C.A.M., Reis, M.A.M., and Crespo, J.G. (2004) Supported liquid membranes using ionic liquids: Study of stability and transport mechanisms. *J. Membr. Sci.*, 242: 197–209.
68. Takeuchi, H., Takahashi, K., and Goto, W. (1987) Some observations on the stability of supported liquid membranes. *J. Membr. Sci.*, 34: 19–31.
69. Zha, F.F., Fane, A.G., and Fell, C.J.D. (1995) Effect of surface tension gradients on stability of supported liquid membranes. *J. Membr. Sci.*, 107:75–86.
70. Matson, S.L., Herrick, C.S., and Ward Iii, W.J. (1977) Progress on the selective removal of H₂S from gasified coal using an immobilized liquid membrane. *Ind. Eng. Chem. Proc. Des. Devel.*, 16: 370–374.
71. Malik, M.A., Hashim, M.A., and Nabi, F. (2011) Ionic liquids in supported liquid membrane technology. *Chem. Eng. J.*, 171: 242–254.
72. Ríos, A.P. d.l., Hernández-Fernández, F.J., Tomás-Alonso, F., Palacios, J.M., Gómez, D., Rubio, M., and Vllora, G. (2007) A SEM-EDX study of highly stable supported liquid membranes based on ionic liquids. *J. Membr. Sci.*, 300: 88–94.
73. Fortunato, R., Afonso, C.A.M., Benavente, J., Rodriguez-Castellón, E., and Crespo, J.G. (2005) Stability of supported ionic liquid membranes as studied by X-ray photoelectron spectroscopy. *J. Membr. Sci.*, 256: 216–223.
74. Haerens, K., Van Deuren, S., Matthijs, E., and Van Der Bruggen, B. (2010) Challenges for recycling ionic liquids by using pressure driven membrane processes. *Green Chem.*, 12: 2182–2188.
75. Dupont, J., De Souza, R.F., and Suarez, P.A.Z. (2002) Ionic liquid (molten salt) phase organometallic catalysis. *Chem. Rev.*, 102: 3667–3692.
76. Holbrey, J. D., and Seddon, K. R. (1999) The phase behaviour of 1-alkyl-3-methylimidazolium tetrafluoroborates; ionic liquids and ionic liquid crystals. *J. Chem. Soc., Dalton Trans.*, 2133–2139.
77. Kohoutová, M., Sikora, A., Hovorka, S., Randová, A., Schauer, J., Tišma, M., Setnicková, K., Petrickovic, R., Guernik, S., Greenspoon, N., and Izák, P. (2009) Influence of ionic liquid content on properties of dense polymer membranes. *Eur. Polym. J.*, 45: 813–819.
78. Noble, R.D. and Gin, D.L. (2011) Perspective on ionic liquids and ionic liquid membranes. *J. Membr. Sci.*, 369: 1–4.
79. Marciniak, A. (2010) Influence of cation and anion structure of the ionic liquid on extraction processes based on activity coefficients at infinite dilution. A review. *Fluid Phase Equilib.*, 294: 213–233.

80. Baker, G.A., Baker, S.N., Pandey, S., and Bright, F.V. (2005) An analytical view of ionic liquids. *Analyst*, 130: 800–808.
81. Brennecke, J.F. and Maginn, E.J. (2001) Ionic liquids: Innovative fluids for chemical processing. *AIChE J.*, 47: 2384–2389.
82. Carlisle, T.K., Bara, J.E., Gabriel, C.J., Noble, R.D., and Gin, D.L. (2008) Interpretation of CO₂ solubility and selectivity in nitrile-functionalized room-temperature ionic liquids using a group contribution approach. *Ind. Eng. Chem. Res.*, 47: 7005–7012.
83. Huang, R.Y.M. (1990) *Pervaporation Membrane Separation Processes*; Elsevier: Amsterdam.
84. Kislik, V.S. (2010) Introduction, General description, definitions, and classification. Overview. In *Liquid Membranes*; Kislik, V.S., ed.; Elsevier, Amsterdam.
85. Way, J.D., Noble, R.D., and Bateman, B.R. (1985) Selection of supports for immobilized liquid membranes. *ACS Symp. Ser.*, 269: 119–128.
86. de Bruijn, F.T., Sun, L., Olujic, Z., Jansens, P.J., and Kapteijn, F. (2003) Influence of the support layer on the flux limitation in pervaporation. *J. Membr. Sci.*, 223: 141–156.
87. Matson, S.L., Lopez, J., and Quinn, J.A. (1983) Separation of gases with synthetic membranes. *Chem. Eng. Sci.*, 38: 503–524.
88. Gan, Q., Rooney, D., Xue, M., Thompson, G., and Zou, Y. (2006) An experimental study of gas transport and separation properties of ionic liquids supported on nanofiltration membranes. *J. Membr. Sci.*, 280: 948–956.
89. Izák, P., Köckerling, M., and Kragl, U. (2006) Stability and selectivity of a multiphase membrane, consisting of dimethylpolysiloxane on an ionic liquid, used in the separation of solutes from aqueous mixtures by pervaporation. *Green Chem.*, 8: 947–948.
90. Strathmann, H., Giorno, L., and Drioli, E. (2010) Basic aspects in polymeric membrane preparation. *Comprehensive Membrane Science and Engineering*; Drioli, E., and Giorno, L., eds.; Elsevier: Oxford, UK.
91. Shen, L. and Chen, Z. (2007) Critical review of the impact of tortuosity on diffusion. *Chem. Eng. Sci.*, 62: 3748–3755.
92. Choudhari, S.K. and Kariduraganavar, M.Y. (2009) Development of novel composite membranes using quaternized chitosan and Na⁺-MMT clay for the pervaporation dehydration of isopropanol. *J. Coll. Interf. Sci.*, 338: 111–120.
93. Wang, Y.-C., Fan, S.-C., Lee, K.-R., Li, C.-L., Huang, S.-H., Tsai, H.-A., and Lai, J.-Y. (2004) Polyamide/SDS-clay hybrid nanocomposite membrane application to water-ethanol mixture pervaporation separation. *J. Membr. Sci.*, 239: 219–226.
94. Chaiko, D.J. and Osseo-Asare, K. (1982) Characterization of liquid membrane supports. *Sep. Sci. Technol.*, 17: 1659–1679.
95. Hernández-Fernández, F.J., de los Ríos, A.P., Rubio, M., Tomás-Alonso, F., Gómez, D., and Vílora, G. (2007) A novel application of supported liquid membranes based on ionic liquids to the selective simultaneous separation of the substrates and products of a transesterification reaction. *J. Membr. Sci.*, 293: 73–80.
96. Matsumoto, M., Ueba, K., and Kondo, K. (2009) Vapor permeation of hydrocarbons through supported liquid membranes based on ionic liquids. *Desalination*, 241: 365–371.

97. Kouki, N., Tayeb, R., Zarrougui, R., and Dhahbi, M. (2010) Transport of salicylic acid through supported liquid membrane based on ionic liquids. *Sep. Purif. Technol.*, 76: 8–14.
98. Qin, Y., Sheth, J.P., and Sirkar, K.K. (2003) Pervaporation membranes that are highly selective for acetic acid over water. *Ind. Eng. Chem. Res.*, 42: 582–595.
99. Thongsukmak, A. and Sirkar, K.K. (2007) Pervaporation membranes highly selective for solvents present in fermentation broths. *J. Membr. Sci.*, 302: 45–58.
100. Duan, S., Ito, A., and Ohkawa, A. (2003) Separation of propylene/propane mixture by a supported liquid membrane containing triethylene glycol and a silver salt. *J. Membr. Sci.*, 215: 53–60.
101. Zhang, L.Z. (2006) Effects of membrane parameters on performance of vapor permeation through a composite supported liquid membrane. *Sep. Sci. Technol.*, 41: 3517–3538.
102. Thongsukmak, A. and Sirkar, K. K. (2009) Extractive pervaporation to separate ethanol from its dilute aqueous solutions characteristic of ethanol-producing fermentation processes. *J. Membr. Sci.*, 329: 119–129.
103. Yu, J., Li, H., and Liu, H. (2006) Recovery of acetic acid over water by pervaporation with a combination of hydrophobic ionic liquids. *Chem. Eng. Commun.*, 193: 1422–1430.
104. Izák, P., Friess, K., Hynek, V., Ruth, W., Fei, Z., Dyson, J.P., and Kragl, U. (2009) Separation properties of supported ionic liquid-polydimethylsiloxane membrane in pervaporation process. *Desalination*, 241: 182–187.
105. Izák, P., Ruth, W., Fei, Z., Dyson, P.J., and Kragl, U. (2008) Selective removal of acetone and butan-1-ol from water with supported ionic liquid-polydimethylsiloxane membrane by pervaporation. *Chem. Eng. J.*, 139: 318–321.
106. Izák, P., Schwarz, K., Ruth, W., Bahl, H., and Kragl, U. (2008) Increased productivity of *Clostridium acetobutylicum* fermentation of acetone, butanol, and ethanol by pervaporation through supported ionic liquid membrane. *Appl. Microbiol. Biotechnol.*, 78: 597–602.
107. Fadeev, A.G., Selinskaya, Y.A., Kelley, S.S., Meagher, M.M., Litvinova, E.G., Khotimsky, V.S., and Volkov, V.V. (2001) Extraction of butanol from aqueous solutions by pervaporation through poly(1-trimethylsilyl-1-propyne). *J. Membr. Sci.*, 186: 205–217.
108. Liu, G., Hou, D., Wei, W., Xiangli, F., and Jin, W. (2011) Pervaporation separation of butanol-water mixtures using polydimethylsiloxane/ceramic composite membrane. *Chin. J. Chem. Eng.*, 19: 40–44.
109. Lee, H.J., Cho, E.J., Kim, Y.G., Choi, I.S., and Bae, H.J. (2012) Pervaporative separation of bioethanol using a polydimethylsiloxane/polyetherimide composite hollow-fiber membrane. *Bioresource Technology*, 109: 110–115.
110. Guo, J., Zhang, G., Wu, W., Ji, S., Qin, Z., and Liu, Z. (2010) Dynamically formed inner skin hollow fiber polydimethylsiloxane/polysulfone composite membrane for alcohol permselective pervaporation. *Chem. Eng. J.*, 158: 558–565.
111. Dobrak, A., Figoli, A., Chovau, S., Galiano, F., Simone, S., Vankelecom, I.F.J., Drioli, E., and Van der Bruggen, B. (2010) Performance of PDMS membranes in

- pervaporation: Effect of silicalite fillers and comparison with SBS membranes. *J. Coll. Interf. Sci.*, 346: 254–264.
112. Rajagopalan, N., Cheryan, M., and Matsuura, T. (1994) Recovery of diacetyl by pervaporation. *Biotechnol. Tech.*, 8: 869–872.
 113. Zhao, W. and Shi, B. (2009) Removal of volatile organic compounds from water by pervaporation using polyetherimide- polyethersulfone blend hollow fiber membranes. *Sep. Sci. Technol.*, 44: 1737–1752.
 114. Wu, Y., Wang, S., Jin, M., and Yang, X. (2001) Poly(acrylate-co-acrylic acid)/polysulfone composite membranes for pervaporation of volatile organic compounds from water. *Sep. Sci. Technol.*, 36: 3529–3540.
 115. Hong, H., Chen, L., Zhang, Q., and Zhang, Z. (2011) Acetic acid/water separation by pervaporation with silica filled PDMS membrane. *Polym. Eng. Sci.*, 51: 819–825.
 116. Sun, W., Wang, X., Yang, J., Lu, J., Han, H., Zhang, Y., and Wang, J. (2009) Pervaporation separation of acetic acid-water mixtures through Sn-substituted ZSM-5 zeolite membranes. *J. Membr. Sci.*, 335: 83–88.
 117. Ikegami, T., Negishi, H., and Sakaki, K. (2011) Selective separation of n-butanol from aqueous solutions by pervaporation using silicone rubber-coated silicalite membranes. *J. Chem. Technol. Biotechnol.*, 86: 845–851.
 118. Tong, C., Bai, Y., Wu, J., Zhang, L., Yang, L., and Qian, J. (2010) Pervaporation recovery of acetone-butanol from aqueous solution and fermentation broth using HTPB-based polyurethaneurea membranes. *Sep. Sci. Technol.*, 45: 751–761.
 119. Liu, F., Liu, L., and Feng, X. (2005) Separation of acetone-butanol-ethanol (ABE) from dilute aqueous solutions by pervaporation. *Sep. Purif. Technol.*, 42: 273–282.
 120. Wu, H., Chen, X.P., Liu, G.P., Jiang, M., Guo, T., Jin, W.Q., Wei, P., and Zhu, D.W. (2012) Acetone-butanol-ethanol (ABE) fermentation using *Clostridium acetobutylicum* XY16 and in situ recovery by PDMS/ceramic composite membrane. *Bioproc. Biosyst. Eng.*, 35: 1057–1065.
 121. Neplenbroek, A.M., Bargeman, D., and Smolders, C.A. (1992) Supported liquid membranes: Instability effects. *J. Membr. Sci.*, 67: 121–132.
 122. Zha, F.F., Fane, A.G., and Fell, C.J.D. (1995) Instability mechanisms of supported liquid membranes in phenol transport process. *J. Membr. Sci.*, 107: 59–74.
 123. Danesi, P.R. (1984) Separation of metal species by supported liquid membranes. *Sep. Sci. Technol.*, 19: 857–894.
 124. Takeuchi, H. and Nakano, M. (1989) Progressive wetting of supported liquid membranes by aqueous solutions. *J. Membr. Sci.*, 42: 183–188.
 125. Danesi, P.R., Reichley-Yinger, L., and Rickert, P.G. (1987) Lifetime of supported liquid membranes: the influence of interfacial properties, chemical composition and water transport on the long-term stability of the membranes. *J. Membr. Sci.*, 31: 117–145.
 126. Neplenbroek, A.M., Bargeman, D., and Smolders, C.A. (1992) Mechanism of supported liquid membrane degradation: Emulsion formation. *J. Membr. Sci.*, 67: 133–148.

127. Dozol, J.F., Casas, J., and Sastre, A. (1993) Stability of flat sheet supported liquid membranes in the transport of radionuclides from reprocessing concentrate solutions. *J. Membr. Sci.*, 82: 237–246.
128. Matsumoto, M., Murakami, Y., and Kondo, K. (2011) Separation of 1-butanol by pervaporation using polymer inclusion membranes containing ionic liquids. *Solvent Extr. Res. Dev.-Jpn.*, 18: 75–83.
129. Nghiem, L.D., Mornane, P., Potter, I.D., Perera, J.M., Cattrall, R.W., and Kolev, S.D. (2006) Extraction and transport of metal ions and small organic compounds using polymer inclusion membranes (PIMs). *J. Membr. Sci.*, 281: 7–41.
130. Kim, J.S., Kim, S.K., Ko, J.W., Kim, E.T., Yu, S.H., Cho, M.H., Kwon, S.G., and Lee, E.H. (2000) Selective transport of cesium ion in polymeric CTA membrane containing calixcrown ethers. *Talanta*, 52: 1143–1148.
131. Scindia, Y.M., Pandey, A.K., and Reddy, A.V.R. (2005) Coupled-diffusion transport of Cr(VI) across anion-exchange membranes prepared by physical and chemical immobilization methods. *J. Membr. Sci.*, 249: 143–152.
132. Vopicka, O., Hynek, V., Friess, K., and Izák, P. (2010) Blended silicone-ionic liquid membranes: Transport properties of butan-1-ol vapor. *Eur. Polym. J.*, 46: 123–128.
133. Jansen, J.C., Friess, K., Clarizia, G., Schauer, J., and Izák, P. (2011) High ionic liquid content polymeric gel membranes: Preparation and performance. *Macromolecules*, 44: 39–45.
134. Voss, B.A., Bara, J.E., Gin, D.L., and Noble, R.D. (2009) Physically gelled ionic liquids: Solid membrane materials with liquidlike CO₂ gas transport. *Chem. Mater.*, 21: 3027–3029.
135. Iijima, S. (1991) Helical microtubules of graphitic carbon. *Nature*, 354: 56–58.
136. Bethune, D. S., Kiang, C. H., De Vries, M. S., Gorman, G., Savoy, R., Vazquez, J., and Beyers, R. (1993) Cobalt-catalysed growth of carbon nanotubes with single-atomic-layer walls. *Nature*, 363: 605–607.
137. Cooper, C.A., Young, R.J., and Halsall, M. (2001) Investigation into the deformation of carbon nanotubes and their composites through the use of Raman spectroscopy. *Compos. Part A*, 32: 401–411.
138. Gao, G., Çağın, T., and Goddard III, W.A. (1998) Energetics, structure, mechanical and vibrational properties of single-walled carbon nanotubes. *Nanotechnology*, 9: 184–191.
139. Moniruzzaman, M. and Winey, K. I. (2006) Polymer nanocomposites containing carbon nanotubes. *Macromolecules*, 39: 5194–5205.
140. Ge, L., Zhu, Z., and Rudolph, V. (2011) Enhanced gas permeability by fabricating functionalized multi-walled carbon nanotubes and polyethersulfone nanocomposite membrane. *Sep. Purif. Technol.*, 78: 76–82.
141. Medina-Gonzalez, Y. and Remigy, J.C. (2011) Sonication-assisted preparation of pristine MWCNT-polysulfone Conductive microporous membranes. *Mater. Lett.*, 65: 229–232.
142. Choi, J.H., Jegal, J., and Kim, W.N. (2006) Fabrication and characterization of multi-walled carbon nanotubes/polymer blend membranes. *J. Membr. Sci.*, 284: 406–415.

143. Vatanpour, V., Madaeni, S.S., Moradian, R., Zinadini, S., and Astinchap, B. (2011) Fabrication and characterization of novel antifouling nanofiltration membrane prepared from oxidized multiwalled carbon nanotube/polyethersulfone nanocomposite. *J. Membr. Sci.*, 375: 284–294.
144. Qiu, S., Wu, L., Pan, X., Zhang, L., Chen, H., and Gao, C. (2009) Preparation and properties of functionalized carbon nanotube/PSF blend ultrafiltration membranes. *J. Membr. Sci.*, 342: 165–172.
145. Mulder, M. (1991) *Basic Principles of Membrane Technology*; Kluwer Academic Publishers: London, UK.
146. Karousis, N., Tagmatarchis, N., and Tasis, D. (2010) Current progress on the chemical modification of carbon nanotubes. *Chem. Rev.*, 110: 5366–5397.
147. Hirsch, A. (2002) Functionalization of single-walled carbon nanotubes. *Angew. Chem. Int. Ed.*, 41: 1853–1859.
148. Chen, S., Wu, G., Sha, M., and Huang, S. (2007) Transition of ionic liquid (bmim)(PF₆) from liquid to high-melting-point crystal when confined in multiwalled carbon nanotubes. *J. Am. Chem. Soc.*, 129: 2416–2417.

Study on the Reusability of Multiwalled Carbon Nanotubes in Biodegradable Chitosan Nanocomposites

Yoke Kooi Cheng, Qian Wen Yeang, Abdul Rahman Mohamed, and Soon Huat Tan
School of Chemical Engineering, Engineering Campus, Universiti Sains Malaysia, Seri Ampangan, Pulau Pinang, Malaysia

The mechanical properties, water absorption, biodegradation, multiwalled carbon nanotubes (MWCNTs) recovery and reusability of chitosan/oxidized MWCNTs nanocomposites were investigated. The highest Young's modulus (E) was obtained by the nanocomposites with 0.1 wt.% MWCNTs, while further increase of MWCNTs loading decreases the tensile strength (TS) and E . The water absorption and degradation rate of the nanocomposites were decreased by the loading of MWCNTs; 89.7% of MWCNTs were recovered by physical base separation. Thermogravimetric analysis (TGA), scanning electron microscopy (SEM) and tensile test results showed that the recovered MWCNTs displayed properties similar to the oxidized MWCNTs, suggesting the possibility of reuse and recycle.

Keywords Biodegradable; Carbon nanotubes; Chitosan; Nanocomposites

INTRODUCTION

Over the last decade, carbon nanotubes (CNTs) have been applied in various applications due to their remarkable mechanical, electrical, chemical, thermal, optical, and magnetic properties, high surface area, high flexibility and low mass density, which lead to many promising applications. Their potential practical applications have been reported, for instance chemical sensors^[1], field emitter devices^[2], nanoelectronic devices^[3], electronic devices^[4], electrochemical devices^[5], catalyst support^[6] and biomedical materials^[7]. Besides, CNTs also act as a high tensile strength fiber that enable the reinforcement of mechanical properties for polymers, such as chitosan^[8].

Chitosan, a linear polysaccharide composed of β -(1-4)-linked D-glucosamine and N-acetyl-D-glucosamine^[9]. Chitosan is known as a biocompatible, and biodegradable polymer and has been used in various agricultural and other applications, such as molecular separation^[10], food packaging^[11,12], water treatment^[13], artificial skin^[14,15],

and bone substitutes^[16,17]. However, its poor mechanical properties are the main limitation to those applications. In order to overcome this problem, CNTs have been introduced into chitosan to form high performance nanocomposites and hence successfully broadened the applications of chitosan^[8,18–20].

Chitosan/CNTs nanocomposites could be produced by several common composite processing methods, such as solution casting and melt processing^[21]. Prior to composite processing, CNTs normally will be functionalized in order to create hydroxyl ($-\text{OH}$) or carboxylic ($-\text{COOH}$) groups. These functional groups are important to further improve the dispersion and alignment stability of CNTs. Besides, the tensile strength of the nanocomposites was enhanced via hydrogen bonding between chitosan molecules and CNTs' functional groups^[22].

On the other hand, researchers have proposed that CNTs could pose an occupational inhalation exposure hazard since they may enter the working environment as suspended particulate matter of respirable sizes^[23,24]. The toxicity of the CNTs has raised the high concern in the society due to its similarities to asbestos in term of shape and size, which may lead to lung cancer^[25]. Some animal and cellular studies by Poland and his co-workers showed that CNTs can cause toxic responses similar to asbestos fibers^[26], such as elicit pathological changes in the lungs and other cardiopulmonary diseases. In addition, CNTs are practically insoluble and non-biodegradable fibers^[27,28]. This will result in environmental pollution as well.

The risk of CNTs had become worse due to the expanding production and widespread application of CNTs^[29]. World production capacity for MWCNTs exceeded 390 tons in 2008 and reached 1500 tons in 2009. Besides, global production for MWCNTs at year 2015 is projected to reach 9400 tons^[30]. This may lead to a situation whereby the world would be threatened by the potential hazard and environmental pollution of CNTs.

In concern to the adverse biological effects of CNTs and its potential reusability, 3 R (Reuse, Recycling and Reduce) concept can be implemented to overcome the issues^[31].

Address correspondence to Soon Huat Tan, School of Chemical Engineering, Engineering Campus, Universiti Sains Malaysia, Seri Ampangan, 14300 Nibong Tebal, Pulau Pinang, Malaysia. E-mail: chshtan@eng.usm.my

Color versions of one or more of the figures in the article can be found online at www.tandfonline.com/lpte.

Although many chitosan biodegradation studies have been conducted by previous researches, but most of them were focused on drug delivery system^[32–36], food additives^[37,38], biomedical and biotechnological fields^[39,40]. Unlike the previous studies, the present work focused on the reusability of the MWCNTs and its recycling efficiency.

The biodegradation of chitosan/oxidized MWCNTs nanocomposites were analyzed in order to reveal the effects of MWCNTs on their hydrolytic degradation. This article presented the preparation of chitosan/oxidized MWCNTs nanocomposites which consisted of different MWCNTs wt%, effect of buffer concentration and enzyme concentration on the biodegradation of chitosan film and chitosan/oxidized MWCNTs nanocomposites and MWCNTs recoverability percentage and its reusability.

EXPERIMENTAL

Materials

Low molecular weight chitosan (75–85% degree of deacetylation and Mw of ranged from 50 kDa to 190 kDa), pepsin (800–2500 U/mg of specific enzyme activity), sodium acetate (NaAc) buffer and glucosamine chloride were purchased from Sigma Aldrich. MWCNTs with purity of $\geq 95\%$, length ranged from 5–15 μm and diameters ranging from 40–60 nm were obtained from Shenzhen Nanotech Port Co. Ltd. Concentrated nitric acid (65%) and acetic acid (99.8%) were supplied by Merck.

Preparation of the Chitosan/Oxidized MWCNTs Nanocomposites

Functionalization of MWCNTs with –COOH and –OH Groups

A mass of 1 g of MWCNTs were bath sonicated (Branson 2510 Ultrasonic) at 42 kHz in 100 ml of HNO_3 for 15 min followed by vigorous stirring at 1000 rpm at room temperature for 48 h. The MWCNTs were collected on 0.22 μm GV Durapore filter paper by filtration and washed several times with deionized water until the filtrate gave a neutral pH 7. Finally, the oxidized MWCNTs residues were dried in the oven at 110°C for 24 h.

Preparation of Samples

Nanocomposites were prepared using the solution processing method. The 3 wt.% of chitosan powder was added in 2 wt.% of acetic acid. It was then stirred at 750 rpm at room temperature until a complete dissolution was achieved. Similarly, chitosan/oxidized MWCNTs mixtures were prepared by adding various wt.% of oxidized MWCNTs (0.1, 0.3, 0.5, 0.7 and 0.9) to the chitosan solution. The mixture was stirred vigorously at 750 rpm for 48 h to obtain a homogeneous mixture. The homogeneous mixture was dispersed by high power tip sonication (Hielscher UP200S Ultrasonic) at 24 kHz for 5 min,

prior to transferring them into the petri dish. Each petri dish was filled with 4 g of chitosan/oxidized MWCNTs mixtures.

The chitosan/oxidized MWCNTs mixtures in the petri dishes were dried at 60°C for 1 h and 45 min, and then left at room temperature for 1 day to further investigate the effect of drying temperature on the mechanical properties of chitosan/oxidized MWCNTs nanocomposites. The petri dishes were then dipped into neutralizing solution of $\text{NaOH-CH}_3\text{CH}_2\text{OH}$. Then they were washed with deionized water and heated at 60°C for 10 min, and left at room temperature for 3 days.

Biodegradation Studies

Effects of Different Solutions on the Chitosan Films Biodegradation

0.2 M NaAc buffer solution (solution A), 5 mg pepsin solution in 20 ml deionized water (solution B), and 5 mg pepsin in 20 ml of 0.2 M NaAc buffer solution (solution C) were prepared. Chitosan films were immersed separately into each petri dish that contains 50 ml of solution A, B and C for 3 h to investigate the performance of chitosan films biodegradation.

Effects of Buffer Concentration on the Chitosan Films and 0.1 Wt.% Chitosan/Oxidized MWCNTs Nanocomposites Biodegradation

First, 20 ml of NaAc buffer solutions were prepared at 5 different concentrations ranging from 0.1 to 0.5 M. 5 mg of pepsin were dissolved in 20 ml of buffer solution. Chitosan films and 0.1 wt.% chitosan/oxidized MWCNTs nanocomposites were placed into the petri dishes that contain 50 ml of NaAc buffer solution with various concentrations for 3 h under room temperature in order to investigate their effects on the biodegradation of the chitosan films and 0.1 wt.% chitosan/oxidized MWCNTs nanocomposites.

Effects of MWCNTs on the Chitosan/Oxidized MWCNTs Nanocomposites Biodegradation

The degradation of the chitosan film and chitosan/oxidized MWCNTs nanocomposites were conducted in pepsin and NaAc solutions (5 mg pepsin/20 ml 0.2 M NaAc), which named as degradation solution under acidic (pH 4.6) at room temperature. Chitosan/oxidized MWCNTs nanocomposites with different loading of MWCNTs, 0 to 0.9 wt.% were placed into the petri dishes each that contained 50 ml of degradation solution.

The samples were left at room temperature for 3 h. The performance of the chitosan/oxidized MWCNTs nanocomposites biodegradation was predicted based on the observation of the chitosan/oxidized MWCNTs nanocomposites morphology changes. On the other hand, a similar experiment was repeated but with the change of the

condition where 5 ml of the solution collected from each samples for every 30 min for the period of 2 h. The trend of the degradation based on time interval was analyzed.

Recovery of MWCNTs

Chitosan/oxidized MWCNTs nanocomposites were degraded by degradation solution. The resulted degraded solutions were centrifuged (Sigma Laboratory Centrifuge 4-15) at 12,500 rpm for 2 h. MWCNTs residues were removed from each tube and then filtered, followed by drying in the oven at 110°C for 24 h. The recovered MWCNTs were placed in a 200 ml beaker, which contained 120 ml degradation solution for further treatment to ensure that all chitosan was completely degraded. The recovered MWCNTs were washed with deionized water and followed by filtration process. Finally, it was dried in the oven at 110°C for 24 h. The recovery efficiency of the oxidized MWCNTs, η was calculated based on Eq. (1), where W_1 is the weight of the oxidized MWCNTs, and W_2 is the final weight of the recovered MWCNTs.

$$\eta = \frac{W_2}{W_1} \times 100\% \quad (1)$$

Recycle and Reuse of MWCNTs

The recovered MWCNTs were reused as a raw material to fabricate new chitosan/oxidized MWCNTs nanocomposites which contain of 0.1 wt.% of MWCNTs. Tensile strength comparison was then measured between chitosan/oxidized MWCNTs nanocomposites fabricated from oxidized MWCNTs and that using the recovered MWCNTs.

Characterizations of Biodegradation Process

Visualization on Chitosan Films and Chitosan/Oxidized MWCNTs Nanocomposites

The degradation of chitosan films and chitosan/oxidized MWCNTs nanocomposites were captured every 10 min by using a Samsung L100 digital camera at ambient temperature for 3 h. The photos were taken at macro mode.

DNS Assay

A calibration curve for glucosamine (GlcN) was prepared by glucosamine chloride⁹ standard with the increase of 0.2 mg/ml (0 mg/ml to 2.0 mg/ml). The evaluation of biodegradation process was based on the concentration of reducing sugar, GlcN. Chitosan hydrolysis was evaluated by colorimetric quantification at the wavelength of 535 nm using DNS solution^[41]. Each degraded sample was mixed with DNS solution in the volumetric ratio of 2 to 3 ml. The mixed samples were placed in hot water (~100°C) for 5 min, under dark condition. The samples were cooled down in a water bath at room temperature

and then analyzed using a Thermo Scientific Genesys 20 Spectrophotometer. Similarly, degraded specimens were tested with DNS reagent and the GlcN concentrations were individually determined. Prior to DNS testing, 0.2 μ m Minisart syringe filter was used to remove any remaining films or MWCNTs.

Water Absorption

The equilibrium water absorption is defined as the fraction of the saturated gained weight of the sample. The values of water absorption were calculated by Eq. (2), where M_1 is the initial weight of the specimen, and M_2 is the weight of the specimen after dipping in the deionized water for 24 h. The water droplets on the surface of the dipped specimen were dried with a filter paper before they were weighed. The average value was obtained based on five samples.

$$\text{Water absorption} = \frac{M_2 - M_1}{M_1} \times 100\% \quad (2)$$

Fourier Transformation Infrared (FTIR)

Fourier transformation infrared (FTIR) testing of the chitosan/oxidized MWCNTs nanocomposites was conducted in attenuated total reflectance (ATR) mode, using the Thermo Scientific Nicolet iS10 model with a diamond as the internal reflection element wafer. On the other hand, FTIR spectrum of the oxidized MWCNTs was operated in transmission mode, where MWCNTs were well-mixed with dry potassium bromide salt and then pressed to form a homogenous pellet.

Universal Tensile Tester

Tensile tests were carried out on the Instron Table Mounted universal testing machine equipped with a maximum load cell and operated at the crosshead speed of 1 mm/min at 23°C. All specimens were cut into dumbbell shape with the length of 3.8 cm. The thickness of each dumbbell shape specimen's neck was measured by using a 25 mm digimatic micrometer (Mitutoyo brand). The maximum tensile strength and elongation at break were then determined from the specimens. The average values of tensile strength (TS), Young's modulus (E), and elongation at break (ϵ) were obtained based on five samples.

Thermogravimetric Analysis (TGA)

The thermal stability of the MWCNTs was investigated by TGA. The specimens were prepared in the powder form and located in alumina crucible. It was then heated from 30°C to 900°C at the heating rate of 10°C/min in the presence of air. TGA analyses were run using TA Thermogravimetry SDTQ600V20.0.

Field Emission Scanning Electron Microscopy (FE-SEM) and Energy Dispersive Spectroscopy (EDS)

FE-SEM Quanta 450 FEG was used to study the morphologies of both MWCNTs and chitosan/oxidized MWCNTs nanocomposites as well as the dispersion of the MWCNTs in chitosan/oxidized MWCNTs nanocomposites. The images were taken in which 15 kV was used to generate the electron beam.

RESULTS AND DISCUSSION

Mechanical Properties of the Chitosan Film and Chitosan/Oxidized MWCNTs Nanocomposites

The mechanical properties of the chitosan/oxidized MWCNTs nanocomposites with different loadings of MWCNTs were shown in Table 1. The tensile strength (TS) and Young's modulus (E) of the 0.1 wt.% chitosan/oxidized MWCNTs nanocomposites increased by about 7.3%- and 34.0%-fold respectively, as compared to chitosan film. Olivas-Armendáriz et al.^[42] and Wang et al.^[8] reported that CNTs managed to improve the mechanical properties of the chitosan. However, there was a dramatic drop in the TS and E of the nanocomposite when the loading of MWCNTs was higher than 0.1 wt.%. Even though acid-treated MWCNTs managed to reduce the Van der Waals forces between MWCNTs, yet further increase of MWCNTs would cause aggregation of MWCNTs within the polymer matrix due to oversaturation of MWCNTs in the polymer matrix^[8,22].

Therefore, deterioration of MWCNTs dispersion occurred and prohibited the creation of a close interface between the MWCNTs and chitosan matrix. In general, the elongation at break (ϵ) of the chitosan/oxidized MWCNTs nanocomposites reduced as the loading of MWCNTs increased. The chitosan-MWCNTs interface might have introduced stress concentrations which might cause the chitosan/oxidized MWCNTs nanocomposites to fracture at smaller strains. The presence of MWCNTs acted as the anti-plasticizer in the nanocomposites since they provide the rigid constraints that could limit the

chitosan elastic deformation behavior, and hence lowering the elongation at break of the nanocomposites^[43,44].

Water Absorption of the Chitosan/Oxidized MWCNTs Nanocomposites

Water absorption is mainly used to determine the amount of water absorbed by a material. It was found that the chitosan/oxidized MWCNTs nanocomposites with 0, 0.1, 0.3, 0.5, 0.7 and 0.9 wt.% MWCNTs absorbed water of 69.3, 66.2, 65.2, 64.5, 63.3 and 61.3%, respectively, as shown in Figure 1. Increasing of MWCNTs loading improved the water-resistance of the chitosan/oxidized MWCNTs nanocomposites due to hydrophobic nature of MWCNTs. The percentage of water absorbed was reduced about 8% when the loading of MWCNTs increased from 0 to 0.9 wt.%. However, the water absorption of all chitosan/oxidized MWCNTs nanocomposites were considered high due to abundant amount of hydroxyl and free amino groups existed in the chitosan matrix^[45].

FTIR of the MWCNTs, Chitosan Film and Chitosan/Oxidized MWCNTs Nanocomposites

Figure 2 shows the FTIR spectra of the MWCNTs, chitosan film and chitosan/oxidized MWCNTs nanocomposites. An absorption peak near 1380 cm^{-1} was found on both FTIR spectra of the MWCNTs, which can be associated to C–O stretching vibrations^[46] and OH bending deformation in $-\text{COOH}$ ^[47] existed on the surface of the MWCNTs. A broad absorption peak at 3440 cm^{-1} was observed on both FTIR spectra for the OH functionality^[47,48]. Absorption peak at 1650 cm^{-1} corresponds to the amide C=O stretching vibrations in the chitosan^[49], and 1580 cm^{-1} appeared in the spectra of the chitosan film

TABLE I
Mechanical properties of the chitosan/oxidized MWCNTs nanocomposites with different loadings of MWCNTs

MWCNTs loading (wt.%)	d (MPa)	E (MPa)	ϵ (%)
0	33.7	1773.1	13.8
0.1	36.2	2376.3	11.6
0.3	11.9	752.0	5.2
0.5	9.4	470.4	8.6
0.7	8.9	417.9	7.5
0.9	6.6	360.0	7.1

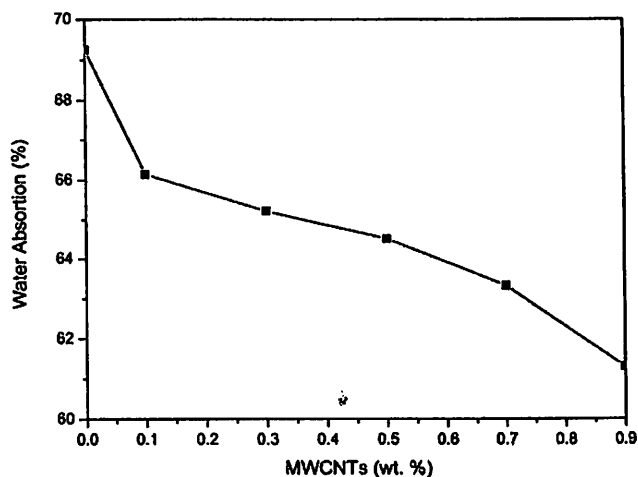


FIG. 1. Water absorption of chitosan/oxidized MWCNTs nanocomposites with different loading of MWCNTs.

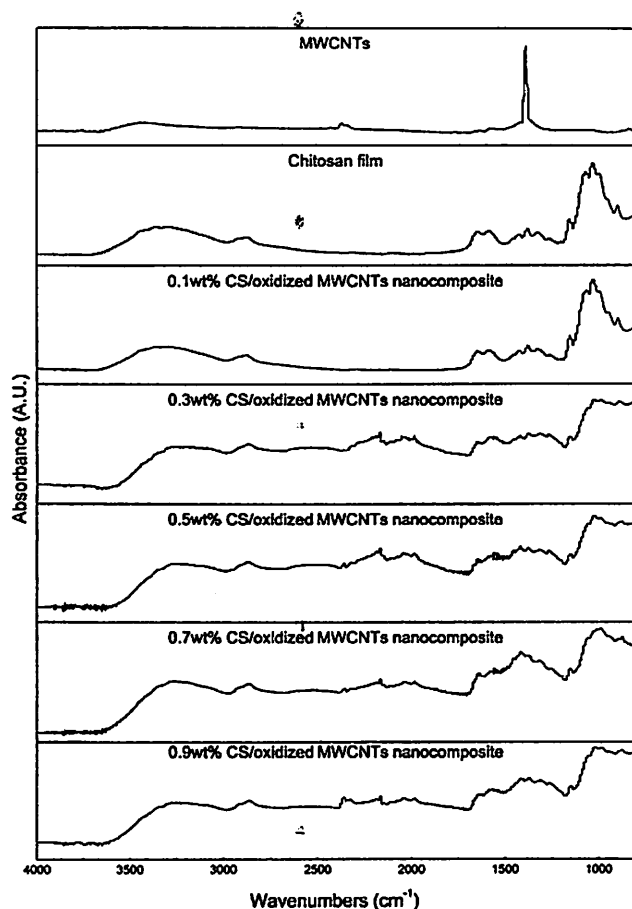


FIG. 2. FTIR spectra of MWCNTs, heated chitosan film and chitosan/oxidized MWCNTs nanocomposites with loading of 0.1 wt.%, 0.3 wt.%, 0.5 wt.%, 0.7 wt.% and 0.9 wt.% MWCNTs.

and chitosan/oxidized MWCNTs nanocomposites referred to amide bending vibration in the chitosan^[50] and C=C stretching of the CNTs^[51]. Peak absorption at 1151 cm^{-1} attributed to C–O–C asymmetric stretching, 2872 cm^{-1} can be assigned to symmetric C–H stretching vibrations, 1027 cm^{-1} and 1060 cm^{-1} were due to C–O stretching vibrations, and 3373 cm^{-1} correlated to the stretching vibration of O–H, the N–H extension vibrations, and inter hydrogen bonds of the chitosan polysaccharide structure^[49,52,53]. Band due to O=C=O asymmetric stretching vibrations provided adsorption peak at 2350 cm^{-1} .

The spectra of chitosan/oxidized MWCNTs nanocomposites with the loading of 0.1 wt.% MWCNTs exhibited similar absorption peaks as compared to the chitosan film. Therefore, this defines that small amount of MWCNTs added hardly influenced the chemical structure of the chitosan. The main interaction between both of them was proposed to be governed by physical adsorption due to the weak Van der Waals forces.

However, two newly existing peaks which were located at 2000 cm^{-1} and 2180 cm^{-1} were found when the loading of MWCNTs was 0.3 wt.% or higher for chitosan/oxidized MWCNTs nanocomposites. There is a possibility due to the chemical reactions that took place between the chitosan matrix and the MWCNTs during the heating process. This suggested that significant increment in MWCNTs might affect the chemical structure of the chitosan in the chitosan/oxidized MWCNTs nanocomposites during the heating process, as given in Figures 3a and 3b.

The amine groups from the chitosan are postulated undergo amidation reaction with the carboxylic groups from oxidized MWCNTs in order to form the amide groups and water molecules are released. It is known that the amide group is more effective than hydroxyl group to stabilize the resonance of the double bond of carboxylate group and thus decrease the C–O bond vibration. On

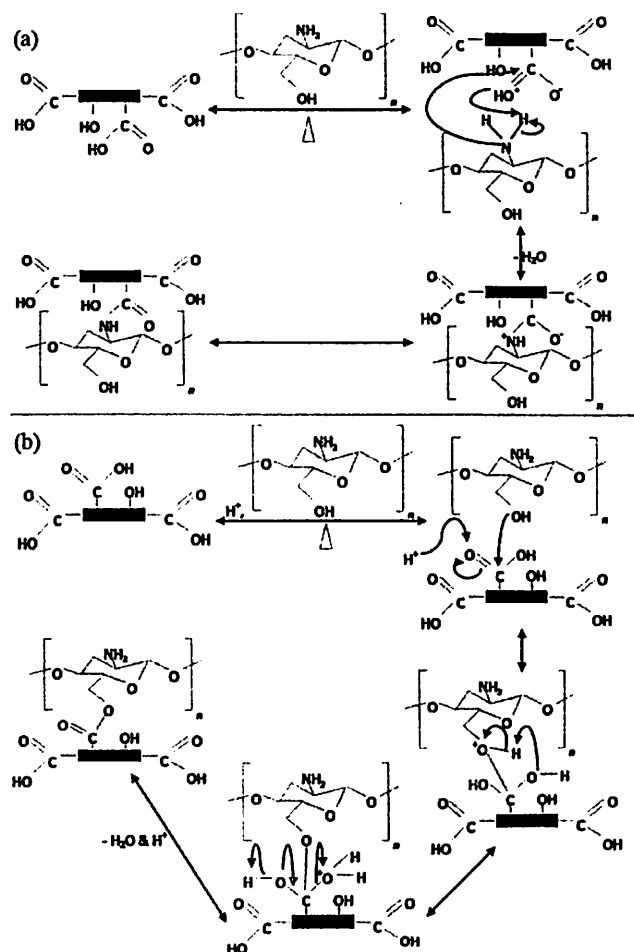


FIG. 3. Scheme of possible reactions to modify chemical structure of chitosan and oxidized MWCNTs: (a) amidation reaction; (b) esterification reaction.

the other hand, the hydroxyl groups from chitosan are postulated had undergone Fisher esterification reaction with the carboxylic groups from oxidized MWCNTs in order to form the ester groups and water molecules are released. The oxidized MWCNTs that treated by nitric acid contain enough trace acid to act as the driven catalyst for esterification process. Thus, the addition of an acid catalyst is not necessary.

Biodegradation Studies

A calibration curve for the interrelationship between GlcN concentration and Abs was obtained, as provided in Figure 4.

Effects of Different Solution on Chitosan Films Biodegradation

The effect of solution A, B and C on the chitosan films biodegradation process was studied. Table 2 presents the GlcN concentrations of the degraded solutions A, B and C. The degraded solution C that consisted of pepsin and NaAc buffer solution has the highest GlcN concentration, followed by degraded solution A and degraded solution B.

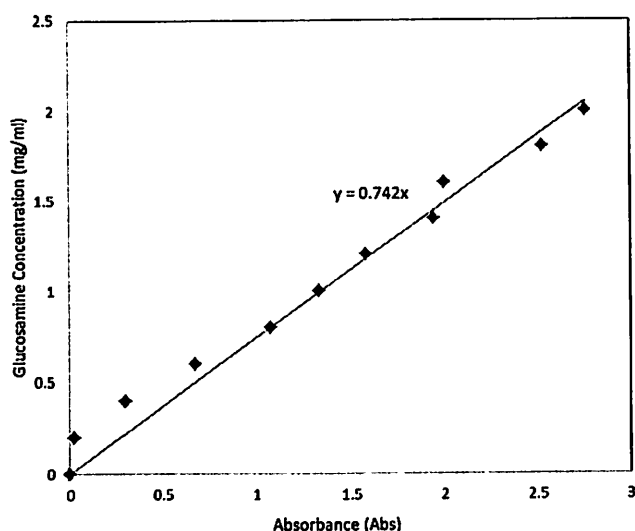


FIG. 4. Calibration curve of absorbance reading on different concentration of GlcN standards.

TABLE 2
GlcN concentration existed in different degraded solutions

Solution	GlcN concentration (mg/ml)
A	0.291
B	0.013
C	0.436

The degradation rate of the chitosan film in solution C was hastened where its production of GlcN was about 34-fold faster than solution B.

The pH of the solution was 4.61, which was lower than the chitosan pKa 6.3 and hence chitosan films suffered modifications depending on the present of buffer solution ions^[54,55]. Moreover, the degradation process was accelerated with the aid of pepsin, where GlcN concentration in degraded solution C was 49.8% higher than degraded solution A. Pepsin-catalyzed chitosan hydrolysis; especially in low weight molecular chitosan and produced a relatively high level of monomers, such as D-glucosamine and N-acetyl-D-glucosamine^[56-58].

The results suggested that enzyme and buffer solution are necessary for hastening the chitosan biodegradation process. The morphological changes of chitosan films in different solutions were analyzed. When the films were immersed into each solution for 10 min, the films in solution A and C, as shown in Figure 5 a(i) and c(i) experienced significant swelling whereas film in solution B showed only slight changes, as depicted in Figure 5 b(i). The swelling of chitosan films was expected due to its solubility in the acetic buffer^[55].

Similar to the DNS test results, the film in solution C showed the fastest disappearance in comparison to solution A and B, as shown in Figure 5-a(iii), b(iii) and c(iii). There was a tiny piece of film still managed to be observed in solution A. On the other hand, Figure 5 b(iv) shows that the chitosan film in solution B at 80 min did not have much difference with its appearance at 10 min, as shown in Figure 5 b(i). The complete disappearance of film in solution C and A occurred at 60 min (picture not shown) and 80 min, but it was unpredictable for the film in solution B. The disappearance of the films was due to the dissolving process and enzymatic degradation^[59].

Effects of Buffer Concentration on the Chitosan Film and Chitosan/Oxidized MWCNTs Nanocomposites

Table 3 and Table 4 show the biodegradation results that obtained from varying the buffer concentrations on chitosan films and 0.1 wt.% chitosan/oxidized MWCNTs nanocomposites, respectively. The pH values for all buffer solutions were within 4.43 to 4.82. The degradation solution with the 0.2 M buffer concentration was found to be the best buffer concentration throughout, as it attained the highest GlcN concentration not only in chitosan films, but also chitosan/oxidized MWCNTs nanocomposites. It was found that biodegradation rate on chitosan film was slightly faster than chitosan/oxidized MWCNTs nanocomposites.

Furthermore, the existence of NaAc buffer was important as it could be observed that when buffer concentration was increased from 0 M to 0.1 M, the GlcN concentration ascended dramatically at 33-fold and 131-fold for chitosan

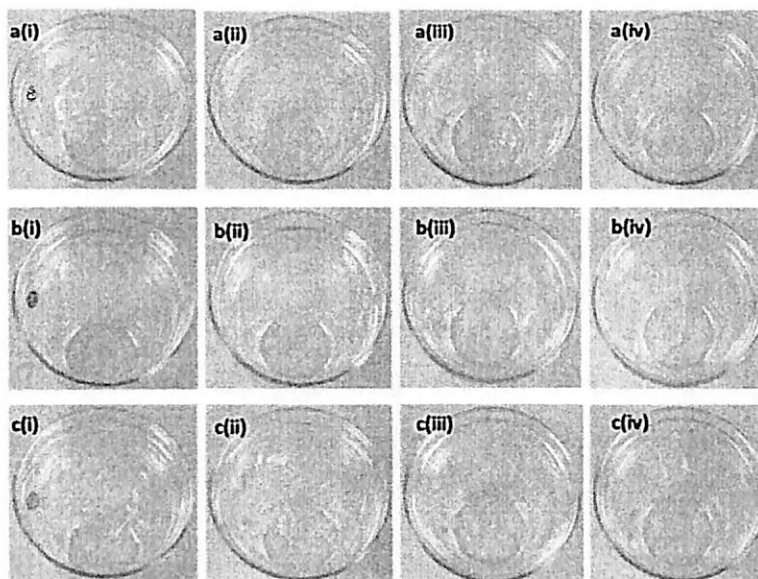


FIG. 5. Morphological changes of chitosan films at (i) 10 min, (ii) 20 min, (iii) 40 min, and (iv) 80 min in different solutions: (a) solution A; (b) solution B; and (c) solution C.

TABLE 3
GlcN concentration released from chitosan films

Solution	GlcN concentration (mg/ml)
0	0.013
0.1	0.429
0.2	0.436
0.3	0.384
0.4	0.359
0.5	0.343

TABLE 4
GlcN concentration released from 0.1 wt.% chitosan/oxidized MWCNTs nanocomposites

Solution	GlcN concentration (mg/ml)
0	0.003
0.1	0.393
0.2	0.401
0.3	0.364
0.4	0.352
0.5	0.306

films and chitosan/oxidized MWCNTs nanocomposites, respectively. However, there was a slight increment in GlcN concentration when the buffer concentration was

increased from 0.1 M to 0.2 M. Nevertheless, the GlcN concentration was decreasing when buffer concentration exceeded 0.2 M. It was postulated that when NaAc buffer concentration higher than 0.2 M, pepsin would be deactivated and hence lowering the degradation rate. The biodegradation rate of the chitosan films and chitosan/oxidized MWCNTs nanocomposites was decreased in the order of 0.2 M, 0.1 M, 0.3 M, 0.4 M, 0.5 M, and 0 M NaAc buffer concentrations.

The morphological change of chitosan films that was immersed in buffer solution with various concentrations were shown in Figure 6. Similar to the previous test, most films encountered a swelling stage, followed by disappearance. However, Figure 6 a(i), (ii), (iii) and (iv) revealed that film immersed in 0 M NaAc buffer solution did not experience significant morphology changes. Figure 6 f(i) shows the film that was dipped in 0.5 M NaAc undergoing the highest swelling degree and fastest disappearance. This film only took 20 min for complete disappearance (picture not shown). Figure 6 b(ii) and c(ii) show that the films immersed in 0.1 M and 0.2 M NaAc buffer solution at 40 min experienced significant changes where both films were swelled and dissolved. Figure 6 d(ii) shows that there was only a slight piece of film remained in 0.3 M NaAc buffer solution at 40 min. Moreover, the films immersed in 0.4 M and 0.5 M NaAc buffer solution were completely disappeared, as shown in Figure 6 e(ii) and f(ii).

At 80 min, the film immersed in 0.2 M NaAc buffer solution was completely disappeared but a slight piece of film still remained in 0.1 M NaAc buffer solution, as shown

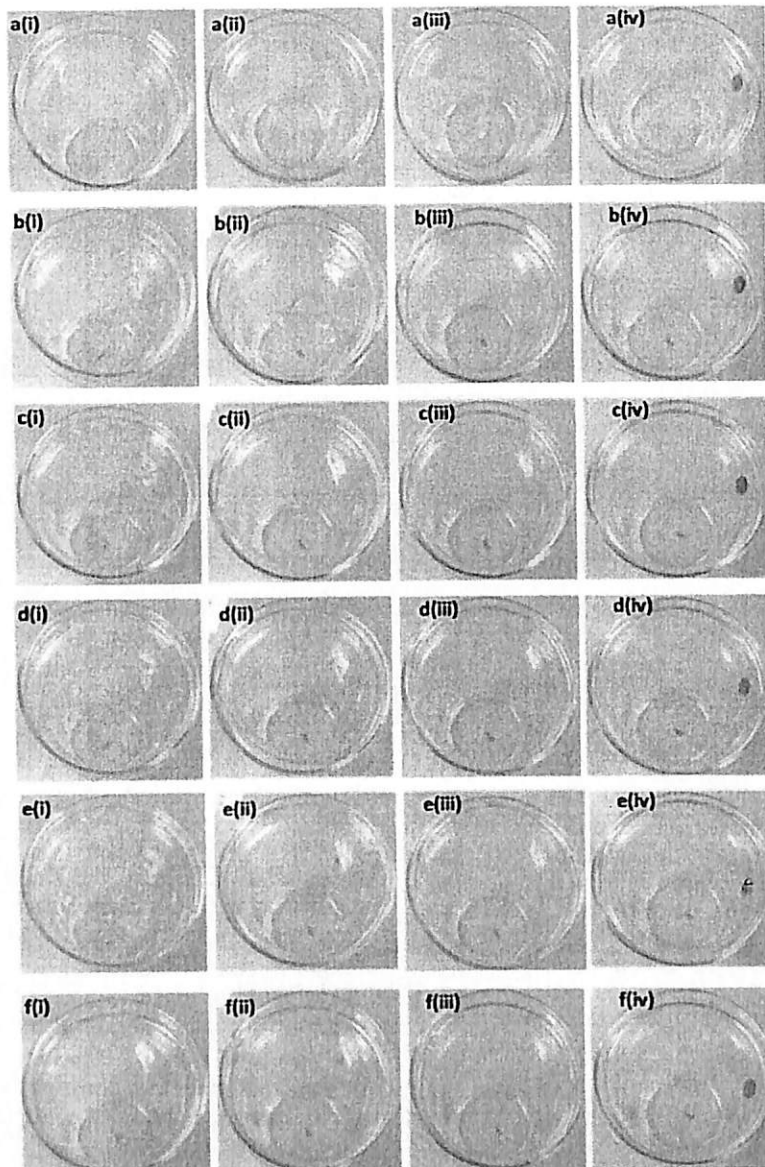


FIG. 6. Morphological change of chitosan films at (i) 10 min, (ii) 40 min, (iii) 80 min, and (iv) 130 min in NaAc buffer solution with different concentration: (a) 0 M; (b) 0.1 M; (c) 0.2 M; (d) 0.3 M; (e) 0.4 M; and, (f) 0.5 M.

in Figure 6 b(iii) and c(iii). Hence, the disappearance of the films was directly proportionate to the concentration of NaAc buffer solution. Previous research conducted by Shepherd et al.^[60] proved that the solubility of chitosan was increased when the buffer concentration increased. In comparison, both morphological changes and GlcN production were not giving a parallel conclusion. The disappearance of the films was not the key measurement for chitosan films biodegradation rate. It could be explained where the disappearance of the chitosan films might due

to the dissolution and biodegradation that occurred simultaneously.

It was also found through observation that the viscosity of solution was increasing at the beginning because of dissolution, and became diluted after certain period of time due to the chitosanolytic activity. The disappearance rates of the films were 40, 50, 60, and 110 min for 0.4, 0.3, 0.2 and 0.1 M of NaAc buffer solution respectively (picture not shown). On the other hand, disappearance rate of the film in 0 M NaAc buffer solution was undefined.

Figure 7 shows the morphology change of 0.1 wt.% chitosan/oxidized MWCNTs nanocomposites. Figure 7 b(i), c(i), d(i), e(i) and f(i) showed that all films experienced swelling, except the film that immersed in 0 M NaAc buffer solution, as shown in Figure 7 a(i). Unlike chitosan film, the disappearance of the chitosan/oxidized MWCNTs nanocomposites was directly proportionate to the concentration of NaAc buffer solution up to 40 min of immersion. Films that immersed in 0.3 M, 0.4 M and 0.5 M NaAc

buffer solution were not only swelled, but also dissolved, as shown in Figure 7 d(ii), e(ii), f(ii). As immersion time increased, the disappearance of the nanocomposite in 0.2 M NaAc buffer solution was expedited and experienced full disappearance at the shortest time, as shown in Figure 7 c(iii) and c(iv). Therefore, 0.2 M NaAc buffer solution was identified as the best concentration to dissolve and degrade 0.1 wt.% chitosan/oxidized MWCNTs nanocomposites. The full disappearance of chitosan/oxidized MWCNTs

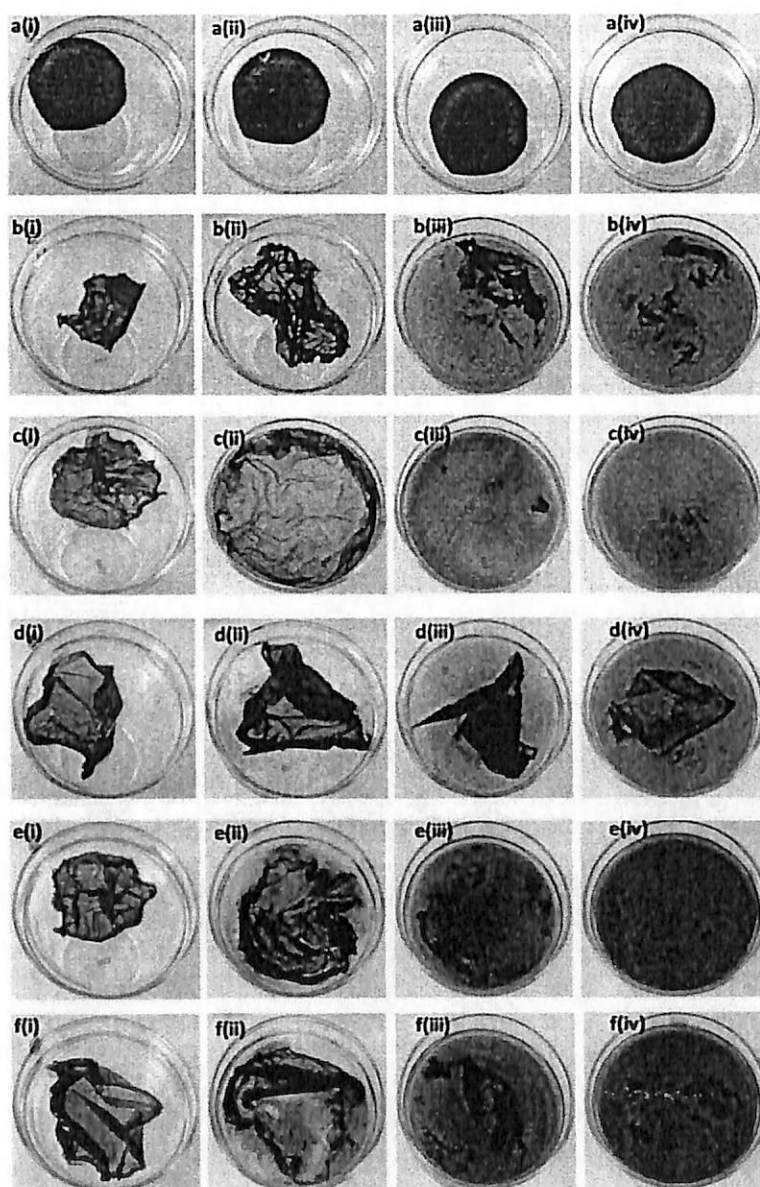


FIG. 7. Morphological change of 0.1 wt.% chitosan/oxidized MWCNTs nanocomposites at (i) 10 min, (ii) 40 min, (iii) 80 min, and (iv) 130 min in NaAc buffer solution with different concentrations: (a) 0 M; (b) 0.1 M; (c) 0.2 M; (d) 0.3 M; (e) 0.4 M; and, (f) 0.5 M.

TABLE 5

GlcN concentration existed in degradation solution with chitosan film and chitosan/oxidized MWCNTs nanocomposites that consisted of different MWCNTs loadings

MWCNTs wt.%	GlcN Concentration (mg/ml)
0.0	0.436
0.1	0.401
0.3	0.390
0.5	0.366
0.7	0.353
0.9	0.318

nanocomposites was then followed by NaAc buffer solution with 0.4 M, 0.5 M, 0.3 M, 0.1 M and 0 M. Similarly, the disappearance of chitosan/oxidized MWCNTs nanocomposites occurred due to the dissolution and biodegradation process.

Effects of MWCNTs on the Chitosan/Oxidized MWCNTs Nanocomposites Biodegradation

Table 5 shows the degradation products, GlcN tended to reduce as the MWCNTs loading in chitosan/oxidized MWCNTs nanocomposites increased. This result illustrated that by adding of the MWCNTs, it could lower the degradation rate of the chitosan/oxidized MWCNTs nanocomposites because of the physical adsorption of the

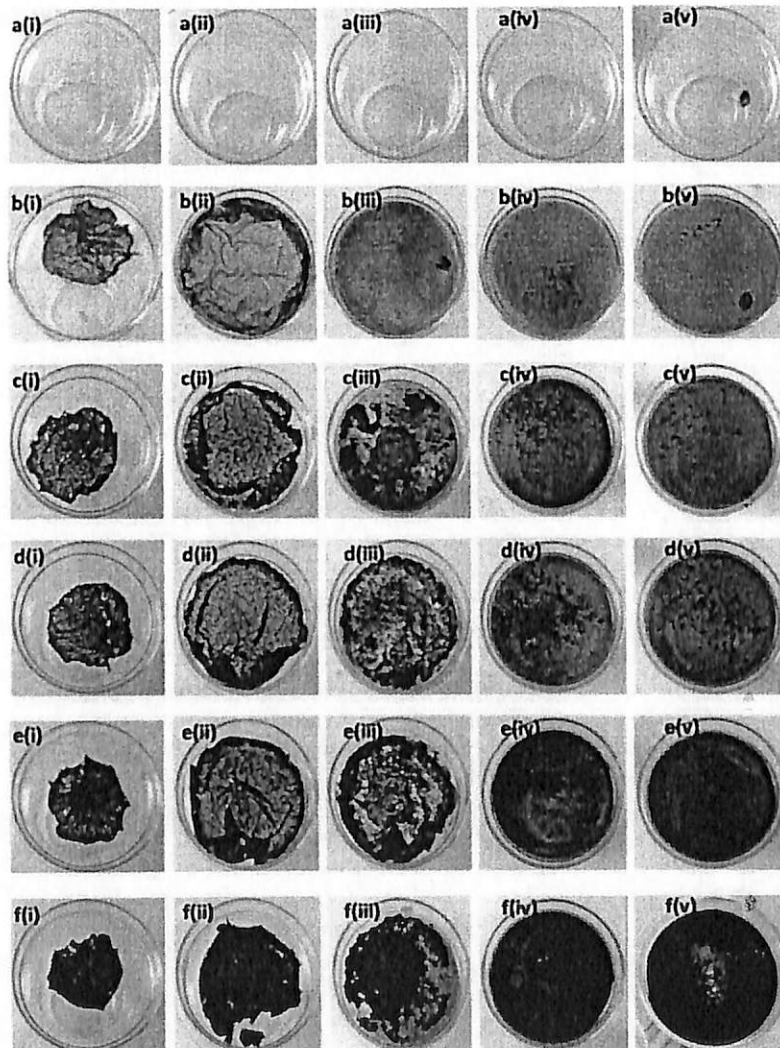


FIG. 8. Morphological change of chitosan/oxidized MWCNTs nanocomposites with different loadings of MWCNTs at (i) 10 min, (ii) 40 min, (iii) 80 min, (iv) 130 min, (v) 180 min in degradation solution: (a) 0 wt.%; (b) 0.1 wt.%; (c) 0.3 wt.%; (d) 0.5 wt.%; (e) 0.7 wt.%; (f) 0.9 wt.%. (Note: Image f(v) was taken under light bulb).

MWCNTs. The nature hydrophobicity of the MWCNTs further slowed down the chitosan/oxidized MWCNTs nanocomposites dissolution process and hence hampered the chitosanolytic activity. Water absorption was found to have similar trend with biodegradation rate where both of their performances became poorer as the loading of MWCNTs increased.

The amount of degradation products was reduced as much as 27.1% when the loading of MWCNTs increased from 0 to 0.9 wt.%. It was found that 0.1 wt.% chitosan/oxidized MWCNTs nanocomposites gave the highest Young's Modulus and degradation rate among the nanocomposites. Hence, it was selected as a standard nanocomposite in the experiment of MWCNTs recovery. The disappearance rate of chitosan/oxidized MWCNTs nanocomposites with different loadings of MWCNTs is given in Figure 8.

Figure 8 a(i), b(i), c(i), d(i), e(i) and f(i) show all films experienced swelling after 10 min of immersion. The swelling degree of the films in degradation solution became higher after 40 min of immersion. Figure 8 b(ii) showed that 0.1 wt.% chitosan/oxidized MWCNTs nanocomposite experienced higher swelling degree as compared to the nanocomposites loaded with higher wt.% of MWCNTs at 40 min, as shown in Figure 8 c(ii), d(ii), e(ii) and f(ii). The chitosan/oxidized MWCNTs nanocomposites were breaking into pieces due to the effect of dissolution and biodegradation. At 80 min, Figure 8 b(iii) showed that 0.1 wt.% chitosan/oxidized MWCNTs nanocomposite disappeared faster, compared to nanocomposites that consisted of higher wt.% of MWCNTs, as shown in Figure 8 c(iii), d(iii), e(iii) and f(iii). Chitosan/oxidized MWCNTs nanocomposites with lower loading of MWCNTs experienced a faster disappearance rate. The complete disappearance of all chitosan/oxidized MWCNTs nanocomposites in degradation solution was achieved within 3 h.

Effects of MWCNTs on the Chitosan/Oxidized MWCNTs Nanocomposites Biodegradation Base on Time Intervals

Figure 9 shows the concentration of GlcN released from the biodegradation of chitosan/oxidized MWCNTs nanocomposites that contained of different loadings of MWCNTs. The concentration of GlcN reduced as the MWCNTs loading in chitosan/oxidized MWCNTs nanocomposites increased. All chitosan/oxidized MWCNTs nanocomposites encountered higher degradation rate at the first 30 min. The biodegradation rate of the chitosan film surpassed the rest of chitosan/oxidized MWCNTs nanocomposites for the first 30 min due to chitosan hydrophilic nature.

After that, the releasing rate of GlcN from the chitosan film had slowed down. In the period of 30 min to 60 min, GlcN generated from chitosan/oxidized MWCNTs nanocomposites with the loading of 0.5 wt.%, 0.7 wt.% and

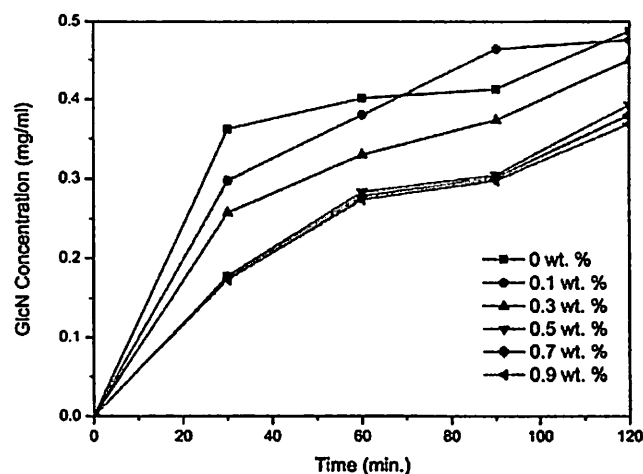


FIG. 9. GlcN concentration released from chitosan/oxidized MWCNTs nanocomposites with different loading of MWCNTs based on 30 min time intervals.

0.9 wt.% MWCNTs increased significantly. This might be due to the dissolved chitosan molecules released in the degradation solution in the first 30 min were further hydrolyzed into GlcN. The biodegradation rate for 0.1 wt.% and 0.3 wt.% chitosan/oxidized MWCNTs nanocomposites remained constant at 30 min to 90 min. After 2 h, the amount of GlcN generated from chitosan film was higher than chitosan/oxidized MWCNTs nanocomposites. Hence, it could be postulated that the releasing of the GlcN was reduced when the loading of MWCNTs increased, except during the time interval from 60–90 min.

Comparison Between Oxidized MWCNTs and Recovered MWCNTs

DTG Analyses

The DTG results for the oxidized MWCNTs and recovered MWCNTs (first stage) were shown in Figure 10. The decomposition temperature for chitosan was about 300°C. A small peak found around 300°C was due to the remaining nondegraded chitosan films. Besides, the decomposition temperature of the recovered MWCNTs (first stage) was shifted to the left, which was lower than the oxidized MWCNTs. The deviation of decomposition temperature of MWCNTs was due to the remaining chitosan, which has a lower decomposition temperature.

The remaining chitosan was further degraded by fresh degradation solution in the second stage. Figure 11 shows the DTG analysis of oxidized MWCNTs and recovered MWCNTs (second stage). Based on the DTG data, it was clearly revealed that all chitosan films had been detached from MWCNTs and the thermo properties of the recovered MWCNTs (second stage) were similar with

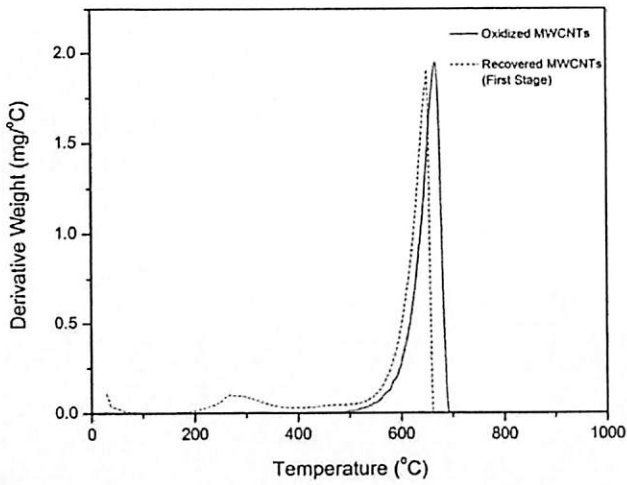


FIG. 10. DTG curves of oxidized MWCNTs and recovered MWCNTs (first stage) versus temperature.

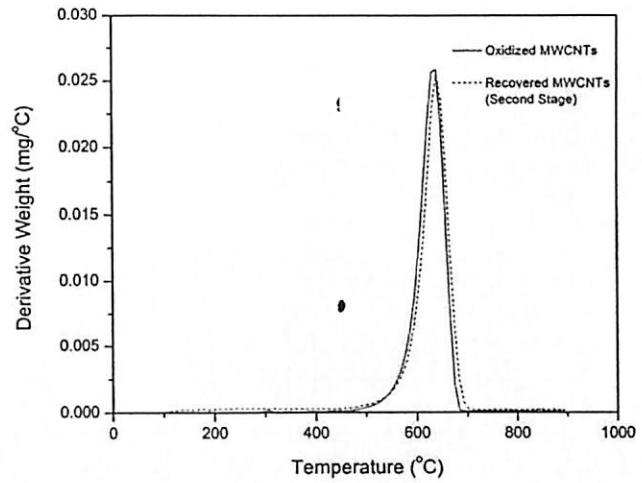


FIG. 11. DTG curves of oxidized MWCNTs and recovered MWCNTs (second stage) versus temperature.

oxidized MWCNTs. This means the recovered MWCNTs can be used to replace the oxidized MWCNTs for the chitosan/MWCNTs re-fabrication nanocomposites or other applications. The concept of MWCNTs reuse and recycling led to reduction of MWCNTs waste.

SEM of the Oxidized MWCNTs and Recovered MWCNTs (Second Stage)

It was found that oxidized MWCNTs and recovered MWCNTs (second stage) were having almost similar morphology structure, as shown in Figure 12. The diameter

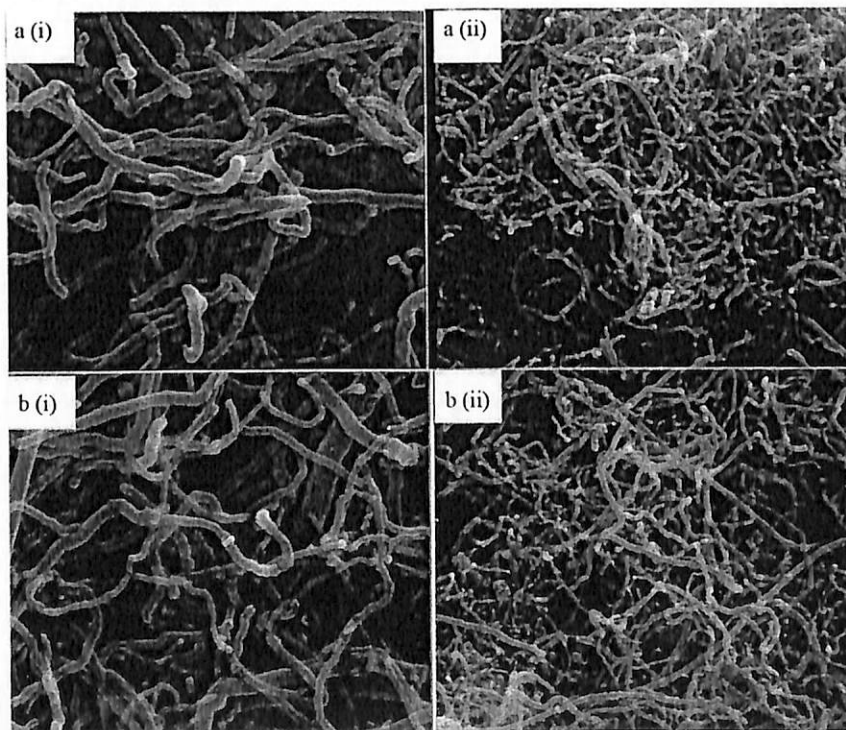


FIG. 12. SEM with resolution (i) 100kX and (ii) 40kX: (a) oxidized MWCNTs; (b) recovered MWCNTs (second stage).

TABLE 6
Mechanical properties of the chitosan/MWCNTs nanocomposites with 0.1 wt.% loading of oxidized MWCNTs and recovered MWCNTs (second stage)

Mechanical properties	€	Oxidized MWCNTs	Recovered MWCNTs (second stage)	Variances
TS (MPa)		36.2	32.3	-10.0
E (MPa)		2376.3	2162.3	-9.0
ϵ (%)		11.6	13.0	12.0

size of both MWCNTs were measured based on the average value of 40 random stands of nanotubes from Figure 12 a(i) and b(i). Both the oxidized and second recovered MWCNTs have the similar average diameter size of 57.8 nm and 58.5 nm, respectively. It was also observed that the morphology of both MWCNTs was almost the same in Figure 12 a(ii) and b(ii). Hence, the similarities between both of the MWCNTs were acknowledged.

Recovery Efficiency of the Oxidized MWCNTs

The weight of the oxidized MWCNTs used for 60 g chitosan solution was 0.06 g for the fabrication of chitosan/oxidized MWCNTs nanocomposites with 0.1 wt.% loading of MWCNTs. The total weight of the recovered MWCNTs (second stage) was 0.0538 g. This meant that the recovery efficiency, η , of MWCNTs was about 89.7%.

Tensile Test Comparison Between Chitosan/Oxidized MWCNTs and Chitosan/Recovered MWCNTs Nanocomposites

The mechanical properties of chitosan/MWCNTs fabricated from oxidized MWCNTs and recovered MWCNTs (second stage) are recorded in Table 6. Comparison between both chitosan/MWCNTs nanocomposites was made and the variant between each property was calculated. The variants were about 10%, which means the properties of the recovered MWCNTs (second stage) sustained their outstanding mechanical properties, further evidence of the reusability of MWCNTs.

CONCLUSION

The chitosan/oxidized MWCNTs nanocomposites prepared by the solution processing method reached the highest Young's modulus when the loading of MWCNTs was 0.1 wt.%. However, the TS and E of the chitosan/oxidized MWCNTs nanocomposites decreased dramatically with the loading of the MWCNTs higher than 0.1 wt.%. The main interaction between chitosan and MWCNTs was physical absorption. Water absorption of the chitosan/oxidized MWCNTs nanocomposites was reduced with increased MWCNTs loadings. The disappearance rate of

the chitosan film and chitosan/oxidized MWCNTs nanocomposites was dependent on the dissolution and biodegradation process.

The GlcN release was increased 33-fold and 131-fold, correspondingly, for chitosan film and chitosan/oxidized MWCNTs nanocomposites, when buffer concentration was slightly increased from 0 to 0.1 M. The optimum concentration of NaAc buffer was 0.2 M, and the presence of pepsin hastened the biodegradation rate of chitosan by 42.5%. The biodegradation rate of chitosan/oxidized MWCNTs nanocomposites degradation solution was reduced as the loading of MWCNTs was increased. Also, it was found that the purified MWCNTs with alumina resulted in a slower biodegradation process compared to the oxidized MWCNTs. The chitosan/oxidized MWCNTs nanocomposites required 3 h for the full disappearance in degradation solution.

The recovery efficiency of MWCNTs by physical base separation was 89.7%. The DTG and SEM results for recovered MWCNTs (second stage) and oxidized MWCNTs suggested that they have similarities in terms of structure and thermal properties. In addition, chitosan/MWCNTs nanocomposites produced by recovered MWCNTs further support the potential of MWCNT reusability. The sustainable properties of MWCNTs and high recovery efficiency of MWCNTs within the short period concluded that the 3R concept can be applied on chitosan/MWCNTs nanocomposites, as well as other biodegradable polymer/MWCNTs. Application of the 3R concept on MWCNTs is not only managed to secure public health by preventing toxic MWCNTs from entering the ecological cycle, but it also does not hinder the growth of the MWCNTs applications in different nanotechnology researches.

FUNDING

The authors acknowledge fellowship support from the USM fellowship. This research was also financially supported by a Universiti Sains Malaysia Research University (RU) grant (A/C:814142), Fundamental of Research Grant Scheme (FRGS) (A/C:6071212).

REFERENCES

- Kong, J.; Franklin, N.R.; Zhou, C.; Chapline, M.G.; Peng, S.; Cho, K.; Dai, H. Nanotube molecular wires as chemical sensors. *Science* 2000, 287, 622–625.
- Tans, S.J.; Verschueren, A.R.M.; Dekker, C. Room-temperature transistor based on a single carbon nanotube. *Nature* 1998, 393, 49–52.
- Tsukagoshi, K.; Yoneya, N.; Uryu, S.; Aoyagi, Y.; Kanda, A.; Ootuka, Y.; Alphenaar, B.W. Carbon nanotube devices for nano-electronics. *Phys. B: Condens. Matt.* 2002, 323, 107–114.
- Saito, S. Carbon nanotubes for next-generation electronics devices. *Science* 1997, 278, 77–78.
- Baughman, R.H.; Zakhidov, A.A.; de Heer, W.A. Carbon nanotubes—The route toward applications. *Science* 2002, 297, 787–792.
- Planeix, J.M.; Coustel, N.; Coq, B.; Brotons, V.; Kumbhar, P.S.; Dutartre, R.; Geneste, P.; Bernier, P.; Ajayan, P.M. Application of carbon nanotubes as supports in heterogeneous catalysis. *J. Am. Chem. Soc.* 1994, 116, 7935–7936.
- Armentano, I.; Dottori, M.; Fortunati, E.; Mattioli, S.; Kenny, J.M. Biodegradable polymer matrix nanocomposites for tissue engineering: A review. *Polym. Degrad. Stab.* 2010, 95, 2126–2146.
- Wang, S.-F.; Shen, L.; Zhang, W.-D.; Tong, Y.-J. Preparation and mechanical properties of chitosan/carbon nanotubes composites. *Biomacromolecules* 2005, 6, 3067–3072.
- Roberts, G.A.F. *Chitin Chemistry*, Macmillan: London, 1992.
- Chen, X.-G.; Zheng, L.; Wang, Z.; Lee, C.-Y.; Park, H.-J. Molecular affinity and permeability of different molecular weight chitosan membranes. *J. Agric. Food. Chem.* 2002, 50, 5915–5918.
- Dutta, P.K.; Tripathi, S.; Mehrotra, G.K.; Dutta, J. Perspectives for chitosan based antimicrobial films in food applications. *Food Chem.* 2009, 114, 1173–1182.
- Yeng, C.M.; Husseinsyah, S.; Ting, S.S. Modified corn cob filled chitosan biocomposite films. *Polym.-Plast. Technol. Eng.* 2013, 52, 1496–1502.
- Zeng, D.; Wu, J.; Kennedy, J.F. Application of a chitosan flocculant to water treatment. *Carbohydr. Polym.* 2008, 71, 135–139.
- Mao, J.; Zhao, L.; de Yao, K.; Shang, Q.; Yang, G.; Cao, Y. Study of novel chitosan-gelatin artificial skin in vitro. *J. Biomed. Mater. Res. Pt. A* 2003, 64A, 301–308.
- Liu, Y.; An, M.; Qiu, H.-X.; Wang, L. The properties of chitosan-gelatin scaffolds by once or twice vacuum freeze-drying methods. *Polym.-Plast. Technol. Eng.* 2013, 52, 1154–1159.
- Li, Z.; Yubao, L.; Aiping, Y.; Xuelin, P.; Xuejiang, W.; Xiang, Z. Preparation and *in vitro* investigation of chitosan/nano-hydroxyapatite composite used as bone substitute materials. *J. Mater. Sci. - Mater. Med.* 2005, 16, 213–219.
- El-Sherbiny, I.M.; Yahia, S.; Messierey, M.A.; Reicha, F.M. Preparation and physicochemical characterization of new nanocomposites based on β -Type chitosan and nano-hydroxyapatite as potential bone substitute materials. *Inter. J. Polym. Mater. Polym. Biomater.* 2013, 63, 213–220.
- Ong, Y.T.; Ahmad, A.L.; Zein, S.H.S.; Sudesh, K.; Tan, S.H. Poly(3-hydroxybutyrate)-functionalised multi-walled carbon nanotubes/chitosan green nanocomposite membranes and their application in pervaporation. *Separ. Purif. Technol.* 2011, 76, 419–427.
- Yeang, Q.W.; Zein, S.H.S.; Sulong, A.B.; Tan, S.H. Comparison of the pervaporation performance of various types of carbon nanotube-based nanocomposites in the dehydration of acetone. *Separ. Purif. Technol.* 2013, 107, 252–263.
- Marroquin, J.B.; Rhee, K.Y.; Park, S.J. Chitosan nanocomposite films: Enhanced electrical conductivity, thermal stability, and mechanical properties. *Carbohydr. Polym.* 2013, 92, 1783–1791.
- Coleman, J.N.; Khan, U.; Blau, W.J.; Gun'ko, Y.K. Small but strong: A review of the mechanical properties of carbon nanotube-polymer composites. *Carbon* 2006, 44, 1624–1652.
- Ma, C.; Zhang, W.; Zhu, Y.; Ji, L.; Zhang, R.; Koratkar, N.; Liang, J. Alignment and dispersion of functionalized carbon nanotubes in polymer composites induced by an electric field. *Carbon* 2008, 46, 706–710.
- Lam, C.-w.; James, J.T.; McCluskey, R.; Arepalli, S.; Hunter, R.L. A review of carbon nanotube toxicity and assessment of potential occupational and environmental health risks. *Crit. Rev. Toxicol.* 2006, 36, 189–217.
- Fleury, D.; Bomfim, J.A.S.; Vignes, A.; Girard, C.; Metz, S.; Muñoz, F.; R'Mili, B.; Ustache, A.; Guiot, A.; Bouillard, J.X. Identification of the main exposure scenarios in the production of CNT-polymer nanocomposites by melt-moulding process. *J. Clean. Product.* 2013, 53, 22–36.
- Donaldson, K.; Aitken, R.; Tran, L.; Stone, V.; Duffin, R.; Forrest, G.; Alexander, A. Carbon nanotubes: A review of their properties in relation to pulmonary toxicology and workplace safety. *Toxicol. Sci.* 2006, 92, 5–22.
- Poland, C.A.; Duffin, R.; Kinloch, I.; Maynard, A.; Wallace, W.A.H.; Seaton, A.; Stone, V.; Brown, S.; MacNee, W.; Donaldson, K. Carbon nanotubes introduced into the abdominal cavity of mice show asbestos-like pathogenicity in a pilot study. *Nat. Nano.* 2008, 3, 423–428.
- Zhang, X.; Prasad, S.; Niyogi, S.; Morgan, A.; Ozkan, M.; Ozkan, C.S. Guided neurite growth on patterned carbon nanotubes. *Sens. Actuat. B* 2005, 106, 843–850.
- Qiu, J.; Wang, G.; Zhao, C. Preparation and characterization of amphiphilic multi-walled carbon nanotubes. *J. Nanopart. Res.* 2008, 10, 659–663.
- Lim, J.H.; Kim, S.H.; Shin, I.S.; Park, N.H.; Moon, C.; Kang, S.S.; Park, S.C.; Kim, J.C. Maternal exposure to multi-wall carbon nanotubes does not induce embryo-fetal developmental toxicity in rats. *Birth Defects Res. B Dev. Reprod. Toxicol.* 2011, 92, 69–76.
- Innovative Research and Products (iRAP). *Production and Applications of Carbon Nanotubes, Carbon Nanofibers, Fullerenes, Graphene and Nanodiamonds: A Global Technology Survey and Market Analysis*, CNT Technology and Industry Overview Chapter, Innovative Research and Products: Stamford, CT, 2011; pp. 1–48.
- Ong, Y.T.; Ahmad, A.L.; Zein, S.H.S.; Tan, S.H. A review on carbon nanotubes in an environmental protection and green engineering perspective. *Braz. J. Chem. Eng.* 2010, 27, 227–242.
- Tada, D.B.; Singh, S.; Nagesha, D.; Jost, E.; Levy, C.O.; Gultepe, E.; Cormack, R.; Makrigiorgos, G.M.; Sridhar, S. Chitosan film containing poly(D,L-Lactic-co-glycolic acid) nanoparticles: A platform for localized dual-drug release. *Pharm. Res.* 2010, 27, 1738–1745.
- Narayana Reddy, C.L.; Swamy, B.Y.; Prasad, C.V.; Madhusudhan Rao, K.; Prabhakar, M.N.; Aswini, C.; Subha, M.C.S.; Rao, K.C. Development and characterization of chitosan-poly (vinyl pyrrolidone) blend microspheres for controlled release of metformin hydrochloride. *Inter. J. Polym. Mater. Polym. Biomater.* 2012, 61, 424–436.
- Kafshgari, M.H.; Mansouri, M.; Khorram, M.; Samimi, A.; Osfouri, S. Bovine serum albumin-loaded chitosan particles: An evaluation of effective parameters on fabrication, characteristics, and *in vitro* release in the presence of non-covalent interactions. *Inter. J. Polym. Mater. Polym. Biomater.* 2012, 61, 1079–1090.
- Balamuralidhara, V.; Pramod Kumar, T.M.; Vishal Gupta, N.; Getyala, A.; Gangadharappa, H.V. Development of a novel biodegradable superporous hydrogel for gastroretentive application. *Inter. J. Polym. Mater. Polym. Biomater.* 2013, 62, 524–532.
- Xiong, L.; He, Z. Release behavior and cytotoxicity of poly(vinyl alcohol)/chitosan blend microspheres containing 2,4-dihydroxy-5-fluoropyrimidine. *Polym.-Plast. Technol. Eng.* 2012, 51, 729–733.
- Muzzarelli, R.A.A.; Xia, W.; Tomasetti, M.; Ilari, P. Depolymerization of chitosan and substituted chitosans with the aid of a wheat germ lipase preparation. *Enzyme Microb. Technol.* 1995, 17, 541–545.

38. Lin, H.-R.; Chen, Y.-C.; Lin, Y.-J.; Ling, M.-H.; Chou, C.-W.; Hseu, Y.-C.; Kuo, Y.-H.; Senthil Kumar, K.J. pH-Sensitive hollow alginate-chitosan hydrogel beads for bitter melon delivery. *Inter. J. Polym. Mater. Polym. Biomater.* **2013**, *63*, 41–47.
39. Zhang, H.; Neau, S.H. In vitro degradation of chitosan by a commercial enzyme preparation: effect of molecular weight and degree of deacetylation. *Biomaterials* **2001**, *22*, 1653–1658.
40. Zhang, H.; Neau, S.H. In vitro degradation of chitosan by bacterial enzymes from rat cecal and colonic contents. *Biomaterials* **2002**, *23*, 2761–2766.
41. Fen, L.L.; Md.Illias, R.; Kamaruddin, K.; Maskat, M.Y.; Hassan, O. Development of rapid screening method for low-yielding chitosanase activity using Remazol Brilliant Blue-chitosan as substrate. *Enzyme Microb. Technol.* **2006**, *38*, 215–219.
42. Olivas-Armendáriz, I.; García-Casillas, P.; Martínez-Sánchez, R.; Martínez-Villafañe, A.; Martínez-Pérez, C.A. Chitosan/MWCNT composites prepared by thermal induced phase separation. *J. Alloys Compd.* **2010**, *495*, 592–595.
43. Nogueira Campos, M.G.; Ferreira Grosso, C.R.; Cárdenas, G.; Inocentinni Mei, L.H. Effects of neutralization process on preparation and characterization of chitosan membranes for wound dressing. *Macromol. Symp.* **2005**, *229*, 253–257.
44. Spinks, G.M.; Shin, S.R.; Wallace, G.G.; Whitten, P.G.; Kim, S.I.; Kim, S.J. Mechanical properties of chitosan/CNT microfibers obtained with improved dispersion. *Sens. Actuat. B* **2006**, *115*, 678–684.
45. Liu, Q.; Wu, J.; Tan, T.; Zhang, L.; Chen, D.; Tian, W. Preparation, properties and cytotoxicity evaluation of a biodegradable polyester elastomer composite. *Polym. Degrad. Stab.* **2009**, *94*, 1427–1435.
46. Baby, T.; Ramaprabhu, S. Enhanced convective heat transfer using graphene dispersed nanofluids. *Nanoscale Res. Lett.* **2011**, *6*, 289.
47. Kathi, J.; Rhee, K. Surface modification of multi-walled carbon nanotubes using 3-aminopropyltriethoxysilane. *J. Mater. Sci.* **2008**, *43*, 33–37.
48. Dutta, D.; Dubey, R.; Yadav, J.; Shami, T.C.; Rao, K.U.B. Preparation of spongy microspheres consisting of functionalized multiwalled carbon nanotubes. *New Carbon Mater.* **2011**, *26*, 98–102.
49. Chiono, V.; Pulieri, E.; Vozi, G.; Ciardelli, G.; Ahluwalia, A.; Giusti, P. Genipin-crosslinked chitosan/gelatin blends for biomedical applications. *J. Mater. Sci. - Mater. Med.* **2008**, *19*, 889–898.
50. Suyatma, N.E.; Copinet, A.; Tighzert, L.; Coma, V. Mechanical and barrier properties of biodegradable films made from chitosan and poly (lactic acid) blends. *J. Polym. Environ.* **2004**, *12*, 1–6.
51. Bag, D.S.; Dubey, R.; Zhang, N.; Xie, J.; Varadan, V.K.; Lal, D.; Mathur, G.N. Chemical functionalization of carbon nanotubes with 3-methacryloxypropyltrimethoxysilane (3-MPTS). *Smart Mater. Struct.* **2004**, *13*, 1263.
52. Sharma, A.K.; Mishra, A.K. Microwave assisted synthesis of chitosan-graft-styrene for efficient Cr(VI) removal. *Adv. Mat. Lett.* **2010**, *1*, 59–66.
53. Khanna, R.; Katti, K.S.; Katti, D.R. In situ swelling behavior of chitosan-polygalacturonic acid/hydroxyapatite nanocomposites in cell culture media. *Inter. J. Polym. Sci.* **2010**, *12*.
54. Bigucci, F.; Luppi, B.; Cerchiara, T.; Sorrenti, M.; Bettinetti, G.; Rodriguez, L.; Zecchi, V. Chitosan/pectin polyelectrolyte complexes: Selection of suitable preparative conditions for colon-specific delivery of vancomycin. *Eur. J. Pharm. Sci.* **2008**, *35*, 435–441.
55. Flores, E.B.; Vasconcelos, F.C.; Batagliolli, R.; Beppu, M.M. *Chitosan Membrane Physico-Chemical Changes Induced By Buffer Solutions*, 6th Latin American Congress Artificial Organs and Biomaterials, 17–20 August 2010, Brazil.
56. Roncal, T.; Oviedo, A.; de Armentia, I.L.; Fernández, L.; Villarán, M.C. High yield production of monomer-free chitosan oligosaccharides by pepsin catalyzed hydrolysis of a high deacetylation degree chitosan. *Carbohydr. Res.* **2007**, *342*, 2750–2756.
57. Tao, H.; Wei, W.; Mao, Y.; Zhang, S.; Xia, J. Study on degradation characteristics of chitosan by pepsin with piezoelectric quartz crystal Impedance Analysis technique. *Anal. Sci.* **2005**, *21*, 1057–1061.
58. Vishu Kumar, A.B.; Tharanathan, R.N. A comparative study on depolymerization of chitosan by proteolytic enzymes. *Carbohydr. Polym.* **2004**, *58*, 275–283.
59. Kulish, E.; Volodina, V.; Kolesov, S.; Zaikov, G. Enzymatic degradation of chitosan films by collagenase. *Polym. Sci. Ser. B* **2006**, *48*, 244–246.
60. Shepherd, R.; Reader, S.; Falshaw, A. Chitosan functional properties. *Glycoconjug. J.* **1997**, *14*, 535–542.



ELSEVIER

Contents lists available at ScienceDirect

Energy Conversion and Management

journal homepage: www.elsevier.com/locate/enconman

Feasibility study of various sulphonation methods for transforming carbon nanotubes into catalysts for the esterification of palm fatty acid distillate



Siew Hoong Shuit, Soon Huat Tan *

School of Chemical Engineering, Universiti Sains Malaysia, Engineering Campus, Seri Ampangan, 14300 Nibong Tebal, Pulau Pinang, Malaysia

ARTICLE INFO

Article history:

Available online 10 February 2014

Keywords:

Sulphonated multi walled carbon nanotubes
Esterification
Palm fatty acid distillate
Biodiesel

ABSTRACT

Sulphonated multi-walled carbon nanotubes were synthesised and utilised as catalysts to transform palm fatty acid distillate, the low-value by-product of palm oil refineries, into the more valuable product of biodiesel. The most common method to prepare carbon-based solid acid catalysts is thermal treatment with concentrated sulphuric acid, which is a time-consuming and energy-intensive process. Therefore, the feasibility of other sulphonation methods, such as the in situ polymerisation of acetic anhydride and sulphuric acid, the thermal decomposition of ammonium sulphate and the in situ polymerisation of poly(sodium4-styrenesulphonate), were examined in this study. The esterification reaction was performed at 170 °C for 3 h at a methanol to palm fatty acid distillate ratio of 20 and catalyst loading of 2 wt% in a pressurised reactor. The fatty acid methyl esters yields achieved by the sulphonated multi-walled carbon nanotubes prepared via thermal treatment with concentrated sulphuric acid, the in situ polymerisation of acetic anhydride and sulphuric acid, the thermal decomposition of ammonium sulphate and the in situ polymerisation of poly(sodium4-styrenesulphonate) were 78.1%, 85.8%, 88.0% and 93.4%, respectively. All catalysts could maintain a high catalytic activity even during the fifth cycle. Among the sulphonation methods, the in situ polymerisation of poly(sodium4-styrenesulphonate) produced the catalyst with the highest acid group density. In addition, the resonance structures of the benzenesulphonic acid groups attached to the surface of the multi-walled carbon nanotubes generated additional active sites for esterification that led to a higher biodiesel yield.

© 2014 Elsevier Ltd. All rights reserved.

1. Introduction

Fatty acid methyl esters (FAME), collectively known as biodiesel, have been hailed as a potential substitute fuel for petroleum-derived diesel due to their physical and chemical similarities to diesel. Biodiesel is superior to petroleum-derived diesel because it is biodegradable, renewable, clean and non-toxic, exhibits a low emission profile and is environmentally friendly [1,2]. Biodiesel is commonly produced from edible oils, such as palm, rapeseed, canola and sunflower oil. However, the major obstacles in this practice that prohibit the further development of biodiesel are the fluctuating price of refined vegetable oils and the food versus fuel issue [3]. In this regard, the production of biodiesel from non-edible oils, such as palm fatty acid distillate (PFAD) [4], *Jatropha curcas* L. seeds, karanja, castor [5], rubber seed, jojoba, waste animal fat [6] and sea mango (*Cerbera odollum*) [7] would be a solution to this problem. Among

these non-edible oils, PFAD represents a promising feedstock for biodiesel production because it is a low-value by-product generated during the fatty acid stripping and deodorisation stages of the purification process carried out in palm oil refineries [4]; thus, PFAD is much cheaper than other refined oils. Moreover, the high miscibility of free fatty acid (FFA) in methanol [8] makes PFAD even more suitable as a feedstock for biodiesel production because it can reduce the mass transfer limitation caused by the immiscibility between oil and methanol [1].

Homogeneous catalysts were the first generation of catalysts used in biodiesel production. However, the major drawbacks of using homogeneous catalysts in biodiesel production are the corrosion caused by the homogeneous acid catalysts (HCl and H₂SO₄), the difficulty to separate catalysts and the generation of wastewater [9,10]. Therefore, heterogeneous catalysts are preferred to homogeneous catalysts, because their products are easy to separate, the catalysts are reusable and the process is more environmentally friendly [11,12]. Common heterogeneous catalysts used in biodiesel production include mixed metal oxides, alkali metal oxides, ion-exchange resins and sulphated oxides. However, these

* Corresponding author. Tel.: +60 4 5996475; fax: +60 4 5941013.

E-mail address: chshtan@eng.usm.my (S.H. Tan).

conventional heterogeneous catalysts still feature limitations, such as mass transfer resistance, high catalyst cost and low catalyst stability because of leaching [11]. Due to the excellent catalyst stability induced by the covalent bonding between multi-walled carbon nanotubes (MWCNTs) with either basic or acidic functional groups and their high surface areas, MWCNTs can overcome the limitations faced by conventional heterogeneous catalysts and therefore seem to be good catalyst supports for biodiesel production. MWCNTs must be functionalised with acidic groups to convert PFAD, which contains mostly FFA, to biodiesel. The sulphonic group (SO_3H) has been identified as a promising acid catalyst for the catalysis of both transesterification and esterification processes because a high yield of biodiesel can be obtained [11].

The process of functionalising MWCNTs with SO_3H is known as sulphonation [13]. Among the studies reported on the sulphonation of MWCNTs, the process been applied to produce a catalyst for biodiesel production in two studies (the esterification of pure oleic acid and the transesterification of cottonseed oil) [14,15]. MWCNTs sulphonated by other sulphonation methods are usually used as catalysts for oxidation processes [16,17] or to enhance the metal utilisation in fuel cells [18]. Therefore, the main objective of this study was to compare and determine the feasibility of MWCNT-based catalysts produced by various sulphonation methods, including thermal treatment with concentrated sulphuric acid, the thermal decomposition of ammonium sulphate, the in situ polymerisation of acetic anhydride and sulphuric acid and the in situ polymerisation of poly(sodium 4-styrenesulphonate) for the esterification of the low-value industrial by-product PFAD.

2. Materials and methods

2.1. Materials

MWCNTs (Shenzhen Nanotechnologies Port Co.), PFAD (obtained from a local edible oil manufacturing company), nitric acid (HNO_3) (69–70%, JT Baker), sulphuric acid (H_2SO_4) (96%, Fisher Scientific), ammonium sulphate ($(\text{NH}_4)_2\text{SO}_4$) (Fisher Scientific), methanol and n-hexane (Fisher Scientific), acetic anhydride ($(\text{CH}_3\text{CO})_2\text{O}$) (99%, Acros Organics), ammonium persulphate ($(\text{NH}_4)_2\text{S}_2\text{O}_8$) (98%, Acros Organics), poly(sodium 4-styrenesulphonate) (PSS) (Sigma Aldrich) and methyl heptadecanoate (Sigma Aldrich) were used as received.

2.2. Purification of MWCNTs

The process used to purify MWCNTs in this study is similar to that reported elsewhere in the literature [13,19]. A mixture of pristine MWCNTs (1 g) and HNO_3 (100 ml) was subjected to 1 h of ultrasonication treatment before being heated to 80 °C for 8 h. The treated MWCNTs were then filtered, washed with distilled water until the pH of the filtrate was the same as the pH of the distilled water and then dried at 120 °C for 12 h to obtain MWCNTs-COOH, which were then subjected to sulphonation.

2.3. Sulphonation by in situ polymerisation of poly(sodium 4-styrenesulphonate)

This sulphonation method is similar to that reported elsewhere in the literature [18]. In this process, 0.4 g of MWCNTs-COOH was vigorously stirred in a mixture of 0.8 g PSS and 100 ml deionised water (DI) at room temperature for 10 h. Subsequently, 1.6 g $(\text{NH}_4)_2\text{S}_2\text{O}_8$ was added, and the mixture was stirred and heated to 65 °C for 48 h to initiate polymerisation. After cooling to room temperature, the mixture was diluted with 100 ml of DI water, followed by sonication for 1 h, and then washed repeatedly with DI water. The mixture was filtered, mixed with 500 ml of 4 M

H_2SO_4 and then stirred at room temperature for 24 h. Finally, the mixture was filtered, washed with DI water until the pH of the filtrate was the same as that of the pH of distilled water and then dried at 120 °C for 12 h.

2.4. Sulphonation by in situ polymerisation of acetic anhydride and sulphuric acid

The sulphonation conditions and amount of chemicals used in this sulphonation method are based on those reported elsewhere in the literature [16,17]. In this process, 0.2 g MWCNTs-COOH was loaded into a mixture containing 300 ml $(\text{CH}_3\text{CO})_2\text{O}$ and 20 ml concentrated H_2SO_4 . The mixture was stirred and heated to 70 °C for 2 h. The mixture was then continuously stirred until reaching room temperature. The resultant product was filtered, washed with distilled water until the pH of the filtrate was same as the pH of distilled water and then dried at 120 °C for 12 h.

2.5. Sulphonation by thermal decomposition of ammonium sulphate

The sulphonation procedures and amount of chemicals used in this sulphonation method were modified according to those reported elsewhere in the literature [18,20]. In this process, 0.4 g of MWCNTs-COOH was mixed with 30 ml 10% $(\text{NH}_4)_2\text{SO}_4$ solution and sonicated for 10 min. The mixture was then heated to 235 °C for 30 min. The mixture was then washed with distilled water to remove excess $(\text{NH}_4)_2\text{SO}_4$ and dried at 120 °C for 12 h.

2.6. Sulphonation by thermal treatment with concentrated sulphuric acid

This sulphonation method is similar to those reported elsewhere in the literature [19]. In this process, 1 g of MWCNTs-COOH was mixed with 50 ml concentrated H_2SO_4 and sonicated for 30 min. The mixture was then stirred for 12 h at 250 °C under nitrogen flow (100 ml min^{-1}). After cooling to room temperature, the product was filtered, washed with distilled water until the pH of the filtrate was the same as the pH of distilled water and then dried at 120 °C for 12 h.

2.7. Esterification

The esterification of PFAD was carried out in a pressurised reactor under the following conditions: reaction temperature of 170 °C, reaction period of 3 h, methanol-to-PFAD ratio of 20 and catalyst loading of 2 wt%. These reaction conditions were selected based on the trial and error experimentation conducted prior to this study. Upon completion of the reaction period, the mixture was cooled to room temperature and filtered. The excess methanol was removed using a rotary evaporator. Two layers of liquids formed after the evaporation of methanol; the upper layer (dark yellow) was crude fatty acid methyl esters, whereas the bottom layer was water. The volume of the crude fatty acid methyl esters was measured and recorded.

2.8. FAME analysis

The composition and yield of FAME or biodiesel were analysed using a PerkinElmer Clarus 500 gas chromatograph equipped with a flame ionisation detector (FID) and a Nukol™ capillary column. n-Hexane was used as the solvent, and helium was used as the carrier gas. The oven temperature was set to 110 °C and then increased to 220 °C at a rate of 10 °C/min. The temperatures of the detector and injector were set to 220 and 250 °C, respectively. Methyl heptadecanoate was used as an internal standard [21,22]. The yield of FAME in the samples was calculated by the following equation:

$$\text{Yield(\%)} = \frac{(\Sigma \text{Concentration of each methyl esters}) \times (\text{Volume of oil layer})}{10\text{g of PFAD}} \times 100\%$$

2.9. Catalysts characterisations

The zeta potentials of MWCNTs were measured with a Zetasizer Nano-ZS (Malvern Instruments). The presence of SO₃H groups was verified by FT-IR analysis using a SHIMADZU IRPrestige-21 spectrometer. The strength and density of the acid sites of the catalysts were determined by ammonia temperature program desorption (TPD) and pulse chemisorptions, respectively, using a Micromeritics: Auto Chem II 2920 instrument.

3. Results and discussion

3.1. Acid density and FAME yield achieved by various sulphonated MWCNTs

Prior to sulphonation, MWCNTs were refluxed in 69.0% of HNO₃ at 80 °C for 8 h to remove impurities, such as amorphous carbon, graphite compounds, fullerenes, metal particles and most importantly to decorate the ends and sidewalls of MWCNTs with a high density of carboxyl groups for the sulphonation process. The acid treatment was combined with ultrasonication for 1 h to open the tube caps and create defects in the sidewalls to increase the oxidation and sulphonation rate of the MWCNTs [23]. As shown in Table 1, MWCNTs sulphonated via the in situ polymerisation of 4-styrenesulphonate produced the highest FAME yield of 93.4%. MWCNTs sulphonated via the thermal decomposition of ammonium sulphate and in situ polymerisation of acetic anhydride and sulphuric acid produced similar FAME yields of 88.0% and 85.8%, respectively. Moreover, the lowest FAME yield of 78.1% was obtained for MWCNTs sulphonated via thermal treatment with concentrated sulphuric acid.

Because SO₃H groups are active sites for the esterification of PFAD and methanol, the conversion or yield of FAME is directly proportional to the density of SO₃H groups on the surface of MWCNTs. The densities of SO₃H groups grafted on the MWCNT surfaces are listed in Table 1. Among the sulphonation methods, the in situ polymerisation of poly(sodium4-styrenesulphonate) yielded the highest acid site density of 0.061 mmol/g. Thus, the MWCNTs sulphonated via the in situ polymerisation of poly(sodium4-styrenesulphonate) produced the highest FAME yield of 93.4%. The acid densities of MWCNTs sulphonated via the in situ polymerisation of acetic anhydride and sulphuric acid and thermal decomposition of ammonium sulphate were 0.03 mmol/g and 0.029 mmol/g, respectively. Therefore, similar FAME yields were achieved by these two types of sulphonated MWCNTs. Sulphonation via thermal treatment with concentrated sulphuric acid produced the lowest acid group density and FAME yield of 0.016 mmol/g and 78.1%, respectively.

3.2. Zeta potential analysis of the sulphonated MWCNTs

The zeta potential is an electrical potential at the boundary of the hydrodynamic shear plane on the surface of a charged particle

in suspension [24–26]. The magnitude of the zeta potential shows the degree of repulsion or attraction between the suspended particles and thus indicates the potential stability of the colloidal system [26]. In other words, the zeta potential can also be used as an indicator to investigate and compare the surface modification of MWCNTs before and after the acid purification and sulphonation processes. Zeta potential data for the pristine, purified and sulphonated MWCNTs are shown in Table 2. The zeta potential value for pristine MWCNTs in this study was –24.5 mV. Moreover, the zeta potential values for the purified and the four types of sulphonated MWCNTs ranged between –54 and –61 mV. Similarly, the zeta potentials of acid-purified and oxidant modified MWCNTs are reportedly more negative than the pristine MWCNTs [25,27–30]. The high negative surface charge of the acid-purified and sulphonated MWCNTs was due to the presence of acidic groups, such as carboxylic acid and SO₃H groups. In general, particles with zeta potentials more negative than –30 mV are considered stable in the suspension. Therefore, the zeta potential analysis proved that the acid purification and sulphonation processes could modify the surface of MWCNTs.

3.3. IR spectra analysis of the sulphonated MWCNTs

The FTIR spectra of the purified MWCNTs and the four types of sulphonated MWCNTs are shown in Fig. 1. The spectra show significant differences between the purified MWCNTs and sulphonated MWCNTs; the peaks at 1409, 1254, 1062 and 675 cm⁻¹ appear only in the spectra of the sulphonated MWCNTs. The peak at 3691 cm⁻¹ was assigned to the –OH groups [31]. The formation of –OH groups on the sulphonated MWCNTs is very useful because it enhances the catalytic activities of the solid acid catalysts [32]. The band at 1409 cm⁻¹ was attributed to the stretching mode of sulphate groups [19]. The peak at 1254 cm⁻¹ also indicated the presence of sulphonate groups [33]. Moreover, the absorption peak at 1062 cm⁻¹ was attributed to asymmetric and symmetric O=S=O stretching vibrations, and the peak at 675 cm⁻¹ indicated the presence of S–O groups on the surface of the functionalised MWCNTs [34]. In short, the FTIR spectra indicated the feasibility of grafting SO₃H groups on the surfaces of MWCNTs using the four different sulphonation methods.

3.4. TPD analysis of the sulphonated MWCNTs

The TPD profiles of desorbed ammonia (NH₃) on different sulphonated MWCNTs are shown in Fig. 2. The desorption peaks observed at temperatures above 200 °C were attributed to strong acid sites [31]. The TPD results show that the desorption peaks of all of the sulphonated MWCNTs were observed at temperatures above 200 °C, which further demonstrates the ability of all tested sulphonation methods to graft strong acid groups on the surface of MWCNTs, although the resulting acid densities are different. The TPD results also indicate that the sulphonated MWCNTs are stable at the reaction temperature (170 °C) because of the high stability of the active sites on the catalysts. Thus, the problem of leaching of the sulphate groups from sulphonated MWCNTs into

Table 1
Acid density and FAME yield of different sulphonated MWCNTs.

Method of sulphonation	Acid density (mmol/g)	FAME yield (%)
MWCNTs sulphonated by thermal treatment with concentrated sulphuric acid	0.016	78.1
MWCNTs sulphonated by thermal decomposition of ammonium sulphate	0.029	88.0
MWCNTs sulphonated by in situ polymerisation of acetic anhydride and sulphuric acid	0.030	85.8
MWCNTs sulphonated by in situ polymerisation of poly(sodium4-styrenesulphonate)	0.061	93.4

Table 2
Zeta potential of pristine, modified and sulphonated MWCNTs.

MWCNTs	Zeta potential, (mV)
Pristine MWCNTs	-24.5
MWCNTs-COOH	-54.2
MWCNTs sulphonated by thermal treatment with concentrated sulphuric acid	-57.8
MWCNTs sulphonated by thermal decomposition of ammonium sulphate	-57.9
MWCNTs sulphonated by in situ polymerisation of acetic anhydride and sulphuric acid	-58.2
MWCNTs sulphonated by in situ polymerisation of poly(sodium4-styrenesulphonate)	-60.7

the reaction medium can be reduced and thereby enhance the reusability of the catalysts.

In addition to having the highest density of SO_3H groups, the MWCNTs sulphonated via the in situ polymerisation of poly(sodium4-styrenesulphonate) may have shown highest FAME yield due to the resonance structures generated by the benzenesulphonic acid group contained in poly(sodium4-styrenesulphonate). The presence of the three electronegative oxygen atoms not only makes SO_3H a strong acidic group but also an electron-withdrawing group (EWG). As shown in Fig. 3, when the SO_3H group is attached to a benzene molecule, it will remove the electron density from the conjugated π system of the benzene ring via resonance or inductive electron withdrawal, which deactivates the π system by making it

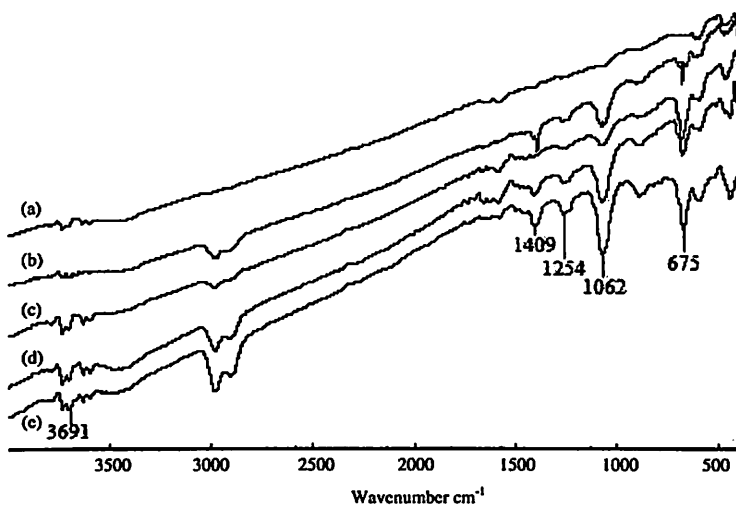


Fig. 1. FT-IR spectra of various sulphonated MWCNTs: (a) purified MWCNTs, (b) MWCNTs sulphonated by thermal treatment with concentrated sulphuric acid, (c) MWCNTs sulphonated by thermal decomposition of ammonium sulphate, (d) MWCNTs sulphonated by in situ polymerisation of acetic anhydride and sulphuric acid and (e) MWCNTs sulphonated by in situ polymerisation of poly(sodium4-styrenesulphonate).

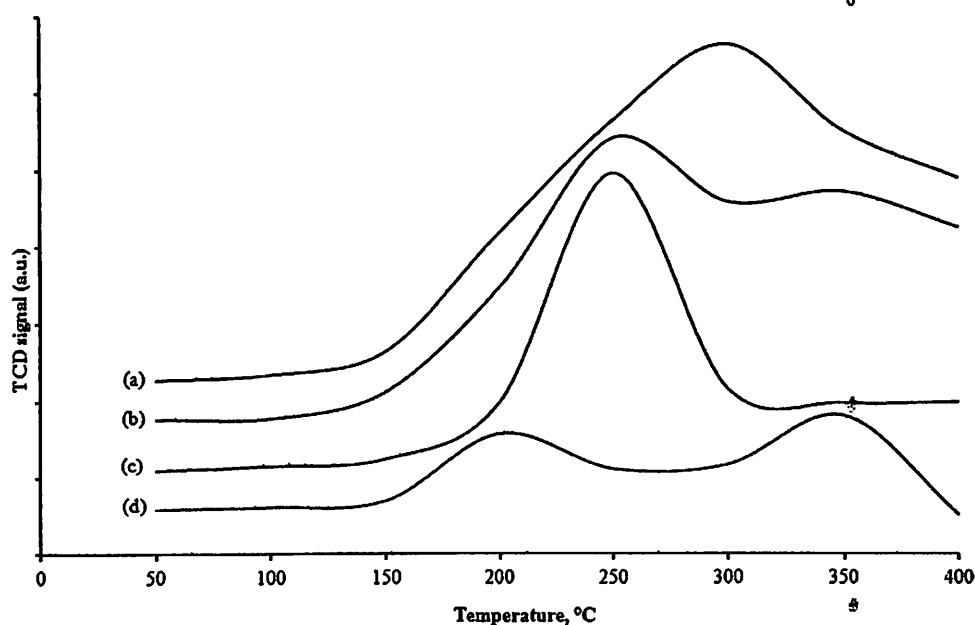


Fig. 2. NH_3 -TPD profiles for different sulphonated MWCNTs: (a) MWCNTs sulphonated by thermal treatment with concentrated sulphuric acid, (b) MWCNTs sulphonated by thermal decomposition of ammonium sulphate, (c) MWCNTs sulphonated by in situ polymerisation of acetic anhydride and sulphuric acid and (d) MWCNTs sulphonated by in situ polymerisation of poly(sodium4-styrenesulphonate).

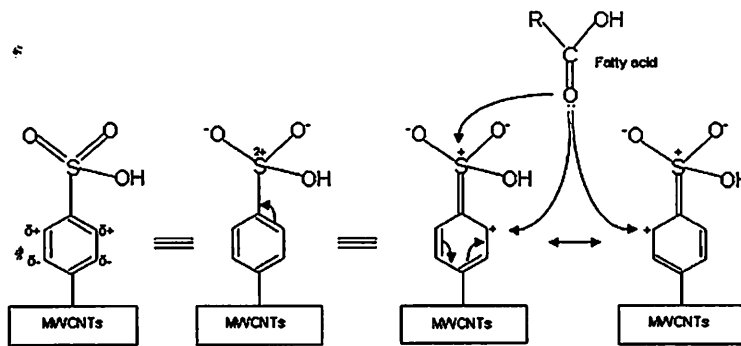


Fig. 3. Possible active sites for the esterification of PFAD generated by the resonance structures of benzenesulphonic acid group attached to the surface of MWCNTs sulphonated via in situ polymerisation of poly(sodium4-styrenesulphonate).

Table 3
Effect of catalyst washing after sulphonation via thermal treatment with concentrated sulphuric acid on the yield of FAME.

Catalysts washing condition	FAME yield (%)
Unwashed sulphonated MWCNTs ^a	95.1
Semi-washed sulphonated MWCNTs ^b	85.8
Washed sulphonated MWCNTs ^c	78.1

^a The mixture of MWCNTs and H₂SO₄ was filtered and directly dried in an oven without washing with distilled water.

^b The mixture of MWCNTs and H₂SO₄ was diluted with distilled water, filtered and dried in oven.

^c The mixture of MWCNTs and H₂SO₄ was filtered and washed repeatedly with distilled water until the pH of the filtrate was the same as the pH of distilled water before drying in oven.

more electrophilic. However, the presence of positive charges in the ortho positions via the deactivation of the benzene ring by SO₃H favours an esterification reaction because the charges at these positions can play a role similar to that of the sulphur atom in the SO₃H group to serve as active sites for the esterification of PFAD with methanol. Among the four sulphonation methods, only the in situ polymerisation of poly(sodium4-styrenesulphonate) can produce

sulphonated MWCNTs with benzenesulphonic acid groups, which possess more active sites for the esterification of PFAD with methanol and thereby enhance the reaction rate and FAME yield.

Even though the sulphonated MWCNTs prepared via the in situ polymerisation of poly(sodium4-styrenesulphonate) showed the highest FAME yield, this particular method required a longer synthesis duration (approximately 4 days) and involved more chemicals and processing steps. Conversely, the in situ polymerisation of acetic anhydride and sulphuric acid and thermal treatment using sulphuric acid required the use of concentrated sulphuric acid as sulphonating agent. This approach will generate wastewater from the repeating washing process. Sulphonation via the thermal decomposition of ammonium sulphate seems to be the best method to prepare sulphonated MWCNTs because this sulphonation method is facile and acid-free.

3.5. Effect of catalyst washing after sulphonation process

Interestingly, the washing of the catalyst after sulphonation is extremely important because it significantly affects the yield of FAME. As shown in Table 3, the unwashed sulphonated MWCNTs

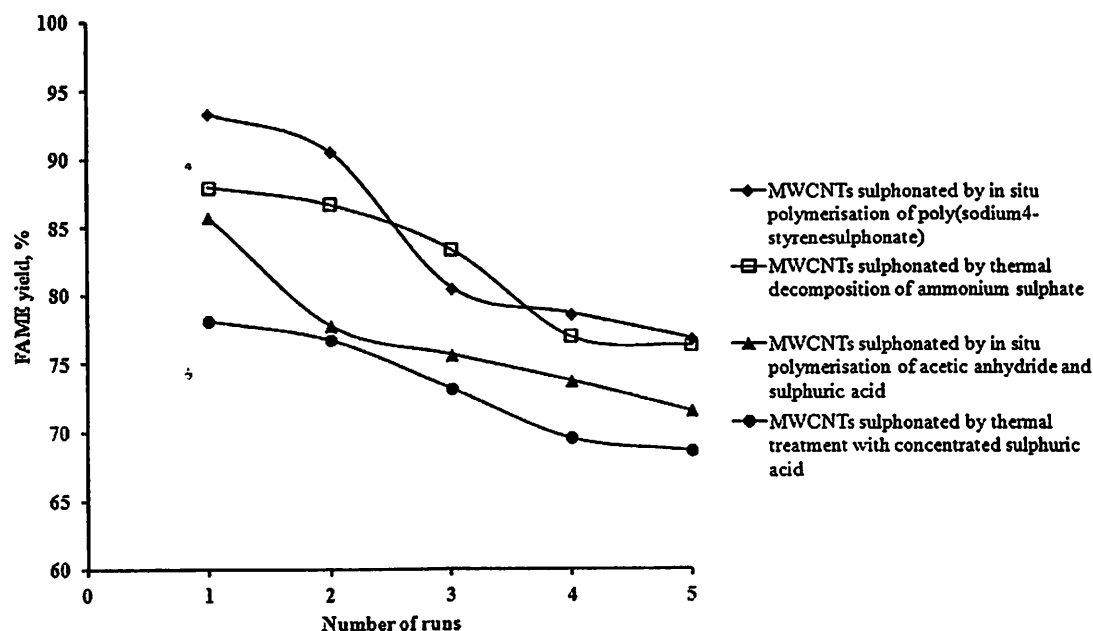


Fig. 4. Reusability of the sulphonated MWCNTs in the esterification of PFAD (reaction temperature of 170 °C, methanol to palm fatty acid distillate ratio of 20, catalyst loading of 2 wt% and reaction period of 3 h).

Table 4
Comparison of the performance of various solid acid catalysts with that of sulphonated MWCNTs for biodiesel production.

Solid acid catalyst	Temperature (°C)	Methanol to oil ratio	Catalysts loading (wt%)	Reaction time (h)	FAME yield (%)
Sulphonated MWCNTs in this study	170	20:1	2.0	3.0	78–93
Sulphated titania-silica composite (S-TSC) [43]	120	20:1	10.0	3.0	77
VOP [37]	150	27:1	6.5	1.0	80
Fe-Zn-1 [38]	170	15:1	3.0	8.0	98
15 WZ-750 [39]	200	20:1	3.0	5.0	97
SO ₄ ²⁻ /SnO ₂ [40]	200	6:1	3.0	4.2	81
SO ₄ ²⁻ /ZrO ₂ [7]	150	12:1	800.0	3.0	97.5
SO ₄ ²⁻ /ZrO ₂ [41]	230	12:1	2.0	8.0	>90
WZ [42]	250	40:1	6.7	4.0	>90

produced the highest FAME yield of 95.1%, which was similar to the FAME yield achieved by using homogeneous H₂SO₄ as catalysts [35,36]. This result further indicates that most of the catalytic effect of the unwashed sulphonated MWCNTs during the esterification of PFAD was attributed to the excess H₂SO₄ attached to the MWCNTs but not the SO₃H groups covalently bonded to the MWCNTs. A similar explanation can be applied to sulphonated MWCNTs that have not been thoroughly washed, for which the FAME yield was higher than that of the thoroughly washed sulphonated MWCNTs. Therefore, the reproducibility of the unwashed and not thoroughly washed sulphonated MWCNTs in the ensuing esterification reaction was expected to be significantly reduced because the attached H₂SO₄ had been leached into the reaction medium.

3.6. Catalysts reusability

The reusability of the sulphonated MWCNTs was evaluated through five consecutive cycles. After esterification, the sulphonated MWCNTs were separated from the reaction mixture by filtration and then sonicated in methanol for 20 min. Next, the catalyst was filtered and repeatedly rinsed with methanol. The washed catalysts were then dried at 120 °C for 12 h. The recovered catalyst was then subjected to esterification under the same reaction conditions. The FAME yields achieved by the sulphonated MWCNTs in five consecutive cycles are shown in Fig. 4. The results show that the four types of sulphonated MWCNTs could maintain the FAME yield above 70% after five cycles. The high reusability of the sulphonated MWCNTs in the esterification was attributed by the ability of MWCNTs to form strong covalent bonds with SO₃H groups.

Comparing the results obtained in this work with those reported in the literature for other solid acid catalysts revealed that the maximum FAME yield obtained (93.4%) for the sulphonated MWCNTs was actually higher than that of most other popular solid acid catalysts, as shown in Table 4 [37–42]. Moreover, sulphonated MWCNTs required 5 times less catalysts than the sulphated titania-silica composite and 3 times less catalysts than the expensive VOP and WZ. Moreover, the sulphonated MWCNTs synthesised in this study required shorter reaction times to achieve yields similar to those obtained using other solid acid catalysts. In short, sulphonated MWCNTs required mild reaction conditions to achieve high FAME yields. Therefore, sulphonated MWCNTs have the potential to reduce the overall production cost of biodiesel if more studies on process optimisation can be carried out to further improve the reaction conditions without sacrificing the FAME yield.

4. Conclusions

In conclusion, the four different sulphonation methods employed in this study could be used to functionalise MWCNTs with strong and stable SO₃H groups. The sulphonated MWCNTs could

result in high yields of biodiesel using PFAD as a feedstock. The MWCNTs sulphonated via the in situ polymerisation of poly(sodium 4-styrenesulphonate) constituted best catalyst, producing the highest FAME yield due to the highest acid group density among all catalysts and the generation of additional active sites for the esterification via the resonance structures of the benzene-sulphonic acid groups attached to the surface of the MWCNTs. Moreover, the sulphonated MWCNTs were also observed to perform better than other popular solid acid catalysts used in esterification or transesterification. The washing of the catalysts after sulphonation was extremely crucial because washing affects the performance of the sulphonated MWCNTs in the esterification reaction. In addition, the sulphonated MWCNTs can maintain a high catalytic activity under the reaction conditions and be reused for a minimum of five cycles. In short, the sulphonated MWCNTs used as catalysts could represent a breakthrough technology for biodiesel production, which warrants further study.

Acknowledgements

Siew Hoong Shuit acknowledges the support of the Ministry of Higher Education of Malaysia through the MyPhD Fellowship. This research was also financially supported by Universiti Sains Malaysia Research University (RU) grant (A/C:814142), USM Membrane Cluster Grant, Fundamental of Research Grant Scheme (FRGS) (A/C:6071212) and Postgraduate Research Grant Scheme (PRGS) (A/C: 8044028).

References

- [1] Shuit SH, Ong YT, Lee KT, Subhash B, Tan SH. Membrane technology as a promising alternative in biodiesel production: a review. *Biotechnol Adv* 2012;30:1364–80.
- [2] Pasupulety N, Gunda K, Liu Y, Rempel GL, Ng FT. Production of biodiesel from soybean oil on CaO/Al₂O₃ solid base catalysts. *Appl Catal A: Gen* 2013;452:189–202.
- [3] Choudhury HA, Malani RS, Moholkar VS. Acid catalyzed biodiesel synthesis from jatropha oil: mechanistic aspects of ultrasonic intensification. *Chem Eng J* 2013;231:262–72.
- [4] Cho HJ, Kim J-K, Hong SW, Yeo Y-K. Development of a novel process for biodiesel production from palm fatty acid distillate (PFAD). *Fuel Process Technol* 2012;104:271–80.
- [5] Helwani Z, Aziz N, Bakar MZA, Mukhtar H, Kim J, Othman MR. Conversion of jatropha curcas oil into biodiesel using re-crystallized hydrotalcite. *Energy Convers Manag* 2013;73:128–34.
- [6] Gürü M, Artukoğlu BD, Keskin A, Koca A. Biodiesel production from waste animal fat and improvement of its characteristics by synthesized nickel and magnesium additive. *Energy Convers Manag* 2009;50:498–502.
- [7] Kansedo J, Lee KT. Process optimization and kinetic study for biodiesel production from non-edible sea mango (cerbera odollam) oil using response surface methodology. *Chem Eng J* 2013;214:157–64.
- [8] Lee JS, Saka S. Biodiesel production by heterogeneous catalysts and supercritical technologies. *Bioresour Technol* 2010;101:7191–200.
- [9] Samart C, Chaiya C, Reubroycharoen P. Biodiesel production by methanolysis of soybean oil using calcium supported on mesoporous silica catalyst. *Energy Convers Manag* 2010;51:1428–31.
- [10] Miao X, Li R, Yao H. Effective acid-catalyzed transesterification for biodiesel production. *Energy Convers Manag* 2009;50:2630–4.

- [11] Shuit SH, Yee KF, Lee KT, Subhash B, Tan SH. Evolution towards the utilisation of functionalised carbon nanotubes as a new generation catalyst support in biodiesel production: an overview. *RSC Adv* 2013;3:9070–94.
- [12] Feyzi M, Hassankhani A, Afafee HR. Preparation and characterization of Cs/Al/Fe₃O₄ nanocatalysts for biodiesel production. *Energy Convers Manag* 2013;71:62–8.
- [13] Yu H, Jin Y, Li Z, Peng F, Wang H. Synthesis and characterization of sulfonated single-walled carbon nanotubes and their performance as solid acid catalyst. *J Solid State Chem* 2008;181:432–8.
- [14] Shu Q, Zhang Q, Xu G, Wang J. Preparation of biodiesel using s-MWCNT catalysts and the coupling of reaction and separation. *Food Bioprod Process* 2009;87:164–70.
- [15] Shu Q, Zhang Q, Xu G, Nawaz Z, Wang D, Wang J. Synthesis of biodiesel from cottonseed oil and methanol using a carbon-based solid acid catalyst. *Fuel Process Technol* 2009;90:1002–8.
- [16] Ramulifho T, Ozoemena KI, Modibedi RM, Jafta CJ, Mathe MK. Fast microwave-assisted solvothermal synthesis of metal nanoparticles (Pd, Ni, Sn) supported on sulfonated mwcnts: Pd-based bimetallic catalysts for ethanol oxidation in alkaline medium. *Electrochim Acta* 2012;59:310–20.
- [17] Sun Z-P, Zhang X-G, Liang Y-Y, Li H-L. A facile approach towards sulfonate functionalization of multi-walled carbon nanotubes as pd catalyst support for ethylene glycol electro-oxidation. *J Power Sources* 2009;191:366–70.
- [18] Du CY, Zhao TS, Liang ZX. Sulfonation of carbon-nanotube supported platinum catalysts for polymer electrolyte fuel cells. *J Power Sources* 2008;176:9–15.
- [19] Peng F, Zhang L, Wang H, Lv P, Yu H. Sulfonated carbon nanotubes as a strong protonic acid catalyst. *Carbon* 2005;43:2405–8.
- [20] Xu Z, Qi Z, Kaufman A. Superior catalysts for proton exchange membrane fuel cells. *Electrochem Solid-State Lett* 2005;8: A313–A5.
- [21] Shuit SH, Lee KT, Kamaruddin AH, Yusup S. Reactive extraction and in situ esterification of *Jatropha curcas* l. Seeds for the production of biodiesel. *Fuel* 2010;89:527–30.
- [22] Shuit SH, Lee KT, Kamaruddin AH, Yusup S. Reactive extraction of *Jatropha curcas* l. Seed for production of biodiesel: process optimization study. *Environ Sci Technol* 2010;44:4361–7.
- [23] Balasubramanian K, Burghard M. Chemically functionalized carbon nanotubes. *Small* 2005;1:180–92.
- [24] Lin D-Q, Brixius PJ, Hubbuch JJ, Thömmes J, Kula M-R. Biomass/adsorbent electrostatic interactions in expanded bed adsorption: a zeta potential study. *Biotechnol Bioeng* 2003;83:149–57.
- [25] Kuo C-Y. Comparison with as-grown and microwave modified carbon nanotubes to removal aqueous bisphenol A. *Desalination* 2009;249:976–82.
- [26] Simate GS, Iyuke SE, Ndlovu S, Heydenrych M. The heterogeneous coagulation and flocculation of brewery wastewater using carbon nanotubes. *Water Res* 2012;46:1185–97.
- [27] Pu Y, Yang X, Zheng H, Wang D, Su Y, He J. Adsorption and desorption of thallium(i) on multiwalled carbon nanotubes. *Chem Eng J* 2013;219:403–10.
- [28] Li Y-H, Wang S, Luan Z, Ding J, Xu C, Wu D. Adsorption of cadmium(ii) from aqueous solution by surface oxidized carbon nanotubes. *Carbon* 2003;41:1057–62.
- [29] Lu C, Chiu H. Adsorption of zinc(ii) from water with purified carbon nanotubes. *Chem Eng Sci* 2006;61:1138–45.
- [30] Li Y-H, Zhu Y, Zhao Y, Wu D, Luan Z. Different morphologies of carbon nanotubes effect on the lead removal from aqueous solution. *Diamond Relat Mater* 2006;15:90–4.
- [31] Lam MK, Lee KT, Mohamed AR. Sulfated tin oxide as solid superacid catalyst for transesterification of waste cooking oil: an optimization study. *Appl Catal, B* 2009;93:134–9.
- [32] Park Y-M, Lee D-W, Kim D-K, Lee J-S, Lee K-Y. The heterogeneous catalyst system for the continuous conversion of free fatty acids in used vegetable oils for the production of biodiesel. *Catal Today* 2008;131:238–43.
- [33] Tripathi BP, Schieda M, Shahi VK, Nunes SP. Nanostructured membranes and electrodes with sulfonic acid functionalized carbon nanotubes. *J Power Sources* 2011;196:911–9.
- [34] Lin Y-W, Wu T-M. Synthesis and characterization of externally doped sulfonated polyaniline/multi-walled carbon nanotube composites. *Compos Sci Technol* 2009;69:2559–65.
- [35] Narasimharao K, Lee A, Wilson K. Catalysts in production of biodiesel: a review. *J Biobased Mater Bioenergy* 2007;1:19–30.
- [36] Wang Y, Ou S, Liu P, Xue F, Tang S. Comparison of two different processes to synthesize biodiesel by waste cooking oil. *J Mol Catal A: Chem* 2006;252:107–12.
- [37] Di Serio M, Cozzolino M, Tesser R, Patrono P, Pinzari F, Bonelli B, et al. Vanadyl phosphate catalysts in biodiesel production. *Appl Catal A: Gen* 2007;320:1–7.
- [38] Sreeprasanth PS, Srivastava R, Srinivas D, Ratnasamy P. Hydrophobic, solid acid catalysts for production of biofuels and lubricants. *Appl Catal A: Gen* 2006;314:148–59.
- [39] Sunita G, Devassy BM, Vinu A, Sawant DP, Balasubramanian VV, Halligudi SB. Synthesis of biodiesel over zirconia-supported isopoly and heteropoly tungstate catalysts. *Catal Commun* 2008;9:696–702.
- [40] Jitputti J, Kitiyanan B, Rangsunvigit P, Bunyakit K, Attanatho L, Jenvanitpanjakul P. Transesterification of crude palm kernel oil and crude coconut oil by different solid catalysts. *Chem Eng J* 2006;116:61–6.
- [41] Chen H, Peng B, Wang D, Wang J. Biodiesel production by the transesterification of cottonseed oil by solid acid catalysts. *Front Chem Eng Chin* 2007;1:11–5.
- [42] Furuta S, Matsuhashi H, Arata K. Biodiesel fuel production with solid superacid catalysis in fixed bed reactor under atmospheric pressure. *Catal Commun* 2004;5:721–3.
- [43] Shao GN, Sheikh R, Hilonga A, Lee JE, Park Y-H, Kim HT. Biodiesel production by sulfated mesoporous titania-silica catalysts synthesized by the sol-gel process from less expensive precursors. *Chem Eng J* 2013;215–216:600–7.

common catalyst supports for transesterification or esterification.

2.2 Low reusability and stability of the catalysts

Low catalyst reusability and stability are the major hurdles encountered when using heterogeneous catalysts for transesterification.³⁴ Leaching of the active species and fouling of the catalyst surface by organic substances in the reaction media have been identified as the main factors in catalysts deactivation.^{34,50,66} Although CaO is very active in the chemical reaction that produces biodiesel, significant leaching of CaO was observed during transesterification.^{67,68} Kouzu *et al.* (2009)⁶⁸ reported that 10.5 wt% of CaO was found to have leached away from the solid base catalyst in the first cycle of transesterification, causing the yield of biodiesel to drop when the catalyst was recycled and reused. Additionally, it was reported that the leaching of CaO was more significant in the presence of glycerol due to the formation of calcium diglyceride.⁶⁷ Mootabadi *et al.* (2010)⁶⁹ reported that when BaO (an alkaline earth metal oxide) was used to produce biodiesel from palm oil, 14 wt% of the catalyst was found to have leached into the biodiesel layer after reaction. In addition, the experiment conducted by López *et al.* (2005)⁷⁰ showed that ETS-10 (Na, K) exhibited a significant drop in triacetin conversion from 90% in the first cycle to 56% in the second cycle, eventually dropping to 28% in the fifth cycle. The reaction liquid was analysed to contain 14 wt% of the Na originally present in ETS-10 (Na, K). The leaching of the active species into the reaction media usually occurred when the catalysts were prepared *via* the wet impregnation method.^{53,66,71} The leaching of metal oxide catalysts is more severe in the presence of polar substances, such as water, free fatty acids (FFA), methanol and glycerol,^{34,67} limiting the use of only refined oil in transesterification. In addition to leaching, the adsorption of organic substances onto the catalysts' surface is another cause of catalyst deactivation. Ngamcharussrivichai *et al.* (2008)⁷² reported that more than 12 wt% of organic substances (methyl esters, glycerol and mono/diglycerides) deposited onto a CaO-ZnO catalyst used in the transesterification of palm kernel oil. However, the spent catalyst could be regenerated and restored to a level of activity comparable to the fresh catalyst by washing with a mixture of methanol and 5 M NH₄OH solution or by thermal treatment at 800 °C.

2.3 High cost of catalysts

The high cost of conventional heterogeneous catalysts is another drawback that limits their use in biodiesel production.⁴¹ Most of the metal catalysts are expensive compared to conventional homogeneous catalysts.³⁴ Due to their superacidity, SO₄²⁻/SnO₂, SO₄²⁻/ZrO₂ and SO₄²⁻/TiO₂ have been used to produce biodiesel from oil sources with high contents of free fatty acids (FFA).^{19,73,74} These catalysts have shown good catalytic activities and stability when esterifying and transesterifying oils with high contents of FFA simultaneously. However, these catalysts, especially Zr, have not been widely applied in commercial biodiesel production mainly because they are rare and expensive metals.^{75,76} Although enzymes (lipases) are potentially more flexible than homogeneous alkali

and acid catalysts in managing a wide range of feedstock conditions and are able to drastically reduce the amount of wastewater generated,^{77,78} their high market price is the major barrier that prevents their industrial application.^{77,79-81}

3 Advantages of CNTs over conventional catalysts in biodiesel production

The limitations of the conventional transesterification catalysts described above, including the mass transfer problem, low stability, limited reusability and high catalyst costs, can be improved by using CNTs as catalyst supports. CNTs are cylinder-shaped macromolecules, a few nanometers in radius, that can grow up to 20 cm in length.⁸² The CNT walls are composed of a hexagonal lattice of carbon atoms. CNTs can be categorised as single-walled carbon nanotubes (SWCNTs) with diameters ranging between 0.4 and 3 nm or multi-walled carbon nanotubes (MWCNTs) with diameters reaching up to 100 nm.⁸³ The intrinsic properties of CNTs, such as high surface area, well-defined morphology and chemical composition, inherent size, hollow geometry, and their ability to graft specific functional groups onto their surfaces, make them suitable catalyst supports.⁸³⁻⁸⁶ The advantages of CNTs over other conventional catalysts in biodiesel production will be discussed in the following section.

3.1 High surface area and well developed porosity

The surface area of porous supports is highly correlated with their pore sizes, which means that supports with large amounts of ultrafine micropores possess high surface areas.⁸⁷ Although the mass transfer limitation encountered in the liquid phase reaction can be significantly reduced by using a catalyst support with a high external surface area,⁸⁸ that limitation will still exist if the catalyst support possesses only micropores, especially when large molecules are involved,^{87,89} because the active phase particles that are located in the micropores limit the accessibility to the reactants and products, thus reducing the effectiveness of the microporosity.⁸⁹ Activated carbon is supposed to be an ideal choice as a catalyst support because it has a larger surface area compared with MWCNTs.⁹⁰ However, the large surface area of activated carbon is mainly concentrated in its microporosity,^{89,90} which may affect the catalytic activity in transesterification involving large molecules such as triglycerides and long chain fatty acids. Therefore, a catalyst support with a large and easily accessible surface area, coupled with the right pore size distribution, is needed.⁸⁹ Table 1 shows the surface area, average pore diameter and porosity type of the various catalysts used in transesterification.^{13,16-19,57,69,70,90-104} The data shows that the specific surface area of MWCNTs is higher than that of most conventional heterogeneous catalysts. Moreover, due to their mesoporous nature and the absence of microporosity, MWCNTs allow high accessibility of the active sites to reactants and products, thus reducing mass transfer limitations.^{105,106} Therefore, MWCNTs are potential catalyst supports for transesterification.

Table 1 Specific surface area, average pore diameter and type of porosity for the various transesterification catalysts

Catalyst	^a	Specific surface area (m ² g ⁻¹)	Average pore diameter (Å)	Porosity ⁹¹	Reference
SWCNTs		400–900	—	Microporous	90
MWCNTs		200–400	—	Mesoporous	90
Activated carbon (AC)		700–1200	—	Microporous	90
CaO		8.1–21.0	44.00–85.91	Mesoporous ^a	69,92,93
SrO		1.05–11.0	135.60	Mesoporous ^a	69,94
BaO		4.0	123.80	Mesoporous ^a	69
VOP	^b	2–4	—	—	95
MgO		96 ± 4	—	—	93
Mg ₃ Al ₂ thoroughly washed		96.0	—	—	13
K/BaO		6.1	50.20	Mesoporous ^a	96
Li/BaO		4.0	66.40	Mesoporous ^a	96
Na/BaO		3.8	66.40	Mesoporous ^a	96
Li/CaO (with 1.25 wt% of Li)		6.9	90.63	Mesoporous ^a	92
Na/CaO (with 1.25 wt% of Na)		12.5	167.17	Mesoporous ^a	92
K/CaO (with 1.25 wt% of K)		18.7	203.79	Mesoporous ^a	92
CaO/ZrO ₂ (Ca to Zr ratio of 0.25)		18.9	79.00	Mesoporous ^a	97
CaO/ZrO ₂ (Ca to Zr ratio of 0.5)		7.3	253.00	Mesoporous ^a	97
WO ₃ /ZrO ₂ (powder)		57.0	130.00	Mesoporous ^a	98
WO ₃ /ZrO ₂ (pellet)		40.0	110.00	Mesoporous ^a	98
CaTiO ₃		4.9	—	—	99
CaMnO ₃		1.5	—	—	99
Ca ₂ Fe ₂ O ₅		0.71	—	—	99
CaZrO ₃		1.8	—	—	99
CaCeO ₃		2.9	—	—	99
CaCO ₃	^c	0.6 ± 0.1	—	—	93
Ca ₃ La ₁		62.6	—	—	100
γ-Al ₂ O ₃		143.1	134.30	Mesoporous ^a	101
NaOH/γ-Al ₂ O ₃		120.7	137.80	Mesoporous ^a	101
Na/γ-Al ₂ O ₃		97.7	148.20	Mesoporous ^a	101
Na/NaOH/γ-Al ₂ O ₃		83.2	155.00	Mesoporous ^a	101
K ₂ CO ₃ /Al ₂ O ₃		118.0	130.20	Mesoporous ^a	96
SBA-15		413	4.20	Microporous ^a	57
SBA-CaO (with 14 wt% of CaO)		7.4	5.40	Microporous ^a	57
SBA-15/MgO		252.0	37.60	Mesoporous ^a	102
MCM-41/MgO		391.0	27.00	Mesoporous ^a	102
KIT-6/MgO		112.0	46.80	Mesoporous ^a	102
Mg(OH) ₂ ·4MgCO ₃		20 ± 0.5	—	—	93
SO ₄ ²⁻ /SnO ₂		6.77	164.00	Mesoporous ^a	19
SO ₄ ²⁻ /SnO ₂ -SiO ₂		13.90	137.00	Mesoporous ^a	19
SO ₄ ²⁻ /SnO ₂ -Al ₂ O ₃		14.04	132.00	Mesoporous ^a	19
Tungstated zirconia (WZ)		68.0–89.2	—	—	103
Sulfated zirconia (SZ)		134.4 ± 5.3	—	—	70
Amberlyst-15		37.8 ± 2.6	—	—	70
Nafion NR50		0.02	—	—	70
Supported phosphoric acid (SPA)		2.6 ± 0.1	—	—	70
Titanosilicate (ETS-10)		440.8 ± 11.8	—	Microporous	70
Zeolite Hβ		620.0	—	—	70
Eggshell		1.1	—	—	17
Golden apple snail shell		0.9	—	—	17
Meretrix venus shell		0.5	—	—	17
Waste mud crab shell		13.0	—	—	16
Calcined waste fish scale		39.0	—	—	18
Cesium-exchanged NaCsX zeolites		450	—	—	104
Hydrotalcite		160	—	—	104

^a The porosity of the catalysts is defined based on the definition stated by Köhn and Fröba, 2003.⁹¹

3.2 Excellent catalyst stability

Unlike other conventional transesterification catalysts, which are prepared by precipitation or impregnation methods, CNTs can be tuned to be catalytically active *via* functionalisation with specific functional groups onto their surfaces.^{83,84} It has been reported that the leaching problem under liquid-phase reaction conditions occurs because the active species are not covalently bonded to the solid support.¹⁰⁷ CNTs appear to be

the perfect candidate to serve as a catalyst support for transesterification/esterification because the functional groups or active species can be chemically modified to covalently bond to the CNTs.⁸³ Covalent bonds between the active species and CNTs are strong bonds that will not easily rupture under the reaction temperature;¹⁰⁸ therefore, the leaching of the active species^{108,109} into the reaction medium can be prevented. Experimental studies wherein no leaching problem occurred during a reaction with covalently modified

CNTs have been reported.^{108,110,111} Because covalent bonding provides the best stability, accessibility and selectivity for the catalysts,¹⁰⁹ CNTs are an ideal alternative catalyst support to overcome the low stability problem encountered by the conventional catalysts used in transesterification.

3.3 Low catalyst cost

As mentioned in section 2.3, the high cost of metal catalysts prevents them from being used in the production of biodiesel. Replacing precious metal catalysts with functionalised CNTs as catalyst supports in transesterification can be more economically feasible. Various technologies, such as electric arc discharge,^{83,112,113} laser ablation pyrolysis,^{83,113–115} chemical vapour deposition (CVD),^{83,113,116} plasma and laser assisted CVD^{117,118} and mechanochemical methods¹¹⁹ have been developed to produce both SWCNTs and MWCNTs. Among these techniques, CVD was determined to be the best method that could produce CNTs in large quantities with low production cost.¹¹³ The price for SWCNTs and MWCNTs is reported to be approximately 50–100 and 15–50 euros per kg, respectively.⁹⁰ The price of CNTs, especially MWCNTs, is actually comparable to that of ZrO₂ (28.34 euros per kg) but much lower than that of WO₃ (61.32 euros per kg).¹²⁰ High catalyst costs can also be the result of using mixed oxide catalysts such as CaO–CeO₂, CaO–MgO and WO₃–ZrO₂. In addition, the price of MWCNTs is even more attractive compared to the price of enzymes (lipases) for industrial-scale use, which cost approximately 774.25 euros per kg.⁷⁷

3.4 Other excellent properties of CNTs

Even though CNTs are considered to be inert compared to other catalyst support materials such as alumina and silica, the presence of five-membered rings at the caps, unsaturated valences at the edges and defects in the graphitic hexagonal crystallites lead to relatively higher reactive sites^{83,89} that enable CNTs to be functionalised through chemical methods. Furthermore, compared to activated carbon, the high purity of CNTs can avoid self-poisoning^{105,106,121} and eventually increase the catalyst's life-time.

The ability to introduce a variety of functional groups onto the CNTs' surface with the purpose of designing specific physicochemical properties^{84,122} allows CNTs to serve as catalyst supports in various catalytic reactions, especially transesterification. A wide variety of feedstocks, such as palm oil, soybean oil, corn oil, jatropha oil, sea mango oil, neem oil, palm fatty acid distillate (PFAD) and waste cooking oil, are now available in the market for biodiesel production. In general, the oil sources can be classified as oil with high contents of water and free fatty acids (FFA) or refined oil. To avoid soap formation when reacting an oil with high FFA and water contents, such as jatropha oil or waste cooking oil,^{74,123} CNTs can be functionalised with an acid group. For reactions with refined oil, CNTs can be functionalised with a base group. Moreover, the impressive mechanical properties and thermal stability^{105,113,121} exhibited by CNTs have encouraged the development of mixed matrix membranes (MMM) used for transesterification. The role of functionalised CNTs can be extended beyond catalyst support to include membrane filling

to enhance the mechanical strength, as well as the chemical and thermal stability, of the membrane.⁴

4 Functionalisation methods to transform CNTs into catalysts for transesterification

CNTs can become catalytically active *via* chemical functionalisation. The CNTs involved in biodiesel production are usually MWCNTs^{8,21} because of their lower price compared to SWCNTs. To create catalysts for transesterification, MWCNTs can be functionalised with 4 different functional groups: a base group,^{8,63} an acid group,²¹ an enzyme,^{124,125} coated with metal oxides or sulfated metal oxides.^{126–128} Prior to functionalisation, CNTs need to be purified to remove the metal catalysts used in the synthesis of the CNTs, as well as other carbon-based impurities. The purification and functionalisation of MWCNTs to create catalysts for transesterification will be discussed in detail in the following sections.

4.1 Purification of CNTs

The purification of CNTs is needed to remove impurities, such as amorphous carbon, graphite compound, fullerenes and metal particles, that form during the CNTs' synthesis process.¹¹³ Among the available purification techniques, liquid phase oxidation by refluxing in an acid solution^{129,130} has been adopted to purify MWCNTs prior to functionalisation to generate catalyst supports for transesterification. This acid treatment is usually associated with the ultrasonication treatment because it can help to disentangle and open the tube caps, forming defects in the sidewalls, followed by oxidation along the walls. Aside from purification, the acid treatment plays another vital role by incorporating the ends and sidewalls of the MWCNTs with a high density of oxygen-containing groups (mainly the carboxyl groups).⁸³ The presence of carboxyl groups on the sidewalls of the MWCNTs is crucial because these groups can undergo a variety of reactions that then enable the MWCNTs to be functionalised with specific functional groups.¹⁰⁹ The MWCNTs used in the production of biodiesel are usually treated in concentrated HNO₃, a mixture of HNO₃ and HCl (in a ratio of 1 : 1) or a mixture of concentrated H₂SO₄ and HNO₃ (in a ratio of 3 : 1) in the temperature range of 50–80 °C for 3 to 24 h.^{129–131} Prior to acid treatment, the MWCNTs are suspended in the acid solution and sonicated for 1 h.¹³⁰ After acid treatment, the MWCNTs are filtered, washed with excess water until neutral, and then dried at 120 °C for 12 h. The purified and treated MWCNTs are denoted as MWCNTs-COOH.¹³¹ The MWCNTs-COOH are then ready to be functionalised with specific functional groups (base, acid or enzyme), depending on the feedstock used in transesterification.

4.2 Functionalisation with amino groups

Amino groups have been reported to be able to anchor onto MWCNTs, transforming them into base catalysts for transesterification.^{8,63} The synthesis routes for the preparation of amino-functionalised MWCNTs are shown in Fig. 2. Amino groups can be grafted onto MWCNTs *via* direct thermal mixing

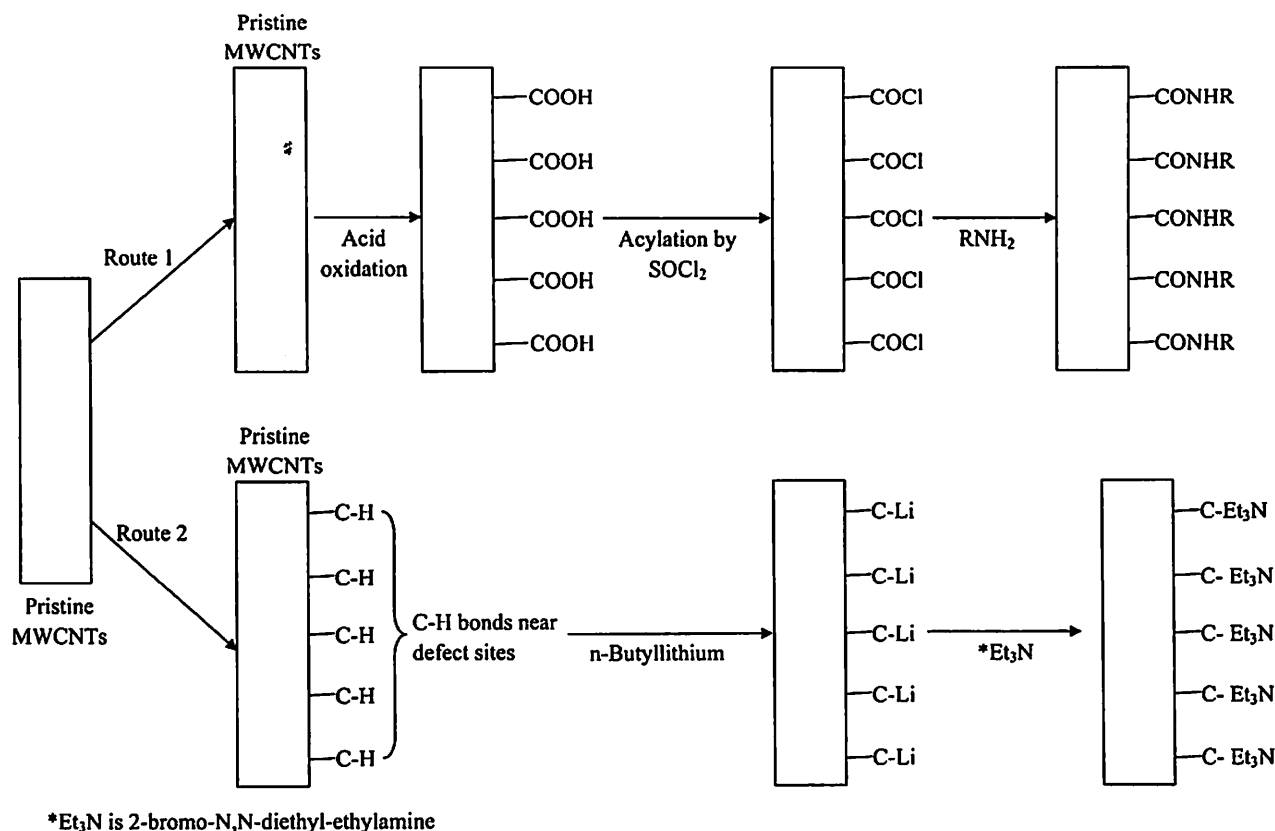


Fig. 2 Synthetic routes for the preparation of amino-functionalised MWCNTs.^{63,132}

of the MWCNTs with long chain amines^{132,133} or direct grafting of the amino groups to surface defects by the C-C coupling reaction.^{8,63} The direct thermal mixing method consists of 3 steps: acid oxidation to create the carboxylic groups, acylation (usually with thionyl chloride (SOCl₂)) and amidation.¹³² The drawback of this technique is that the basic properties of the amino groups will be negatively affected by the nearby acidic O-containing functional groups, causing poor catalytic activity and low stability.⁶³ Therefore, Villa *et al.* (2009, 2010)^{8,63} developed a technique to directly graft the desired amino groups to surface defects by C-C coupling reactions. In their method, pristine MWCNTs are first reacted with *n*-butyl lithium (*n*-BuLi) in excess to activate the terminal C-H bonds near the defect sites and create nucleophilic carbon atoms (C-Li). Then, bromo amino derivatives or bromoalkylamine is added to perform the electrophilic attack on the C-Li bonds to anchor the amino groups to the surface of the MWCNTs, forming N-MWCNTs. Lithium bromide is formed as a by-product.^{8,63} The amine groups, triethylamine, ethylamine and pyrrolidine are then grafted onto the MWCNTs to create the transesterification catalysts Et₃N-CNTs, EtNH₂-CNTs and C₄H₉N-CNTs, respectively. Results from thermogravimetric analysis-mass spectrometry (TG-MS) indicated that the amine groups were successfully anchored on the MWCNTs because all three amino-functionalised MWCNTs were stable at a temperature higher than the boiling point of the corresponding amines. These catalysts were tested in the

transesterification of glyceryl tributyrate with methanol (a model reaction for the production of biodiesel) to produce methyl butanoate. The basic site densities, in mmol g⁻¹, for Et₃N-CNTs, EtNH₂-CNTs and C₄H₉N-CNTs were reported to be 1, 0.99 and 0.54, respectively. With the highest basic site density, Et₃N-CNTs were found to be the most active catalyst, achieving 77% conversion in 8 h of reaction time. Meanwhile, under the same reaction conditions, the EtNH₂-CNTs and C₄H₉N-CNTs catalysts reached much lower conversions of 55% and 20%, respectively.⁸ It was reported that the washing of the amino-functionalised MWCNTs before and after the reaction was a vital procedure.^{8,63} The amino-functionalised MWCNTs were washed after the functionalisation process to remove excess lithium. The trace amount of lithium in the catalyst may contribute to its catalytic activity because lithium is known to be able to catalyse the transesterification reaction.^{63,134,135} Therefore, the amino-functionalised MWCNTs synthesised using *n*-BuLi were thoroughly washed in a methanol solution.⁶³

4.3 Functionalisation with acid catalyst groups

The process of functionalising CNTs with a sulfonic group (SO₃H) is known as sulfonation.¹³⁰ SO₃H has been identified as a promising catalyst group for use in transesterification because high yields of biodiesel can be obtained.¹³⁶⁻¹³⁹ Thus, SO₃H seems to be the perfect candidate to be grafted onto the surface of MWCNTs for the catalysis of transesterification/

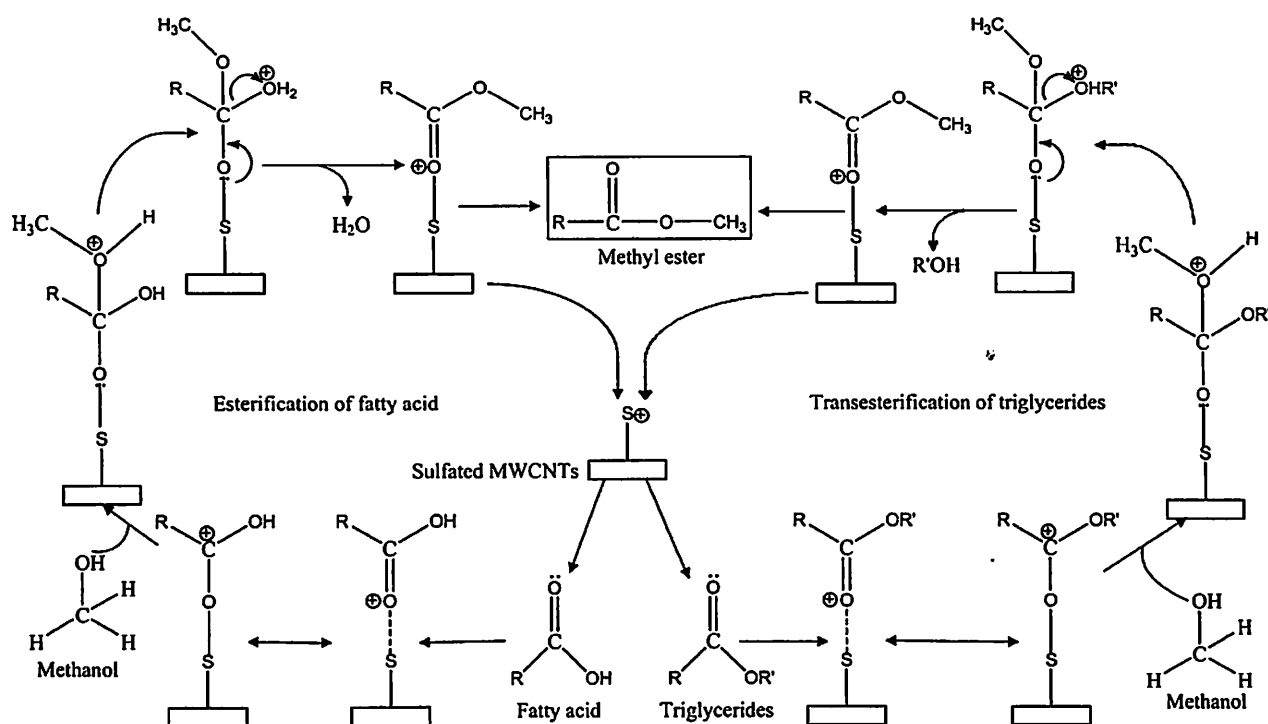


Fig. 3 Reaction mechanism of sulfonated MWCNTs for the transesterification of triglycerides and esterification of fatty acid.¹⁴⁰

esterification. There are 7 types of sulfonation methods that have been reported to functionalise MWCNTs with SO_3H groups. The reaction mechanisms of sulfonated MWCNTs in the transesterification of TG and the esterification of fatty acid have been proposed, as shown in Fig. 3. MG (RCOOR') represents TG in this case. First, the carbonyl oxygen of the free fatty acid and monoglyceride interact with the acidic sites (SO_3H groups) on the MWCNTs' surface to form the carbocation. Then, a tetrahedral intermediate is produced by the nucleophilic attack of the methanol on the carbocation. In the esterification reaction, the tetrahedral intermediate eliminates a water molecule to form one mole of methyl ester. Transesterification is a stepwise reaction in which the TG is

converted to DG, then to MG, and finally to glycerol. Therefore, the tetrahedral intermediate formed during the reaction removes DG, MG and glycerol when TG, DG and MG come in contact with the acidic sites, respectively.¹⁴⁰

4.3.1 Thermal treatment with concentrated H_2SO_4 . Functionalisation of MWCNTs *via* a thermal treatment with concentrated H_2SO_4 is the only reported sulfonation method that has been used to transform MWCNTs into catalysts for biodiesel production.²¹ Sulfonated MWCNTs with a high density of SO_3H groups can be prepared by treating MWCNTs with concentrated H_2SO_4 at high temperature.¹²⁹ The synthesis route of sulfonated MWCNTs is shown in Fig. 4. MWCNTs-COOH obtained from acid oxidation were first

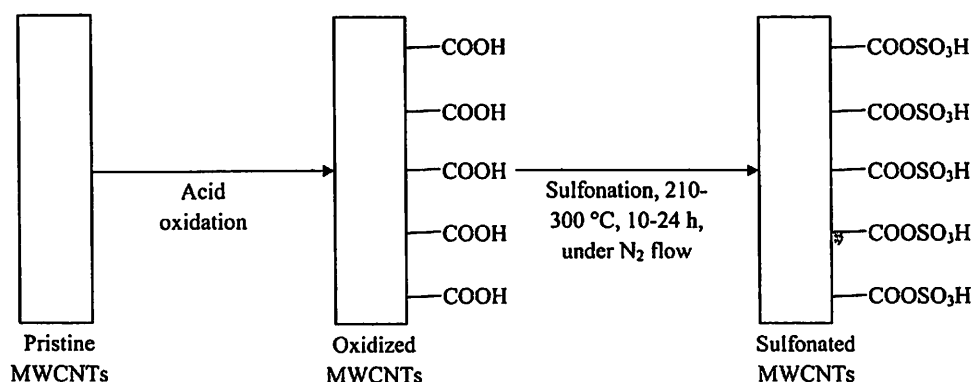


Fig. 4 Sulfonation of MWCNTs *via* thermal treatment with concentrated H_2SO_4 .

mixed with concentrated H_2SO_4 (96–98%)^{21,129,130} and then sonicated for 30 min.^{130,141} The temperature reported for this sulfonation method ranged between 120–300 °C. The functionalisation was carried out for 10–28 h under a blanket of nitrogen (80 mL min^{-1})^{21,129,130,141} to purge or remove moisture in the reaction chamber.¹⁴² After the treatment, the product was washed repeatedly with distilled water to remove excess acid and then was dried at 120 °C for 12 h.^{129,130} The sulfonated MWCNTs are denoted as s-MWCNTs.¹³⁰ It was reported that a higher sulfonation temperature could produce MWCNTs with a higher density of SO_3H groups²¹ because high temperatures favours the surface functionality of MWCNTs with SO_3H groups. High energy must be provided to overcome the energy barrier in the formation of C–S bonds. The presence of SO_3H groups in the MWCNTs was confirmed by the appearance of bands at 1317 cm^{-1} (SO_2 asymmetric stretching mode), 1179 cm^{-1} (SO_2 symmetric stretching mode), 520 cm^{-1} (C–S stretching mode) and 684 cm^{-1} (S=O stretching mode of SO_3H) in the FTIR spectrum. A considerable sulfur element shown in energy dispersive spectrometer (EDS) also indicated the presence of sulfur groups in the MWCNTs. In addition, the binding energy value of 288.8 eV which was assigned as carbon atoms bounded with oxygen or sulfur functionalized groups in X-ray photoelectron spectroscopy (XPS) spectra further confirmed the existence of sulfur groups in MWCNTs. It was estimated that approximately 20 wt% of the SO_3H groups could be anchored onto the CNTs. The surface acidities of the s-MWCNTs were determined by the ammonia temperature-programmed adsorption-desorption technique (NH_3 -TPD) and were reported to be 1.90 mmol g^{-1} .¹³⁰ The acid density of these s-MWCNTs was approximately 32 times higher than that of sulfonated activated carbon (0.06 mmol g^{-1}) produced under the same sulfonation conditions.¹³⁰ The s-MWCNTs were found to disperse well in alcohol (ethanol).^{130,141} This property is believed to provide good contact between the oil, alcohol and catalyst, thus enhancing the reaction rate of transesterification/esterification.

4.3.2 *In situ* polymerisation of acetic anhydride and H_2SO_4 . MWCNTs-COOH from acid oxidation were added to a mixture of 20 mL of H_2SO_4 (95–97% purity) and 300 mL of acetic anhydride ($(\text{CH}_3\text{-CO})_2\text{O}$). The mixture was continuously stirred

for 2 h at 70 °C and allowed to cool to room temperature. The resulting product was repeatedly washed with ultrapure water and dried overnight in an oven at 70 °C. The synthesis route is shown in Fig. 5. The presence of SO_3H groups in the MWCNTs was confirmed by the sulfur peak appeared in EDS spectra¹⁴³ and the FTIR spectrum bands at 682, 1382 and 1726 cm^{-1} (the stretching modes of sulfonic acid groups).¹⁴⁴ This sulfonation method is usually used to adopt metal nanoparticles (Pd, Ni and Sn) to serve as catalysts for oxidation processes such as ethylene glycol electro-oxidation and ethanol oxidation. The deposition of metal nanoparticles onto the s-MWCNTs is based on the electrostatic interaction between the positively charged metal nanoparticles and the negatively charged SO_3H groups.^{143,144}

4.3.3 *In situ* polymerisation of 4-styrenesulfonate. *In situ* polymerisation of 4-styrenesulfonate is another sulfonation approach that can be used to anchor SO_3H groups on the MWCNTs' surface. Two types of 4-styrenesulfonate mixtures have been reported to functionalise MWCNTs: sodium 4-styrenesulfonate (NaSS) mixed with ammonium persulfate ($(\text{NH}_4)_2\text{S}_2\text{O}_8$) and 4-styrenesulfonate mixed with isoamyl nitrite.^{145,146} In the first combination, a predetermined amount of NaSS and purified MWCNTs were mixed with some deionised (DI) water and stirred vigorously for 10 h at room temperature. Then, $(\text{NH}_4)_2\text{S}_2\text{O}_8$ was added, and the mixture was heated to 65 °C with continuous stirring for 48 h to start the polymerisation. After cooling to room temperature, the mixture was diluted with some DI water and sonicated for 1 h. The mixture was then washed several times with DI water and filtered. Then, a large amount of 4M H_2SO_4 was added to the filtered product and stirred for 24 h at room temperature to transform the sulfonated MWCNTs from the Na^+ form to the H^+ form. Eventually, the mixture was washed with excess DI water, filtered and dried in a vacuum oven at 60 °C for 12 h.¹⁴⁶ In the second combination, a proper amount of isoamyl nitrite, purified MWCNTs and 4-styrenesulfonate were stirred for 1 h at room temperature. Then, the temperature was gradually increased to 70 °C with continued stirring for 2 h. The resulting product was washed with dimethylformamide and hot chloroform 3 times and then dried at 70 °C overnight in a vacuum oven to obtain the sulfonated MWCNTs (s-

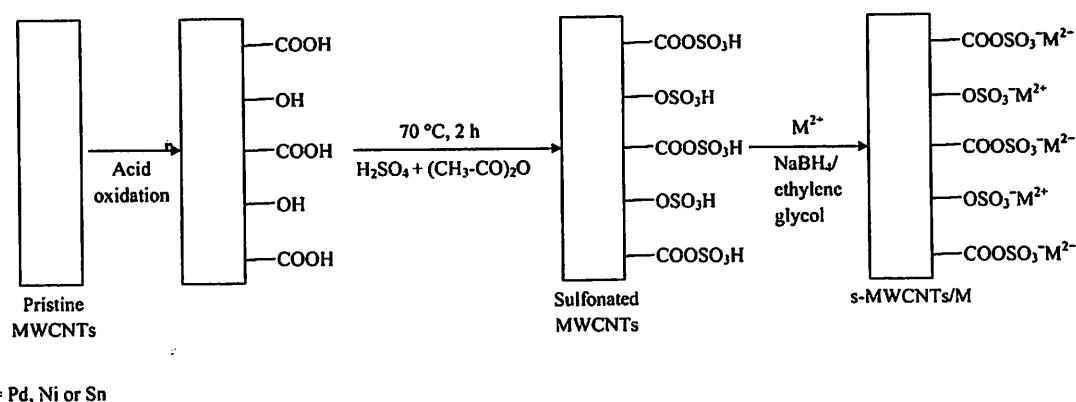


Fig. 5 Sulfonation of MWCNTs via *in situ* polymerisation of acetic anhydride and H_2SO_4 .^{143,144}

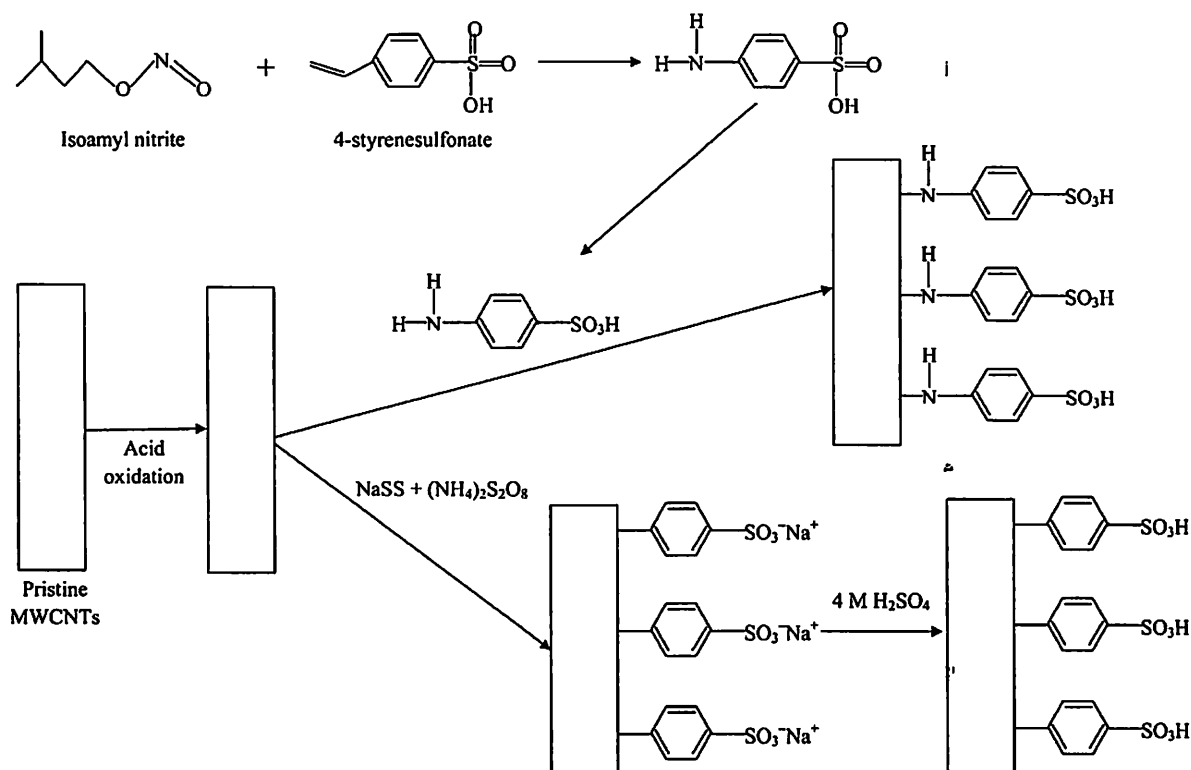


Fig. 6 Sulfonation of MWCNTs *via in situ* polymerisation of 4-styrenesulfonate.^{145,146}

MWCNTs).¹⁴⁵ The synthesis routes for both combinations of 4-styrenesulfonate are shown in Fig. 6. The successful of this method to graft polystyrene sulfonic acid groups onto the MWCNTs was confirmed by FTIR spectra and thermogravimetric analysis (TGA). The peaks at 1044 and 1190 cm^{-1} in FTIR spectra indicated the SO_3 group asymmetric and symmetric vibrational adsorption respectively. Furthermore, a sharp weight loss at 150 °C due to the decomposition of polystyrene sulfonic acid groups in TGA further strengthen the presence of sulfonic groups in MWCNTs.¹⁴⁶ The s-MWCNTs produced by this sulfonation method were used to increase platinum utilisation in fuel cells.^{145,146}

4.3.4 Thermal treatment of *p*-toluenesulfonic acid (TsOH) with *D*-glucose. MWCNTs can also be sulfonated *via* the thermal treatment of *p*-toluenesulfonic acid (TsOH) with *D*-glucose. The sulfonated MWCNTs prepared by this method are also known as carbohydrate-derived solid acid catalysts.¹⁴⁷ The aqueous mixture of purified MWCNTs, TsOH and *D*-glucose was suspended by ultrasonication for 2 h. Then, the suspension was thermally treated in a Teflon-sealed autoclave at 180 °C for 24 h. The products were filtered and washed repeatedly with deionised water and ethanol and then dried in a vacuum oven at 50 °C for 24 h.^{147,148} MWCNTs sulfonated by this method are denoted as MWCNTs/C-SO₃H.¹⁴⁸ The possible mechanism in the synthesis of MWCNTs/C-SO₃H is illustrated in Fig. 7. Glucose was dehydrated to form 5-(hydroxymethyl)-2-furaldehyde (HMF), which would then absorb on to the MWCNTs' surface *via* π - π^* interactions. Next, the HMF was

hydrothermally carbonised and reacted with TsOH to produce C-SO₃H on the surface of the MWCNTs.^{147,148} Finally, the MWCNTs/C-SO₃H was further reacted with pyrrole to obtain the MWCNTs/C-SO₃H/Ppy composite. This composite was obtained *via* low temperature *in situ* polymerisation caused by the strong electron and hydrogen bonding interactions between the SO₃H groups and the amino groups of the pyrrole.¹⁴⁸ The presence of SO₃H groups in MWCNTs was supported by the absorption bands at 1007, 1032 and 1118 cm^{-1} in FTIR spectra and the considerable sulfur element in EDS.¹⁴⁷ This carbon base solid catalyst was used as the electrode material for electrochemical capacitors¹⁴⁸ and in catalysing the esterification reaction of succinic acid and ethanol.¹⁴⁷

4.3.5 Thermal decomposition of ammonium sulfate ((NH₄)₂SO₄). MWCNTs have been sulfonated *via* the thermal decomposition of (NH₄)₂SO₄. First, the MWCNTs were mixed with a predetermined weight percentage of the (NH₄)₂SO₄ solution. The weight percentage was defined as the ratio of the weight of (NH₄)₂SO₄ to the total weight of (NH₄)₂SO₄ and the MWCNTs. After the mixture was well agitated, it was heated at 235 °C for 30 min to produce sulfonated MWCNTs.^{146,149} The synthesis route for this sulfonation method is illustrated in Fig. 8. Hydrogen atoms are always found on the surface of the MWCNTs because they are usually produced from hydrocarbon materials.^{149,150} Therefore, it is believed that the SO₃ groups produced from the decomposition of (NH₄)₂SO₄ at 235 °C react with carbon *via* the surface hydrogen atoms on the

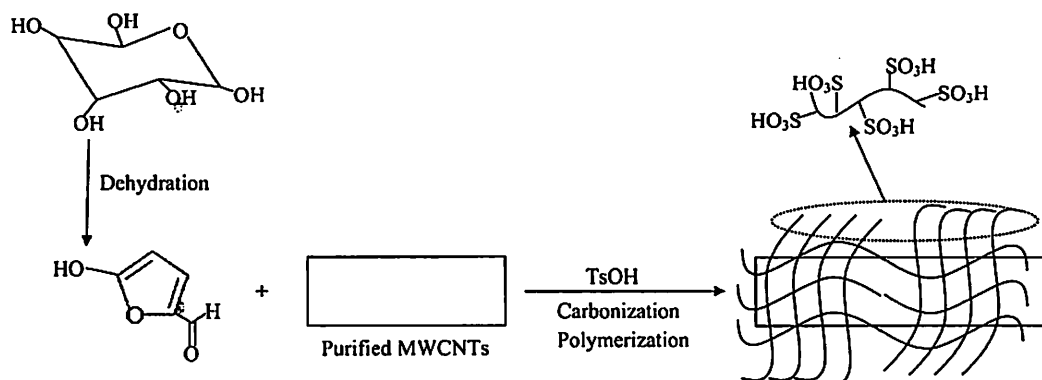


Fig. 7 Proposed mechanism for the synthesis of MWCNTs/C-SO₃H via thermal treatment of *p*-toluenesulfonic acid (TsOH) with D-glucose.^{147,148}

MWCNTs to form the SO₃H groups. EDS confirmed the existence of sulfur group in the sulfonated MWCNTs.¹⁴⁹ This method is normally used to sulfonate the MWCNT-supported platinum catalysts for proton exchange membrane fuel cells and polymer electrolyte fuel cells.^{146,149}

4.3.6 Reaction with aminomethanesulfonic/aminobenzenesulfonic acid. The reaction of MWCNTs with aminomethanesulfonic/aminobenzenesulfonic acid is another sulfonation approach that has been used to graft SO₃H groups onto MWCNTs. Before the reaction with aminomethanesulfonic or aminobenzenesulfonic acid, MWCNTs-COOH was dispersed in a SOCl₂ solution with the aid of sonication for 2 h and then was refluxed with stirring at temperatures in the range of 60–65 °C for 12–24 h.^{131,151} The residual SOCl₂ was removed by either distillation¹⁵¹ or filtration of the homogeneous suspension and then washed with excess distilled water¹³¹ to obtain MWCNTs-COCl. The aminomethanesulfonic acid solution was prepared by dissolving 2 g of aminomethanesulfonic acid in 250 mL of deionised water. Then, the MWCNTs-COCl powder was added to the solution and stirred for 24 h at 80 °C. The resulting product was recovered by filtration through a nylon membrane, followed by drying at 100 °C.¹³¹ In contrast, for the reaction with aminobenzenesulfonic acid, the MWCNTs-COCl was first dispersed in THF and then reacted with a

4-aminobenzene sulfonic acid solution in a slightly basic medium under reflux (60 °C). The mixture was filtered and washed several times with deionised water followed by drying in a vacuum oven for 24 h at 60 °C.¹⁵¹ The effectiveness of this sulfonation method was confirmed by the EDS analysis and the appearance of the absorption bands at 1266 cm⁻¹ (asymmetric stretching vibrations of O=S=O in the SO₃H groups) in the FTIR spectra.¹³¹ Tripathi *et al.* (2011)¹⁵¹ used TGA to confirm and quantify the amount of SO₃H groups grafted into the MWCNTs and the calculated SO₃H groups content was about 8 wt%.

Yang *et al.* (2008)¹⁵² reported a different approach to sulfonate MWCNTs with 4-aminobenzenesulfonic acid. A mixture containing 150 mL H₂SO₄ (96%), 200 mg purified MWCNTs and 100 g (NH₄)₂S₂O₈ was stirred for 6 h. Then, 5.54 g of 4-aminobenzenesulfonic acid was added to the mixture, and stirring was continued for 2 h to effectively disperse the aniline (aminobenzene) throughout the mixture. This was followed by the addition of 2.208 g NaNO₂ and the slow addition of 2,2-azobisisobutyronitrile (AIBN) (1.2 g). The mixture was then homogenised for 6 h at 80 °C in an oil bath. The resulting product was filtered and washed with deionised water, acetone and fresh *N,N*-dimethylformamide (DMF) and then dried in a vacuum oven for 24 h at 50 °C. The

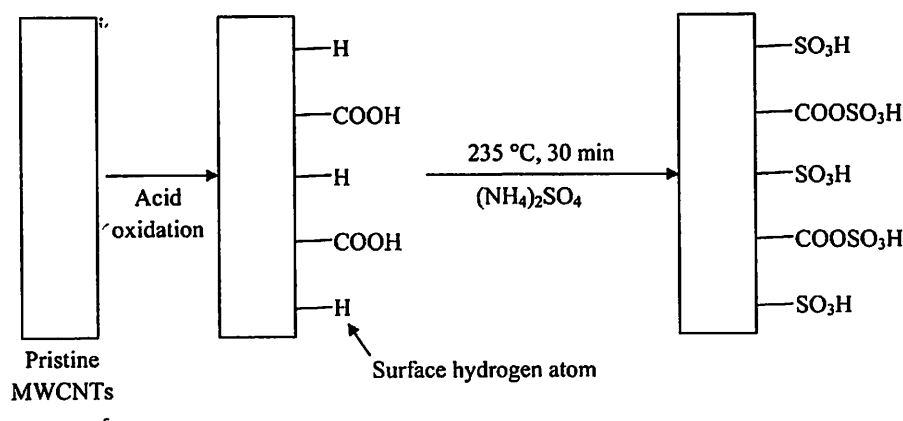


Fig. 8 Sulfonation of MWCNTs via thermal decomposition of (NH₄)₂SO₄.^{146,149}

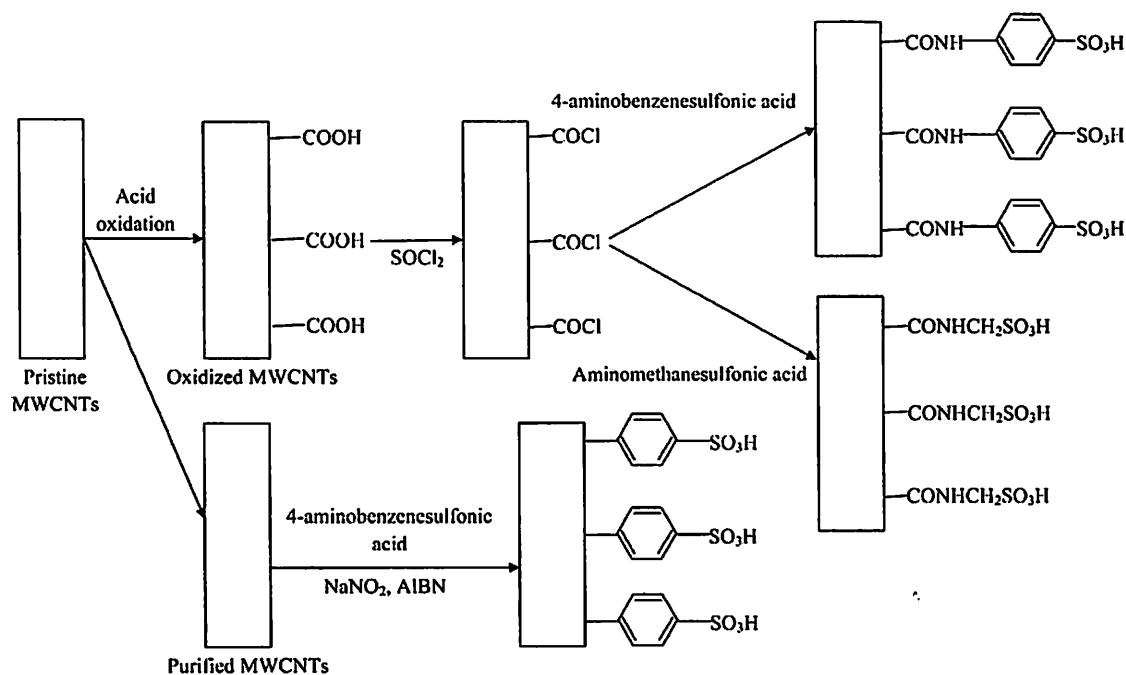


Fig. 9 Sulfonation of MWCNTs via reaction with aminomethanesulfonic/aminobenzenesulfonic acid.^{131,151,152}

presence of SO₃H groups in the MWCNTs was confirmed by the absorption bands at 681 and 1170 cm⁻¹ (S–O group) in the FTIR spectra. Unlike the method of Tripathi *et al.* (2011)¹⁵¹ and Yun *et al.* (2011),¹³¹ the method of Yang *et al.* (2008)¹⁵² did not need –NH₂ groups in the sulphonated MWCNTs. This observation was confirmed when no –NH₂ groups with peaks at 3200–3400 cm⁻¹ appeared in the IR spectrum. This type of sulfonated MWCNTs was used in fuel cell applications.^{131,151,152} Fig. 9 summarised the sulfonation routes of MWCNTs with aminomethanesulfonic/aminobenzenesulfonic acid.

4.3.7 Oxidation of thiol groups by H₂O₂. In this type of sulfonation method, fluorinated single-walled carbon nanotubes (CNT-F) were used instead of MWCNTs-COOH. First, 70 mg of P₄S₁₀ was stirred into a solution that contained 60 mg of sodium and 7 mL of ethanol for 15 min to generate hydrogen sulfide (H₂S), which further reacted with sodium ethoxide to produce soluble H₂S in the suspension. Then, 22 mg of CNT-F was added to the suspension and heated at 70 °C for 3 h. The black product was filtered, washed with ethanol (3 portions in 10 mL) and dried under vacuum to obtain sidewall thiolated carbon nanotubes (CNT-SH). Then, CNT-SH was oxidised in 5 mL of 30% H₂O₂ at 60 °C for 1 h. The product was filtered, washed with ethanol and re-suspended in 10% H₂SO₄ (10 mL) with constant stirring for 1 h to complete the protonation. The final product was filtered, washed until a neutral pH was obtained, and then dried at 80 °C for 12 h. The effectiveness of this sulfonation method was confirmed by FTIR, XPS and TGA analysis. The absorption bands at 700, 1145 and 1202 cm⁻¹ indicated the existence of S–H and SO₃H in the sample. In XPS analysis, the appearance of peak at 169.5 eV was assigned to a higher oxidation state of sulfur, CNT-SO₃H, while the peak at

163.5 eV was assigned to a reduced form of sulfur, CNT-SH. In TGA analysis, the weight loss between 300 and 560 °C caused by the decomposition of SO₃H side groups further confirmed the existence of sulfur groups in the CNTs.¹⁵³ Fig. 10 illustrates the sulfonation route of CNT-F via the oxidation of thiol groups by H₂O₂.

4.4 Functionalisation with enzymes

The biocompatibility of CNTs at the cellular level enables them to be applied in the biological and medical fields.^{154,155} Therefore, many efforts have been focused on the biological functionalisation of CNTs such as enzyme immobilisation.^{124,125,156,157} The resulting enzyme functionalised CNTs have been used in biosensors,^{158,159} biological recognition,^{160,161} the delivery of bioactive molecules^{162–164} and biocatalysts.¹²⁵ The covalent enzyme immobilisation technique has been adopted to prepare biosensors,^{165–167} biofuel cells^{168,169} and biocatalysts.¹²⁵ Both SWCNTs^{154,157} and MWCNTs^{124,125,170} have been used for enzyme immobilisation. It was reported that transesterification and esterification can be catalysed by lipases.^{32,171} Different types of lipases such as *Candida rugosa*,¹²⁴ *Candida antarctica*¹²⁵ and *Pseudomonas cepacia*,¹⁵⁷ have been immobilised on CNTs. To immobilise *Candida rugosa*, MWCNTs were first converted into MWCNTs-COOH via acid oxidation. Then, the MWCNTs-COOH was sonicated in n-hexane for 30 min to produce a homogeneous suspension. Then, *Candida rugosa* was added and the suspension was stirred for 24 h at 60 °C. The lipase functionalised MWCNTs were separated via a centrifuge and washed with ethanol in an ultrasonic bath 3 times. The covalent bonding between the MWCNTs and lipase involved the formation of the sp³, and the disruption of π-electrons by

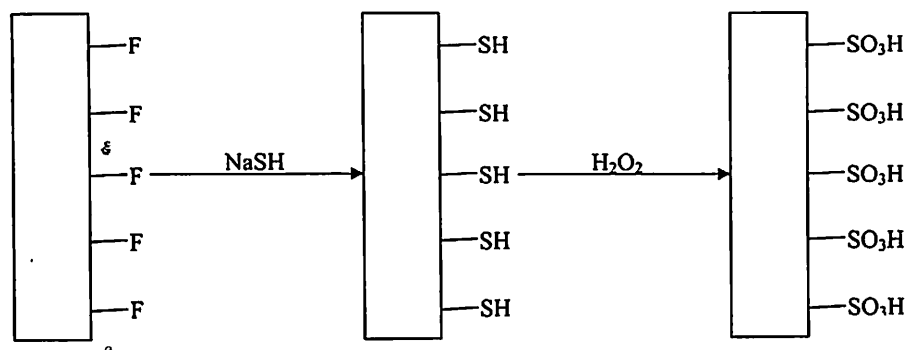


Fig. 10 Sulfonation route of CNT-F via the oxidation of thiol groups by H₂O₂.¹⁵³

the lipase treatment was confirmed by the increase of the A_D/A_G ratio in the Raman spectra from 0.64 to 1.2.¹²⁴

To immobilise *Candida antarctica*, 5 mg of MWCNT-COOH was first sonicated in 11 mL of Tris-HCl buffer at a concentration of 0.05 M and pH 7.5 for 1 h, followed by the addition of 1 mL of enzyme solution. Next, the mixture was incubated, with constant stirring, at 30 °C for 1 h and then at 4 °C for 24 h. The functionalised MWCNTs were centrifugally separated and then washed with water and hexane. If reverse micelles (water in oil microemulsions) were used as the dispersion medium, 5 mg of MWCNTs-COOH was added to 1 mL of iso-octane that contained 0.2 M bis-(2-ethylhexyl) sulfosuccinate sodium salt (AOT). The mixture was subjected to sonication for 5 min. Then, 36 μ L of the enzyme solution was added and vigorously shaken to formulate the reverse micelles. After that, the washing process was similar to that described above. Pavlidis *et al.* (2010)¹²⁵ investigated the ability of enzymes to be immobilised onto different types of functionalised MWCNTs, such as carboxylated MWCNTs (MWCNTs-COOH), poly-amine terminated MWCNTs (MWCNTs-NH) and alkylated MWCNTs (MWCNTs-R), that could be used as immobilisation carriers. Their results showed that a higher enzyme loading was obtained with MWCNTs-COOH due to the recognition of the carboxyl groups by the active sites of the enzyme, leading to the covalent attachment of the enzyme to the MWCNTs-COOH.¹²⁵

In general, the immobilisation of enzymes is carried out in a buffer solution. Owing to the intrinsic van der Waals forces, CNTs are not soluble in the buffer solution, causing the immobilisation process to be inefficient. To overcome this limitation, Lee *et al.* (2010)¹⁵⁷ investigated the immobilisation of *Pseudomonas cepacia* in an ionic liquid at room temperature. SWCNTs were used as the immobilization carrier. The SWCNTs were first suspended in 6 mL of the ionic liquid 1-butyl-3-methylimidazolium tetrafluoroborate (BMIM-BF₄) and then functionalised by reacting with 1-pyrenebutyric acid N-hydroxysuccinimide ester in dimethylformamide (DMF). The mixture was stirred at room temperature for 12 h, followed by the precipitation of the functionalised SWCNTs using 30 mL of methanol. The precipitate was washed with pure methanol and dried under vacuum. Subsequently, the functionalised SWCNTs were re-suspended in BMIM-BF₄, followed by the addition of the *Pseudomonas cepacia* lipase. The heterogeneous

mixture was stirred at room temperature for 24 h. The mixture was then filtered, washed with a phosphate buffer and then dried under vacuum. The results showed that the enzyme immobilisation was most efficient when conducted in an ionic liquid medium. Fig. 11 summarises the synthesis routes of lipase functionalised CNTs.

4.5 CNTs coated with metal oxides or sulfated metal oxides.

Metal oxides such as ZrO₂ or TiO₂ and their sulfated derivatives (SO₄²⁻/ZrO₂ and SO₄²⁻/TiO₂) have been reported as transesterification/esterification catalysts. Therefore, it is possible that the CNTs coated with these metal oxides or their sulfated derivatives could serve as catalysts in biodiesel production. There are several ways to synthesise CNTs/ZrO₂, including the hydrothermal crystallisation of zirconium hydroxide in the presence of CNTs at 200 °C,¹⁷² hydrothermal treatment of MWCNTs in an ZrOCl₂·8H₂O aqueous solution,¹⁷³ isothermal hydrolysis of ZrOCl₂·8H₂O and the conventional chemical precipitation method.¹²⁶ In the isothermal hydrolysis process, a 0.2 M solution was prepared from solid ZrOCl₂·8H₂O (the precursor to the synthesis of the ZrO₂ coating). Then, 30 mg of MWCNTs (without any pretreatment) was added to the aqueous solution, and the mixture was subjected to 30 min of sonication to produce a black suspension of MWCNTs. The resulting suspension was then refluxed in a thermostatic water bath at 100 °C to carry out the isothermal hydrolysis of ZrOCl₂. During the hydrolysis process, the suspension was sonicated for 10 min every 24 h to maintain a good dispersion of the MWCNTs in the aqueous solution. The reaction was stopped when the black suspension turned grey. High-resolution transmission electron microscopy (HRTEM) images showed that the isothermal hydrolysis process was able to produce MWCNTs with uniform coverage of the ZrO₂ nanoparticles. However, the chemical precipitation process produced a non-homogeneous and non-uniform ZrO₂ coating because of the rapid reaction caused by the addition of NH₄OH into the suspension.¹²⁶

Sulfated zirconia and sulfated TiO₂ supported on MWCNTs composites have been prepared using a similar method. Their synthesis begins with the use of ZrOCl₂·8H₂O or Ti(SO₄)₂, ammonia (NH₃) and H₂SO₄ as the starting material, precipitating agent and sulfating agent, respectively. First, a predetermined amount of MWCNTs was mixed with the 0.2 M ZrOCl₂·8H₂O solution or Ti(SO₄)₂ solution. Then, the NH₃

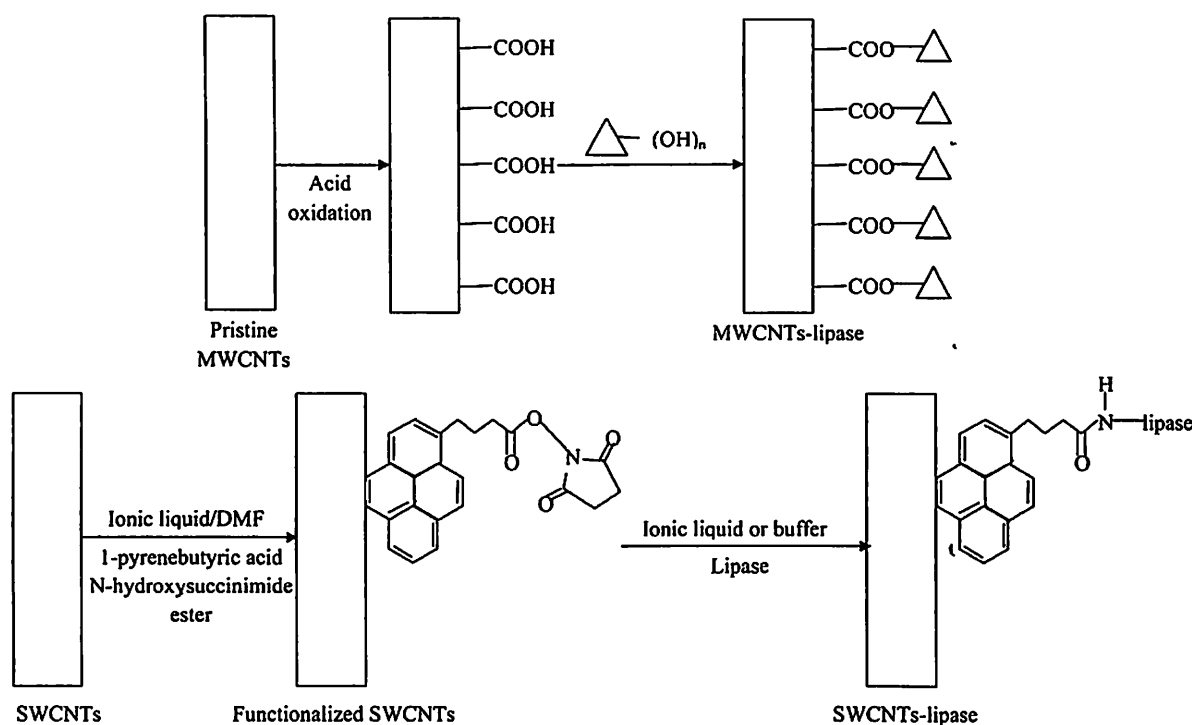


Fig. 11 The synthetic routes of lipase functionalised CNTs.^{124,125,157}

aqueous solution was gradually dropped into the mixture to adjust the pH to 10, and the mixture was stirred for 24 h at room temperature. No washing was performed for the sulfated TiO_2 , and the solution was subjected to the drying process at 110°C for 24 h. In the case of the sulfated ZrO_2 , the obtained $\text{ZrO}_2 \cdot n\text{H}_2\text{O}$ sol was centrifugally washed with distilled water until none of the Cl^- ions could be detected by AgNO_3 , and then it was dried at 110°C for 10 h. The sulfating agent of 0.5 M H_2SO_4 was mixed with the grounded $\text{ZrO}_2 \cdot n\text{H}_2\text{O}/\text{MWCNTs}$ composites or $\text{TiO}_2/\text{MWCNTs}$ composites and vigorously stirred for 15 min or 1 h, respectively. After filtration and drying at $90\text{--}100^\circ\text{C}$, the powder was calcined at 550°C under N_2 flow for 1 h to produce the $s\text{-ZrO}_2/\text{MWCNTs}$ or $s\text{-TiO}_2/\text{MWCNTs}$. The presence of sulfate groups in these composites were confirmed by IR spectra analysis. Both the $s\text{-ZrO}_2/\text{MWCNTs}$ and $s\text{-TiO}_2/\text{MWCNTs}$ composites were used to enhance electron and proton conductivity as well as the catalytic activity of the Pt electrocatalyst in alcohol (methanol and ethanol) electro-oxidation.^{127,128} It is believed that both composites could be used as transesterification/esterification catalysts because the superacid nature of the sulfated TiO_2 and sulfated ZrO_2 remained unchanged in the MWCNTs composites.^{127,128}

5 Process parameters for biodiesel production using functionalised CNTs as catalysts

To produce biodiesel in a more sustainable and cost effective manner, the most important process parameters that should

be taken into consideration will be discussed in the following sections. The performance of various catalysts and their reaction conditions are summarised in Table 2.^{21,28,35,63,95,101,130,174-189}

5.1 Reaction temperature

Villa *et al.* (2010)⁶³ investigated the effects of the reaction temperature on the catalytic activity of amino-functionalised MWCNTs ($\text{Et}_3\text{N-CNT}$) in the transesterification of glyceryl tributyrate with methanol. At 90°C , a complete conversion of glyceryl tributyrate could be achieved in 2 h. If the reaction temperature was lower than 75°C , 6 h were needed to achieve 90% conversion. A higher energy consumption and higher pressure were needed to maintain methanol in the liquid phase at the higher reaction temperature; thus, a lower reaction temperature is more suitable. However, the lower reaction temperature needed a longer reaction time. At a reaction temperature of 60°C and a reaction time of 8 h, a conversion of 77% was reported. Similar to the other basic catalysts, such as NaOH , $\text{Na}/\text{NaOH}/\gamma\text{-Al}_2\text{O}_3$, BaZnO and KF/ZnO , $\text{Et}_3\text{N-CNT}$ showed good activities at low temperature. Other basic catalysts such as MgO(III) , CHT , ZnO , KNO_3/KL zeolite and $\text{KNO}_3/\text{ZrO}_2$, required much higher reaction temperatures because the basic sites of these catalysts are of medium strength.¹⁹⁰

The CNTs-based solid acid catalyst $s\text{-MWCNTs}$ produced *via* thermal treatment with concentrated H_2SO_4 were used to catalyse the esterification of oleic acid with methanol to produce methyl oleate. An increase in the reaction temperature from 120 to 135°C caused a significant increase in the conversion of oleic acid, from 93.2 to 95.5%, in a reaction time

Table 2 Comparison of reaction conditions and performances of various biodiesel production catalysts

Reaction conditions										
	Feedstock	Catalyst used	<i>T</i> (°C)	Methanol to oil molar ratio	Catalyst concentration, wt%	Reaction time, <i>t</i>	Catalyst basicity/acidity, mmol g ⁻¹	Yield (%)	References	
Homogeneous base	Sunflower oil	NaOH	60	6 : 1	1.0	2.0	—	97	174	
Homogeneous acid	Soybean oil	H ₂ SO ₄	65	30 : 1	1.0	50.0	—	Conversion >99	175	
	Waste cooking oil	H ₂ SO ₄	95	20 : 1	4.0	10.0	—	Conversion >90	176	
Heterogeneous base	Soybean oil	Na/NaOH/γ-Al ₂ O ₃	60	9 : 1	2.3	2.0	—	83	101	
	Glyceryl tributyrate	Et ₃ N-CNT	60	12 : 1	2.0	8.0	1.00	77	63	
	Soybean oil	Ba/ZnO	65	12 : 1	6.0	1.0	14.54	Conversion = 95	177	
	Soybean oil	KF/ZnO	65	10 : 1	3.0	9.0	1.62	Conversion = 87	178	
	Soybean oil	KNO ₃ /Al ₂ O ₃	Methanol reflux temperature	15 : 1	6.5	7.0	6.67	Conversion = 87	179	
	Soybean oil	KI/Al ₂ O ₃	Methanol reflux temperature	15 : 1	2.5	8.0	1.56	Conversion = 96	28	
	Soybean oil	MgO (III)	200	11 : 1	5.0	1.0	3.9 CO ₂ μmol m ⁻²	>95	180	
	Soybean oil	CHT	200	11 : 1	5.0	1.0	2.6 CO ₂ μmol m ⁻²	>95	180	
	Crude coconut oil	KNO ₃ /KL zeolite	200	6 : 1	3.0	4.2	—	77	181	
	Crude coconut oil	KNO ₃ /ZrO ₂	200	6 : 1	3.0	4.2	—	66	181	
	Crude coconut oil	ZnO	200	6 : 1	3.0	4.2	—	78	181	
	Heterogeneous acid	Oleic acid	HMF(25) zeolites	60	15 : 1	5.6	1.0	0.08	85	182
		Oleic acid	s-MWCNTs	135	6.4 : 1	0.2	1.5	1.9 ¹³⁰	Conversion = 96	21
		Soybean oil	VOP	150	27 : 1	6.5	1.0	—	80	95
Acidic sunflower oil		Fe-Zn-1	170	15 : 1	3.0	8.0	1.96 ¹⁸³	Conversion = 98	184	
Crude coconut oil		SO ₄ /SnO ₂	200	6 : 1	3.0	4.2	—	81	181	
Sunflower, mustard and sesame oil		15 WZ-750	200	20 : 1	3.0	5.0	2.6 NH ₃ nm ⁻²	97	185	
Soybean oil		WZ	250	40 : 1 ^a	6.7 ^a	4.0	—	Conversion >90	35	
Cottonseed oil		SO ₄ ²⁻ /ZrO ₂	230	12 : 1	2.0	8.0	—	>90	186	
Purified palm oil		SO ₄ ²⁻ /ZrO ₂	250	24 : 1	0.5	10 min	0.495	Conversion = 90	187	
Palm fatty acid		SO ₄ ²⁻ /ZrO ₂	250	6 : 1	0.5	1 min	0.495	Conversion = 75	187	
Immobilised enzyme	Soybean oil	SZA	300	40 : 1 ^a	6.7 ^a	4.0	—	80	35	
	Crude palm oil	Lipase <i>T. lanuginosus</i>	30	6.5 : 1	6.7	6	—	85	188	
	Jatropha <i>curcas</i> oil	Lipase from <i>E. aerogenes</i>	Room temperature	4 : 1	5	30 min	—	Conversion = 85	189	

^a Self-estimation.

of 1.5 h. The conversion slightly decreased to 95.4% when the temperature was further increased to 145 °C. The decrease in oleic acid conversion implied that the reaction equilibrium was achieved. Therefore, the optimum temperature for the esterification of oleic acid catalysed by s-MWCNTs is 135 °C, with a reaction time of 1.5 h.²¹ As shown in Table 2, the reaction temperature required for s-MWCNTs is approximately 50% less than that for other solid acid catalysts such as SO₄²⁻/ZrO₂, WZ and SZA.

Due to the slower reaction rate of acid catalysed transesterification/esterification, the reaction temperature required for acid catalysts is higher than that for basic catalysts. However, acid catalysts are more flexible than basic catalysts because they are less sensitive to FFA and can perform transesterification and esterification reactions simultaneously.^{191,192} Therefore, s-MWCNTs can potentially produce biodiesel from cheaper feedstocks, such as non-edible oils, waste cooking oils and even unrefined crude oils with high FFA content, to reduce the overall biodiesel production cost. Irrespective of the type of catalysts used to produce biodiesel, the conversion of oil to FAME was found to be positively affected by increasing the reaction temperature. This increase can be easily justified because transesterification/esterification is an endothermic process.^{193,194} According to the Le Chatelier's principle, by increasing the temperature, the equilibrium of the reaction can shift to the forward direction, favouring the conversion of oil or FFA into FAME.

5.2 Methanol to oil ratio

The molar ratio of the oil/FFA to methanol is another crucial factor in transesterification or esterification. Based on the stoichiometric equation, three moles of methanol per mole of TG are required for transesterification. Meanwhile, one mole of methanol per mole of fatty acid is needed for esterification.¹⁹⁵ Due to the reversible nature of both the transesterification and esterification reactions, a large excess of methanol is required to drive the reaction forward towards the formation of FAME.⁵ Different molar ratios of methanol to glyceryl tributyrates (6 : 1, 12 : 1, 24 : 1 and 60 : 1) were studied in the transesterification reaction catalysed by Et₃N-CNT. It was reported that the system became more active with a higher amount of methanol. Complete conversion was achieved for molar ratios of 24 : 1 and 60 : 1 in 4 h and 2 h, respectively. When using a molar ratio of 12 : 1, 77% conversion was obtained after 8 h. In contrast, for a molar ratio of 6 : 1, a fast deactivation of the catalysts was observed, which may have been due to the strong adsorption of oil (glyceryl tributyrates) to the active sites. Considering the overall production cost of biodiesel, the optimum methanol to glyceryl tributyrates ratio was determined to be 12 : 1.⁶³

In the esterification reaction with s-MWCNTs as the catalyst, the effect of different molar ratios of methanol to oleic acid (5.2 : 1, 5.8 : 1, 6.4 : 1, 7 : 1 and 7.6 : 1) was studied. The oleic acid conversions for methanol to oleic acid ratios of 5.2 and 6.4 were 94.4 and 95.9%, respectively. Further increasing the molar ratio to 7.6 only caused a slight 0.2% increase in the oleic acid conversion, to 96.1%. Therefore, the optimum methanol to oleic acid ratio for the esterification catalysed by s-MWCNTs was reported to be 6.4 : 1.²¹ It is believed that both

the transesterification and esterification reactions begin with the chemisorptions of the triglycerides and fatty acids on the active sites of the catalysts. These chemisorbed molecules are then protonated at the carbonyl group to form carbocations, which are then attacked by methanol to produce esters. In an environment with excess methanol, the attack of the methanol molecules on the carbocations is enhanced, thus increasing the conversion. However, if the molar ratio of methanol to oil/fatty acid is too extreme, the catalyst active sites will be flooded by an excess of methanol instead of triglycerides or fatty acid. Therefore, a concentration of methanol that is too high in the transesterification/esterification system will prevent the TG or fatty acid molecules from being protonated at the active sites of the catalysts.^{21,65} In addition, the higher the methanol to oil/fatty acid ratios, the more difficult the separation of the non-polar phase from the polar phase.¹⁹⁶ Moreover, when the molar ratio increases, the separation cost of excess methanol *via* distillation also increases.¹⁹⁷

5.3 Catalyst concentration

Shu *et al.* (2009)²¹ studied the effect of various s-MWCNTs loadings on the conversion of oleic acid with methanol. The amount of s-MWCNTs used in the reaction varied from 0.14 to 0.24 wt% based on the weight per cent of oleic acid. The reaction temperature and methanol ratio were fixed at 135 °C and 6.4, respectively. The conversion of oleic acid was found to be positively affected by the catalyst concentration because the total number of available active sites for reaction increased when the catalyst concentration increased. An increase in the catalyst concentration from 0.14 to 0.20 wt% caused an increase in the conversion of oleic acid from 93.6 to 95.4%. However, a further increase in the catalyst loading, from 0.2 to 0.24 wt%, caused only a minor conversion increase of 0.6%. Therefore, the reported optimum catalyst concentration for the esterification of oleic acid using s-MWCNTs was determined to be 0.2 wt%. It is interesting to note that the esterification process of oleic acid using the s-MWCNTs catalyst required 5 times less catalyst than the homogeneous NaOH catalysts, as shown in Table 2. This can further reduce the overall production cost of biodiesel.

Regardless of the MWCNTs' functionality (either base or acid catalyst groups), the catalyst concentration used in the reaction was strongly dependent on the amount of functional groups grafted on the MWCNTs.^{8,63} In other words, the catalyst concentration is correlated to the basic or acid site density of the functionalised MWCNTs. Villa *et al.* (2009)⁸ compared the performance of different amines grafted on MWCNTs in the transesterification of glyceryl tributyrates with methanol. C₄H₉N-CNTs showed the lowest catalytic performance because they contained the least number of amino groups grafted on the MWCNTs and the lowest basic site density (0.54 mmol g⁻¹) compared to Et₃N-CNTs and EtNH₂-CNTs (which had basic site densities of 1.00 and 0.99 mmol g⁻¹, respectively). To achieve the same yield, a higher amount of catalyst with a lower basic or acid density is required. Using the same type of amino-functionalised MWCNTs (Et₃N-CNTs) but with a different basic site density, which could be tuned by grafting amines at different pK_a values, Villa *et al.* (2010)⁶³ further confirmed that the catalyst with the highest concen-

tration of basic groups was the most active catalyst in the transesterification of glyceryl tributyrate with methanol. Therefore, the abundance of functional groups on the surface of the MWCNTs is a key factor for highly active catalysts.

5.4 Reaction time

The reaction time for the transesterification catalysed by Et_3N -CNTs was greatly influenced by the reaction temperature and methanol to oil ratio used during the reaction. At a fixed catalyst concentration and methanol to oil ratio, complete conversion was achieved in only 2 h if the reaction temperature was increased to 90 °C. As the reaction temperature decreased to 75 °C, the reaction time required to achieve 90% conversion was increased to 6 h, whereas at 60 °C, it took 8 h to achieve only 77% conversion. However, when using the highest methanol to oil ratio, 60 : 1, complete conversion was achieved in 2 h. Meanwhile, for a methanol to oil ratio of 24 : 1, 50% more time (4 h) was required to achieve complete conversion.⁶³ It is believed that the same situation arises wherein an increase in catalyst concentration can reduce the reaction time because the active sites available for reaction are increased.

Regardless of the catalyst types (homogeneous or heterogeneous)^{19,20,198} and the technologies (conventional, supercritical and reactive extraction)^{123,199} used to produce biodiesel, the conversion or yield of biodiesel is found to increase with longer reaction times until equilibrium is achieved. When using *s*-MWCNTs as the catalyst at 135 °C and with a 6.4 : 1 methanol to oleic acid ratio, an increase in the reaction time from 1.5 to 2 h caused a slight decrease in oleic acid conversion, from 95.5 to 95.1%. Therefore, it can be concluded that the reaction equilibrium was reached after 1.5 h when using *s*-MWCNTs as a catalyst, and the reaction time of 1.5 h was reported to be the optimum reaction time.²¹

6 Possible configurations of functionalised MWCNTs in transesterification/esterification reaction systems

Several configurations of functionalised MWCNTs are used in transesterification/esterification reaction systems, such as the direct dispersion of functionalised MWCNTs in a reaction medium and operation coupled with membranes incorporating functionalised CNTs. Each configuration uses a different approach to biodiesel production.

6.1 Direct dispersion of functionalised MWCNTs in a reaction medium

The direct mixing of catalysts with reactants is the most common configuration in heterogeneous catalysis. In this configuration, functionalised MWCNTs were dispersed into oil and methanol, which is then stirred during the reaction.^{8,21} Prior to the reaction, the mixture was ultrasonicated to improve the dispersion of functionalised MWCNTs in the reaction medium. The ultrasonic shock-waves promote the separation of functionalised MWCNTs from bundles or agglomerations,²⁰⁰ thus increasing the contact area between

the active sites and reactants. After reaction, the functionalised MWCNTs were filtered and the product mixtures were subjected to further purification to remove by-products (glycerol and water), excess alcohol and DG. When functionalised MWCNTs are used as catalysts for transesterification, the reaction mixture consists of a three-phase system in which the reaction rate will be limited by mass transfer.²⁰¹ Therefore, the effect of stirring is crucial to overcoming this limitation, especially for this configuration. For a fixed reaction time, a higher biodiesel yield could be achieved using a higher stirring speed.¹²

6.2 Combination of functionalised MWCNTs with membrane

Recent biodiesel production technology uses a membrane reactor that combines the catalysts and membrane in a reaction system.⁴ A membrane reactor is also known as a membrane-based reactive separator.²⁰² The three different combinations of functionalised MWCNTs and membranes are membranes without functionalised MWCNTs incorporated, packed bed membrane reactors and mixed matrix membranes (MMMs) with embedded functionalised MWCNTs. Each configuration will be discussed in the following section.

6.2.1 Membrane without functionalised MWCNTs incorporated. This type of noncontact configuration between the membrane and the catalyst is known as a catalytically inert membrane in which the functionalised MWCNTs are added to the reaction medium but not embedded inside the membrane.^{4,203} In this catalyst configuration, functionalised MWCNTs are directly dispersed in the reactants and the mixture is stirred during the reaction. The membranes can be tubular or disc-shaped.^{204,205} When the transmembrane pressure (TMP) is increased, the desired products will permeate through the membrane.²⁰⁶ The components that permeate through the membrane depend on the membrane type:⁴ hydrophilic, hydrophobic or organophilic. The operational concept for ceramic/carbon membranes and polymeric membranes is completely different. Separation by ceramic and carbon membranes is based on the oil droplet size.²⁰⁴ Therefore, methanol, with a relatively small molecular size, and other soluble components such as glycerol, water and biodiesel are able to pass through the membrane into the permeate stream²⁰⁶ and then be separated into non-polar and polar phases.²⁰⁷ The non-polar phase contains over 85% of FAME and the remaining is methanol as well as trace amounts of DG.²⁰⁸ To comply with the American Society for Testing and Materials (ASTM) or European Standards (EN) for biodiesel, further purification of the separated biodiesel is needed to remove the excess methanol and DG. Meanwhile, the separation concept for polymeric membranes is based on the interaction between the target component (usually glycerol and water) and the polymer functional groups of the membrane.²⁰⁵ Glycerol, water and methanol can be removed from the reaction mixture because they can form hydrogen bonds with the OH groups in the polymer membrane.^{205,209}

6.2.2 Packed bed membrane reactor with functionalised MWCNTs. A packed bed membrane reactor consisting of potassium hydroxide (KOH) catalyst supported on palm-shell-activated carbon has been developed to produce biodiesel in a continuous process. The catalysts were packed inside the

tubular $\text{TiO}_2/\text{Al}_2\text{O}_3$ ceramic membrane reactor. The reactants were charged into the reactor using a circulating pump. The reaction occurred when oil and methanol passed through the catalyst bed in the reactor. High-quality biodiesel can be produced from the packed bed membrane reactor.²¹⁰ Therefore, functionalised MWCNTs can be used to replace the activated carbon to be packed inside the membrane reactor, serving as a transesterification catalyst.

6.2.3 Mixed matrix membrane (MMM). MMM is a membrane that contains inorganic filler in a polymer matrix. MMM combines the superior permeability and selectivity of inorganic membranes with the economical processing capabilities of polymeric membranes.²¹¹ MMM is also known as a catalytically active membrane.²⁰³ CNTs are one of the common inorganic fillers for MMM²¹² because of their unique properties, such as high surface area and ability to be functionalised and dispersed into an organic polymer matrix to enhance the mechanical strength of MMM with minimal filler content.²¹¹ Therefore, the embedded functionalised MWCNTs play two roles in MMM: that of a membrane filler and that of a transesterification catalyst. Two approaches can be applied to produce biodiesel using MMM membranes: 1) cutting the MMM membrane into small squares and loading them together with the reactants and 2) placing the disc-shaped MMM membrane into a membrane reactor.²⁰⁵ The separation principle of MMM membranes is the same as that of conventional polymeric membranes because the MMM matrix is also polymer-based. The advantage of this catalytically active membrane is the reduction of the need of a purification process for the post-reaction permeate stream because by-products such as glycerol and water were continuously removed during the reaction.⁴

7 Catalyst life-time and regeneration

Similar to other transesterification catalysts, the Et_3N -CNTs also suffered from a significant deactivation after the first reaction cycle in which the conversion of glyceryl tributyrates dropped to almost 60% in the second run of the reaction and continued to drop for subsequent cycles. This decrease was due to the strong adsorption of triglycerides on the active sites. This attribution has been supported by the TEM images of the spent catalysts in which the amorphous species was observed around the CNTs and inside their channels. However, these adsorbed triglycerides can be easily removed by washing the spent catalyst in methanol several times and drying at 80 °C after each transesterification cycle. The washed and regenerated catalyst was deactivated slightly but still showed an extremely stable catalytic activity in which the conversion was maintained above 90%, even after 6 reaction cycles.⁸ Thus, it was recommended that the amino-functionalised MWCNTs be pre-contacted with methanol for 10 min before adding the oil to avoid the adsorption of triglycerides to the inner and outer catalyst surfaces.⁶³ Villa *et al.* (2009)⁸ studied the leaching of grafted amine by performing acid–base titrations on the spent catalyst. The titration result showed that the generated pH of the spent Et_3N -CNT catalyst was 10.26 and that the content of

the corresponding basic groups in the catalyst was 0.96 mmol g^{-1} . In comparison to the freshly synthesised Et_3N -CNT catalyst, with a basic site density of 1.00 mmol g^{-1} (Table 2), the leaching of the basic groups was only 4% after the 6 cycles. Moreover, the use of gas chromatography–mass spectrometry (GC-MS) to analyse the reaction solution after each reaction indicated the absence of Et_3N , most likely because the concentration of the leached amines in the solution was too low to be detected. Therefore, the amino groups were well anchored on the surface of the MWCNTs.

To the best of our knowledge, no studies have been performed to investigate the reusability and regeneration of s-MWCNTs used in biodiesel production. However, the spent s-MWCNTs could be reactivated using the regeneration method for sulfonated carbon-based catalysts derived from a glucose-starch mixture. The sulfonated carbon-based catalyst, when treated in concentrated H_2SO_4 (98%), exhibited a catalytic activity close to its original level. Meanwhile, the regeneration of the spent sulfonated carbon-based catalyst after treatment with 5% diluted H_2SO_4 could achieve a FAME yield of 60%. On the other hand, the washing of the spent catalyst in methanol and cyclohexane did not affect the regeneration of the catalyst activity, producing a FAME yield of below 10%. This low value might be due to the leaching of SO_3H groups from polycyclic aromatic hydrocarbons during the extensive methanol washing.²¹³

8 Other catalytic applications of carbon nanotubes

In addition to esterification and transesterification, functionalised CNTs have also been used to serve as a novel support materials in other catalytic reactions, such as Fischer–Tropsch synthesis,²¹⁴ selective hydrogenation,^{215,216} polymerisation,²¹⁷ cyanosilylation,²¹⁸ gas oil hydrotreatment,²¹⁹ bioethanol synthesis,²²⁰ polysaccharide degradation²²¹ and oxidation reaction for fuel cells^{222–226} as well as wastewater treatment.²²⁷

Iron catalysts supported on oxygen-functionalised MWCNTs (O-MWCNTs) or nitrogen-functionalised MWCNTs (N-MWCNTs) were used in high-temperature Fischer–Tropsch syntheses to produce short-chain olefins. O-MWCNTs were obtained *via* gas-phase treatment using nitric acid vapour at 200 °C for 24 h. Meanwhile, to introduce N-containing functional groups, the O-MWCNTs were further treated at 400 °C for 6 h under an ammonia flow. Iron nanoparticles with particle sizes below 9 nm were deposited on the functionalised MWCNTs *via* ammonium iron citrate impregnation process followed by calcination and finally reduction in pure H_2 at 380 °C to form Fe/O-MWCNTs and Fe/N-MWCNTs. Short-chain olefins were synthesised by passing the syngas (45% CO, 45% H_2 and 10% Ar) over the catalysts with a specific flow rate of 833 sccm/g min^{-1} and an absolute pressure of 25 bar. Both catalysts (Fe/O-MWCNTs and Fe/N-MWCNTs) showed excellent olefin selectivity in the short-chain region [$\text{S}(\text{C}_3\text{–C}_6) > 85\%$] and low chain growth probability ($\alpha \leq 0.5$). Fe/N-

MWCNTs exhibited almost twofold higher activity than Fe/O-MWCNTs after 50 h on stream under steady-state conditions. Therefore, Fe/N-MWCNT catalysts are more suitable Fischer-Tropsch catalysts for the production of short-chain olefins due to their high catalytic activity, high selectivity of olefins, low chain growth probability and superior long-term stability.²¹⁴

In addition, functionalised MWCNT-supported metal catalysts were also applied to the selective hydrogenation of phenylacetylene and *p*-chloronitrobenzene. MWCNT-supported Pt catalysts were used for the hydrogenation of phenylacetylene (PA). MWCNTs were functionalised with oxygen-containing groups by oxidative treatment with 100 mL of 0.2 M HNO₃ and 0.6 M H₂SO₄ for 4 h. The deposition of Pt particles onto MWCNTs was achieved *via* the chemical reduction of H₂PtCl₆·6H₂O by ethylene glycol in the presence of NaOH. The catalyst was then activated under a hydrogen stream at 300 °C for 2 h followed by cooling to room temperature. Pre-determined amounts of the catalyst, ethanol and PA were mixed, and the hydrogenation reaction was carried out at 50 °C for 1 h under stirring in a H₂ environment (0.4 MPa). The MWCNT-supported Pt catalysts showed superior catalytic activity, with PA conversion and selectivity to styrene of 99% and 88%, respectively. This high catalytic activity was most likely due to better dispersion of the Pt nanoparticles MWCNTs.²¹⁵ On the other hand, MWCNT-supported ruthenium catalysts were used for the hydrogenation of *p*-chloronitrobenzene with methanol to selectively produce *p*-chloroaniline. The purified MWCNTs were first subjected to surface activation by refluxing the MWCNTs in nitric acid to produce hydrophilic MWCNTs with oxygen-containing surface groups. Next, the ruthenium catalysts were prepared by impregnation from triruthenium dodecacarbonyl (99%) in hexane at approximately 20 °C. The hydrogenation reaction was performed between 40 °C and 60 °C under a hydrogen pressure of 10 to 35 bar in an autoclave under stirring. The catalysts showed excellent performance in producing *p*-chloroaniline with 94% selectivity. The catalytic activity of the MWCNT-supported ruthenium catalysts was reported to be one order of magnitude higher than that of a commercial Ru/Al₂O₃ catalyst.²¹⁶

A SWCNT-supported nickel(II) carborane complex, [(*closo*-1-Ni(PPh₃)₂-2-Me-3-((CH₂)₄NH)-n⁵-2,3-C₂B₉H₉)[OEt]_n](SWCNT), was studied in olefin (ethylene and vinyl chloride) polymerisation. This catalysts were synthesised *via* the *in situ* preparation of *nido*-C₂B₉-carborane-functionalised SWCNTs with dichlorobis(triphenylphosphine)nickel(II). The polymerisation of ethylene and vinyl chloride catalysed by the SWCNT-supported nickel(II) carborane complex was carried out in THF in the presence of methylaluminoxane (MAO, 10 wt% solution in toluene) as a co-catalyst. The SWCNT-supported nickel(II) carborane complex was more active for olefin polymerisation than its homogeneous analogue, *closo*-1-Ni(PPh₃)₂-2-Me-3-Pentyl-n⁵-2,3-C₂B₉H₉, in the presence of MAO co-catalyst.²¹⁷

SWCNT-supported vanadyl salen complexes were used to catalyse the cyanosilylation of aldehydes with trimethylsilylcy-

nide. SWCNTs were first functionalised at the tips with terminal thiol groups *via* nitric acid treatment followed by reaction with thionyl chloride in DMF and subsequently transformed into amides by treating with 2-aminoethanethiol in the presence of a tertiary amine to trap the evolved hydrochloric acid. Styryl-functionalised vanadyl Schiff base was covalently bonded on the modified SWCNTs by a radical chain mechanism initiated by azoisobutyronitrile (AIBN). The SWCNT-supported vanadyl salen complex catalysts showed a high activity for cyanosilylation using benzaldehyde as a substrate to catalyse the reaction, even at a low substrate-to-catalyst ratio. The conversions of benzaldehyde by SWCNT-supported vanadyl salen complexes catalysts were similar to that by a homogeneous catalyst (tetrabutyl vanadyl salen dissolved in chloroform). No leaching was observed for the SWCNT-supported vanadyl salen complex catalysts, and the catalysts can be reused for five consecutive runs without a decrease in activity.²¹⁸

Hydrotreatment is a crude oil refining process to remove hydrocarbon molecules that contain nitrogen and sulfur groups from gas oil using H₂ over a catalyst. MWCNT-supported NiMo catalysts (NiMo/MWCNTs) were used to hydrotreat gas oil derived from Athabasca bitumen. The MWCNTs were first treated with 52% nitric acid and refluxed for 8 h to create carboxylic functional groups on the surface. The functional groups on the surface of MWCNTs play an important role in preventing the leaching of Ni and Mo particles during the reaction. The NiMo/MWCNT catalysts were prepared by a pore-filling wet impregnation method. The hydrotreatment of light gas oil (LGO) derived from Athabasca bitumen was performed in a trickle bed reactor under typical industrial conditions: pressure of 8.8 MPa, H₂/feed ratio of 600 mL ml⁻¹, weight hourly space velocity (WHSV) of 4.5 h⁻¹ and temperature of 345, 360 and 375 °C. To achieve high hydrotreating activity, 3 wt% Ni and 12 wt% Mo was the optimum catalyst loading on MWCNTs. The catalytic activity of 3 wt% Ni-12 wt% Mo/MWCNT catalysts was significant higher than that of conventional Al₂O₃-based catalysts due to the uniform pore size of MWCNTs, which can reduce the mass transfer problem during the reaction. In addition, the absence of strong acid sites in MWCNTs reduces the strong interaction between metal particles and support and favours the complete sulfidation of Mo species.²¹⁹

The conversion of syngas from biomass gasification is an alternative to fermentation for bioethanol production. MWCNT/silica-supported Cu-Co catalysts have been used to produce bioethanol from biomass-derived syngas. The purified MWCNTs were functionalised with pyrogallol. Next, amino silica was added to the solution and sonicated for 1 h. The introduction of pyrogallol on the support surface enhances the interaction of metal ions with the support. Next, the MWCNT/silica composite was used as support for the preparation of catalysts *via* incipient wetness impregnation of copper nitrate (Cu(NO₃)₂·3H₂O) and cobalt nitrate (Co(NO₃)₂·6H₂O). The catalysts were reduced *in situ* under H₂ flow (45 mL min⁻¹) at 300 °C for 14 h before synthesis gas (85

mL min⁻¹) with a H₂/CO ratio of 1.0 was introduced and the pressure of the reactor was increased to 5 MPa. The increase of MWCNT content in the catalyst support could reduce methanol production and increase the production of C₂ + alcohol.²²⁰

The biomass component, cellulose, is degraded by different cellulases (enzymes) produced by microorganisms. Recently, a unique bio-inspired catalyst that mimics the structure of active sites in real enzymes using functionalised CNTs has been synthesised for cellobiose degradation. CNTs were first subjected to acid treatment to create carboxylic groups on the CNT surface. The carboxyl group on CNTs contributes to the cellobiose degradation. The catalysts functioned optimally at a pH of approximately 3, which allowed the artificial catalysts to better mimic the steric orientation of the nucleophilic and acid-base catalytic active sites of the sugar degradable enzyme. The COOH-CNTs only mimicked the active site conformation of the natural cellulase. Therefore, the catalytic effect of COOH-CNTs was only partial. However, the number of catalytic sites per molecule of the COOH-CNTs was higher than that of other sugar degradable catalysts, such as β -glucosidase and exoglucanase.²²¹

Platinum (Pt)-based catalysts are the best and most commonly used catalyst for fuel cells. However, Pt catalysts are usually easily poisoned due to the gradual deposition of the dissociated organic molecular species on the metal surface.^{228,229} Therefore, intensive research has been carried out to improve the kinetic and poison tolerance of Pt-based catalysts.²²² The hydrofluoric acid (HF)-treated MWCNT-supported Pt catalysts²²³ as well as chitosan and heteropolyacid of phosphomolybdic acid functionalised MWCNT-supported PtRu catalysts (PtRu/HPMo-CS-MWCNTs)²²² are commonly used for direct methanol fuel cells (DMFCs). To prepare the HF-treated MWCNT-supported Pt catalysts, the MWCNTs were first treated in HF solution to induce defects on the surface of the pristine MWCNTs. Intermittent microwave heating (IMH) of H₂O₂ solution is then employed to form functional groups on the defect areas. The treated MWCNTs were then added into a well mixed mixture of chloroplatinic acid (the starting precursor) and ethylene glycol. The pH of the mixture was adjusted to above 10, and a well dispersed slurry was obtained upon stirring and ultrasonication for 15 min. Next, the slurry was microwave-heated and hydrochloric acid was added. The HF-treated MWCNT-supported Pt catalysts prepared using a 10 s-on/20 s-off pulsing protocol over five cycles exhibited the best activity towards methanol oxidation. The catalysts also showed significantly improved stability towards the methanol oxidation conditions, which was attributed to the improved MWCNT modifications, which enhance the interaction between the Pt nanoparticles and MWCNTs.²²³ To prepare the PtRu/HPMo-CS-MWCNTs, MWCNTs were first functionalised noncovalently with phosphomolybdic acid and chitosan at room temperature without the use of corrosive acids to produce a homogeneous surface of functional groups with no detrimental effect on the graphene structures of the MWCNTs. An impregnation

method was used to deposit PtRu nanoparticles on functionalised MWCNTs. The PtRu/HPMo-CS-MWCNTs catalysts showed higher electrocatalytic activity for methanol oxidation and better tolerance toward CO poisoning due to the finer particle size and uniform distribution of PtRu nanoparticles on HPMo-CS-MWCNTs than those of the PtRu nanoparticles supported on conventional acid-treated MWCNTs. In addition, the presence of heteropolyacids enhances the electrooxidation of intermediate species such as CO and eventually reduces the poisoning of catalysts.²²² Similarly to DMFC, the catalysts for direct ethanol fuel cells (DEFCs) are also PtRu nanoparticles. Yang *et al.* (2012)²²⁴ reported the use of polyoxyethylene bis(amine)-functionalised MWCNTs as supports for PtRu nanoparticles for ethanol oxidation. MWCNTs wrapped by polyoxyethylene bis(amine) linear molecules were denoted as POB-MWCNTs. The deposition of PtRu nanoparticles on the POB-MWCNTs was achieved *via* polyol reduction. The PtRu/POB-MWCNTs catalysts showed a higher electrochemical active surface area (EAS) based on CO stripping voltammograms, better electrocatalytic activity and higher stability for ethanol oxidation in acidic solution than those for PtRu nanoparticles deposited on acid-treated MWCNTs and carbon black catalysts. On the other hand, palladium (Pd) and Pd-derived catalysts were used as in direct formic acid fuel cell (DFAFCs) because of their better performance in formic acid oxidation relative to Pt-derived catalysts. In DFAFC, MWCNTs were noncovalently functionalised with 1,10-phenanthroline (phen). The Pd/phen-MWCNTs catalysts were prepared using PdCl₂ as starting precursor. The phen-MWCNTs possess supramolecular π - π stacking, which preserves the integrity and electronic structure of the MWCNTs, in contrast to acid-treated MWCNTs. Moreover, the presence of N atoms in phen enables the Pd nanoparticles to homogeneously anchor onto the phen-MWCNTs and generate good electrocatalytic activity and stability for formic acid oxidation.²²⁶

Wet air oxidation (WAO) is an effective alternative to eliminating hazardous, toxic and highly concentrated organic compounds in wastewater produced by the chemical, petrochemical, pharmaceutical, agricultural and textile industries.^{227,230,231} The oxygen-containing functional groups and carboxylic acid groups play an important role in WAO. Therefore, MWCNTs were functionalised by different oxidants, such as HNO₃/H₂SO₄, H₂O₂, O₃ and air, to serve as catalysts for the WAO of phenol. The WAO of phenol using functionalised MWCNTs was carried out under a reaction temperature of 155 °C and total pressure of 2.5 MPa. The results showed that the MWCNTs treated with O₃ exhibited the highest catalytic activity, with the ability to remove 100% phenol and 80% total organic carbon (TOC). This high removal was O₃-treated MWCNTs possessing more oxygen-containing functional groups and carboxylic acid groups and having a weakly acidic nature. In addition, the O₃-treated MWCNTs showed good catalytic stability, with almost the same phenol and TOC removal observed in 4 cyclic reactions.²²⁷

9 Challenges and future outlook of using functionalized CNTs as catalyst support

Both theoretical and experimental works have proven that CNTs can be functionalised to serve as catalysts for biodiesel production. However, many technical barriers still must be overcome, including catalyst reproducibility, environmental compatibility and scaling-up. In the synthesis of high-purity CNTs, the large-scale synthesis of high-purity CNTs with controllable diameters, lengths, chiralities and conductivities remains a challenge.²³² The synthesis of MWCNTs with a controllable number of walls is another significant challenge.²³³ The MWCNT type (thin MWCNTs with three to six walls or thick MWCNTs with more than six walls) suitable for use as the catalyst support in biodiesel production remains unknown. Moreover, the synthesis of isolated CNTs with the desired structures has not yet reached maturity in which a single CNT itself does not possess the same diameter and chirality over its entire length.^{232,233} As noted, CNTs have been successfully produced using almost all metals; however, the effects of different metal catalysts on the physical and chemical properties of the grown CNTs remain unstudied. The required properties of CNTs as the catalyst support in transesterification/esterification are thought to differ from the CNTs used in other applications, such as in electronic devices and hydrogen storage. Thus, if the type of metal used and the properties of the grown CNTs are well correlated, it would be easier to select CNTs with the optimal properties for different applications.²³³

The raw CNTs must be purified because they contain amorphous carbon and metal catalyst impurities. Therefore, the demand for uniform, high-purity CNTs with low cost and on large scales is another major challenge that must be overcome. An effective technique to purify, tailor the structure and properties of and sort CNTs needs to be developed.²³² In addition, a standard characterisation protocol or quality control assessment of CNTs is critically needed for evaluating and comparing the characteristics of CNTs synthesis by different methods.^{232,233}

The functionalisation of CNTs has broadened the application of CNTs in heterogeneous catalysis. However, the structure of the functionalised CNTs on an atomic scale has not been fully studied. Although scanning tunnelling microscopy (STM), which can record atomically resolved images of bare CNTs and structural defects, can be used for this purpose, the unequivocal imaging of individual functional groups located on the sidewall of CNTs still remains to be investigated. Moreover, future investigation should focus on the study of the density and distribution of functional groups/moieties for both the convex and concave surfaces of CNTs. This study is vital because it helps provide a clearer picture of the dependence of chemical reactivity on the detailed structure of CNTs.⁸³ There is still a room to improve the functionalisation of MWCNTs with basic or acidic groups to improve the active catalytic sites to serve as catalysts in biodiesel production. Therefore, the reported catalysts might not be

the best catalyst for transesterification/esterification. Optimisation and modelling will be needed to advance the catalyst into commercial application. Moreover, the applicability of base or acid functionalised MWCNTs in common biodiesel feedstock, such as refined oil, crude oil, waste oil, the low-value by-product PFAD or even municipal activated sludge containing lipid²³⁴ has been minimally studied because, before this study, functionalised MWCNTs had only been applied in pure and single-components (such as glyceryl tributyrates and oleic acid) forms.

10 Conclusion

The obstacles encountered by conventional heterogeneous catalysts in transesterification/esterification have hindered fully economically feasible biodiesel production. The emergence of functionalised CNTs as catalyst support offers a solution for future biodiesel production that has the potential to be developed into large-scale production. The main advantages of functionalised CNTs as catalyst support in biodiesel production are that they overcome the mass transfer limitation, low catalyst stability and high cost of precious metal catalysts faced by the conventional heterogeneous catalysts in transesterification/esterification. MWCNTs are normally used as the catalyst support in transesterification/esterification reaction. MWCNTs can be functionalised with four different functional groups to serve as a catalyst in transesterification or esterification reactions, including basic catalyst groups, acidic catalyst groups, enzymes and metal particles. The reported functionalised MWCNTs involved in biodiesel production are amino functionalised MWCNTs and sulfonated MWCNTs *via* thermal treatment with concentrated H₂SO₄. The findings indicated that the functionalised MWCNTs required a lower reaction temperature, methanol-to-oil ratio and catalyst concentration in transesterification/esterification reaction compared to conventional catalysts. However, the application of functionalised MWCNTs to the biodiesel production industry requires more studies to optimise the density of functional groups anchored on MWCNTs and the regeneration of the spent catalyst to increase the lifetime of functionalised MWCNTs. In addition, more studies are needed to demonstrate the application of the functionalised MWCNTs in common biodiesel feedstock.

Acknowledgements

Siew Hoong Shuit acknowledges the MyPhD fellowship support from the Ministry of Higher Education of Malaysia. This research was also financially supported by Universiti Sains Malaysia Research University (RU) grant (A/C:814142), USM Membrane Cluster Grant, Fundamental of Research Grant Scheme (FRGS) (A/C:6071212) and Postgraduate Research Grant Scheme (PRGS) (A/C: 8044028).

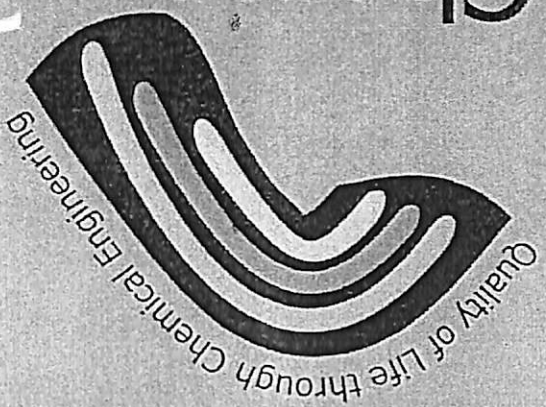
References

- 1 A. A. Apostolou, I. K. Kookos, C. Marazioti and K. C. Angelopoulos, *Fuel Process. Technol.*, 2009, **90**, 1023–1031.
- 2 F. Ma and M. A. Hanna, *Bioresour. Technol.*, 1999, **70**, 1–15.
- 3 G. Knothe, *Green Chem.*, 2011, **13**, 3048–3065.
- 4 S. H. Shuit, Y. T. Ong, K. T. Lee, B. Subhash and S. H. Tan, *Biotechnol. Adv.*, 2012, **30**, 1364–1380.
- 5 J. M. Marchetti, V. U. Miguel and A. F. Errazu, *Renewable Sustainable Energy Rev.*, 2007, **11**, 1300–1311.
- 6 S. Bancquart, C. Vanhove, Y. Pouilloux and J. Barrault, *Appl. Catal., A*, 2001, **218**, 1–11.
- 7 A. P. S. Chouhan and A. K. Sarma, *Renewable Sustainable Energy Rev.*, 2011, **15**, 4378–4399.
- 8 A. Villa, J.-P. Tessonnier, O. Majoulet, D. S. Su and R. Schlögl, *Chem. Commun.*, 2009, 4405–4407.
- 9 S. Semwal, A. K. Arora, R. P. Badoni and D. K. Tuli, *Bioresour. Technol.*, 2011, **102**, 2151–2161.
- 10 F. Abreu, D. Lima, E. Hamú, S. Einloft, J. Rubim and P. Suarez, *J. Am. Oil Chem. Soc.*, 2003, **80**, 601–604.
- 11 X. Yu, Z. Wen, H. Li, S.-T. Tu and J. Yan, *Fuel*, 2011, **90**, 1868–1874.
- 12 S. Yan, H. Lu and B. Liang, *Energy Fuels*, 2008, **22**, 646–651.
- 13 J. M. Fraile, N. García, J. A. Mayoral, E. Pires and L. Roldán, *Appl. Catal., A*, 2010, **387**, 67–74.
- 14 S. Nakagaki, A. Bail, V. C. D. Santos, V. H. R. D. Souza, H. Vrabel, F. S. Nunes and L. P. Ramos, *Appl. Catal., A*, 2008, **351**, 267–274.
- 15 R. B. da Silva, A. F. Lima Neto, L. S. Soares dos Santos, J. R. de Oliveira Lima, M. H. Chaves, J. R. dos Santos Jr, G. M. de Lima, E. M. de Moura and C. V. R. de Moura, *Bioresour. Technol.*, 2008, **99**, 6793–6798.
- 16 P. L. Boey, G. P. Maniam and S. A. Hamid, *Bioresour. Technol.*, 2009, **100**, 6362–6368.
- 17 N. Viriya-Empikul, P. Krasae, B. Puttasawat, B. Yoosuk, N. Chollacoop and K. Faungnawakij, *Bioresour. Technol.*, 2010, **101**, 3765–3767.
- 18 R. Chakraborty, S. Bepari and A. Banerjee, *Bioresour. Technol.*, 2011, **102**, 3610–3618.
- 19 M. K. Lam, K. T. Lee and A. R. Mohamed, *Appl. Catal., B*, 2009, **93**, 134–139.
- 20 K. F. Yee, K. T. Lee, R. Ceccato and A. Z. Abdullah, *Bioresour. Technol.*, 2011, **102**, 4285–4289.
- 21 Q. Shu, Q. Zhang, G. Xu and J. Wang, *Food Bioprod. Process.*, 2009, **87**, 164–170.
- 22 R. Liu, X. Wang, X. Zhao and P. Feng, *Carbon*, 2008, **46**, 1664–1669.
- 23 S. Yan, C. DiMaggio, S. Mohan, M. Kim, S. Salley and K. Ng, *Top. Catal.*, 2010, **53**, 721–736.
- 24 G. Vicente, M. Martínez and J. Aracil, *Bioresour. Technol.*, 2004, **92**, 297–305.
- 25 M. Hasheminejad, M. Tabatabaei, Y. Mansourpanah, M. K. Far and A. Javani, *Bioresour. Technol.*, 2011, **102**, 461–468.
- 26 J. A. Melero, J. Iglesias and G. Morales, *Green Chem.*, 2009, **11**, 1285–1308.
- 27 A. Salvini, D. Giomi, G. Cipriani, G. Bartolozzi, R. Alfani and A. Brandi, *RSC Adv.*, 2012, **2**, 4864–4868.
- 28 W. Xie and H. Li, *J. Mol. Catal. A: Chem.*, 2006, **255**, 1–9.
- 29 S. Shah and M. N. Gupta, *Process Biochem.*, 2007, **42**, 409–414.
- 30 S. Shah, S. Sharma and M. N. Gupta, *Energy Fuels*, 2004, **18**, 154–159.
- 31 S. Tamalampudi, M. R. Talukder, S. Hama, T. Numata, A. Kondo and H. Fukuda, *Biochem. Eng. J.*, 2008, **39**, 185–189.
- 32 J. H. Sim, A. H. Kamaruddin and B. Subhash, *Energy Fuels*, 2009, **23**, 4651–4658.
- 33 G. J. Suppes, M. A. Dasari, E. J. Doskocil, P. J. Mankidy and M. J. Goff, *Appl. Catal., A*, 2004, **257**, 213–223.
- 34 J. S. Lee and S. Saka, *Bioresour. Technol.*, 2010, **101**, 7191–7200.
- 35 S. Furuta, H. Matsuhashi and K. Arata, *Catal. Commun.*, 2004, **5**, 721–723.
- 36 W. Xie, X. Huang and H. Li, *Bioresour. Technol.*, 2007, **98**, 936–939.
- 37 X. Liang, G. Gong, H. Wu and J. Yang, *Fuel*, 2009, **88**, 613–616.
- 38 X. Li and W. Huang, *Energy Sources, Part A*, 2009, **31**, 1666–1672.
- 39 M. K. Lam and K. T. Lee, *Fuel Process. Technol.*, 2011, **92**, 1639–1645.
- 40 I. Mbaraka and B. Shanks, *J. Am. Oil Chem. Soc.*, 2006, **83**, 79–91.
- 41 X. Mo, E. Lotero, C. Lu, Y. Liu and J. Goodwin, *Catal. Lett.*, 2008, **123**, 1–6.
- 42 H. Li and W. Xie, *Catal. Lett.*, 2006, **107**, 25–30.
- 43 R. Sawangkeaw, K. Bunyakit and S. Ngamprasertsith, *Green Chem.*, 2007, **9**, 679–685.
- 44 S. H. Shuit, K. T. Lee, A. H. Kamaruddin and S. Yusup, *Fuel*, 2010, **89**, 527–530.
- 45 R. Peña, R. Romero, S. L. Martínez, M. J. Ramos, A. Martínez and R. Natividad, *Ind. Eng. Chem. Res.*, 2009, **48**, 1186–1189.
- 46 G. Guan, K. Kusakabe and S. Yamasaki, *Fuel Process. Technol.*, 2009, **90**, 520–524.
- 47 A. Šalić and B. Zelić, *Goriva I Maziva*, 2011, **50**, 85–110.
- 48 M. Zabeti, W. M. A. Wan Daud and M. K. Aroua, *Fuel Process. Technol.*, 2009, **90**, 770–777.
- 49 *Concepts of modern catalysis and kinetics*, ed. I. Chorkendorff and J. W. Niemantsverdriet, Wiley-VCH Verlag GmbH & Co. KGaA, Weinheim, Germany, 2003.
- 50 D. W. Lee, Y. M. Park and K. Y. Lee, *Catal. Surv. Asia*, 2009, **13**, 63–77.
- 51 T. Ebiura, T. Echizen, A. Ishikawa, K. Murai and T. Baba, *Appl. Catal., A*, 2005, **283**, 111–116.
- 52 E. S. Umdu and E. Seker, *Bioresour. Technol.*, 2012, **106**, 178–181.
- 53 M. Verziu, M. Florea, S. Simon, V. Simon, P. Filip, V. I. Parvulescu and C. Hardacre, *J. Catal.*, 2009, **263**, 56–66.
- 54 T. M. Sankaranarayanan, A. Pandurangan, M. Banu and S. Sivasanker, *Appl. Catal., A*, 2011, **409–410**, 239–247.
- 55 M. J. Kim, M.-Y. Kim, O. Z. Kwon and G. Seo, *Fuel Process. Technol.*, 2011, **92**, 126–131.
- 56 N. Pal, M. Paul and A. Bhaumik, *J. Solid State Chem.*, 2011, **184**, 1805–1812.
- 57 M. C. G. Albuquerque, I. Jiménez-Urbistondo, J. Santamaría-González, J. M. Mérida-Robles, R. Moreno-Tost, E. Rodríguez-Castellón, A. Jiménez-López, D. C.

- S. Azevedo, C. L. Cavalcante Jr and P. Maireles-Torres, *Appl. Catal., A*, 2008, 334, 35–43.
- 58 W. Xie and D. Yang, *Bioresour. Technol.*, 2011, 102, 9818–9822.
- 59 Y. Liu, E. Lotero, J. G. Goodwin Jr and C. Lu, *J. Catal.*, 2007, 246, 428–433.
- 60 E. A. Faria, H. F. Ramalho, J. S. Marques, P. A. Z. Suarez and A. G. S. Prado, *Appl. Catal., A*, 2008, 338, 72–78.
- 61 Z. Wan and B. H. Hameed, *Bioresour. Technol.*, 2011, 102, 2659–2664.
- 62 S. Baroutian, M. K. Aroua, A. A. Raman and N. M. N. Sulaiman, *Fuel Process. Technol.*, 2010, 91, 1378–1385.
- 63 A. Villa, J.-P. Tessonier, O. Majoulet, D. S. Su and R. Schlögl, *ChemSusChem*, 2010, 3, 241–245.
- 64 Q. Shu, J. Gao, Z. Nawaz, Y. Liao, D. Wang and J. Wang, *Appl. Energy*, 2010, 87, 2589–2596.
- 65 Q. Shu, Q. Zhang, G. Xu, Z. Nawaz, D. Wang and J. Wang, *Fuel Process. Technol.*, 2009, 90, 1002–1008.
- 66 D. M. Alonso, R. Mariscal, R. Moreno-Tost, M. D. Z. Poves and M. L. Granados, *Catal. Commun.*, 2007, 8, 2074–2080.
- 67 M. L. Granados, D. M. Alonso, I. Sádaba, R. Mariscal and P. Ocón, *Appl. Catal., B*, 2009, 89, 265–272.
- 68 M. Kouzu, S.-Y. Yamanaka, J.-S. Hidaka and M. Tsunomori, *Appl. Catal., A*, 2009, 355, 94–99.
- 69 H. Mootabadi, B. Salamatinia, S. Bhatia and A. Z. Abdullah, *Fuel*, 2010, 89, 1818–1825.
- 70 D. E. López, J. G. Goodwin Jr, D. A. Bruce and E. Lotero, *Appl. Catal., A*, 2005, 295, 97–105.
- 71 M. J. Ramos, A. Casas, L. Rodríguez, R. Romero and Á. Pérez, *Appl. Catal., A*, 2008, 346, 79–85.
- 72 C. Ngamcharussrivichai, P. Totarat and K. Bunyakiat, *Appl. Catal., A*, 2008, 341, 77–85.
- 73 K. F. Yee, J. C. S. Wu and K. T. Lee, *Biomass Bioenergy*, 2011, 35, 1739–1746.
- 74 M. K. Lam, K. T. Lee and A. R. Mohamed, *Biotechnol. Adv.*, 2010, 28, 500–518.
- 75 A. A. Refaat, *Int. J. Environ. Sci. Technol.*, 2011, 8, 203–221.
- 76 M.-H. Zong, Z.-Q. Duan, W.-Y. Lou, T. J. Smith and H. Wu, *Green Chem.*, 2007, 9, 434–437.
- 77 L. Fjerbaek, K. V. Christensen and B. Norddahl, *Biotechnol. Bioeng.*, 2009, 102, 1298–1315.
- 78 Y. Yan, L. Xu and M. Dai, *RSC Adv.*, 2012, 2, 6170–6173.
- 79 T. Tan, J. Lu, K. Nie, L. Deng and F. Wang, *Biotechnol. Adv.*, 2010, 28, 628–634.
- 80 H. Taher, S. Al-Zuhair, A. H. Al-Marzouqi, Y. Haik and M. M. Farid, *Enzyme Res.*, 2011, 468292.
- 81 A. Bajaj, P. Lohan, P. N. Jha and R. Mehrotra, *J. Mol. Catal. B: Enzym.*, 2010, 62, 9–14.
- 82 H. W. Zhu, C. L. Xu, D. H. Wu, B. Q. Wei, R. Vajtai and P. M. Ajayan, *Science*, 2002, 296, 884–886.
- 83 K. Balasubramanian and M. Burghard, *Small*, 2005, 1, 180–192.
- 84 X. Peng and S. S. Wong, *Adv. Mater.*, 2009, 21, 625–642.
- 85 G. G. Wildgoose, C. E. Banks and R. G. Compton, *Small*, 2006, 2, 182–193.
- 86 J.-P. Tessonier, A. Villa, O. Majoulet, D. S. Su and R. Schlögl, *Angew. Chem., Int. Ed.*, 2009, 48, 6543–6546.
- 87 M. W. Ryoo, S. G. Chung, J. H. Kim, Y. S. Song and G. Seo, *Catal. Today*, 2003, 83, 131–139.
- 88 C. Pham-Huu, N. Keller, G. Ehret, L. C. J. Charbonniere, R. Ziessel and M. J. Ledoux, *J. Mol. Catal. A: Chem.*, 2001, 170, 155–163.
- 89 F. Rodríguez-Reinoso, *Carbon*, 1998, 36, 159–175.
- 90 P. Serp, M. Corrias and P. Kalck, *Appl. Catal., A*, 2003, 253, 337–358.
- 91 R. Köhn and M. Fröba, *Z. Anorg. Allg. Chem.*, 2003, 629, 1673–1682.
- 92 L. C. Meher, M. G. Kulkarni, A. K. Dalai and S. N. Naik, *Eur. J. Lipid Sci. Technol.*, 2006, 108, 389–397.
- 93 G. Arzamendi, E. Arguiñarena, I. Campo, S. Zabala and L. M. Gandía, *Catal. Today*, 2008, 133–135, 305–313.
- 94 X. Liu, H. He, Y. Wang and S. Zhu, *Catal. Commun.*, 2007, 8, 1107–1111.
- 95 M. Di Serio, M. Cozzolino, R. Tesser, P. Patrono, F. Pinzari, B. Bonelli and E. Santacesaria, *Appl. Catal., A*, 2007, 320, 1–7.
- 96 A. D'Cruz, M. Kulkarni, L. Meher and A. Dalai, *J. Am. Oil Chem. Soc.*, 2007, 84, 937–943.
- 97 A. Molaei Dehkordi and M. Ghasemi, *Fuel Process. Technol.*, 2012, 97, 45–51.
- 98 Y.-M. Park, D.-W. Lee, D.-K. Kim, J.-S. Lee and K.-Y. Lee, *Catal. Today*, 2008, 131, 238–243.
- 99 A. Kawashima, K. Matsubara and K. Honda, *Bioresour. Technol.*, 2008, 99, 3439–3443.
- 100 S. Yan, M. Kim, S. O. Salley and K. Y. S. Ng, *Appl. Catal., A*, 2009, 360, 163–170.
- 101 H.-J. Kim, B.-S. Kang, M.-J. Kim, Y. M. Park, D.-K. Kim, J.-S. Lee and K.-Y. Lee, *Catal. Today*, 2004, 93–95, 315–320.
- 102 E. Li and V. Rudolph, *Energy Fuels*, 2008, 22, 145–149.
- 103 D. E. López, K. Suwannakarn, D. A. Bruce and J. G. Goodwin Jr, *J. Catal.*, 2007, 247, 43–50.
- 104 E. Leclercq, A. Finiels and C. Moreau, *J. Am. Oil Chem. Soc.*, 2001, 78, 1161–1165.
- 105 P. Serp and E. Castillejos, *ChemCatChem*, 2010, 2, 41–47.
- 106 O. V. S. G. P. Soares, J. J. M. Órfão and M. F. R. Pereira, *Ind. Eng. Chem. Res.*, 2010, 49, 7183–7192.
- 107 Y. Li, J. H.-C. Liu, C. A. Witham, W. Huang, M. A. Marcus, S. C. Fakra, P. Alayoglu, Z. Zhu, C. M. Thompson, A. Arjun, K. Lee, E. Gross, F. D. Toste and G. A. Somorjai, *J. Am. Chem. Soc.*, 2011, 133, 13527–13533.
- 108 G. Sanjay and S. Sugunan, *Catal. Commun.*, 2005, 6, 81–86.
- 109 K. Jiang, L. S. Schadler, R. W. Siegel, X. Zhang, H. Zhang and M. Terrones, *J. Mater. Chem.*, 2004, 14, 37–39.
- 110 M. Salavati-Niasari and M. Bazarganipour, *Appl. Surf. Sci.*, 2008, 255, 2963–2970.
- 111 K. Sadowska, K. Stolarczyk, J. F. Biernat, K. P. Roberts, J. Rogalski and R. Bilewicz, *Bioelectrochemistry*, 2010, 80, 73–80.
- 112 S. Iijima, P. M. Ajayan and T. Ichihashi, *Phys. Rev. Lett.*, 1992, 69, 3100–3103.
- 113 M. Paradise and T. Goswami, *Mater. Des.*, 2007, 28, 1477–1489.
- 114 A. Thess, R. Lee, P. Nikolaev, H. Dai, P. Petit, J. Robert, C. Xu, Y. H. Lee, S. G. Kim, A. G. Rinzler, D. T. Colbert, G. E. Scuseria, D. Tománek, J. E. Fischer and R. E. Smalley, *Science*, 1996, 273, 483–487.
- 115 T. Guo, P. Nikolaev, A. Thess, D. T. Colbert and R. E. Smalley, *Chem. Phys. Lett.*, 1995, 243, 49–54.
- 116 H. Allouche, M. Monthieux and R. L. Jacobsen, *Carbon*, 2003, 41, 2897–2912.

- 117 S. N. Bondi, W. J. Lackey, R. W. Johnson, X. Wang and Z. L. Wang, *Carbon*, 2006, 44, 1393–1403.
- 118 K. H. Jung, J.-H. Boo and B. Hong, *Diamond Relat. Mater.*, 2004, 13, 299–304.
- 119 S. A. Manafi, M. H. Amin, M. R. Rahimpour, E. Salahi and A. Kazemzadeh, *New Carbon Mater.*, 2009, 24, 39–44.
- 120 Inframat Corporation. Inframat Advanced Materials, <<http://www.advancedmaterials.us/index.htm>>, Accessed 5th May 2012.
- 121 Q. Zeng, Z. Li and Y. Zhou, *J. Nat. Gas Chem.*, 2006, 15, 235–246.
- 122 C. M. Hussain, C. Saridara and S. Mitra, *RSC Adv.*, 2011, 1, 685–689.
- 123 S. H. Shuit, K. T. Lee, A. H. Kamaruddin and S. Yusup, *Environ. Sci. Technol.*, 2010, 44, 4361–4367.
- 124 Q. Shi, D. Yang, Y. Su, J. Li, Z. Jiang, Y. Jiang and W. Yuan, *J. Nanopart. Res.*, 2007, 9, 1205–1210.
- 125 I. V. Pavlidis, T. Tsoufis, A. Enotiadis, D. Gournis and H. Stamatis, *Adv. Eng. Mater.*, 2010, 12, B179–B183.
- 126 K. Pal, D. J. Kang, Z. X. Zhang and J. K. Kim, *Langmuir*, 2010, 26, 3609–3614.
- 127 D. J. Guo, X. P. Qiu, L. Q. Chen and W. T. Zhu, *Carbon*, 2009, 47, 1680–1685.
- 128 D. J. Guo, X. P. Qiu, W. T. Zhu and L. Q. Chen, *Appl. Catal., B*, 2009, 89, 597–601.
- 129 F. Peng, L. Zhang, H. Wang, P. Lv and H. Yu, *Carbon*, 2005, 43, 2405–2408.
- 130 H. Yu, Y. Jin, Z. Li, F. Peng and H. Wang, *J. Solid State Chem.*, 2008, 181, 432–438.
- 131 S. Yun, H. Im, Y. Heo and J. Kim, *J. Membr. Sci.*, 2011, 380, 208–215.
- 132 D. Tasis, N. Tagmatarchis, A. Bianco and M. Prato, *Chem. Rev.*, 2006, 106, 1105–1136.
- 133 Y.-P. Sun, K. Fu, Y. Lin and W. Huang, *Acc. Chem. Res.*, 2002, 35, 1096–1104.
- 134 M. Kaur and A. Ali, *Renewable Energy*, 2011, 36, 2866–2871.
- 135 J. Wang, K. Chen, S. Huang and C. Chen, *J. Am. Oil Chem. Soc.*, 2012, 1–7.
- 136 B. Karimi, H. M. Mirzaei and A. Mobaraki, *Catal. Sci. Technol.*, 2012, 2, 828–834.
- 137 J. A. Melero, L. F. Bautista, G. Morales, J. Iglesias and R. Sánchez-Vázquez, *Chem. Eng. J.*, 2010, 161, 323–331.
- 138 M. Han, W. Yi, Q. Wu, Y. Liu, Y. Hong and D. Wang, *Bioresour. Technol.*, 2009, 100, 2308–2310.
- 139 X. Liang and J. Yang, *Green Chem.*, 2010, 12, 201–204.
- 140 M. G. Kulkarni, R. Gopinath, L. C. Meher and A. K. Dalai, *Green Chem.*, 2006, 8, 1056–1062.
- 141 W. Zhou, J. Xiao, Y. Chen, R. Zeng, S. Xiao, H. Nie, F. Li and C. Song, *Polym. Adv. Technol.*, 2011, 22, 1747–1752.
- 142 B. L. Erickson, H. Asthana and L. T. Drzal, *J. Adhes. Sci. Technol.*, 1997, 11, 1249–1267.
- 143 T. Ramulifho, K. I. Ozoemena, R. M. Modibedi, C. J. Jafta and M. K. Mathe, *Electrochim. Acta*, 2012, 59, 310–320.
- 144 Z.-P. Sun, X.-G. Zhang, Y.-Y. Liang and H.-L. Li, *J. Power Sources*, 2009, 191, 366–370.
- 145 Z.-P. Sun, X.-G. Zhang, R.-L. Liu, Y.-Y. Liang and H.-L. Li, *J. Power Sources*, 2008, 185, 801–806.
- 146 C. Y. Du, T. S. Zhao and Z. X. Liang, *J. Power Sources*, 2008, 176, 9–15.
- 147 B. Zhang, J. Ren, X. Liu, Y. Guo, Y. Guo, G. Lu and Y. Wang, *Catal. Commun.*, 2010, 11, 629–632.
- 148 Q. Fu, B. Gao, H. Dou, L. Hao, X. Lu, K. Sun, J. Jiang and X. Zhang, *Synth. Met.*, 2011, 161, 373–378.
- 149 Z. Xu, Z. Qi and A. Kaufman, *Electrochem. Solid-State Lett.*, 2005, 8, A313–A315.
- 150 Y. M. Ho, J. W. Liu, J. L. Qi and W. T. Zheng, *J. Phys. D: Appl. Phys.*, 2008, 41, 065308.
- 151 B. P. Tripathi, M. Schieda, V. K. Shahi and S. P. Nunes, *J. Power Sources*, 2011, 196, 911–919.
- 152 S. Yang, X. Zhang, H. Mi and X. Ye, *J. Power Sources*, 2008, 175, 26–32.
- 153 L. Adams, A. Oki, T. Grady, H. McWhinney and Z. Luo, *Phys. E.*, 2009, 41, 723–728.
- 154 N. W. S. Kam and H. Dai, *J. Am. Chem. Soc.*, 2005, 127, 6021–6026.
- 155 N. W. S. Kam, Z. Liu and H. Dai, *Angew. Chem., Int. Ed.*, 2006, 45, 577–581.
- 156 W. Feng and P. Ji, *Biotechnol. Adv.*, 2011, 29, 889–895.
- 157 H. K. Lee, J. K. Lee, M. J. Kim and C. J. Lee, *Bull. Korean Chem. Soc.*, 2010, 31, 650–652.
- 158 Y. Lin, F. Lu, Y. Tu and Z. Ren, *Nano Lett.*, 2004, 4, 191–195.
- 159 K. Balasubramanian and M. Burghard, *Anal. Bioanal. Chem.*, 2006, 385, 452–468.
- 160 T. Akasaka and F. Watari, *Fullerenes, Nanotubes, Carbon Nanostruct.*, 2008, 16, 114–125.
- 161 L. Goux-Capes, A. Filoramo, D. Cote, J. P. Bourgoin and J. N. Patillon, *Phys. Status Solidi A*, 2006, 203, 1132–1136.
- 162 C. Ménard-Moyon, E. Venturelli, C. Fabbro, C. Samori, T. Da Ros, K. Kostarelos, M. Prato and A. Bianco, *Expert Opin. Drug Discovery*, 2010, 5, 691–707.
- 163 S. Prakash and A. G. Kulamarva, *Recent Pat. Drug Delivery Formulation*, 2007, 1, 214–221.
- 164 S. Li, H. He, Q. Jiao and P. H. Chuong, *Progress in Chemistry*, 2008, 20, 1798–1803.
- 165 S. C. Li, J. H. Chen, H. Cao, D. Ss. Yao and D. L. Liu, *Food Control*, 2011, 22, 43–49.
- 166 S. G. Wang, Q. Zhang, R. Wang, S. F. Yoon, J. Ahn, D. J. Yang, J. Z. Tian, J. Q. Li and Q. Zhou, *Electrochem. Commun.*, 2003, 5, 800–803.
- 167 Y. Wang, Z. Iqbal and S. V. Malhotra, *Chem. Phys. Lett.*, 2005, 402, 96–101.
- 168 M. Holzinger, A. Le Goff and S. Cosnier, *Electrochim. Acta*, 2012.
- 169 X.-Y. Yang, G. Tian, N. Jiang and B.-L. Su, *Energy Environ. Sci.*, 2012, 5, 5540–5563.
- 170 J. M. Gómez, M. D. Romero and T. M. Fernández, *Catal. Lett.*, 2005, 101, 275–278.
- 171 M. Raita, T. Laothanachareon, V. Champreda and N. Laosiripojana, *J. Mol. Catal. B: Enzym.*, 2011, 73, 74–79.
- 172 F. Lupo, R. Kamalakaran, C. Scheu, N. Grobert and M. Rühle, *Carbon*, 2004, 42, 1995–1999.
- 173 Y. Shan and L. Gao, *Nanotechnology*, 2005, 16, 625–630.
- 174 U. Rashid, F. Anwar, B. R. Moser and S. Ashraf, *Biomass Bioenergy*, 2008, 32, 1202–1205.
- 175 K. Narasimharao, A. Lee and K. Wilson, *J. Biobased Mater. Bio.*, 2007, 1, 19–30.
- 176 Y. Wang, S. Ou, P. Liu, F. Xue and S. Tang, *J. Mol. Catal. A: Chem.*, 2006, 252, 107–112.
- 177 W. Xie and Z. Yang, *Catal. Lett.*, 2007, 117, 159–165.
- 178 W. Xie and X. Huang, *Catal. Lett.*, 2006, 107, 53–59.

- 179 W. Xie, H. Peng and L. Chen, *Appl. Catal., A*, 2006, **300**, 67–74.
- 180 M. Di Serio, M. Ledda, M. Cozzolino, G. Minutillo, R. Tesser and E. Santacesaria, *Ind. Eng. Chem. Res.*, 2006, **45**, 3009–3014.
- 181 J. Jitputti, B. Kitiyanan, P. Rangsunvigit, K. Bunyakiat, L. Attanatho and P. Jenvanitpanjakul, *Chem. Eng. J.*, 2006, **116**, 61–66.
- 182 K.-H. Chung and B.-G. Park, *J. Ind. Eng. Chem.*, 2009, **15**, 388–392.
- 183 R. Srivastava, D. Srinivas and P. Ratnasamy, *J. Catal.*, 2006, **241**, 34–44.
- 184 P. S. Sreeprasanth, R. Srivastava, D. Srinivas and P. Ratnasamy, *Appl. Catal., A*, 2006, **314**, 148–159.
- 185 G. Sunita, B. M. Devassy, A. Vinu, D. P. Sawant, V. V. Balasubramanian and S. B. Halligudi, *Catal. Commun.*, 2008, **9**, 696–702.
- 186 H. Chen, B. Peng, D. Wang and J. Wang, *Front. Chem. Eng. China*, 2007, **1**, 11–15.
- 187 A. Petchmala, N. Laosiripojana, B. Jongsomjit, M. Goto, J. Panpranot, O. Mekasuwandumrong and A. Shotipruk, *Fuel*, 2010, **89**, 2387–2392.
- 188 J. H. Sim, A. H. Kamaruddin and S. Bhatia, *Bioresour. Technol.*, 2010, **101**, 8948–8954.
- 189 G. Kumar, D. Kumar, S. Poonam, R. Johari and C. P. Singh, *Ultrason. Sonochem.*, 2011, **18**, 923–927.
- 190 M. Di Serio, R. Tesser, L. Pengmei and E. Santacesaria, *Energy Fuels*, 2008, **22**, 207–217.
- 191 E. Lotero, Y. Liu, D. E. Lopez, K. Suwannakarn, D. A. Bruce and J. G. Goodwin, *Ind. Eng. Chem. Res.*, 2005, **44**, 5353–5363.
- 192 X. Miao, R. Li and H. Yao, *Energy Convers. Manage.*, 2009, **50**, 2680–2684.
- 193 C. Samart, P. Sreetongkittikul and C. Sookman, *Fuel Process. Technol.*, 2009, **90**, 922–925.
- 194 S. Shanmugam, B. Viswanathan and T. K. Varadarajan, *J. Mol. Catal. A: Chem.*, 2004, **223**, 143–147.
- 195 J. M. Marchetti, V. U. Miguel and A. F. Errazu, *Fuel*, 2007, **86**, 906–910.
- 196 K. de Boer and P. A. Bahri, *Biomass Bioenergy*, 2011, **35**, 983–991.
- 197 N. N. Mahamuni and Y. G. Adewuyi, *Energy Fuels*, 2009, **23**, 2757–2766.
- 198 G. Vicente, A. Coteron, M. Martinez and J. Aracil, *Ind. Crops Prod.*, 1998, **8**, 29–35.
- 199 M. M. Gui, K. T. Lee and S. Bhatia, *J. Supercrit. Fluids*, 2009, **49**, 286–292.
- 200 P.-C. Ma, N. A. Siddiqui, G. Marom and J.-K. Kim, *Composites, Part A*, 2010, **41**, 1345–1367.
- 201 A. K. Dalai, M. G. Kulkarni and L. C. Meher, *IEC Climate Change Technology*, 2006 IEEE, 2006.
- 202 J. G. Sanchez Marcano and T. T. Tsotsis, *Catalytic membranes and Membrane Reactor*, Wiley-VCH Weinheim, 2002, pp. 5–14.
- 203 M. G. Buonomenna, S. H. Choi and E. Drioli, *Asia-Pac. J. Chem. Eng.*, 2010, **5**, 26–34.
- 204 M. A. Dubé, A. Y. Tremblay and J. Liu, *Bioresour. Technol.*, 2007, **98**, 639–647.
- 205 L. Guerreiro, J. E. Castanheiro, I. M. Fonseca, R. M. Martin-Aranda, A. M. Ramos and J. Vital, *Catal. Today*, 2006, **118**, 166–171.
- 206 S. Baroutian, M. K. Aroua, A. A. A. Raman and N. M. N. Sulaiman, *Sep. Purif. Technol.*, 2010, **76**, 58–63.
- 207 P. Cao, M. A. Dubé and A. Y. Tremblay, *Biomass Bioenergy*, 2008, **32**, 1028–1036.
- 208 P. Cao, M. A. Dubé and A. Y. Tremblay, *Fuel*, 2008, **87**, 825–833.
- 209 J. Saleh, A. Y. Tremblay and M. A. Dubé, *Fuel*, 2010, **89**, 2260–2266.
- 210 S. Baroutian, M. K. Aroua, A. A. A. Raman and N. M. N. Sulaiman, *Bioresour. Technol.*, 2011, **102**, 1095–1102.
- 211 A. F. Ismail, P. S. Goh, S. M. Sanip and M. Aziz, *Sep. Purif. Technol.*, 2009, **70**, 12–26.
- 212 F. Peng, C. Hu and Z. Jiang, *J. Membr. Sci.*, 2007, **297**, 236–242.
- 213 G. Chen and B. Fang, *Bioresour. Technol.*, 2011, **102**, 2635–2640.
- 214 H. J. Schulte, B. Graf, W. Xia and M. Muhler, *ChemCatChem*, 2012, **4**, 350–355.
- 215 C. Li, Z. Shao, M. Pang, C. T. Williams and C. Liang, *Catal. Today*, 2012, **186**, 69–75.
- 216 M. Oubenali, G. Vanucci, B. Machado, M. Kacimi, M. Ziyad, J. Faria, A. Raspolli-Galetti and P. Serp, *ChemSusChem*, 2011, **4**, 950–956.
- 217 Z. Yinghuai, S. L. P. Sia, K. Carpenter, F. Kooli and R. A. Kemp, *J. Phys. Chem. Solids*, 2006, **67**, 1218–1222.
- 218 C. Baleizão, B. Gigante, H. Garcia and A. Corma, *J. Catal.*, 2004, **221**, 77–84.
- 219 I. Eswaremoorthi, V. Sundaramurthy, N. Das, A. K. Dalai and J. Adjaye, *Appl. Catal., A*, 2008, **339**, 187–195.
- 220 W. Feng, J. Yao, H. Wu and P. Ji, *Biotechnol. Adv.*, 2012, **30**, 874–878.
- 221 Y. Sugano, M. D. C. Vestergaard, M. Saito and E. Tamiya, *Chem. Commun.*, 2011, **47**, 7176–7178.
- 222 Z. Cui, C. M. Li and S. P. Jiang, *Phys. Chem. Chem. Phys.*, 2011, **13**, 16349–16357.
- 223 S. Yin, Q. Zhu, Y. Qiang and L. Luo, *Chin. J. Catal.*, 2012, **33**, 290–297.
- 224 X. Yang, J. Zheng, M. Zhen, X. Meng, F. Jiang, T. Wang, C. Shu, L. Jiang and C. Wang, *Appl. Catal., B*, 2012, **121–122**, 57–64.
- 225 F. Li, B. Zhang, X. Li, Y. Jiang, L. Chen, Y. Li and L. Sun, *Angew. Chem., Int. Ed.*, 2011, **50**, 12276–12279.
- 226 Z. Bai, Y. Guo, L. Yang, L. Li, W. Li, P. Xu, C. Hu and K. Wang, *J. Power Sources*, 2011, **196**, 6232–6237.
- 227 S. Yang, X. Wang, H. Yang, Y. Sun and Y. Liu, *J. Hazard. Mater.*, 2012, **233–234**, 18–24.
- 228 Y.-W. Chang, C.-W. Liu, Y.-C. Wei and K.-W. Wang, *Electrochem. Commun.*, 2009, **11**, 2161–2164.
- 229 J. R. C. Salgado, F. Alcaide, G. Álvarez, L. Calvillo, M. J. Lázaro and E. Pastor, *J. Power Sources*, 2010, **195**, 4022–4029.
- 230 F. Luck, *Catal. Today*, 1999, **53**, 81–91.
- 231 V. S. Mishra, V. V. Mahajani and J. B. Joshi, *Ind. Eng. Chem. Res.*, 1995, **34**, 2–48.
- 232 P. X. Hou, C. Liu and H. M. Cheng, *Carbon*, 2008, **46**, 2003–2025.
- 233 M. Kumar and Y. Ando, *J. Nanosci. Nanotechnol.*, 2010, **10**, 3739–3758.
- 234 E. D. Revellame, R. Hernandez, W. French, W. E. Holmes, T. J. Benson, P. J. Pham, A. Forks and R. Callahan II, *RSC Adv.*, 2012, **2**, 2015–2031.

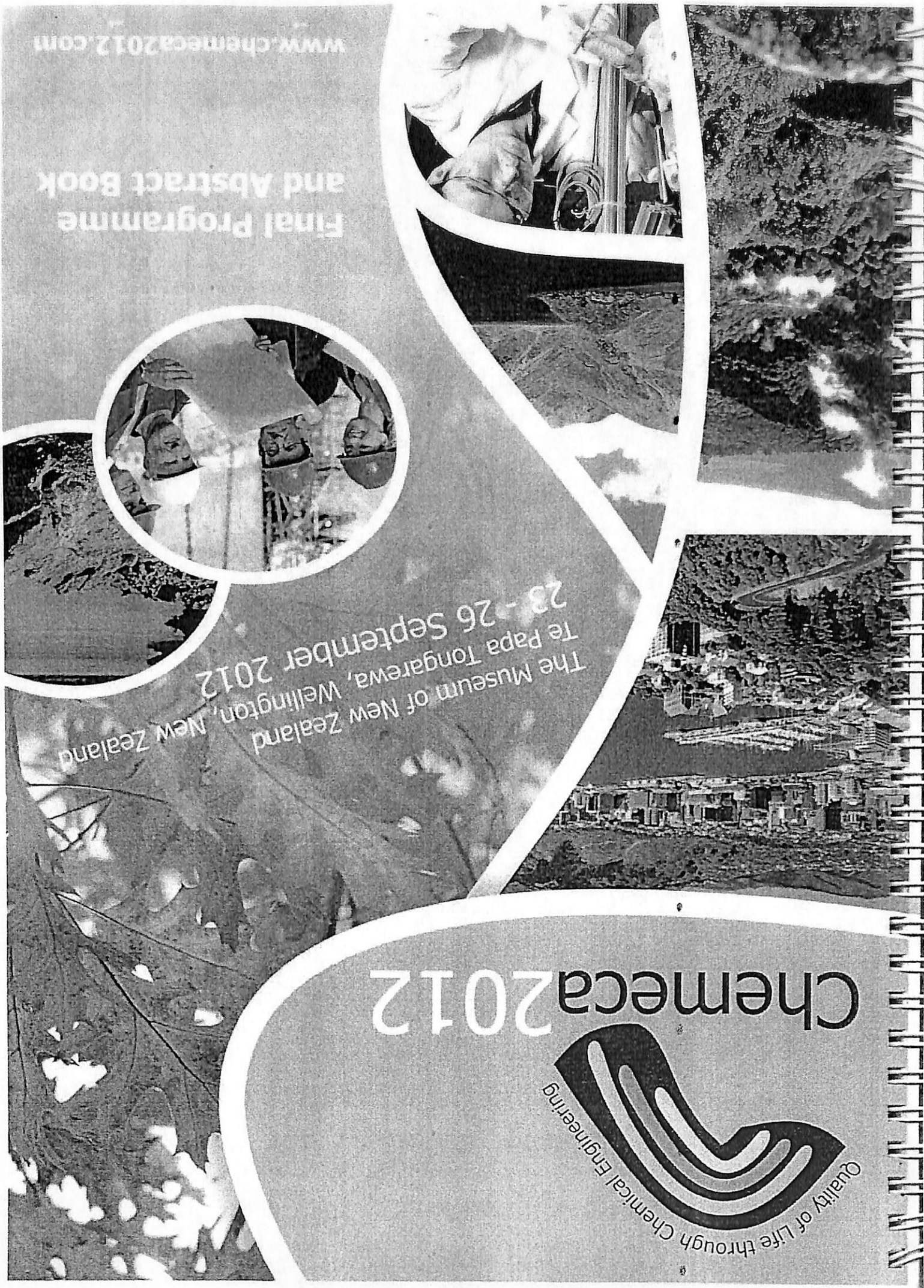


Chemeca 2012

The Museum of New Zealand
Te Papa Tongarewa, Wellington, New Zealand
23 - 26 September 2012

Final Programme
and Abstract Book

www.chemeca2012.com



Sunday, 23 September 2012						
14:00-18:00	Registration					Oceania Room
18:00-19:30	Welcome Reception					Oceania Room
Monday, 24 September 2012						
07:30-18:00	Registration					Oceania Room
08:30-09:00	Welcome <i>Prof Clive Davies, SEAT, Massey University, Palmerston North, New Zealand</i> <i>Gary Romano, Managing Director, NZ Milk Products, Fonterra, New Zealand</i> <i>David Platts, Chairman, SCENZ-ICHEME in New Zealand, Managing Director, PVD Consultants, New Zealand</i>					Soundings Theatre
09:00-09:15	Conference Opening by Her Worship The Mayor of Wellington, Celia Wade-Brown					Soundings Theatre
09:15-10:00	Rolf Prince Plenary: Mr Russell Scott, Institution of Chemical Engineers Chair: David Platts, Chairman, SCENZ-ICHEME in New Zealand; Managing Director, PDV Consultants New Zealand Challenges Facing Chemical Engineers in 2012 - So What! <i>Russell Scott, President, Institution of Chemical Engineers, Australia</i>					Soundings Theatre
10:00-10:45	Plenary: Professor Michael Doherty, University of California, United States Chair: Dr Andrew Cleland, CEO, IPENZ Rapid Process Design for Improved Quality of Life 103 <i>Prof Michael Doherty, University of California, Santa Barbara, United States</i>					Soundings Theatre
10:45-11:15	Morning Tea/ Exhibition/ Poster Session 1 (Refer to poster information on pages 125-126)					Oceania Room
11:15-13:00	S01	S02	S03	S04	S05	S06
	Rangimarie Room 3, The TelstraClear Centre	Angus Room 1, The TelstraClear Centre	Soundings Theatre, Museum of New Zealand Te Papa Tongarewa	Rangimarie Room 2, The TelstraClear Centre	Angus Room 2, The TelstraClear Centre	Rangimarie Room 1, The TelstraClear Centre
	Chemical Engineering Science I Chair: Prof Mark Biggs, The University of Adelaide, Australia	Food and Pharmaceuticals I Chair: Dr Richard Love, Massey University, New Zealand	Modelling and Control I Chair: Dr Trevor Matheson, General Manager operations, CRL Energy Limited, New Zealand	Nanotechnology I Chair: Prof Rose Amal, ARC Centre of Excellence for Functional Nanomaterials, School of Chemical Engineering, The University of New South Wales, Australia	Separations and Extractions Chair: A/Prof Ken Morison, University of Canterbury, New Zealand	Environmental Science and Technology Chair: Prof Jim Jones, School of Engineering and Advanced Technology, Massey University, New Zealand
11:15	104 Interaction Between Two Moving Jets in Immiscible Liquid-liquid Systems: An Experimental Study <i>Chi Phan, Curtin University, Australia</i>	111 An Investigation of Milk Powder Deposition on Parallel Fins <i>Timothy Walmsley, Energy Research Centre, School of Engineering, University of Waikato, New Zealand</i>	117 Modelling and Control for Solid Oxide Fuel Cell (SOFC) Thermal Management: An Integrated Approach <i>Prof Moses Tade, Dean of Engineering, Curtin University, Australia</i>	121 Comparison of n-Dodecane/Brij 30/water and n-Decane/Brij 30/water Nano-emulsions produced by PIT Method <i>Firoozeh Pourjavaheri-Jad, RMIT University, Australia</i>	127 Mitigating the Deposition of Bioactives during Membrane Filtration <i>Dr Zaid Saleh, Plant and Food Research Limited, New Zealand</i> <i>Judie Farr, Plant and Food Research Limited, New Zealand</i> <i>Steffen Friedrich, Plant and Food Research Limited, New Zealand</i>	134 Pyrolysis and Gasification Characteristics of Algal Biomass <i>Chiranjib Saha - Monash University</i>
11:30	105 Convective Amplitudes of Rayleigh-Bénard-Marangoni Cellular Convection with Transient Gas-Liquid Mass Transfer <i>Zhifa Sun, Physics Department, Otago University, New Zealand</i>	112 Adsorption of Proteins on Stainless Steel Surfaces <i>Neha Chandrasekaran, University of Canterbury, New Zealand</i>		122 Amino Acid and Gold Nanoparticles Modified Mesoporous Silica Materials Synthesis and their Applications in DNA Translocation <i>Hemant Daima, RMIT University, Melbourne (VIC) 3000 Australia, Australia</i>	128 Recovery of Engineered Nanomaterials by Dead-End and Cross-Flow Ultrafiltration Membranes from Water <i>So-Ryong Chae, The University of Sydney, Australia</i>	135 Fluidized Bed Gasification of Marine Microalgae in a Spouted Bed Reactor <i>A/Prof Peter Ashman, School of Chemical Engineering, University of Adelaide, Australia</i>

11:45	106	On Virk's Asymptote A/Prof Tuoc Trinh, Massey University, New Zealand	Effect of Surface Modification Techniques on Dairy Fouling Dr Bhan Bansal, Separation Systems Exhibiting Time-Scale Plant-Wide Control of Chemical	Michael Tippelt, The University of New South Wales, Australia Dr Denise Lindsay, Limited, New Zealand Fonterra Co-operative Group Limited, New Zealand	113	
12:00	107	Additive Layers: An Alternative Classification of Flow Regimes A/Prof Tuoc Trinh, Massey University, New Zealand	Zinc Oxide-silica Coatings for the Reduction of Pseudomonas Aeruginosa Proliferation and Biofilm Formation Rose Amal, ARC Centre of Excellence for Functional Nanomaterials, School of Chemical Engineering, The University of New South Wales, Australia	CFD Modelling of Effect of Baffles on Performance of FCC Riser Vishnu Pareek, Department of Chemical Engineering, Curtin University, Australia	114	
12:15	108	Particle Packing Structure in a Rectangular Micro-capillary Prof Mark Biggs, School of Chemical Engineering, The University of Adelaide, Australia	The Dynamics of Volatile Release during Petri Dish based Minimum Inhibitory Concentration Bed Systems Pei Wen Lau, Curtin University, Australia	Modeling and Numerical Simulation of Liquid-Soil Circulating Fluidized of Magnetic Nano-particles in a Bio-compatible Polymeric Electro-spun Nano-fibre Matrix Bradley Hawkins, Curtin University, Australia Dr Deepangshu Chaudhary, Curtin University, Australia	115	
12:30	109	Turbulent Couette Flow: An Analytical Solution A/Prof Tuoc Trinh, Massey University, New Zealand	Analysis of Antioxidant Activities of Beans by Ferric Reducing Antioxidant Power (FRAP) Assays Sulthida Punya-in, School of Chemical Engineering, The University of New South Wales, Australia	Scalable Fabrication of Uniform Microparticles with Highly Ordered Mesoporous Structures Cordelia Selomulya, Monash University, Australia	116	To Be Advised
12:45	110	Blends of Linear Low-Density Polyethylene and Bloodmeal Thermoplastic using Maleic Anhydride grafted Polyethylene as Compatibilizer Ku Marilla Ku Ishak, The University of Waikato, New Zealand	Analysis of Antioxidant Activities of Beans by Ferric Reducing Antioxidant Power (FRAP) Assays Sulthida Punya-in, School of Chemical Engineering, The University of New South Wales, Australia	Structure Modification of Multi-walled Carbon Nanotubes Buckypaper using Polyvinyl Alcohol; Fabrication and Characterization Kian Fei Yee, Universiti Sains Malaysia (USM), Malaysia	126	To Be Advised
13:00-14:00	Lunch/ Exhibition/ Posters					
	129	Non-destructive Characterization of Fluorescent Carbon Nanodots for Medical Research and Light Harvesting Dr Qin Li, Environmental Engineering & Queensland Micro- and Nanotechnology Centre, Griffith University, Australia				
	130	Protein Recovery using Mixed Matrix Membranes Incorporating Hydroxyapatite as Adsorbents Serene Chuan, The University of Auckland, New Zealand				
	131	Innovation and New Product Development in Membranes - Steps and Bed Material on the Effect of Steam to Biomass Ratio				
	138	Effect of Steam to Biomass Ratio and Bed Material on the Development of the Latest Membrane Product from Siemens - The 'N' Series Christopher Kersten, Siemens Ltd, Australia Shusheng Pang, University of Canterbury, New Zealand				
	139	Pyrolytic Conversion of Biomass Residues into Bio-oil and Biochar: Turning Waste into Black Gold Prof Franco Bernuli, Western University, Ontario, Canada				
	132	Production of Optically Pure (S)- Ibuprofen Acid via Enzymatic Dynamic Kinetic Resolution in Hollow Fiber Membrane Reactor Leu Sie Yon, School of Chemical Engineering, Universiti Sains Malaysia				
	322	The Removal of Food Fat based Soils during the Washing of Fabrics Michael Bird, University of Bath, United Kingdom				
	136	Pilot Scale Pyrolysis - Determination of Critical Moisture Content for Sustainable Organic Waste Pyrolysis Kawra Sichone, School of Engineering, University of Waikato, New Zealand				
	137	Development of a Hysys Model for Evaluating the Performance of a DFB Biomass Gasifier Integrated with a Rotary Dryer Nargess Puladian, Chemical and Process Engineering Department, University of Canterbury, New Zealand				
	139	Pyrolytic Conversion of Biomass Residues into Bio-oil and Biochar: Turning Waste into Black Gold Prof Franco Bernuli, Western University, Ontario, Canada				
	132	Production of Optically Pure (S)- Ibuprofen Acid via Enzymatic Dynamic Kinetic Resolution in Hollow Fiber Membrane Reactor Leu Sie Yon, School of Chemical Engineering, Universiti Sains Malaysia				
	322	The Removal of Food Fat based Soils during the Washing of Fabrics Michael Bird, University of Bath, United Kingdom				
	126	Structure Modification of Multi-walled Carbon Nanotubes Buckypaper using Polyvinyl Alcohol; Fabrication and Characterization Kian Fei Yee, Universiti Sains Malaysia (USM), Malaysia				

Oceania Room

Abstracts

DNA and their bigger pore size. Gel-electrophoresis studies reveal that these nanoparticles efficiently complex with plasmid DNA and protect it from enzymatic digestion of DNase I. By the use of MSNs and functionalized MSNs we have achieved low cytotoxicity and higher DNA transformation.

123

Fluorescent Carbon Nanodots for Medical Research and Light Harvesting

Qin Li, Environmental Engineering & Queensland Micro- and Nanotechnology Centre, Griffith University, Australia

Carbon, a material usually associated with 'black', was recently found to be fluorescent in multi-colours when it is in the size of a few nanometers and applied with certain surface functionalisation. These brightly luminescent carbon nanodots have profound implications, because carbon is cheap and abundant, and is chemically inert and biocompatible. Carbon Nanodots represent a promising substitute to semiconductor-based Quantum Dots in various application fields. This talk will present the novel synthesis routes to carbon nanodots and their versatile applications in medical research and light harvesting devices.

124

Analysis of the Interaction and Effect of Magnetic Nanoparticles In a Bio-compatible Polymeric Electro-spun Nano-fibre Matrix

*Bradley R Hawkins, Curtin University, Australia
Deeptangshu S Chaudhary, Curtin University, Australia*

The effect of magnetic nano-particles within bio-compatible nanofibrous mats is a key idea that has been illustrated recently, exploring the interaction between a select few polymers. This research looks at a new bio-polymeric configuration that focusses on other characteristics, such as the uniformity of the nano-structure, and ensuring that the nano-fibres and nano-particles are well-dispersed. Material selection has also been fundamental in identifying a blend that will optimise the physical properties of the nano-structure. Iron-based magnetic nano-particles produce a stimuli-responsive system through the availability of super-paramagnetic particles within the nano-structure. This property has been confirmed through zero-field cooled, field cooled, and hysteresis testing by the use of a superconducting quantum interference device magnetometer. The nano-fibrous mat was produced by electrospinning a blend of chitosan and polycaprolactone. The parameters of this procedure were optimised to achieve the best size consistency. This involved manipulating the applied voltage and polymer concentration. The iron-based magnetic particles were synthesised by the sonication of iron(II) chloride and iron(III) chloride solutions, and were measured to be 15 – 20 nm. They were then integrated into the experiment by adding them to the polymer solution prior to electrospinning. Analysis of the embedded magnetic particles in the polymer matrix was completed using transmission electron microscopy and X-ray diffraction to observe particle agglomeration, differential scanning calorimetry to determine crystallinity changes and thermal properties, and mechanical testing to determine the integrity of the system. The nanoparticles were found to be well-dispersed within the nano-fibre matrix, with minimal agglomeration.

125

Scalable Fabrication of Uniform Microparticles with Highly Ordered Mesoporous Structures

*Kathryn E Waldron, Monash University, Australia
Winston D Wu, Monash University, Australia
Cordelia Selomulya, Monash University, Australia
Wenjie Liu, Monash University, Australia
Dongyuan Zhao, Fudan University, China
Xiao D Chen, Xiamen University, China*

Mesoporous silica is a versatile material with controllable pore size and ease of functionalization, enabling them to be employed in a vast range of applications, such as catalysis, adsorption, and drug delivery. A common method to produce mesoporous silica is via a wet chemistry route involving multiple steps, frequently with organic solvents, while producing relatively small amounts of (often polydisperse) nanoparticles. Spray drying offers a faster, easily scalable route of production without waste. The use of a micro-fluidic jet spray dryer developed at Monash University enables the production of monodisperse microparticles in larger quantities compared to wet synthesis methods. Here, a combination of surfactant templated and evaporation induced self-assembly provides the ability to control the pore size and the particle size of mesoporous microparticles produced. A protocol to assemble these particles was developed with their properties characterized via TEM, SEM, XRD, and nitrogen adsorption. The microparticles demonstrated highly ordered hexagonal mesostructures with high surface areas and pore volumes closely approaching those of mesoporous nanoparticles. The increase in surfactant to silica ratio resulted in increasing surface area and pore volume, provided that the concentration of surfactant was sufficient for the self-organisation of surfactant-silica micelles, while particle size could be controlled by varying the initial solute content in the precursor. This work contributed towards the understanding of formation mechanisms and effects of process parameters on the synthesis of mesoporous materials via the spray drying approach. The knowledge is useful in enabling a rapid and scalable process for the production of functional particles for a wide range of applications.

126

Structure Modification of Multi-walled Carbon Nanotubes Buckypaper using Polyvinyl Alcohol: Fabrication and Characterization

*Kian Fei Yee, Universiti Sains Malaysia (USM), Malaysia
Abdul Rahman Mohamed, Universiti Sains Malaysia (USM), Malaysia
Soon Huat Tan, Universiti Sains Malaysia, Malaysia*

Functionalized multi-walled carbon nanotubes (MWCNTs) were used to prepare buckypaper (BP) via simple filtration method and the resulted BP was modified by polyvinyl alcohol (PVA). In this modification method, firstly, the raw MWCNTs were purified by using nitric acid. Then, sulfonic acid groups (-SO₃H) were covalently grafted onto the surface of purified MWCNTs by treating with concentrated sulfuric acid at temperature 250 °C. The functionalized-MWCNTs were then dispersed in ethanol and the suspension was filtered to form self-supporting functionalized BP. Then, PVA solution was coated on the BP by solution casting method. The raw, purified and functionalized-MWCNTs were

Abstracts

characterized by using scanning electron microscopy (SEM), transmission electron microscopy (TEM), thermogravimetric analysis (TGA) and Fourier transform-infrared spectroscopy (FT-IR). TGA results showed that the thermal stability of MWCNTs increased after treating with acid, whereas FT-IR spectra revealed the appearance of -SO₃H groups on the functionalized-MWCNTs. On the other hand, the dropped of contact angle from 64.5° to 43.7° indicated that the hydrophilicity of PVA coated-purified BP increased after functionalization. The thickness of PVA coated-functionalized BP increased with respect to the increased of functionalized-MWCNTs loading. Tensile test results indicated that the overall mechanical properties of the PVA coated-functionalized BP improved as compared to the PVA film.

127

Mitigating the Deposition of Bioactives during Membrane Filtration

Zaid S Saleh, *Plant and Food Research Limited, New Zealand*
Judie M Farr, *Plant and Food Research Limited, New Zealand*
Steffen A Friedrich, *Plant and Food Research Limited, New Zealand*

The recovery of phenolic compounds from apple juice was studied on a laboratory pilot-scale using a commercially viable filtration process. The fouling mechanism was characterised and modelled using a polysulphone SelRO® spiral-wound membrane with a molecular weight cut-off (MWCO) of 1 kDa and 0.25 kDa. The retention of various compounds including total and individual phenolics proteins and certain types of sugars was determined analytically. The effects of temperature (20, 30, 40, & 50°C), feed concentration (5, 10, 15 & 20° Brix), transmembrane pressure (5, 10, 15, & 20 bar) and pH (2, 3, 4, & 5) on permeate flux, fouling and membrane performance were determined. Different types of fouling mechanisms, including reversible and irreversible concentration polarisation, cake formation, pore blocking, or a combination of the aforementioned, were investigated. Fouling is detected by a decrease in permeate flux with time. The permeate flux was greater at higher temperatures, pH values and pressures, and lower at higher feed concentrations. Modelling of the permeate flux using available predictive fouling models in literature gave comparable results. It was found that cake formation was the dominant reversible fouling mechanism in the 1 kDa membrane and that pore blocking was the dominant type of fouling occurring in the 0.25 kDa membrane. The filtration process was optimised, the optimum operating conditions were identified and a fouling mitigation strategy is recommended.

128

Recovery of Engineered Nanomaterials by Dead-End and Cross-Flow Ultrafiltration Membranes from Water

So-Ryong Chae, *The University of Sydney, Australia*
Hee-Chan Jang, *The University of Sydney, Australia*
Tahereh Noeiaghajaei, *The University of Sydney, Australia*
Soleyman Mamisahebi, *University of Technology, Sydney, Australia*
Ho-Kyong Shon, *University of Technology, Sydney, Australia*
Jong-Oh Kim, *Gangneung-Wonju National University, Korea*
Mark R Wiesner, *Duke University, United States*
Jieun Lee, *The University of Sydney, Australia*

More than one thousand consumer products containing engineered nanomaterials (ENMs) such as silver, carbon, titanium, silica, zinc, and gold are available in the markets. The ever-increasing use of ENMs in commercial products and applications has raised concerns over the potential consequence of environmental and human exposure. Although it is not clear at the outset if the potential for significant harm even exists, the best way to minimise the risks of ENMs might be secure recovery of the materials from manufacturing, recycling, and disposal points before they are discharged into the environments. The mobility of ENMs is influenced by the size and surface charge of the particles in the environmental media in which they are contained. It was clearly shown that primary engineered nanoparticles tend to form colloidal aggregates even in deionized (DI) water. To recover the ENMs from various water streams, it is important to understand fate/transport of ENMs and their interaction with other environmental components. Here, we explore the effects of natural organic matter (NOM) and pressure gradient on recovery efficiency of carbon nanomaterials by membrane filtration. As a result, we show that the more hydrophilic engineered nanoparticles showed lower separation efficiency by membrane filtration than the less hydroxylated nanoparticle aggregates. The results highlight the difficulties encountered when tackling the separation of heterogeneous nanomaterials from aqueous suspension using conventional membranes.

Keywords: Engineered nanomaterials, recovery, colloidal aggregates, natural organic matter, and ultrafiltration membrane.

129

Non-destructive Characterization of Nano-filtration and Reverse Osmosis Membrane Module Fouling using Magnetic Resonance Imaging

Michael L Johns, *School of Mechanical and Chemical Engineering, The University of Western Australia, Australia*
Einar O Fridjonsson, *School of Mechanical and Chemical Engineering, The University of Western Australia, Australia*
Hans S Vrouwenvelder, *Department of Biotechnology, Faculty of Applied Sciences, TU Delft, The Netherlands*

Magnetic Resonance Imaging (MRI) has been applied to non-invasively elucidate several aspects of bio-fouling of nano-filtration and reverse osmosis membranes (ROMs) modules as a function of fouling time. These include the spatial distribution of biomass accumulation and its effect on system hydrodynamics, the effect on these parameters of ROM cleaning protocols and the detailed validation of 3D simulations of ROM bio-fouling. These developments are summarised and preliminary work using the earth's magnetic field for MRI detection purposes of biofouling outlined.

130

Protein Recovery using Mixed Matrix Membranes Incorporating Hydroxyapatite as Adsorbents

Serene WL Chuah, *The University of Auckland, New Zealand*
Darrell Alec Patterson, *Department of Chemical Engineering, University of Bath, United Kingdom*
Mark I Jones, *University of Auckland, New Zealand*

The main aim of this project is to characterise and optimise the use of hydroxyapatite (HAP) as an adsorbent for proteins in mixed



USM UNIVERSITI
SAINS
MALAYSIA

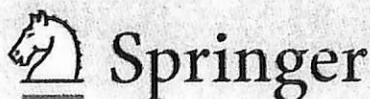
Program & Abstract Book

MAMIP 2012

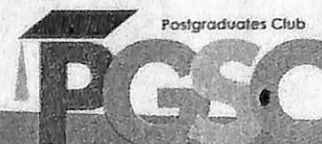
**Asian International Conference on
Materials, Minerals, and Polymer**
23rd - 24th March 2012, Vistana Hotel, Penang

*Bridging Notions,
Sustaining Innovations*

Main Sponsors



Organized by



School of Materials &
Mineral Resources
Engineering



**ASIAN INTERNATIONAL CONFERENCE ON
MATERIALS, MINERALS, AND POLYMER 2012**



**SCHOOL OF MATERIALS AND MINERAL
RESOURCES ENGINEERING,
UNIVERSITI SAINS MALAYSIA**

MARCH 2012

Session 4d		
Venue: Room 4		
Chairperson: Dr. Aidah Jumahat		
0920-0940	R4F16-114	Lupong Kaewsichan , <i>Formulation Factors Effecting Bioactive Properties of Scaffolds Prepared From Nano-Hydroxyapatite and Zirconia</i>
0940-1000	R4F16-115	Soon Huat Tan , <i>Poly(vinyl alcohol) Functionalized Multi-walled Carbon Nanotube-Chitosan Membranes and Their Application in Dehydration of Acetone via Pervaporation</i>
1000-1020	R4F16-116	W P S K Perera , <i>Effects of Nano-Silver Finishing on the Physical and Dyeing Properties of Polyester Fabrics</i>
1020-1040	R4F16-117	W.G.I.U. Rathnayake , <i>Synthesis and Characterization of Various Colors of Silver Nanoparticles by Chemical Reduction Method</i>

Session 5a		
Venue: Room 1		
Chairperson: Dr. R.J. Talib		
1100-1120	R1F17-061	Mat Uzir B. Wahit , <i>Effect of Polypyrrole on the Morphology, Mechanical and Electrical Properties of High Density Polyethylene/Montmorillonite Nanocomposites</i>
1120-1140	R1F17-062	M. Mathialagan , <i>Influence of Maleic Anhydride Grafted Ethylene Propylene Diene Monomer (MAH-G-EPDM) on the Properties of Bentonite Filled EPDM Composites</i>
1140-1200	R1F17-063	MIM Rafiq , <i>Thermal and Mechanical Properties of Injection Moulded Aramid/Carbon Hybrid Fibres Reinforced Polypropylene Composites</i>
1200-1220	R1F17-064	Normasmira A. Rahman , <i>Polypropylene/Glass Fiber/Nanoclay Hybrid Composites: Fabrication and Analysis of Morphological, Thermal and Dynamic Mechanical Behaviors</i>
1220-1240	R1F17-065	Mat Uzir Wahit , <i>Oil Palm Fiber Reinforced Poly (E-Caprolactone) and Poly (Lactic Acid) Composites: Effect on Mechanical Properties</i>
1240-1300	R1F17-066	Sarawut Rimdusit , <i>Synthesis and Characterization of Non-Phosgene Polycarbonate by Melt Transesterification of Bisphenol-A with Diphenyl Carbonate</i>

Session 5b		
Venue: Room 2		
Chairperson: Dr. Yuttanant Boonyongmaneerat		
1100-1120	R2F18-080	S.J. Tan , <i>The Effect of Polyaniline (PANI) Modified Water Hyacinth Fiber (Eichhornia Crassiper) on Mechanical Properties, Morphological Properties and XRD Characterization of Low Density Polyethylene/ Natural Rubber/ Water Hyacinth Fiber Composites</i>
1120-1140	R2F18-081	N.L. Suradi , <i>Natural Fibers Reinforced Recycled Polypropylene/Recycled Polyamide 6 Composites</i>
1140-1200	R2F18-082	Wisut Kaewsakul , <i>Factors Influencing the Flocculation Process in Silica-Reinforced Natural Rubber Compounds</i>
1200-1220	R2F18-083	Waham Ashaier Laftah , <i>Synthesis and Characterization of Polymer Hydrogel Composites Based on Poly (Acrylic Acid) Filled with Cotton Microfiber</i>
1220-1240	R2F18-084	M. W. Adnin , <i>The Effects of Cellulose and Cellulose Acetate as Fillers on the Properties of Biodegradable Low Density</i>

R4F16-114

Formulation Factors Effecting Bioactive Properties of Scaffolds Prepared From Nano-Hydroxyapatite and Zirconia

Jareonporn Saekhow, Jasadee Kaewsrichan and Lupong Kaewsichan*

*Corresponding author: lupong.k@psu.ac.th

Abstract: Nano-hydroxyapatite (nHA) was prepared by sol-gel method using $\text{Ca}(\text{NO}_3)_2$ and $(\text{HN}_4)_2\text{HPO}_4$ as starting reagents. The synthesized nHA was separately blended with ZrO_2 at a mole ratio of 0.01, 0.05, 0.1, 0.2 and 0.5, respectively named as F1, F2, F3, F4 and F5. Scaffolds were fabricated by dipping and then sintering at either 1150 or 1250 °C for 2 h. After immersed in PBS for 3 days, greater amounts of mat-like apatite were apparent for F1 and F3 compared to the others as evaluated by SEM. In regarding to sintering temperatures, more amounts of the apatite were formed at the higher heating level. XRF data showed that the Ca/P ratio decreased by Zr-supplement, resulting in the incorporation of Zr into HA lattices. The new bioactive materials developed might be useful in the fields of bone tissue engineering and functional drug delivery.

R4F16-115

Poly(vinyl alcohol) Functionalized Multi-walled Carbon Nanotube-Chitosan Membranes and Their Application in Dehydration of Acetone via Pervaporation

Qian Wen Yeang, Yoke Kooi Cheng, Sharif Hussein Sharif Zein and Soon Huat Tan*

*Corresponding author: chshtan@eng.usm.my

Abstract: The main obstacle being faced in the process of producing a good quality of the multi-walled carbon nanotubes (MWCNTs) based nanocomposite is achieving homogeneous dispersion of MWCNTs in the polymer matrix as MWCNTs tends to form agglomeration. Thus, the present work focuses on the functionalization of MWCNTs with poly(vinyl alcohol) (PVA) which is miscible with chitosan in order to improve the compatibility and dispersion of MWCNTs in chitosan matrix. Pervaporation results showed that PVA-MWCNT/chitosan nanocomposite membranes exhibited an increase in the selectivity towards water and decrease in permeate flux when the concentration of acetone in the feed solution was increased. Furthermore, the permeability of the PVA-MWCNT membrane increased while the selectivity decreased as compared to pure chitosan membrane. Nevertheless, the selectivity of the nanocomposite decreased while the permeate flux improved when increasing the feed temperature. When low vacuum was applied, both the selectivity and permeate flux declined as a result of the reduced driving force. In another approach, PVA functionalized MWCNT was bulk aligned on the polyvinylidene fluoride (PVDF) membrane by simple filtration method and further coated with chitosan to form a three-layer composite membrane. As for the three-layer nanocomposite membrane, it revealed immense improvement on permeate flux and selectivity compared to the dense nanocomposite membrane.

Technical Report

Title: Development of carbon Nanotubes supported ionic liquid membrane (SILM) and their application in pervaporation process

Introduction

Pervaporation⁶ has been recognized as an energy-efficient process. Its distinguished separation characteristics, i.e., its phase change from liquid to vapour mediated by a driving force induced by a chemical activity difference, provide high efficiency to the separation of close-boiling-point and azeotrope mixtures. To date, most of the pervaporation process have focused on the use of solid membranes fabricated from a pure polymer, such as poly(vinyl alcohol) (PVA) [1, 2] and chitosan [3, 4], or a mix-matrix membrane [5, 6] that incorporates an inorganic filler into the polymer.

Instead of using solid membranes, many studies have started to use SILM in the pervaporation process. Briefly, SILM consists of an ionic liquid that is immobilised into a porous support. The porous support is used to supply the necessary mechanical stability to the SILM, whereas the liquid membrane which involves the use of ionic liquid acts as a semi-permeable barrier and governs^u the mass transport. Ionic liquid is an organic liquid salt that possesses a relatively low melting point, which enables it to remain in the liquid state at room temperature. It has a better thermal stability and a low-to-negligible vapour pressure, which make it difficult to vaporise. Numerous studies on the applications of SILM in pervaporation for the separation of organic compounds from dilute aqueous solutions have been reported [7-13]. Although the use of SILM is always associated with an instability problem caused by the leaching of the liquid membrane from the porous support, particularly under high pressure or vacuum conditions, several methods have been proposed to overcome this limitation, and these include re-immobilisation of the liquid membrane [14], surface coating [15], and mixing with a base polymer to form a thin, stable film [16]. In addition, the use of a porous support with a smaller pore diameter would also help enhance the SILM stability [17, 18].

Other than providing physical stability, the porous support in SILM also plays a significant role as a medium to entrap and firmly hold the liquid membrane. Most of the porous supports are prepared from a polymeric substance, such as polypropylene [14], polyvinylidene fluoride (PVDF) [19] and polysulfone [20]. To improve the performance of SILMs, this research

presents the novel production of a high-stability SILM using buckypaper (BP) as a porous support. BP is one of the carbon-nanotubes (CNTs)-based membranes that are solely composed of entangled assemblies of CNTs held together by van der Waals interactions at tube-tube junctions and arranged as a planar film [21]. The entanglement of the randomly orientated CNT bundles could form a highly porous network structure with a free volume up to 70% of its total volume [22]. BP has exhibited vast potential applications in hydrogen storage [23], actuators [24], sensors [25] and artificial muscles [26]. Recent studies conducted by Yee et al. [27] also reported the application of BP in the membrane separation process. The introduction of BP as a pre-selective layer in an asymmetric membrane was found to control the permeability and enhance the pervaporation performance of the resulting asymmetric membrane.

Objectives

The primary aim of the research is to synthesize a high stability supported ionic liquid membrane (SILM) by employing a liquid membrane phase consists of an ionic liquid blend with polyvinyl alcohol (PVA) polymer and immobilized in a buckypaper (BP) to form a buckypaper supported ionic liquid membrane (BP-SILM). The specific aims are:

- To study on the effectiveness of the BP-SILM in the pervaporation of binary mixtures and ternary azeotropic mixtures.
- To investigate the separation characteristic of the BP-SILM in the pervaporation and evaluate the effect of the operating conditions on its pervaporation performance.

METHODOLOGY

Preparation of PVA and [Bmim][BF₄]

The PVA solution was prepared by dissolving 5 wt.% PVA powder in distilled water under vigorous stirring at 80°C for 6 h. After the PVA powder was fully dissolved in water, the stirring process was maintained at room temperature overnight. In addition, the [Bmim][BF₄] solution was prepared by dissolving 5 wt.% [Bmim][BF₄] in distilled water and stirring at room temperature. Both the [Bmim][BF₄] and PVA solutions were carefully mixed to form a [Bmim][BF₄]-PVA solution at weight ratios of 30/70, 50/50, and 70/30.

Preparation of BP and BP-SILM

The MWCNTs were chemically oxidised and transformed into BP sheets with diameters of 90 mm through a wet processing technique. A pre-weighed amount of oxidised MWCNTs was dispersed in ethanol and sonicated for 15 min, and the MWCNT suspension subjected then to vacuum filtration through a 0.45- μm nylon membrane filter. The resulting BP was then washed with distilled water.⁴ Five different weights of BPs, ranging from 3.44 to 5.88 mg/cm² of MWCNTs, were prepared. The vacuum filtration process was continued to immobilise the [Bmim][BF₄]-PVA solution in the BP, and the process was stopped once a thin visible layer of excess [Bmim][BF₄]-PVA solution was observed on the surface of the BPs. The excess [Bmim][BF₄]-PVA was removed using a transfer pipette, and the as-formed BP-SILM was then peeled off from the membrane filter and dried at room temperature. After drying, the BP-SILM was immersed in a cross-linking bath containing 2.5 mL of glutaraldehyde, 2.5 mL of hydrochloric acid and water-acetone mixtures (30/70 vol.%). BP was infiltrated with three different concentration of [Bmim][BF₄]-PVA mixtures: 30/70, 50/50 and 70/30 wt.%. The resulted BP-SILMs were coded as BP-SILM-30, BP-SILM-50 and BP-SILM-70, respectively. The efficiency of the BP to entrap [Bmim][BF₄]-PVA was calculated based on the following equation:

$$\text{Immobilised content} = \frac{M_{BP-SILM} - M_{BP}}{M_{BP}} \quad (1)$$

where $M_{BP-SILM}$ and M_{BP} refer to the weights of the BP-SILM and BP, respectively.

Liquid sorption study

The BP-SILMs were immersed into solutions and placed in a sealed vessel. The sorption process was then continued at room temperature for 72 h until the equilibrium state was achieved. The swollen BP-SILMs were rapidly removed from the vessel and weighed immediately after blotting the excess adhered liquid. The total amount of liquid sorbed was determined using the following equation:

$$\text{Degree of swelling} = \frac{M_{BP-SILM'} - M_{BP-SILM}}{M_{BP-SILM}} \quad (2)$$

where $M_{BP-SILM}$ and $M'_{BP-SILM}$ represent the weights of the dry and swollen BP-SILMs, respectively. According to the Flory-Huggins theory, the binary interaction parameter χ_{im} between component i and the BP-SILM was calculated using the following equation [28]:

$$\chi_{im} = \frac{\ln(1 - v_m) + v_m}{v_m^2} \quad (3)$$

where v_m is the volume fraction of the membrane in the swollen BP-SILM.

Pervaporation experiments

The pervaporation experiments were performed using a laboratory-scale pervaporation test rig. The BP-SILM was mounted onto a stainless-steel permeation cell supported with a porous stainless-steel plate and supplied an effective surface area of 8.6 cm². Feed solutions were circulated between the feed tank and the permeation cell at a constant flow rate. The operating temperatures of the feed solutions were maintained between 30°C and 70°C and the downstream pressure was maintained within 5 to 25 mmHg. The pervaporation process was operated for 4 h, the permeate vapour was condensed and collected in cold traps immersed in liquid nitrogen. The collected permeate sample was weighed, and its composition was analysed. The pervaporation performance of the BP-SILM was assessed in terms of the permeation flux, J , and the separation factor for component i , β , as expressed in the following equations:

$$J = \frac{Q}{A \times t} \quad (4)$$

$$\beta = \left(\frac{Y_i}{1 - Y_i} \right) \left(\frac{1 - X_i}{X_i} \right) \quad (5)$$

where Q refers to the mass (g) of the permeate collected at time interval t (h), A (m²) is the membrane effective surface area, and X_i and Y_i represent the mass fractions of component i in the feed and permeate, respectively.

In addition, the membrane intrinsic properties can be evaluated in terms of the permeance, P , and the membrane selectivity, α , which were calculated using the following equations:

$$P_i = \frac{J_i}{MW_i(\gamma_i x_i p_i^{sat} - y_i p)} \quad (6)$$

$$\alpha = \frac{P_i}{P_j} \quad (7)$$

where MW_i is the molar mass (g/mol) of component i , γ_i , x_i and p_i^{sat} are the activity coefficient, molar fraction and saturated vapour pressure (mmHg), respectively, of component i at the feed side, y_i is the mole fraction of component i at the permeate side and p is the total downstream pressure (mmHg).

Characterisation

Thermogravimetric analysis (TGA) of the BP-SILMs was performed using a PerkinElmer STA 6000 Simultaneous Thermal Analyzer. The specimens were placed in an alumina crucible and heated from room temperature to 900°C with a heating rate of 10°C/min under air conditions. The surface morphology and cross section of each of the BP-SILMs and the elemental compositions of the samples were visualised using a Quanta 450 FEG scanning electron microscope (SEM) equipped with an energy dispersive X-ray (EDX) apparatus. The membranes were fractured in liquid nitrogen to avoid any polymer deformation prior to the test.

Contact angle measurement

The contact angles of water on the membranes were measured via the sessile drop technique using a Rame-Hart standard goniometer Model 250 equipped with a video camera at room temperature. A controlled volume of 6 μL of deionised water was carefully dropped onto the sample. The image of each drop shape was captured using a video camera, and the corresponding contact angle was determined using the supplied software.

Determination of the mechanical properties

The mechanical properties of the membrane were examined using an Instron table-mounted universal testing machine. Each of the specimens was cut into a dumbbell shape with a gauge length of 22 mm. The load cell was set to maximum with a constant crosshead speed of 1 mm/min. The tensile strength and elongation at break were determined.

RESULTS AND DISCUSSION

Characterisation

The thermal stability of the [Bmim][BF₄]-PVA blended membranes and the pure [Bmim][BF₄] and PVA membranes were also determined using TGA. As shown in the TGA thermogram presented in Figure 1, pure [Bmim][BF₄] exhibited a single-stage degradation, which started at 300°C and was completed at 550°C. Pure PVA membrane exhibited degradation at three different temperature ranges: the first degradation below 100°C involves removal of the residual moisture, the subsequent stage at a temperature between 180 and 400°C appears to involve the elimination of side groups, and the last stage at 400 to 600°C appears to be due to breakdown of the polymer backbone [29]. A decrease in thermal stability was observed in the blended membranes compared with the pure [Bmim][BF₄]. However, note that the decomposition temperature of the blend membrane was increased in the ascending order of 30/70, 50/50 and 70/30 wt.% [Bmim][BF₄]-PVA. This observation reveals that the thermal stability of the blended membrane increased with respect to the content of [Bmim][BF₄] in the blend.

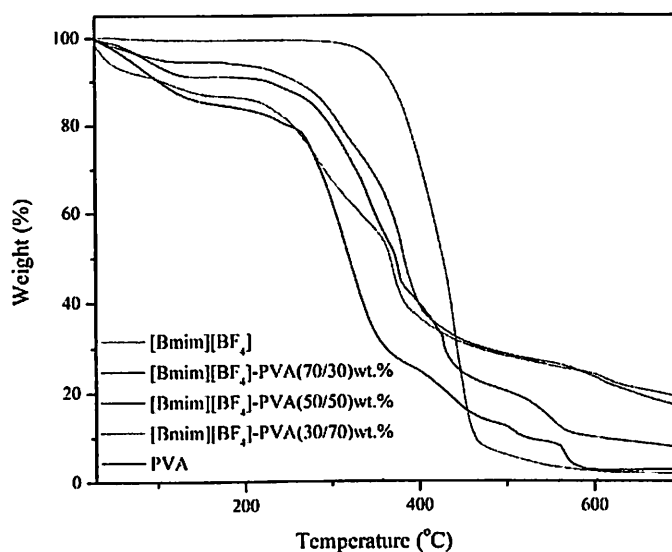
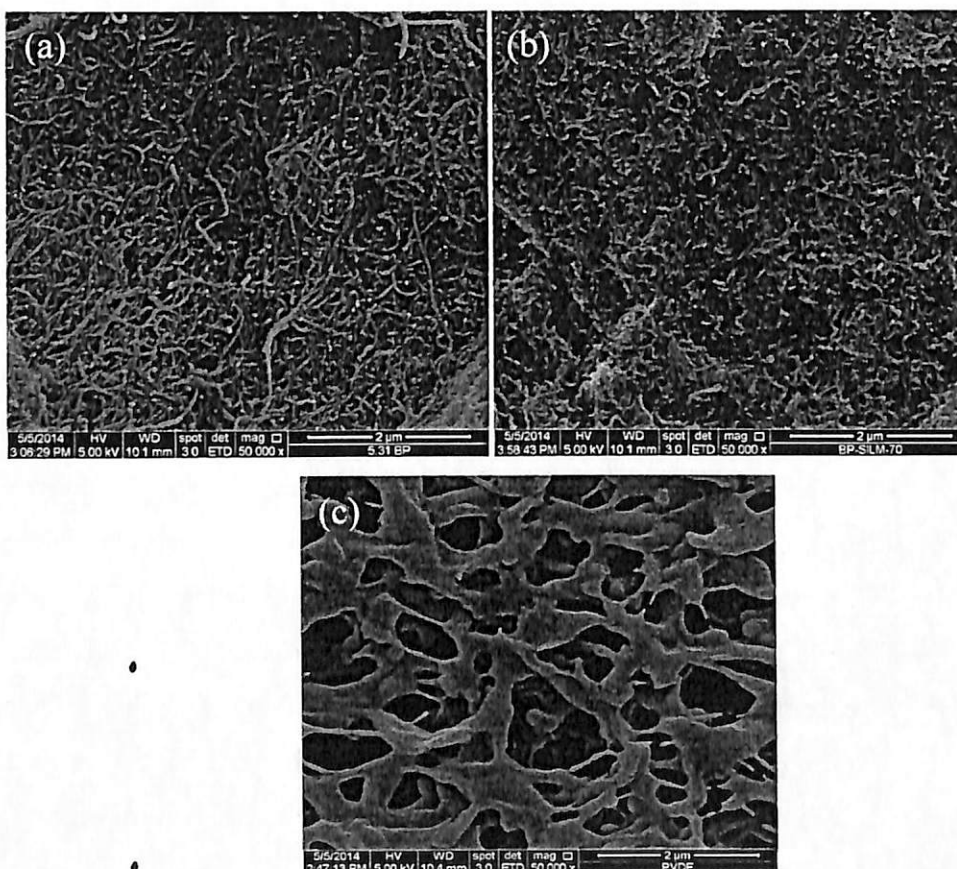


Figure 1: Thermogravimetric thermogram of pure [Bmim][BF₄], [Bmim][BF₄]-PVA in 30/70, 50/50 and 70/30 wt.%, and pure PVA.

The SEM surface morphologies of the BP and BP-SILM are shown in Figure 2. The MWCNT threads were clearly visible, randomly entangled with each other and predominately horizontal to the surface of the BP without any significant agglomeration. The entanglement of

MWCNTs in the BP formed a rather small interstitial pore, whereas the surface of the BP-SILM was denser, and the MWCNTs were found to be covered by [Bmim][BF₄]-PVA. From the cross-sectional view, the texture of the BP-SILM was found to be more closely and neatly packed than the BP. This observation can be attributed to the capability of [Bmim][BF₄]-PVA to penetrate and be immobilised in the deeper interstitial pores in the BP. The presence of [Bmim][BF₄]-PVA in the BP-SILM was further verified through EDX: 1.06% fluorine atoms were detected in the cross-section of BP-SILM, which may be associated with the presence of [Bmim][BF₄]. Thus, the result confirmed that [Bmim][BF₄]-PVA can be effectively immobilised in the interstitial pores of the BP via the vacuum-based technique.



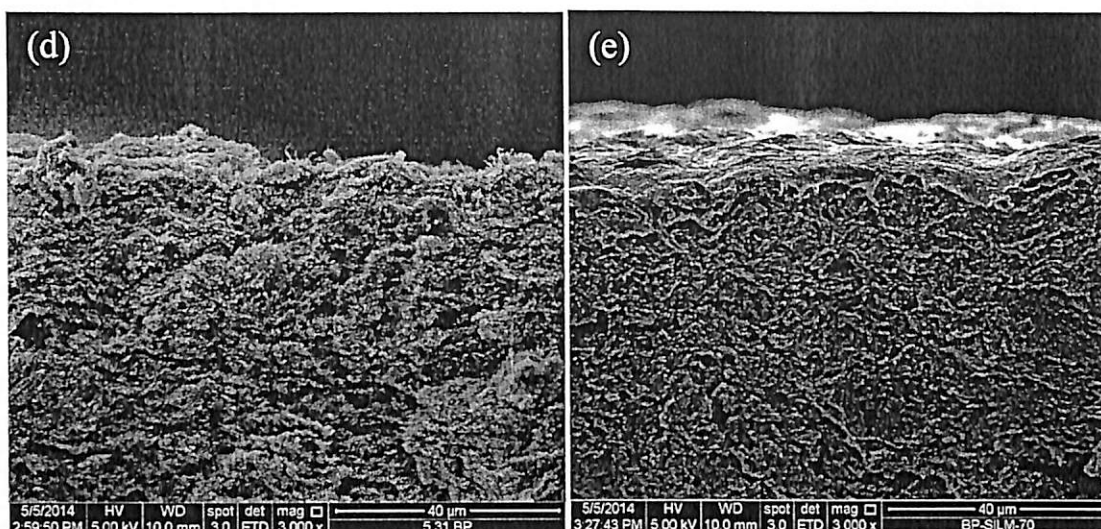


Figure 2: SEM image of the surface morphologies of (a) BP, (b) BP-SILM, and (c) PVDF membrane filter and the cross-sectional views of (d) BP and (e) BP-SILM.

The effect of the MWCNT content in BP on the immobilisation of [Bmim][BF₄]-PVA are summarised in Table 1. Because polymeric membrane filters are commonly used in the fabrication of SLMs, a 0.22- μm PVDF membrane filter was used for comparison purposes. The results revealed that the content of immobilised [Bmim][BF₄]-PVA in BP was significantly higher than that found in the PVDF membrane filters. This difference can be attributed to the tortuosity of the porous structure and the pore size of BP. As the loading of MWCNTs increased, the content of the immobilised [Bmim][BF₄]-PVA also increased until an optimum MWCNT loading in BP of 5.31 mg/cm^2 , at which the immobilisation achieved an optimum content of 0.71 g/g MWCNTs. A further increase in the MWCNT loading in the BP resulted in a decrease in the immobilised [Bmim][BF₄]-PVA content, which may be caused by the fact that aggregated MWCNTs eventually decreased the interstitial pore distribution in the resulting BP, thereby reducing their efficiency to entrap [Bmim][BF₄]-PVA. In addition to the immobilised [Bmim][BF₄]-PVA content, the thickness of the resulting BP-SILM exhibited an increase in the MWCNT content of the BP, and the use of BP as a porous support enabled the formation of a thinner-layer membrane compared with the SILM formed using a PVDF membrane filter as a support.

Table 1. Effect of the CNT content in the BP on the immobilisation of PVA-[Bmim][BF₄].

CNT content in the BP (mg/cm ²)	Immobilised content (g/g MWCNTs)	Thickness (μm)
3.44	0.60	76
4.01	0.63	84
4.59	0.68	90
5.31	0.71	117
5.88	0.65	123
0.22-μm PVDF membrane filter	0.08	125

Based on the mechanical properties presented in Table 2, the tensile stress and elongation of the BP-SILMs were significantly increased with an increase in the MWCNT loading of the BP, and the optimum tensile stress was achieved with MWCNT content in the BP-SILM of 5.31 mg/cm². The increase in the mechanical properties with an increase in the MWCNT loading of the BP may be due to the increase in the number of entangled MWCNTs, which strengthens the MWCNT network. Furthermore, the immobilised [Bmim][BF₄]-PVA may serve as a binder to tighten the connection between the MWCNTs in the BP. However, a decrease in the mechanical properties of the BP-SILM was observed at loadings greater than the optimum MWCNT loading of 5.31 mg/cm². As mentioned earlier, increasing the MWCNT content up to 5.88 mg/cm² caused the formation of aggregated MWCNTs, which impairs the mechanical stability of the BP structure. Moreover, the MWCNT network in the BP with 5.88 mg/cm² MWCNT may be loosely bound because the immobilised content of [Bmim][BF₄]-PVA, which served as a binding agent was reduced. Therefore, after the optimum immobilisation capacity and the mechanical properties were determined, the subsequent experiments were performed using the BP-SILM with 5.31-mg/cm² MWCNT BP.

Table 2. Effect of the CNT content in the BP on the mechanical properties of the BP-SILM.

CNT content in the BP (mg/cm ²)	Tensile stress (MPa)	Elongation at break (%)
3.44	6.83	3.77
4.01	9.15	4.56
4.59	11.34	5.24
5.31	14.18	6.46
5.88	10.62	5.33

The contact angle measurements presented in Table 3 indicate that the contact angle of PVA after infiltration in BP was slightly higher compared with that obtained with a pure PVA membrane: an increase in the contact angle from 55.4° to 73.5° was observed. This increase can be ascribed to the intrinsic hydrophobicity of the MWCNTs. However, the contact angle of the BP-SILM decreased from 68.6° to 46.9° when the content of [Bmim][BF₄] in BP-SILM was increased from 30 to 70 wt.%. This behaviour indicated an increase in the hydrophilicity of the membrane because the presence of [BF₄]⁻ anions in [Bmim][BF₄] tends to form hydrogen bonds with water [30], thereby reducing the surface tension of the water droplet and increasing the wettability of the BP-SILM surface.

Table 3. Contact angle measurements as a function of the weight fraction of [Bmim][BF₄] in the BP-SILM.

Type of membrane	Contact angle (°)
PVA membrane	55.4
BP-PVA ^a	73.5
BP-SILM-30 ^b	68.6
BP-SILM-50 ^c	53.5
BP-SILM-70 ^d	46.9

Liquid sorption study

Ethylene glycol and water

Based on the degree of swelling presented in Table 4, the sorption capability of BP-SILM in water and ethylene glycol was found to be increased with an increase in the content of [Bmim][BF₄] in the BP-SILM. The increase in the sorption of water with increasing [Bmim][BF₄] is simply due to the tendency of the [BF₄]⁻ anions to interact with water and form hydrogen bonds. In addition, the increase in the sorption in ethylene glycol with increasing content of [Bmim][BF₄] in BP-SILM can be attributed to the hydrophobic interaction and the hydrogen bond formed between the [Bmim]⁺ cation with the -O- of the terminal-OH in ethylene glycol [31, 32]. Although the presence of [Bmim][BF₄] increased the sorption of both water and ethylene glycol, the affinity of the membrane can still be traced to the binary interaction parameter, χ_{im} : a stronger affinity between the component and membrane is usually indicated by a lower χ_{im} value. As shown in Table 4, the values of χ_{im} for both water and ethylene glycol with BP-SILM decreased with an increase in the [Bmim][BF₄] content, suggesting a stronger interaction

between the water and ethylene glycol with the increased [Bmim][BF₄] content in the BP-SILM. However, note that the χ_{im} value of water is lower than that of ethylene glycol. This behaviour implies that the interaction of BP-SILM with water is greater than that with ethylene glycol.

Table 4. Sorption data of the BP-SILMs as a function of the weight fraction of [Bmim][BF₄].

Type of BP-SILMs ^a	Degree of swelling (g/g membrane)		Interaction parameter, χ_{im}	
	Water	Ethylene glycol	Water	Ethylene glycol
BP-SILM-30	1.2185	0.6890	0.6990	0.8508
BP-SILM-50	1.3352	0.7867	0.6837	0.8152
BP-SILM-70	1.5520	0.8170	0.6607	0.8057

Ethyl acetate, ethanol and water

As illustrated in the column chart presented in Figure 3, the degrees of swelling of the BP-SILM-70 in pure ethyl acetate, ethanol and water were 0.27, 0.54 and 1.55 g/g membrane, respectively. The results indicate that the sorption capacity of the membrane was the highest in water, followed by ethanol and ethyl acetate. The χ_{im} values for ethyl acetate, ethanol and water were 1.32, 0.84, and 0.77, respectively. This finding indicates that the affinity of the membrane for these three components is in the following descending order: water, ethanol and ethyl acetate. Thus, the differences in membrane sorption capacity are simply due to the preference of the membrane to interact with these components. The sorption behaviour of BP-SILM-70 in water can be explained by the hydrogen bonds formed between [BF₄]⁻ anion with hydrogen atom in water and the imidazolium ring in [Bmin]⁺ cation with an oxygen atom in water. A similar interaction behaviour may also occur in ethanol. A relatively low sorption of ethyl acetate was observed in BP-SILM-70 due to its lower affinity with the membrane. This finding can be credited to the poor miscibility of ethyl acetate in [Bmim][BF₄].

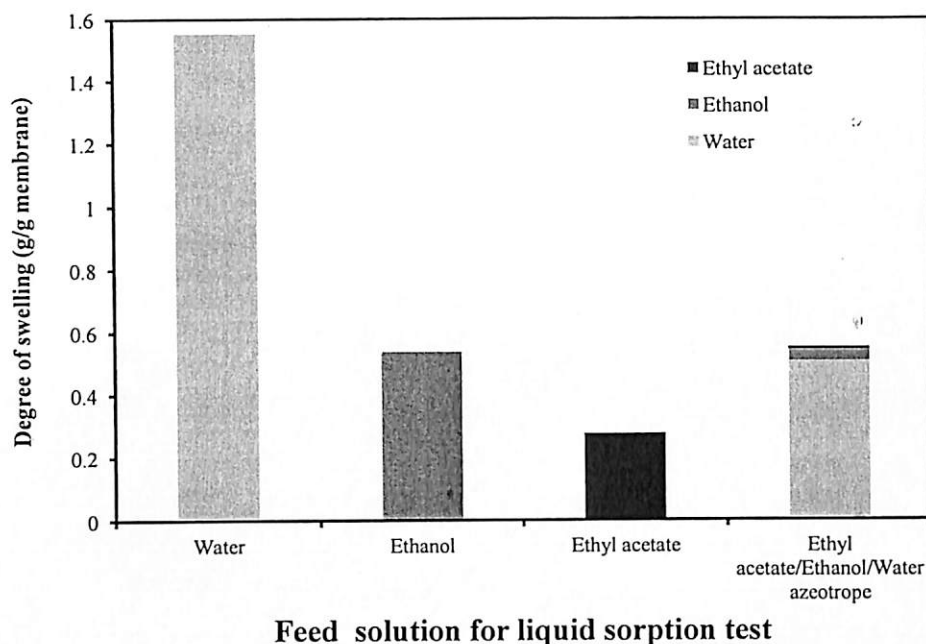


Figure 3: Degree of swelling of BP-SILM-70 at various feed solution conditions

When the BP-SILM-70 was immersed in the azeotropic mixture of ethyl acetate/ethanol/water, the membrane became swollen with a swelling degree of 0.55 g/g membrane. As clearly shown in Figure 3, the composition of the sorbed liquid predominantly consisted of water, which constituted 91.8 wt.% of the total composition of the sorption, whereas ethanol and ethyl acetate appear as minor components of the composition, with contents of 6.9 and 1.3 wt.%, respectively. This result can be attributed to the higher affinity of BP-SILM-70 for water as a result of the presence of [Bmim][BF₄]. Moreover, the strong interaction between ethyl acetate and ethanol would also weaken their capability to interact with the membrane [33], hence favouring the sorption of water. It can be noted that the sorption of ethanol was found to be approximately five-fold higher than that of ethyl acetate. This finding can be explained by the fact that ionic liquids tend to exhibit a greater attractive interaction with molecules of greater polarity [34].

Pervaporation dehydration of ethylene glycol/water binary mixtures

Effect of the [Bmim][BF₄] content in the BP-SILM

The pervaporation experiments were performed under the operating conditions of 10 wt.% water in the feed solution at 30°C and a downstream pressure of 5 mmHg. The impact of the

presence of BP was also studied by comparing the pervaporation performance between the pure PVA and the BP-PVA membranes. As depicted in Figure 4 (a) and (b), the permeation flux of BP-PVA was approximately three-fold higher than that of the pure PVA membranes, but the permeate concentration of water in BP-PVA was slightly lower, which lead to a lower separation factor as compared to the pure PVA membrane. When the pervaporation performances were compared in terms of the membrane intrinsic permeability, as showed in Figure 4 (c), the permeance of water and ethylene glycol in BP-PVA were approximately three-fold higher compared to pure PVA membrane; however the selectivity was considerably lower. This finding demonstrates that the presence of BP increases the permeability of the membrane due to the additional frictionless transport pathway for the permeation of molecules provided by the inner hollow core of the MWCNTs in the BP. The pervaporation performance can be further enhanced with the addition of [Bmim][BF₄]. As observed in Figure 4 (a), the partial permeation flux of water was substantially increased with increasing content of [Bmim][BF₄] in BP-SILM while the partial permeation flux of ethylene glycol remain almost constant. The increase in the [Bmim][BF₄] content improved the hydrophilicity of the membrane, which could facilitate the contact of water with the membrane surface. Additionally, the presence of [Bmim][BF₄] could contribute to a decrease in the mass transfer resistance, thus enabling the rapid permeation of the components through the membrane. Overall, the BP-SILM-70 exhibits the highest separation factor among these three BP-SILMs; therefore, the subsequent pervaporation studies were conducted using the BP-SILM-70.

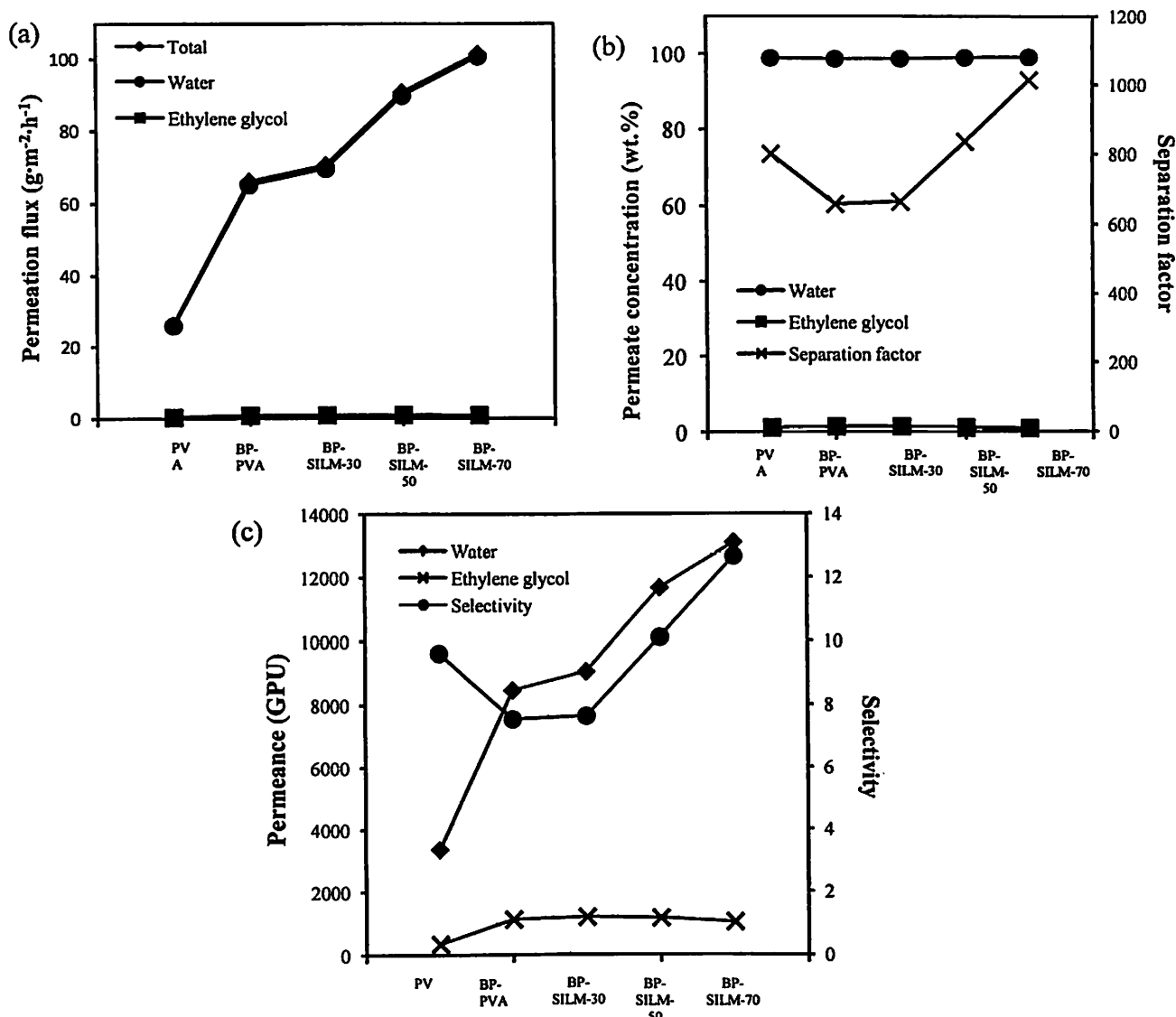


Figure 4: Effect of different type of membrane on the (a) permeation flux, (b) permeate concentration and separation factor and (c) permeance and selectivity in pervaporation separation of ethylene glycol/water

Effect of the feed concentration

The effect of the feed concentration on was studied using a feed water concentration in the range of 10 to 50 wt.% at 30°C and 5 mmHg. As shown in Figure 5 (a), the permeation flux was clearly increased with an increase in the feed water concentration, whereas the separation factor exhibited the opposite trend. At the lower feed water concentration, the high viscosity and slow motion of ethylene glycol provide a steric effect that hinders the transportation of water molecules. Furthermore, the high polarity of ethylene glycol may easily form hydrogen bonds

with water molecules and delay permeation of water. In addition, the lower water activity in the feed side also leads to lower permeation flux. On the other hand, an increase in the feed water concentration caused the BP-SILM-70 to promptly swell and eventually increased the free volume in the membrane; causing the membrane become susceptible to the permeation of both water and ethylene glycol molecules, thereby increased the permeation flux but compromising the separation factor. Figure 5 (b) clearly shows that the permeances of BP-SILM-70 are dependent on the concentration after eliminating the driving force contribution. Increasing the water concentration in the feed solution markedly increased the permeability for ethylene glycol and caused the membrane to be less water selective.

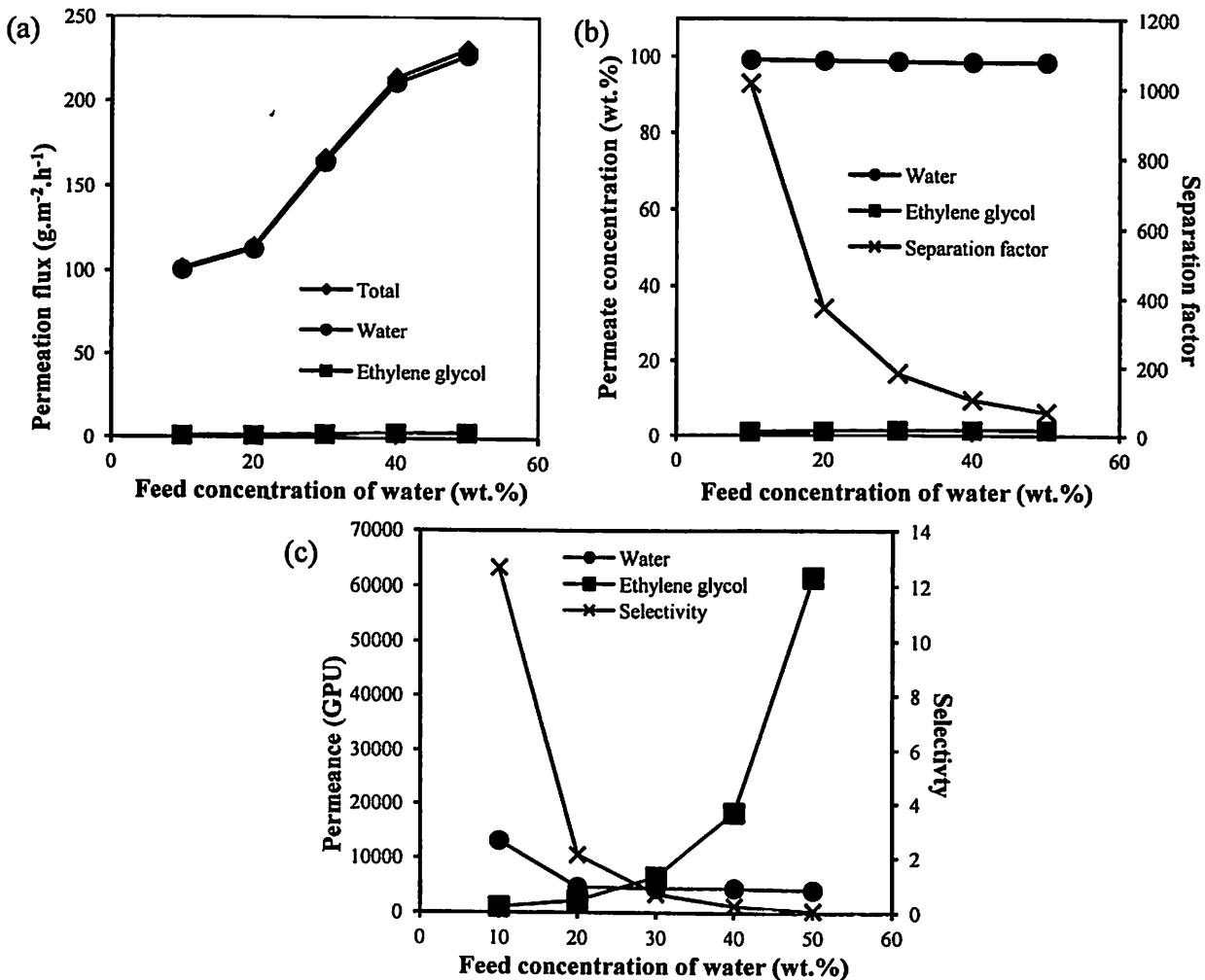
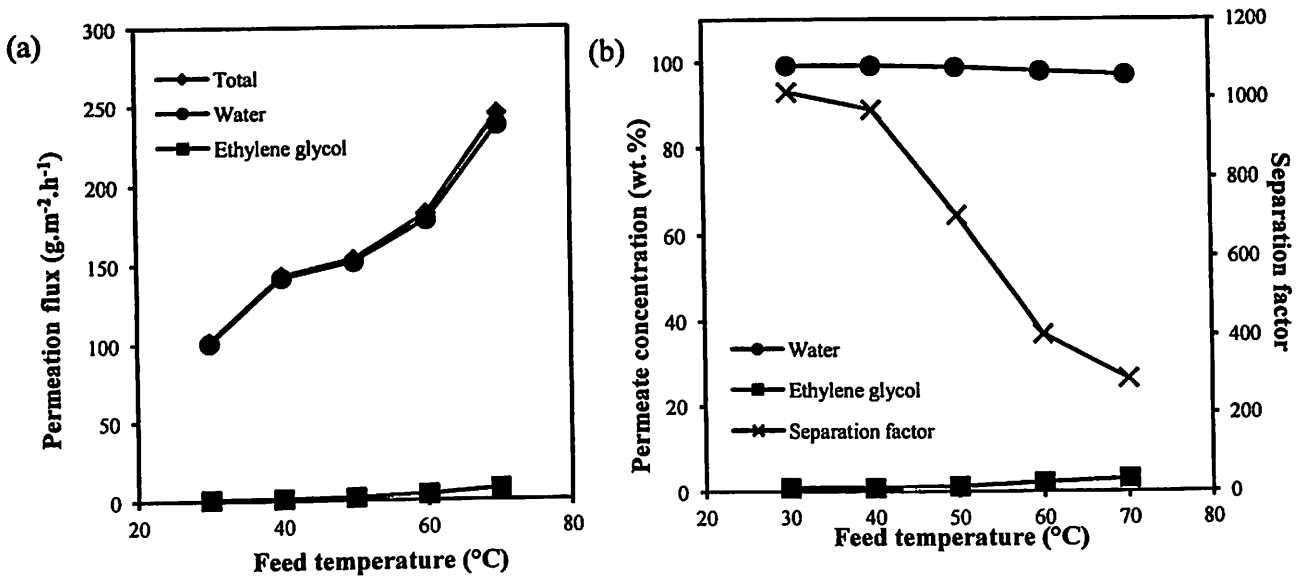


Figure 5: Effect of feed concentration of water on the (a) permeation flux, (b) permeate concentration and separation factor and (c) permeance and selectivity in pervaporation separation of ethylene glycol/water

Effect of the feed temperature

The effect of the feed temperature was investigated by varying the feed temperature from 30°C to 70°C at a feed water concentration of 10 wt.% and 5 mmHg. Based on the results shown in Figure 6 (a) and (b), the permeation flux progressively increased with increasing feed temperature, but the separation factor declined with increasing feed temperature. This behaviour could be the result of the ascending saturated vapour pressure of both water and ethylene glycol with elevated temperature. In addition, an increase in temperature caused the molecules to become sufficiently energetic to break the cohesive force and reduce the viscosity in the feed solution, thereby reducing the mass transport resistance at the membrane-feed solution interface. Moreover, the additional free volume spaces generated as a result of the increase in the thermal mobility of the molecule in the BP-SILM-70 at higher temperature also enhanced the permeation, but this effect was at the expense of decreasing the separation factor of the membrane. The permeance plot in Figure 6 (c) clearly depict an increase in feed temperature would decrease the permeance of water and ethylene glycol. However, a steeper decrease was observed in the permeance of water as compared to ethylene glycol, which implied the feed temperature has a more pronounce impact on the permeance of water, hence decrease the membrane selectivity for water.



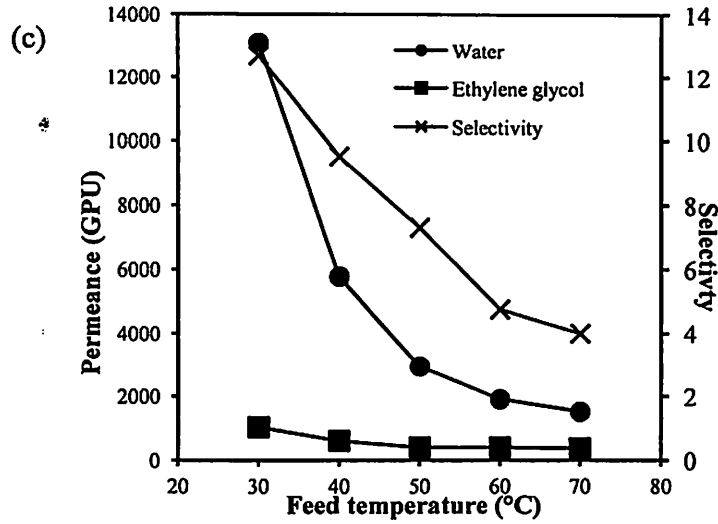


Figure 6: Effect of feed temperature on the (a) permeation flux, (b) permeate concentration and separation factor and (c) permeance and selectivity in pervaporation separation of ethylene glycol/water

The temperature dependence of the permeation flux and permeance were found to be described by an Arrhenius-type relationship:

$$J_i = J_{i0} \exp\left(-\frac{E_{Ji}}{RT}\right) \quad (8)$$

$$P_i = P_{i0} \exp\left(-\frac{E_{Pi}}{RT}\right) \quad (9)$$

where E_{Ji} represents the activation energy for the permeation of component i , which takes into account the impact of the driving force and E_{Pi} is the permeation activation energy that characterised the dependence of the membrane permeability on temperature. As shown in Figure 7 (a), the E_{Ji} values, which were obtained from the slope of a semi-logarithmic plot of the permeation flux as a function of the reciprocal of the absolute temperature ($1/T$), were 17 kJ/mol and 46 kJ/mol for the permeation of water and ethylene glycol, respectively. The obtained E_{Ji} values implied that the effect of temperature on the permeation of ethylene glycol is greater than that on the permeation of water. Thus, the E_{Ji} values explained the reduced separation factor of the membrane with increasing feed temperature.

However, note that both the membrane permeance and the selectivity were found to decrease at elevated feed temperatures. As shown in Figure 7 (b), the E_{Pi} values for water and ethylene glycol were -43 kJ/mol and -21 kJ/mol, respectively. According to the solution-

diffusion mechanism, the permeance was based on the diffusion and sorption of the permeating component; for this reason, the permeation activation energy is the total of the heat of sorption and the activation energy for diffusion [35]. In most cases, the sorption is usually an exothermic process, whereas the diffusion is generally endothermic; therefore, the negative permeation activation energy appears to suggest that the membrane permeance is governed by the exothermic sorption process. Thus, the decreasing permeance observed with elevated temperature may be due to the reduction in sorption. This finding can be explained by the fact that the molecules are energetic at higher temperatures, which results in the molecules being more disordered and highly dispersed, thereby reducing the possibilities for each molecule to interact with the membrane.

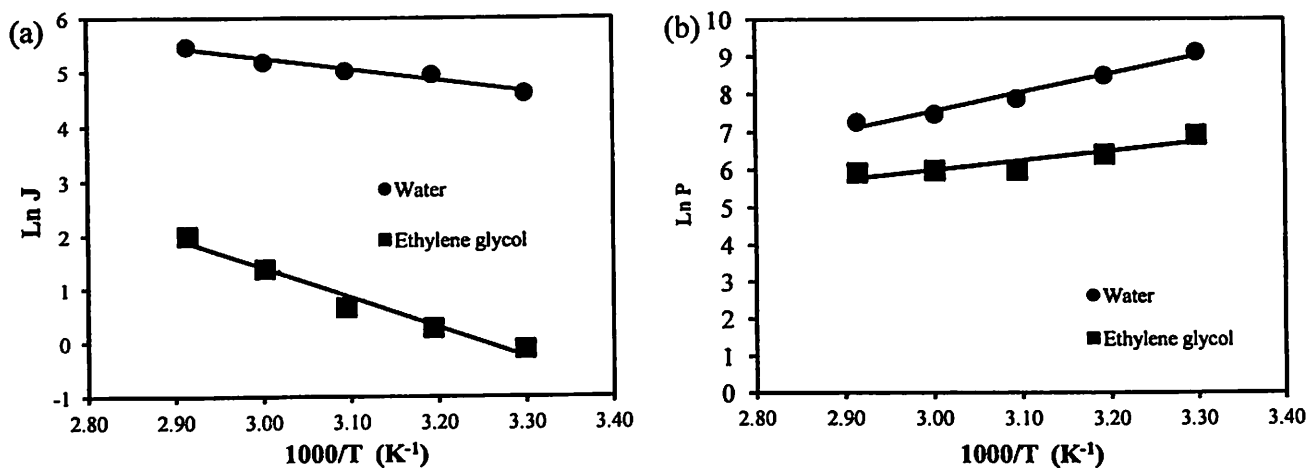


Figure 7: Arrhenius plot of (a) the permeation flux and (b) the permeance.

Pervaporation dehydration of ethyl acetate/ethanol/water ternary azeotropic mixtures

The pervaporation data summarized in Table 5 clearly demonstrate the capability of BP-SILM-70 to dehydrate the ternary azeotropic mixture of ethyl acetate, ethanol and water via a pervaporation process. The permeation flux and permeate concentration showed that water appeared to be a major component in the permeate, followed by ethanol and ethyl acetate. Moreover, the separation factor as well as the permeance and selectivity also indicate the high preference of the membrane for the permeation of water. According to the solution-diffusion mechanism, the separation ability of the membrane is dependent on both its sorption selectivity and diffusion selectivity [36]. However, the data shown in Table 5 clearly suggest that the

permeation in BP-SILM-70 is governed by the sorption process because the sorption selectivity of BP-SILM-70 for water is apparently higher than the diffusion selectivity. This finding can be attributed to the limited interaction between ethyl acetate and [Bmim][BF₄] in BP-SILM-70, and the tendency of ethanol to form interactions with ethyl acetate, which in turn promotes the permeability of water in BP-SILM-70.

Table 5: Performance of BP-SILM-70 for the pervaporation of the ternary azeotropic mixture of ethyl acetate/ethanol/water at 30°C and 5 mmHg.

<u>Ethyl acetate/ethanol/water</u>	
Feed concentration (wt.%)	82.6/8.4/9
<u>Permeation flux (g·m⁻²·h⁻¹)</u>	
Total	385.33
Ethyl acetate	5.09
Ethanol	10.09
Water	370.16
<u>Permeate concentration (wt. %)</u>	
Ethyl acetate	1.32
Ethanol	2.62
Water	96.06
<u>Permeance (Gpu)</u>	
Ethyl acetate	3.94
Ethanol	118.56
Water	4729.93
Separation factor, β	246.65
β_{Sorp}	113.20
β_{Diff}	2.18
Selectivity	38.61

Effect of the feed temperature

The feed temperature was varied from 30 to 70°C with a constant downstream pressure of 5 mmHg. As shown in Figure 8 (a), the permeation fluxes of ethyl acetate, ethanol and water gradually increased as the feed temperature was increased from 30 to 70°C, thereby increasing the overall permeation flux. On the other hand, as observed in Figure 8 (b), the permeate concentration of water was steadily decreased and the concentrations of ethyl acetate and ethanol were slightly increased with elevations in the feed temperature. This eventually caused a decline in the separation factor of BP-SILM-70 for water with an increase in the feed temperature. In general, an increase in the feed temperature would increase the partial pressure of ethyl acetate, ethanol and water on the feed side as a result of increases in their vapour pressures at higher temperature. This increase would therefore induce a greater driving force for the permeation of these three components across the membrane. Moreover, an increase in the feed temperature may also supply the necessary energy to break the cohesive forces within the molecules in the feed mixtures and accelerate their mobility in the membrane. In addition, thermal expansion in the membrane would generate free volume in the membrane, which would allow easier permeation of the molecules. Thus, the combination of all of these effects explains the increase in permeation flux obtained with an increase in the feed temperature at the cost of reducing the separation factor of the membrane for water. Based on the plot of the permeance as a function of the feed temperature presented in Figure 8 (c), the permeance of water is apparently higher than the permeance of ethanol and ethyl acetate, which implies the preference of the membrane for the permeation of water compared with ethanol and ethyl acetate. However, with an increase in the feed temperature, the permeance of water steeply decreased, whereas slight decreases in the permeance values of both ethanol and ethyl acetate were obtained. The steep decrease in the permeance of water obtained with an increase in the feed temperature eventually decreased the selectivity of the membrane for water.

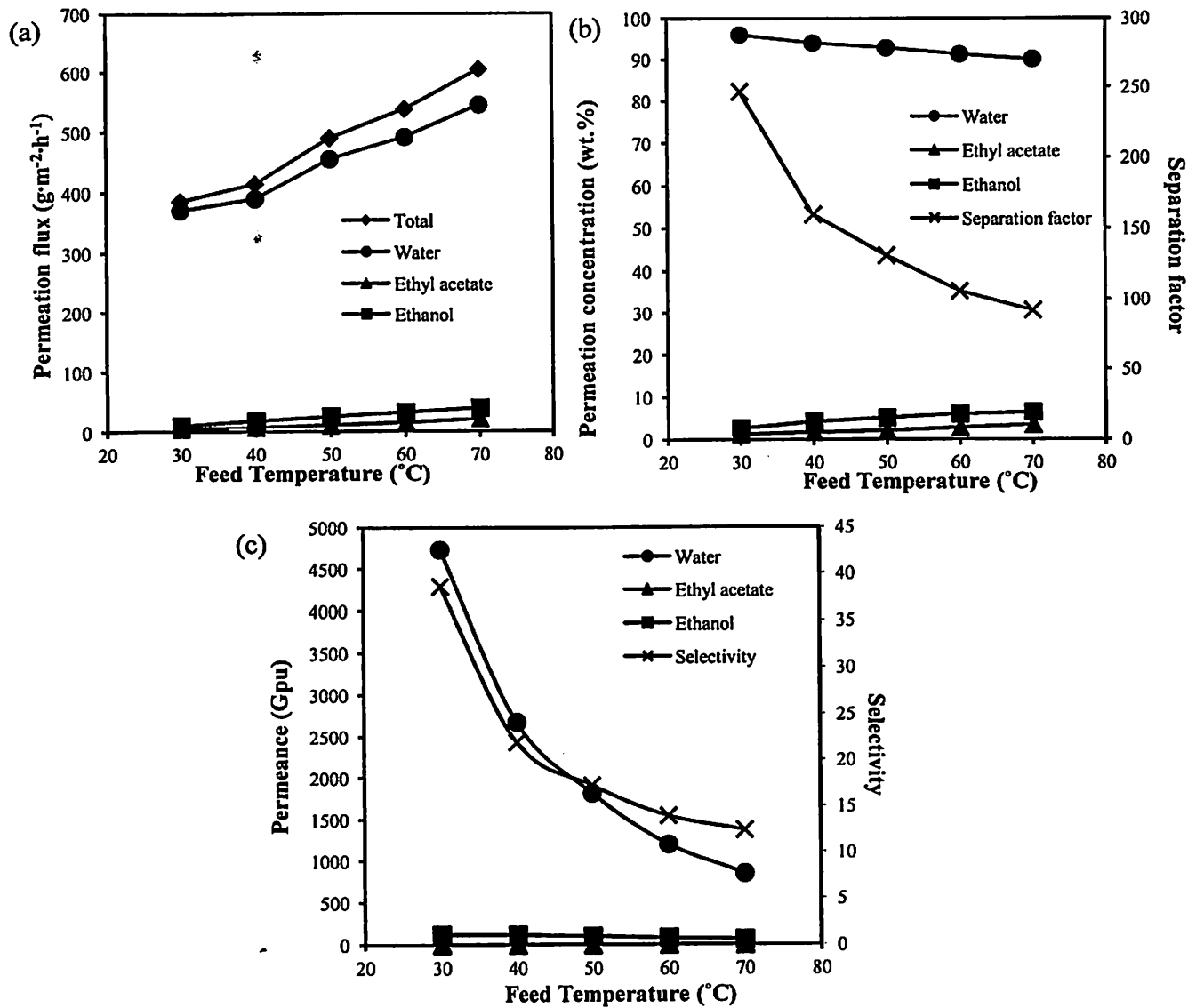


Figure 8: Effect of the feed temperature on the (a) permeation flux, (b) permeate concentration and separation factor and (c) permeance and selectivity in the separation of the ternary azeotropic mixture of ethyl acetate/ethanol/water through pervaporation.

The temperature dependence of the permeation flux and permeance were also expressed through Arrhenius relations and the activation energies, E_{ji} and E_{Pi} , were determined from the slope of the Arrhenius plot presented in Figure 9 and are summarized in Table 6.

Table 6: Activation energy, E_{ji} and E_{Pi} , for ethyl acetate, ethanol and water

	Activation energy (kJ/mol)	
	E_{ji}	E_{Pi}
Ethyl acetate	30.87	-3.24
Ethanol	28.78	-13.27
Water	8.64	-36.69

Based on the data shown in Table 6, the activation energies for both E_{ji} and E_{Pi} , respectively, were in the ascending order of water followed by ethanol and ethyl acetate. The highest E_{ji} value obtained in ethyl acetate imply that the permeation flux of ethyl acetate is more sensitive to variation in feed temperature. In spite of this, the smallest E_{ji} values obtained in water may reflect its higher affinity with the membrane. This may rise from the fact that activation energy can be thought as the minimum energy required for permeation and the smallest activation energy enables the water to easily permeate through the membrane. On the other hand, the lowest E_{Pi} value obtained in water indicates a strong temperature dependence on the permeance of water. As mentioned earlier, the negative E_{Pi} value obtained denotes to the dominant of dissolution process in permeance and caused the decrease of permeance with increasing feed temperature.

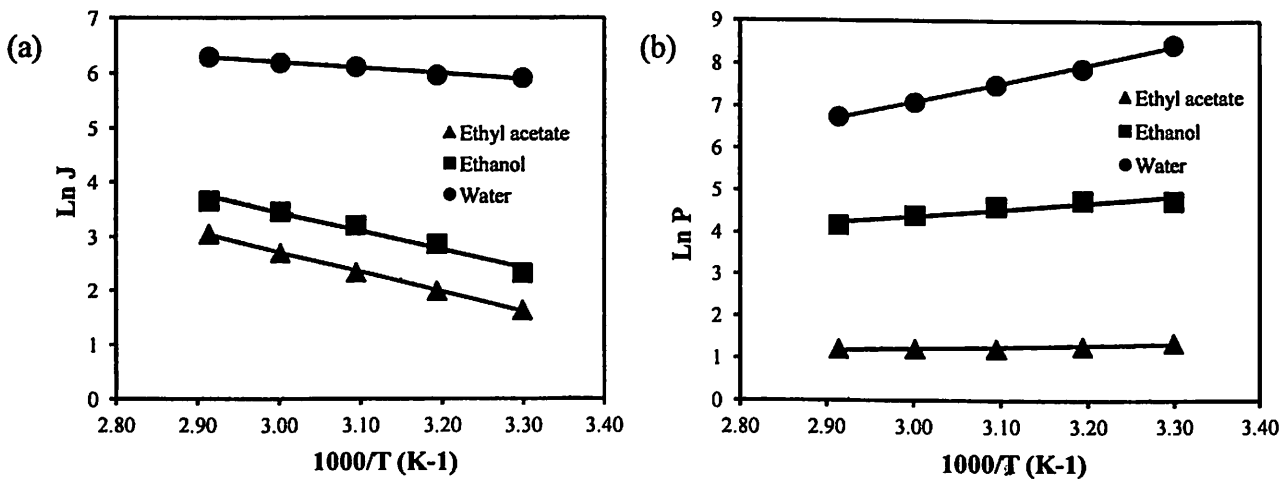
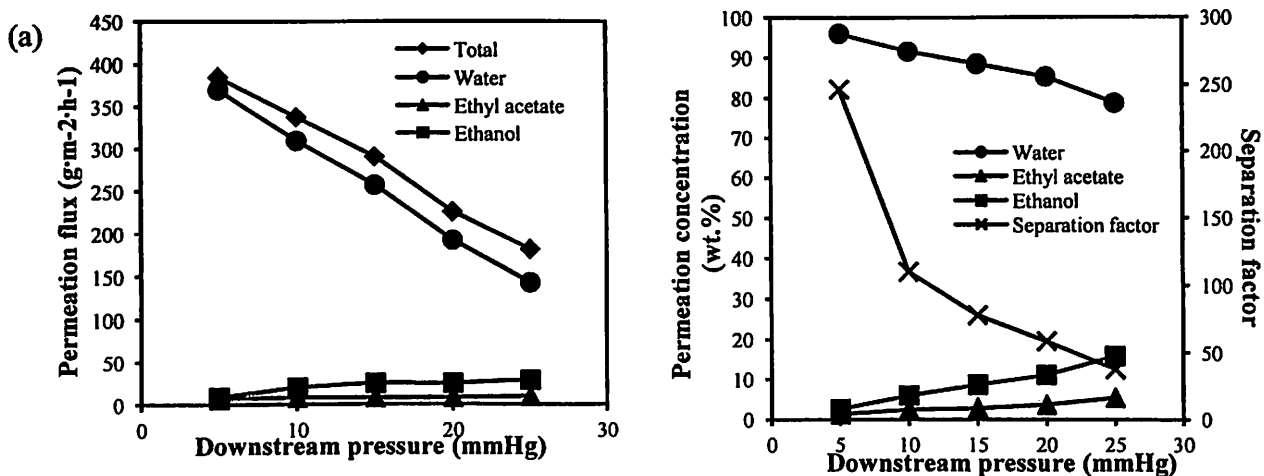


Figure 9: Semi-logarithmic Arrhenius plot of the (a) permeation flux and (b) permeance obtained for separation of the ternary azeotropic mixture of ethyl acetate/ethanol/water through pervaporation as a function of the reciprocal of the absolute temperature.

Effect of the downstream pressure

The downstream pressure was varied from 5 to 25 mmHg while the feed temperature was maintained at 30 °C. As clearly demonstrated in Figure 10 (a), the permeation flux of water was markedly decreased and the permeation fluxes of ethanol and ethyl acetate were slightly increased with increases in the downstream pressure. The permeate concentration of water, as observed in Figure 10 (b), was decreased whereas the permeate concentrations of ethyl acetate and ethanol were increased. Accordingly, the separation factor of the membrane for water decreased with an increase in the downstream pressure.

An increase in downstream pressure will lower the driving force created between the feed and permeate sides of the membrane. This may slow the diffusion and desorption rates of a component across the membrane and may cause a reduction in the permeation flux. However, the increases in the permeation fluxes of ethyl acetate and ethanol obtained with increases in the downstream pressure can be explained by their intrinsic permeability in the membrane. The plot of the permeance in Figure 10 (c), demonstrates that the permeance of water, ethanol and ethyl acetate gradually increased with increases in the downstream pressure. The reduced driving force obtained as a result of increases in the downstream pressure would definitely hinder the diffusivity of a component and its desorption from the membrane, which would cause the sorbed components to be trapped inside the membrane. As discussed earlier, the sorbed components (mainly water molecules due to their higher affinity may cause the membrane swelling, thereby increasing the solubility and permeability of both ethyl acetate and ethanol in the membrane but compromised the separation factor and selectivity of the membrane for water.



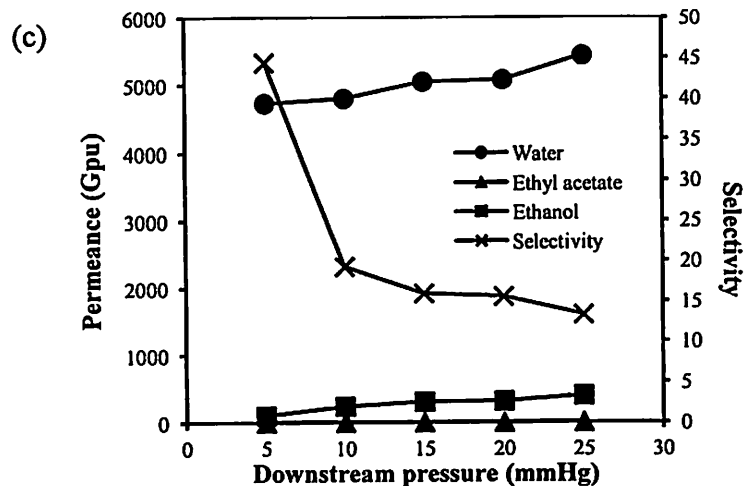


Figure 10: Effect of the downstream pressure on the (a) permeation flux, (b) permeate concentration and separation factor and (c) permeance and selectivity in the separation of the ternary azeotropic mixture of ethyl acetate/ethanol/water through pervaporation.

Membrane stability in binary and ternary mixtures pervaporation

In this study, the stability of the BP-SILM-70 was assessed by continuous operation for 120 hours with 10 wt.% feed concentration of water at 30 °C and the downstream pressure was maintained at 5 mmHg. A fresh feed mixture was prepared at every 12 hours of operation. As shown in Figure 11, the BP-SILM-70 demonstrated a robust pervaporation performance over an operating period of 120 hours in both the binary and ternary mixtures pervaporation. The permeation fluxes were within 5% of deviation. Because of the separation factor of the membrane is very sensitive toward a small changes in the permeate concentration of water, the permeate concentration of water was used to evaluate the stability of the membrane. It is clearly showed that the water permeate concentration were not more than 5% error. In addition, it is interesting to note that there was no significant change in the weight of the BP-SILM-70 throughout the operating periods. The result implied a considerably good long-term physical stability exhibited in BP-SILM-70 without any significant loss of the liquid membrane. This can be credited to the formation of stable compound as a result of the blending of the [Bmim][BF₄] with PVA which enable the [Bmim][BF₄] to be strongly held inside the interstitial pores of BP and withstand its displacement from the BP under higher transmembrane pressure condition. Apart from that, the good stability in the BP-SILM-70 can also attributed to the use of BP as a

membrane support. The highly tortuous porous structure and smaller interstitial pore size in BP could aid in securing the immobilized liquid membrane.

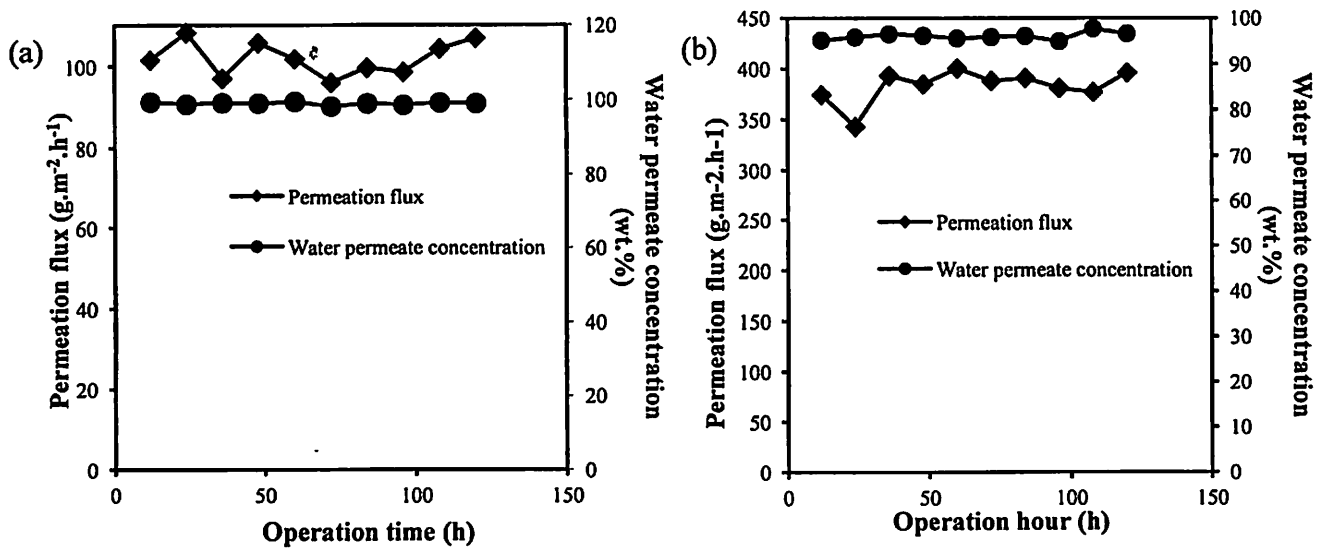


Figure 11: Pervaporation performances of BP-SILM-70 of (a) ethylene glycol/ water binary mixtures and (b) ethyl acetate/ethanol/water ternary azeotropic mixture for 120 h operation time

Conclusions

A novel symmetric SILM was successfully prepared by infiltrating BP with a [Bmim][BF₄]-PVA blend to form a BP-SILM. The immobilisation via a vacuum-based technique allowed the entrapment of the [Bmim][BF₄]-PVA inside the deeper interstitial pores of the BP. The structure of the BP-SILM, in which the support and selective membrane layer of BP-SILM are merged into a single layer to form a symmetric membrane, was found to be different from structure of conventional asymmetric membranes. This novel structure reduced the overall membrane thickness and mass transport resistance. In addition, the use of BP as a support enhanced the thermal and mechanical stability of the BP-SILM and improved the immobilised capacity of the [Bmim][BF₄]-PVA, which can be attributed to the presence of a tortuous pore structure and the small interstitial pore size of the BP. The interaction of BP-SILM with water was found to increase with an increase in the content of [Bmim][BF₄] because the presence of a higher content of [Bmim][BF₄] significantly improved the hydrophilicity of the BP-SILM. The novel BP-SILM was successfully applied in the pervaporation of ethylene glycol/water binary mixture and ethyl acetate/ethanol/water ternary azeotropic mixture. The presence of BP provided an additional

transport pathway to enhance the permeation of the BP-SILM. A higher content of [Bmim][BF₄] in BP-SILM improved the pervaporation performance. The optimum pervaporation performance was obtained using the BP-SILM-70. The BP-SILM demonstrated considerably good membrane stability and a robust performance for an operating period of 120 hours.

Acknowledgments

The authors acknowledge MyPhD fellowships provided by the Ministry of Higher Education of Malaysia. This research work was financially supported by Universiti Sains Malaysia Research University (RU) grant (A/C: 814142) and the Postgraduate Research Grant Scheme (PRGS) (A/C: 8045034).

References

- [1] M.N. Hyder, P. Chen, Pervaporation dehydration of ethylene glycol with chitosan-poly(vinyl alcohol) blend membranes: Effect of CS-PVA blending ratios, *J. Membr. Sci.*, 340 (2009) 171-180.
- [2] M. Shahverdi, T. Mohammadi, A. Pak, Separation of ethylene glycol-water mixtures with composite poly(vinyl alcohol)-polypropylene membranes, *J. Appl. Polym. Sci.*, 119 (2011) 1704-1710.
- [3] P.S. Rao, S. Sridhar, Y.W. Ming, A. Krishnaiah, Pervaporative separation of ethylene glycol/water mixtures by using cross-linked chitosan membranes, *Ind. Eng. Chem. Res.*, 46 (2007) 2155-2163.
- [4] A.S. Reddy, N.S. Kumar, M.V. Subbaiah, M. Suguna, A. Krishnaiah, Maleic anhydride crosslinked alginate-chitosan blend membranes for pervaporation of ethylene glycol-water mixtures, *Journal of Macromolecular Science, Part A: Pure and Applied Chemistry*, 46 (2009) 1069-1077.
- [5] H. Dogan, N.D. Hilmioglu, Chitosan coated zeolite filled regenerated cellulose membrane for dehydration of ethylene glycol/water mixtures by pervaporation, *Desalination*, 258 (2010) 120-127.
- [6] R. Guo, X. Ma, C. Hu, Z. Jiang, Novel PVA-silica nanocomposite membrane for pervaporative dehydration of ethylene glycol aqueous solution, *Polymer*, 48 (2007) 2939-2945.
- [7] J. Yu, H. Li, H. Liu, Recovery of acetic acid over water by pervaporation with a combination of hydrophobic ionic liquids, *Chem. Eng. Commun.*, 193 (2006) 1422-1430.
- [8] D. Yongquan, W. Ming, C. Lin, L. Mingjun, Preparation, characterization of P(VDF-HFP)/[bmim] BF₄ ionic liquids hybrid membranes and their pervaporation performance for ethyl acetate recovery from water, *Desalination*, 295 (2012) 53-60.
- [9] H. Cascon, S. Choudhary, Separation Performance and Stability of PVDF-co-HFP/Alkylphosphonium Dicyanamide Ionic Liquid Gel-Based Membrane in Pervaporative Separation of 1-Butanol, *Separation Science and Technology (Philadelphia)*, 48 (2013) 1616-1626.

- [10] S. Heitmann, J. Krings, P. Kreis, A. Lennert, W.R. Pitner, A. Górak, M.M. Schulte, Recovery of n-butanol using ionic liquid-based pervaporation membranes, *Sep. Purif. Technol.*, (2012).
- [11] A. Plaza, G. Merlet, A. Hasanoglu, M. Isaacs, J. Sanchez, J. Romero, Separation of butanol from ABE mixtures by sweep gas pervaporation using a supported gelled ionic liquid membrane: Analysis of transport phenomena and selectivity, *J. Membr. Sci.*, 444 (2013) 201-212.
- [12] A.B. Beltran, G.M. Nisola, E.L. Vivas, W. Cho, W.J. Chung, Poly(octylmethylsiloxane)/oleyl alcohol supported liquid membrane for the pervaporative recovery of 1-butanol from aqueous and ABE model solutions, *Journal of Industrial and Engineering Chemistry*, 19 (2013) 182-189.
- [13] P. Izák, W. Ruth, Z. Fei, P.J. Dyson, U. Kragl, Selective removal of acetone and butan-1-ol from water with supported ionic liquid-polydimethylsiloxane membrane by pervaporation, *Chem. Eng. J.*, 139 (2008) 318-321.
- [14] Y. Qin, J.P. Sheth, K.K. Sirkar, Pervaporation membranes that are highly selective for acetic acid over water, *Ind. Eng. Chem. Res.*, 42 (2003) 582-595.
- [15] Y. Qin, J.P. Sheth, K.K. Sirkar, Supported liquid membrane-based pervaporation for VOC removal from water, *Ind. Eng. Chem. Res.*, 41 (2002) 3413-3428.
- [16] M. Matsumoto, Y. Murakami, K. Kondo, Separation of 1-Butanol by Pervaporation Using Polymer Inclusion Membranes Containing Ionic Liquids, *Solvent Extr. Res. Dev.-Jpn.*, 18 (2011) 75-83.
- [17] Q. Gan, D. Rooney, M. Xue, G. Thompson, Y. Zou, An experimental study of gas transport and separation properties of ionic liquids supported on nanofiltration membranes, *J. Membr. Sci.*, 280 (2006) 948-956.
- [18] P. Izák, M. Köckerling, U. Kragl, Stability and selectivity of a multiphase membrane, consisting of dimethylpolysiloxane on an ionic liquid, used in the separation of solutes from aqueous mixtures by pervaporation, *Green Chem.*, 8 (2006) 947-948.
- [19] L.C. Branco, J.G. Crespo, C.A.M. Afonso, Studies on the selective transport of organic compounds by using ionic liquids as novel supported liquid membranes, *Chemistry - A European Journal*, 8 (2002) 3865-3871.
- [20] T. He, Towards stabilization of supported liquid membranes: preparation and characterization of polysulfone support and sulfonated poly (ether ether ketone) coated composite hollow fiber membranes, *Desalination*, 225 (2008) 82-94.
- [21] A.I. López-Lorente, B.M. Simonet, M. Valcárcel, The potential of carbon nanotube membranes for analytical separations, *Anal. Chem.*, 82 (2010) 5399-5407.
- [22] C.J. Frizzell, M. In Het Panhuis, D.H. Coutinho, K.J. Balkus, A.I. Minett, W.J. Blau, J.N. Coleman, Reinforcement of macroscopic carbon nanotube structures by polymer intercalation: The role of polymer molecular weight and chain conformation, *Physical Review B - Condensed Matter and Materials Physics*, 72 (2005) 1-8.
- [23] C. Liu, Y.Y. Fan, M. Liu, H.T. Cong, H.M. Cheng, M.S. Dresselhaus, Hydrogen storage in single-walled carbon nanotubes at room temperature, *Science*, 286 (1999) 1127-1129.
- [24] R.H. Baughman, C. Cui, A.A. Zakhidov, Z. Iqbal, J.N. Barisci, G.M. Spinks, G.G. Wallace, A. Mazzoldi, D. De Rossi, A.G. Rinzler, O. Jaschinski, S. Roth, M. Kertesz, Carbon nanotube actuators, *Science*, 284 (1999) 1340-1344.
- [25] P. Dharap, Z. Li, S. Nagarajaiah, E.V. Barrera, Nanotube film based on single-wall carbon nanotubes for strain sensing, *Nanotechnology*, 15 (2004) 379-382.

- [26] U. Vohrer, I. Kolaric, M.H. Haque, S. Roth, U. Detlaff-Weglikowska, Carbon nanotube sheets for the use as artificial muscles, *Carbon*, 42 (2004) 1159-1164.
- [27] K.F. Yee, Y.T. Ong, A.R. Mohamed, S.H. Tan, Novel MWCNT-buckypaper/polyvinyl alcohol asymmetric membrane for dehydration of etherification reaction mixture: Fabrication, characterisation and application, *J. Membr. Sci.*, 453 (2014) 546-555.
- [28] R. Guo, C. Hu, B. Li, Z. Jiang, Pervaporation separation of ethylene glycol/water mixtures through surface crosslinked PVA membranes: Coupling effect and separation performance analysis, *J. Membr. Sci.*, 289 (2007) 191-198.
- [29] A. Ballistreri, S. Foti, G. Montaudo, E. Scamporrino, Evolution of aromatic compounds in the thermal decomposition of vinyl polymers, *Journal of polymer science. Part A-1, Polymer chemistry*, 18 (1980) 1147-1153.
- [30] C. Chiappe, D. Pieraccini, Ionic liquids: Solvent properties and organic reactivity, *Journal of Physical Organic Chemistry*, 18 (2005) 275-297.
- [31] T. Singh, A. Kumar, Fluorescence behavior and specific interactions of an ionic liquid in ethylene glycol derivatives, *Journal of Physical Chemistry B*, 112 (2008) 4079-4086.
- [32] S. Trivedi, S. Pandey, Interactions within a [ionic liquid + poly(ethylene glycol)] mixture revealed by temperature-dependent synergistic dynamic viscosity and probe-reported microviscosity, *Journal of Physical Chemistry B*, 115 (2011) 7405-7416.
- [33] D.L. Zhang, Y.F. Deng, C.B. Li, J. Chen, Separation of ethyl acetate - ethanol azeotropic mixture using hydrophilic ionic liquids, *Ind. Eng. Chem. Res.*, 47 (2008) 1995-2001.
- [34] F. Mutelet, J.N. Jaubert, M. Rogalski, M. Boukherissa, A. Dicko, Thermodynamic properties of mixtures containing ionic liquids: Activity coefficients at infinite dilution of organic compounds in 1-propyl boronic acid-3-alkylimidazolium bromide and 1-propenyl-3-alkylimidazolium bromide using inverse gas chromatography, *J. Chem. Eng. Data*, 51 (2006) 1274-1279.
- [35] X. Feng, R.Y.M. Huang, Liquid Separation by Membrane Pervaporation: A Review, *Ind. Eng. Chem. Res.*, 36 (1997) 1048-1066.
- [36] J. Ma, M. Zhang, Z. Jiang, M. Nie, G. Liu, Facile fabrication of structurally stable hyaluronic acid-based composite membranes inspired by bioadhesion, *J. Membr. Sci.*, 364 (2010) 290-297.
- [37] Y.T. Ong, S.H. Tan, Synthesis of the novel symmetric buckypaper supported ionic liquid membrane for the dehydration of ethylene glycol by pervaporation, *Sep. Purif. Technol.*, 143 (2015) 135-145.